

# Method and Procedure in Metal Detection and Distinctive Discrimination of Size, Shape, and Location of Hidden Single and Multi-Material Targets

THÈSE N° 7759 (2017)

PRÉSENTÉE LE 21 AOÛT 2017

À LA FACULTÉ DES SCIENCES ET TECHNIQUES DE L'INGÉNIEUR

LABORATOIRE D'ACTIONNEURS INTÉGRÉS

PROGRAMME DOCTORAL EN ROBOTIQUE, CONTRÔLE ET SYSTÈMES INTELLIGENTS

ÉCOLE POLYTECHNIQUE FÉDÉRALE DE LAUSANNE

POUR L'OBTENTION DU GRADE DE DOCTEUR ÈS SCIENCES

PAR

**Chafic ABU ANTOUN**

acceptée sur proposition du jury:

Prof. J. A. Schiffmann, président du jury  
Prof. Y. Perriard, Dr C. Köchli, directeurs de thèse  
Prof. B. Dehez, rapporteur  
Prof. C. Würsch, rapporteur  
Prof. A. Skrivervik, rapporteuse



ÉCOLE POLYTECHNIQUE  
FÉDÉRALE DE LAUSANNE

Suisse  
2017



# Acknowledgements

Firstly, I would like to express my sincere gratitude to my thesis director Prof. Yves Perriard and my thesis supervisor Dr. Christian Köchli for the continuous support of my Ph.D. study and related research, for their direction, patience, motivation, and immense knowledge. Their guidance helped me in all the time of research and writing of the papers, journals and this thesis.

Besides my advisors, I would like to thank the rest of my thesis exam jury: Prof. Jürg Alexander Schiffmann, Prof. Anja Skrivervik, and Prof. Christoph Würsch, for their challenging questions and constructive suggestions, but also for the trust they held to me, which planted an extra amount of confidence and motivation in me.

My sincere thanks also go to Dr. Torsten Gogolla, Mr. Dietmar Schoenbeck, and Dr. Geert Kalusche who provided me an opportunity to join their projects. They gave me access to the experiments and opened the way for fruitful discussions. Without their precious support, it would not have been possible to conduct this research.

Additional special gratitude goes to Prof. Christoph Würsch, who was always an inspiration, source of motivation, and a real dreamer. I could not have imagined having a better support especially during hard times concerning the focus on my work.

A final appreciativeness will always be devoted to Hilti AG for the chance it gave me to pursue my advanced studies as well as the flexibility and support through my doctoral studies that I did in parallel to my current job, especially Dr. Till Cramer, and Dr. Andreas Bong, who had to take decisions in that direction. Deep and warm thanks go specially to Mr. Ralph Lohner for being always on my side.

Privately I would like to thank my precious Georgette Makary for being comprehensible and always supportive not only during this period but the last 18 years as well. She is the one who shaped me to be who I am now. I cannot except send my gratitude to my friends Dr. Sigrid Andreae, Dr. Nadine Poser, and Ms. Anja Weigand Meier for being there for me around the clock and forever.

I close with a moment of silence reaching to my absent father who taught me the meaning and purpose of life. I owe him myself and every positive step in my current life.

Lausanne, 12 June 2017

*This work is dedicated to Nabil.*

# Abstract

This work provides a procedure and methodology for the design of an electromagnetic sensor based on induction due to ferromagnetic and pure electrically conductive hidden targets. The electromagnetic sensor is made of one or several excitation coils, which induce eddy currents in the target(s) and one or several sensing coils, which measure the target response. The latter signals are then processed to obtain the wanted properties of the target. Detection by induction at radio frequencies (medium frequencies) is famous for its relative simplicity, cost effective, and precise size discrimination but has disadvantages mainly in signal strength (especially for far hidden targets) and it is less effective in material discrimination in the case where multi-material targets are present. The presented methodology links three main design fields: excitation, sensor design, and post-processing. Its objective is to improve detection by induction in allowing for selectivity in detection or the possibility to distinctively detect targets made of different materials. Implemented simulation models together with experimental verification led to a highly improved procedure in target feature discrimination. Features are defined here as: size, depth, location, and even material of the target(s). A forward model helped in linking the physical aspects of the defined targets to mathematical parametrized equations that contributed easily in a flexible discrete inverse model for both transient (pulse induction) and time harmonic (harmonic induction). Feature discrimination is a necessary step to reach the final aim defined here as distinctive detection. It means being able to distinguish between single material targets and mixed material targets at the same time and still discriminate their features. The proposal is flexible even for relative target orientation, robust in changing environmental conditions, reliable even for relatively far targets, balanced and robust to overcome manufacturing tolerances, precise enough to meet industrial sensor specifications of such technology, and can combine different excitations with their benefits and give the required outcome selectively.

## Keywords

Electromagnetic, induction, quasi-static, sensor, pulse induction, harmonic excitation, finite element, dipole model, optimization, material discrimination, distinctive detection.

# Résumé

Ce travail présente une méthodologie pour la conception d'un capteur électromagnétique basé sur l'induction magnétique créée par des objets cibles cachés ayant des propriétés ferromagnétiques ou électriquement conductrices. Ce capteur est constitué d'une ou plusieurs bobines excitatrices qui induisent des courants de Foucault dans l'objet cible ainsi que d'une ou plusieurs bobines réceptrices qui en mesurent les effets. Les signaux captés par ces dernières sont ensuite traités pour en déduire les propriétés recherchées. La détection par induction à fréquences radio (fréquences moyennes) est connue pour sa relative simplicité, son faible coût et sa capacité à effectuer des estimations géométriques précises. Par contre, cette technique est moins adaptée à la détection d'objets éloignés en raison de la faiblesse du signal qu'ils émettent. Elle est également moins efficace dans les cas où il y a plusieurs objets qui sont constitués de matériaux différents. La méthodologie de ce travail lie les principaux champs de conception du capteur : excitation, mesure de la réponse et traitement du signal mesuré. Son objectif est de pouvoir améliorer la détection par induction en permettant la sélectivité de la détection : à savoir la possibilité de détecter séparément les objets de matériaux différents. Des modèles de simulation couplés avec une validation expérimentale ont conduit à une amélioration significative de la procédure de discrimination des propriétés des objets cachés. Ces dernières sont sa taille, sa position et le matériau dont il est constitué. Afin de pouvoir les déterminer, un modèle mathématique décrivant plusieurs aspects physiques des objets cibles par des équations paramétriques simples a été développé. Il a ensuite été possible d'extraire les propriétés des objets cibles à partir des réponses mesurées en combinant les deux modes d'excitation : transitoire (par impulsion) et harmonique. Grâce à cette méthode, il est possible de mesurer des configurations comprenant plusieurs objets, de matériaux potentiellement différents de manière distincte et de déterminer les propriétés de chacun. La méthode de détection proposée est flexible quant à l'orientation relative de l'objet cible, robuste aux conditions concernant son environnement, fiable pour la mesure d'objets relativement éloignés, peu sensible aux tolérances de fabrication et suffisamment précise pour correspondre aux standards industriels applicables. De plus, elle permet de combiner les avantages de plusieurs excitations pour obtenir les propriétés des objets de divers matériaux de manière sélective.

## Mots-clés

Electromagnétique, induction, quasi-statique, capteur, excitation par impulsion, excitation harmonique, éléments finis, modèle par dipôle, optimisation, discrimination des matériaux, détection spécifique.

# Contents

<b>Acknowledgements</b> .....	<b>iii</b>
<b>Abstract</b> .....	<b>v</b>
<b>Keywords</b> .....	<b>v</b>
<b>Résumé</b> .....	<b>vi</b>
<b>Mots-clés</b> .....	<b>vi</b>
<b>Contents</b> .....	<b>vii</b>
<b>List of Figures</b> .....	<b>x</b>
<b>List of Tables</b> .....	<b>xiv</b>
<b>List of Equations</b> .....	<b>xv</b>
<b>Chapter 1 Introduction</b> .....	<b>17</b>
1.1 Objective.....	23
1.1.1 System.....	23
1.1.2 Approach.....	24
1.1.3 Procedure .....	24
1.2 State-of-the-art.....	25
1.2.1 State-of-the-art in detection methods .....	26
1.2.2 State-of-the-art in electromagnetic induction models and systems ..	29
1.3 Thesis outline .....	31
<b>Chapter 2 EMI sensor</b> .....	<b>33</b>
2.1 Feature discrimination .....	34
2.2 Electrical excitation.....	36
2.2.1 Pulse excitation .....	38
2.2.2 Harmonic excitation .....	40
2.3 Sensor design.....	42
2.3.1 Neutral sensor inductance.....	44
2.3.2 Frequency and geometrical relevance.....	45
2.4 Signal processing.....	47

2.4.1	Signal processing example .....	50
2.4.2	Advanced decay parametrization .....	55
2.5	Summary .....	60
<b>Chapter 3</b>	<b>Computational models .....</b>	<b>62</b>
3.1	Finite element modified model.....	65
3.1.1	Complete 3D simulation model.....	66
3.1.2	Line receiver model .....	69
3.1.3	Volumetric Estimation Method .....	70
3.1.4	Pulse induction of a metallic sphere .....	73
3.2	Dipole model .....	78
3.2.1	Introduction to the theory.....	78
3.2.2	Dipole model implementation .....	79
3.2.3	Cylinder target formulation.....	80
3.2.4	Time domain transformation.....	81
3.3	Experimental verification .....	82
3.3.1	Harmonic excitation validation.....	83
3.3.2	Pulse excitation verification .....	86
3.3.3	Mutual inductance .....	88
<b>Chapter 4</b>	<b>EMI distinctive detection .....</b>	<b>96</b>
4.1	Pulse induction .....	97
4.1.1	Inverse problem as fast estimator .....	98
4.1.2	Inverse problem by decay parametrization.....	108
4.1.3	Material discrimination by pulse induction.....	113
4.2	Harmonic induction.....	116
4.2.1	Design methodology .....	118
4.2.2	Cover independence .....	121
4.2.3	Dimensionless ratios of selective frequencies .....	122
4.2.4	Double balanced configuration .....	123
4.2.5	Spatial phase profile method .....	124
4.2.6	Inverse problem by harmonic induction.....	126



4.2.7 Robustness and reliability .....	132
4.3 Summary .....	135
<b>Chapter 5 Conclusion .....</b>	<b>139</b>
5.1 Main contributions .....	140
5.2 Future scope.....	142
<b>Appendix A.....</b>	<b>144</b>
<b>Appendix B.....</b>	<b>145</b>
<b>Appendix C .....</b>	<b>146</b>
<b>Appendix D .....</b>	<b>147</b>
<b>Appendix E.....</b>	<b>149</b>
<b>Appendix F .....</b>	<b>151</b>
<b>Appendix G.....</b>	<b>153</b>
<b>Appendix H .....</b>	<b>154</b>
<b>Appendix F .....</b>	<b>158</b>
<b>Nomenclature .....</b>	<b>160</b>
<b>References .....</b>	<b>162</b>
<b>Curriculum Vitae .....</b>	<b>167</b>

## List of Figures

Figure 1:1 Detection application examples, a) Landmine detection for humanitarian reasons, b) Defects like cracks in steel pipes for safety, c) Localizing targets in concrete and discriminating their shape and size for construction certification, d) Detection of predefined materials for safety and security reasons.....	17
Figure 1:2 Basis of a detection system: target, sensor, and physical method.....	19
Figure 1:3 The main interconnected areas of study during the research and development of an EMI detection sensor.....	21
Figure 1:4 Workflow proposed for an EMI detection sensor starting with the detection system, then model approach, and ending in a discrimination procedure of the targets or objects.....	22
Figure 2:1 Target features to be detected, transverse location, depth, size, shape, and material. ....	34
Figure 2:2 The three main fields in an EMI system: source field, eddy currents, and back-scattering. ....	36
Figure 2:3 Pulse excitation on the sender source coil a) dc voltage applied and switched off, b) current rise and fall in the sender. ....	38
Figure 2:4 Pulse excitation electronic schematic, including a driver and a MOSFET that are timed according to an external function generator.....	39
Figure 2:5 Experimental setup of a pulse induction scheme. ....	39
Figure 2:6 Source voltage (red) and current (blue) of the sender coil in a harmonic excitation.....	40
Figure 2:7 PCB hardware of the a) sender coil b) receiver coil with their PCB layout design done by Altium Designer c) and d).....	42
Figure 2:8 The simple sensor sketched first in a) CAD software then b) manufactured by rapid prototyping and assembled with the PCBs.....	43
Figure 2:9 Magnetic field lines generated by a coil wire, and the general placement of a receiver (green rectangle).....	44
Figure 2:10 Geometrical balance of the receiver coil against the sender coil by a shift of $D_p$ . ....	45
Figure 2:11 The effect of the sender frequency and the receiver displacement ( $D_p$ ) on the induced a) real voltage and b) imaginary voltage.....	46
Figure 2:12 Pulse excitation done by producing a current (blue) in the sender which induces a voltage (red) in the receiver. ....	47
Figure 2:13 Typical induced voltage decays of different target sizes, depths, and transverse locations.....	48
Figure 2:14 A detection system with some target features $x$ (horizontal position), $c$ (cover depth), and $d$ (target diameter).....	50
Figure 2:15 A classical parameterization of induced signal decay.....	51
Figure 2:16 A new parameterization proposal of an induced signal decay.....	51
Figure 2:17 State-of-the-art evaluation of the induced signals by experiments for different diameters and covers but at $x=0$ . ....	52
Figure 2:18 Alternative evaluation of the induced signals experiments for different diameters and covers but at $x=0$ .....	53
Figure 2:19 Alternative evaluation of the induced signals experiment of one diameter and cover, normalized about $x=0$ .....	54
Figure 2:20 Fitting parameter $c_1$ of the gauss fit as a function of cover; every line is for a specified diameter.....	54

## List of Figures

---

Figure 2:21 a comparison between the general exponential fit and the proposed fit on one experimental case. ....	56
Figure 2:22 A measured voltage decay and its fitting function that can reconstruct the signal especially at the predicted current switch at time. ....	57
Figure 2:23 The two main parameters of the decay fit varying with the diameter and cover. ....	58
Figure 2:24 The parameter $a$ as function of the target diameter; every line represents a cover value. ....	59
Figure 2:25 The parameter $n_a$ as function of the target diameter; it is the time derivative of the voltage at time = $t_0$ . ....	60
Figure 3:1 Comparison in accuracy and computational time for the current work applications of EMI using different models.....	62
Figure 3:2 Skin depth for copper and steel targets depending of the frequency. ....	66
Figure 3:3 Experiment (left) and simulation (right) of the amplitude ratio of the receiver and sender.....	68
Figure 3:4 Line receiver model.....	69
Figure 3:5 Seven different skin designs to be compared to the complete model.....	70
Figure 3:6 Computational time of all cases relative to Case 0. ....	72
Figure 3:7 Pulse induction of a sphere, 2D axisymmetric FEM simulation with experimental verification...	73
Figure 3:8 Space reduction check using the two components of (3.6).....	74
Figure 3:9 Instantaneous plots of vector potential derivative across the radius of the copper sphere.....	75
Figure 3:10 Instantaneous plots of vector potential derivative across the radius of the steel sphere.....	75
Figure 3:11 Flux Density at the surface of the sphere with different material using different methods. ....	77
Figure 3:12 Current density at the surface of the sphere with different material using different methods...	77
Figure 3:13 Experimental verification procedure for different models under frequency and time domain.	82
Figure 3:14 Sensor DESIGN II (Appendix D) including senders and receivers and the position of the target defined by $c$ and $d$ . ....	83
Figure 3:15 The simulated induced flux in receiver 2 and receiver 3 of DESIGN II (Appendix D), 'setup 1', and a copper cylindrical target. ....	84
Figure 3:16 The simulated induced flux in receiver 1 and receiver 2 of DESIGN II (Appendix D), 'setup 1', and a steel cylindrical target. ....	84
Figure 3:17 The simulated induced flux in receiver 1 and receiver 2 of DESIGN II (Appendix D), 'setup 2', and a steel cylindrical target. ....	84
Figure 3:18 Transient induced voltage in receiver 1 for DESIGN II (Appendix D) for 'setup 1' of copper and steel targets. Experiments and both simulation models are compared.....	86
Figure 3:19 Transient induced voltage in receiver 1 for DESIGN II (Appendix D) for 'setup 2' of copper and steel targets. Experiments and both simulation models are compared.....	87
Figure 3:20 Transient induced voltage in the receiver for DESIGN I (Appendix B) of copper and steel targets at 'setup 3'. Both simulation models are compared.....	88
Figure 3:21 Setup of DESIGN I (Appendix B) with two steel cylindrical targets. ....	89
Figure 3:22 The real (upper) and imaginary (lower) flux response of a double cylinder versus the addition of single response. The sensor used is DESIGN I (Appendix B). ....	89
Figure 3:23 Measured and calculated superposition error relative to double cylinder response for both sensors are evaluated: the real and imaginary fluxes in the receiver coil using DESIGN I-sensor 1 (Appendix B) and DESIGN I-sensor 2 (Appendix C) for steel targets. ....	90

## List of Figures

---

Figure 3:24 Relative difference between the coupled and the single target superposition of the induced imaginary flux for two close lying 20 mm diameter steel cylinders for several separation distances. The sensor used is DESIGN I-sensor 1 (Appendix B).....	91
Figure 3:25 Relative difference between the coupled and the single target superposition of the induced imaginary flux for two close lying steel cylinders with several diameters and a fixed separation of 20 mm. The sensor used is DESIGN I-sensor 1 (Appendix B).....	92
Figure 3:26 The decoupling frequencies for fixed diameter ( $d = 20$ mm) and variable separation, as well as the ones for fixed separation ( $s = 5$ mm) and variable diameter.....	93
Figure 3:27 Magnetic flux $\phi$ as function of frequency above two cylindrical targets with (dotted) and without (solid) considering the dipolar coupling between the targets in the quasi-static dipolar approximation. The sensor used is DESIGN I-sensor 1 (Appendix B).....	94
Figure 4:1: Detection sensor DESIGN III (Appendix E) for pulse induction using one excitation mode and one receiver direction. The target features $d$ , and $c$ are unknown as well as the $x$ location. ....	99
Figure 4:2: Lookup table of the function $f = A1 - A2$ plotted versus the diameter $d$ of the targets. Every line corresponds to a cover $c$ . This table corresponds to the value of $x$ equals zero. The sensor used is DESIGN III (Appendix E).....	102
Figure 4:3: Parameter $c_1$ evaluated for 180 $x$ -scans and plotted versus cover $c$ . Every line corresponds to a diameter $d$ . The sensor used is DESIGN III (Appendix E).....	103
Figure 4:4: Illustration of the first estimation of the cover interval by knowing $c_1$ from one scan in $x$ -direction. The sensor used is DESIGN III (Appendix E). ....	103
Figure 4:5 Solution domain bound by the red dashed box by $c_1$ . The line solution 1 is found from known $f$ values. The line solution 2 is found from parametrized decay estimation. The sensor used is DESIGN III (Appendix E).....	104
Figure 4:6 All possible $f$ database equivalences (solid lines corresponding to six different ( $d$ , $c$ ) possible solutions) and plotted against the $x$ -direction (symmetry averaged and normalized), the marked dashed line is the measured response. The sensor used is DESIGN III (Appendix E).....	105
Figure 4:7 Error evaluated between the measured response and the six suggested responses by the database; the letter $f$ in the legend refers to normalized $f$ . The sensor used is DESIGN III (Appendix E).....	106
Figure 4:8 The corresponding errors in a) diameter and b) cover using only one receiver R1, the targets investigated are between 6 mm and 32 mm in diameter placed up to 150 mm away from the sensor. The estimation of $d$ and $c$ features is based on real experiments. The sensor used is DESIGN III (Appendix E). ....	107
Figure 4:9 The corresponding errors in a) diameter and b) cover using the average of responses of all five receivers R1-R5, the targets investigated are between 6 mm and 32 mm in diameter placed up to 150 mm away from the sensor. The estimation of $d$ and $c$ features is based on real experiments. The sensor used is DESIGN III (Appendix E).....	107
Figure 4:10 The two parameters of the experimental voltage fit depending only on the diameter of steel cylindrical targets. The sensor used is DESIGN III (Appendix E).....	108
Figure 4:11 The parameter $a$ of the fitted equation representing the intensity of the signal. The sensor used is DESIGN III (Appendix E). ....	110
Figure 4:12 The time quantity $t_{drop}$ depending only on the target diameter regardless of the cover value. The sensor used is DESIGN III (Appendix E).....	111
Figure 4:13 The corresponding errors in a) diameter and b) cover using only one receiver R1, the targets investigated are between 6 mm and 32 mm in diameter placed up to 150 mm away from the sensor. The sensor used is DESIGN III (Appendix E).....	112
Figure 4:14 The corresponding errors in a) diameter and b) cover using the average of responses of all five receivers R1-R5, the targets investigated are between 6 mm and 32 mm in diameter placed up to 150 mm away from the sensor. The sensor used is DESIGN III (Appendix E). ....	112

## List of Figures

---

Figure 4:15 The two parameters, $t_0$ , and $n$ extracted from the simulation results of the voltage induced by steel cylindrical targets.....	114
Figure 4:16 The two parameters, $t_0$ , and $n$ extracted from the simulation results of the voltage induced by copper cylindrical targets.....	115
Figure 4:17 The 2D lookup table of the parameter $a$ differs in value between a) steel and b) copper based on simulated results. ....	115
Figure 4:18 The four receivers placed relative to two senders as an outcome of an optimized sensor named DESIGN IV (Appendix F).....	119
Figure 4:19 A simple sender-receiver coil is considered one coil used for sending and receiving, this is done for simple simulation concept.....	121
Figure 4:20 The three cases of discrimination and distinctive detection: single copper rod, single steel rod, and double copper-steel rods.....	124
Figure 4:21 Simulation versus experiment for three cases of material discrimination using 10 kHz (left) and 20 kHz (right) sender frequencies. The response is the phase angle of the differential voltage signal relative to the sender current. The sensor used is DESIGN IV (Appendix F).....	125
Figure 4:22 The phase response of steel (left) and copper-steel (right) rods of a fixed diameter of 8 mm and depths variation from 10mm (blue) to 40 mm (black) in 5 mm steps with an active frequency of 25 kHz in the sender coils.....	127
Figure 4:23 The parameter $a_1$ of the parabolic fits of the phase response of every scan over a steel rod (left) and steel-copper rods (right) for all diameters starting from 10mm (blue) to 22 mm (black) in steps of 2 mm, all plotted versus the depth of the target with an active sender frequency of 25 kHz. ....	127
Figure 4:24 a) The plot of the RMS of the differential voltage signal ( $U_{east} - U_{west}$ ) across a transversal scan for an 8 mm steel rod with a variation in depth from 10 mm (blue) to 40 mm (black) in steps of 5 mm. b), c), and d) correspond to the plot of the parameter $A_1$ (the amplitude of the sine fit of the RMS across the scan at frequency $f = 25$ kHz), $A_1$ is plotted versus the depth of the three cases targets for all diameters 10 mm (blue) to 22 mm (black) in steps of 2 mm. ....	130
Figure 4:25 a) left is the plot of the ratio1 in (4.14) which is effective to find diameters of steel or copper-steel rods, b) right is the plot of the ratio2 in (4.15) which is effective to find diameters of copper rods. ..	131
Figure 4:26 The effect of the permeability on the optimum selective frequencies to be used in ratio1 .....	131
Figure 4:27 The mean and standard deviation error in percentage of cover values. This is a statistical analysis of 20 random white noise levels ranging between -0.5% and +0.5% of the maximum signal induced added to all responses of all cover and diameter values performed at 25 kHz excitation frequency. ....	133
Figure 4:28 The value of $a_1$ simulated for double rod case where the diameters of steel and copper are different. The operating frequency is 25 kHz and the rods where placed at $c = 30$ mm. ....	134
Figure 4:29 The workflow of the inverse model by pulse induction to estimate the unknowns $[x, d, c]$ from a single scan.....	136
Figure 4:30 The workflow of the inverse model by harmonic induction to estimate the unknowns $[x, d, c]$ from a single scan.....	137

## List of Tables

Table 1:1 State-of-the-art methods compared to the proposed method showing the advantages, $\oplus$ , and disadvantages, $\ominus$ . The symbol, $\odot$ , means it is neutral or not known. ....	27
Table 1:2 State-of-the-art in computational models compared to the two proposed models showing the advantages, $\oplus$ , and disadvantages, $\ominus$ . The symbol, $\odot$ , means it is neutral or not known. ....	29
Table 2:1 the coefficients of the fits of (2.7) and (2.8) with the corresponding goodness of fit. ....	57
Table 3:1 Response of the seven cases compared to the complete model (case 0). ....	71
Table 3:2 Skin depth for different target materials and excitation frequencies. ....	73
Table 3:3 FEM mesh and current density. ....	76
Table 4:1 Coils characteristics including dimensions of copper pads on the board. ....	101
Table 4:2 The optimum frequencies that generate the steepest ratios. ....	123
Table 5:1 Summary of the main contributions and their references. ....	142

## List of Equations

(2.1).....	35
(2.2).....	40
(2.3).....	41
(2.4).....	41
(2.5).....	43
(2.6).....	55
(2.7).....	55
(2.8).....	56
(2.9).....	56
(2.10).....	56
(2.11).....	57
(2.12).....	58
(2.13).....	59
(3.1).....	68
(3.2).....	69
(3.3).....	69
(3.4).....	71
(3.5).....	72
(3.6).....	72
(3.7).....	76
(3.8).....	79
(3.9).....	79
(3.10).....	79
(3.11).....	79
(3.12).....	79
(3.13).....	80
(3.14).....	80
(3.15).....	80
(3.16).....	80
(3.17).....	80
(3.18).....	80
(3.19).....	81
(3.20).....	81
(3.21).....	81
(3.22).....	81

## List of Equations

---

(3.23).....	82
(3.24).....	93
(3.25).....	94
(3.26).....	94
(4.1).....	106
(4.2).....	109
(4.3).....	111
(4.4).....	114
(4.5).....	118
(4.6).....	122
(4.7).....	122
(4.8).....	122
(4.9).....	122
(4.10).....	123
(4.11).....	126
(4.12).....	128
(4.13).....	128
(4.14).....	129
(4.15).....	129
(4.16).....	132
(4.17).....	132
(4.18).....	132
(0.1).....	144
(0.2).....	144
(0.3).....	144
(0.4).....	144
(0.5).....	144
(0.6).....	144
(0.7).....	144



# Chapter 1 Introduction

Nondestructive Testing (NDT) is demanded in different industrial applications for cost-effectiveness, safety and certification reasons. The American Society for Nondestructive Testing (ASNT) has defined it as: *'Nondestructive testing (NDT) is the process of inspecting, testing, or evaluating materials, components or assemblies for discontinuities, or differences in characteristics without destroying the serviceability of the part or system. In other words, when the inspection or test is completed the part can still be used'* [1]. Worldwide there have been many institutes and federations monitoring, legalizing, certifying, organizing, standardizing, and documenting various kinds of NDT on the national and worldwide levels like:

- European Federation of Non-Destructive Testing [2].
- The British Institute of Non-Destructive Testing [3].
- Australian Institute for Non-Destructive Testing [4].
- Indian Society for Non-Destructive Testing [5].

These and many others are all public organizations putting effort in this field. There are many private companies that are specialized in aspects of NDT as well, due to the huge demand from the industrial sector. NDT methods are classified per the physical fields that their detection devices are based on, like ultra-wideband radar, ultrasound, terahertz radiation or eddy current induction [6] to name a few.

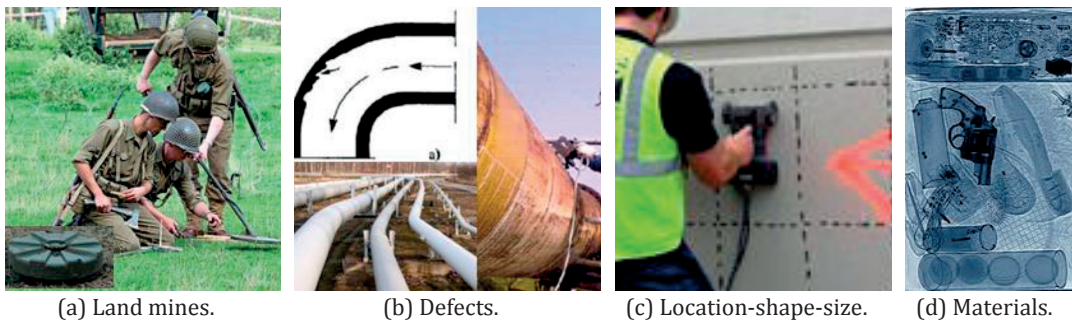


Figure 1:1 Detection application examples, a) Landmine detection for humanitarian reasons, b) Defects like cracks in steel pipes for safety, c) Localizing targets in concrete and discriminating their shape and size for construction certification, d) Detection of predefined materials for safety and security reasons.

The constant requirements of such devices are usually the following: higher precision, more accuracy, and more information or acquirement about hidden targets or defects like material, shape, orientation without having to destroy the detected objects [7]. The fast advances in the field of electronic devices have encouraged the sensor manufacturing industry to continuously develop these devices. There is a potential to produce more

accurate and competitive devices in a challenging environment for the welfare of the end user who is using these devices. There are various reasons behind this need:

- Cost reasons, by saving on the device cost and development time.
- Safety reasons, by gathering information about crack locations in steel pipes [8], [9].
- Humanitarian reasons, by finding leftover mines in previous war zones [10], [11].
- Security reasons, by detecting weapons in airports, or avoiding live copper wires that pass dangerous electric currents.
- Construction safety, by discriminating steel stiffeners in concrete [12], or finding the locations of tension cables in bridges.
- Certification reasons, by estimating the concrete cover over anchors or stiffeners in tunnels [13].

These applications, some of which are shown in Figure 1:1, are categorized per the needs in the application side for example security, or certification. On the other hand, NDT sensors are based on one or more physical methods. *'The British Institute of Non-Destructive Testing'*, [3], has used the term 'inspection task' to evaluate tasks when using NDT methods. They defined a number of tasks like: *surface opening cracks, surface corrosion pits, severe corrosion thinning, internal cracks, porosity, lack-of-fusion defects, internal voids inclusions, defect sizing, thickness measurement, microstructure variation, coating thickness measurement, coating delamination, coating pin holes, fiber-matrix ratio evaluation, incomplete cure of resin, internal porosity, concrete thickness measurement, reinforcing-bar corrosion, surface cracks, internal cracks, assembly verification, and sorting*. It was illustrated that many methods can be suitable fully, partly, or poorly for one or more of the inspection tasks mentioned above. Some of the methods stated are: *Acoustic, Resonant inspection, general Electromagnetic, Magnetic particle inspection, Magnetic flux leakage, Eddy current testing, ACFM Potential drop, Optical, Laser-based inspection, Thermography, Radiography, Radioscopy, Neutron radiography, Stress-strain measurement, Ultrasonic flaw detection and sizing, and Ultrasonic thickness gauging*. The institute categorized detection devices by the material to be detected. The complexity in categorizing NDT becomes difficult because several methods may use the same inspection task for different materials. Also, the same method can use many inspection tasks for the same material.

Worldwide national and international institutes have classified NDT methods, tasks, and detected materials differently. There is no universal unified standard, naming, structure, or documentation. Physical methods and application tasks are usually related to each other, i.e. inspection tasks are defined per method and are restricted to the limitations and capabilities of this method. The detected material is one limitation.

In many scientific publications, it is inferred that such physical methods are shared between application sensors; i.e. an application may be based on more than one physical method. Considering an electromagnetic radar method that is used for detecting land mines as an application [14], it is also used in finding reinforcing steel stiffeners inside concrete [12]. Moreover, several methods can be combined in one application. For instance, induction and radar methods can be used as two complementary methods to detect land mines [11]. By that, electromagnetic induction (EMI) serves for the metal detection, whereas the high frequency radar serves for locating the mine's plastic cover. Therefore, detection methods, in the context of this work are categorized per the physical method implemented rather than the application itself. The physical method is a basic feature of a detection device together with the target, which needs to be identified, and the sensor type. Figure 1:2 depicts the basic components of a detection system: the target, the sensor and the physical method. The sensor output gives information about the target, for instance: material, shape, location, type, and size.

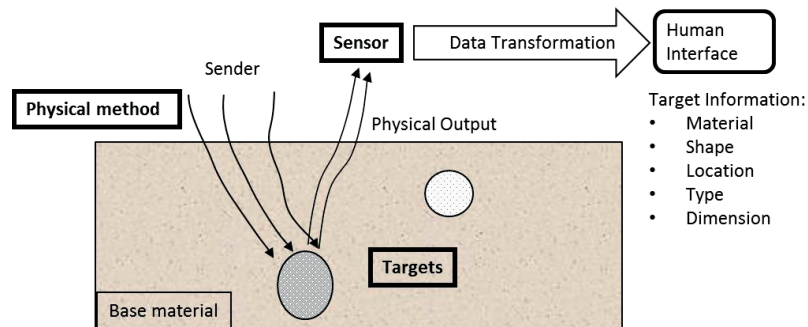


Figure 1:2 Basis of a detection system: target, sensor, and physical method.

During the analysis, design, optimization, and development phases of a detection sensor, it is important to identify these main basis features of the device: physical method, target type, and sensor type. All three components are interconnected and none of them should be treated separately or avoided. After this is done, the system should be represented by models that should be implemented and used to reach the optimum of the specification required overcoming the challenges and reaching limitations of the chosen physical method. Models that represent such systems can be one or a combination of the following: analytical, computational, and experimental. A detailed analysis of the state-of-the-art models is described in section 1.2.2.

Every method has limitations. For example, eddy current induction can only be used to detect magnetically permeable and electrically conductive materials such as steel and copper, but it fails in detecting plastic material. On the other hand, high frequency radar (in the range of GHz frequencies) is better used for such dielectric materials. Nevertheless, electromagnetic induction (EMI) is one of the most promising methods used in detection due to its low cost [15], uncomplicated electronics [16], relative indifference to some environmental effects like moist [10], low or no requirement for certification of devices or users, and precise detection of targeted location for a specified location range.

EMI has the following disadvantages: it is not effective for relatively far objects and it can only detect magnetically permeable and/or electrically conductive objects or targets. It can detect the size of objects but it is very hard if not practically impossible to estimate the sizes out of the backscattered fields.

The current work concentrates on EMI as a method for metal detection. The special features of this method over other methods are described in section 1.2: state-of-the-art. EMI still has potential in innovation and optimization of detection sensors. Industrial requirements lead the design and optimization in this field. The focus is usually on higher precision, and increased range of material discrimination. One of the challenges during this stage is identifying and distinguishing the responses from targets that are made of different materials. The response is physically induced from eddy currents generated in these metallic targets. The deep understanding of the physical response of eddy currents inside the target may allow a possible design of a sensor that can, not only discriminate target features but also 'distinguish' between the detected target feature in the presence of another target feature. Both targets can be made of different materials, for example, detecting only copper in the presence of both copper and steel, or a 6 mm steel cylinder in the presence of another 12 mm steel cylinder but at different depths. This capability is difficult to implement using simple a sensor and electronic design. The current work highlights such challenges and describes possible methods and procedures in this direction. Some other challenges are also tackled in the current work. Many limitations such as low strength of signals, deeper detection, mutual coupled inductance between the targets themselves, mutual coupled inductance between the senders and receivers, and material discrimination of the target are solved. Referring to Figure 1:2; the basic way to activate such a sensor is to create an electromagnetic field by a time variant current in the sender, which is usually a coil with several winded copper turns. This time variant field generates eddy currents in an electrically conductive target lying as close as possible to the source of this field. Thus, a secondary magnetic field is generated in these targets and scatters back through the base material that hides that target. This back-scattering field induces a voltage in the receiver. By recording and analyzing this voltage, information about the target can be processed without the need to destroy the base material. The mutual inductance between the sender coil and the receiver coil is a challenge of such a method because the best setup would be to only detect responses of targets and not allow the receiver to sense the primary field generated by the sender coil.

Any study conducting an analysis, design, optimization, and development of EMI sensors must consider three interconnected areas of research: coil design, excitation scheme, and post-processing as sketched in Figure 1:3. The researcher cannot improve the excitation scheme and be creative in finding the most suitable electrical signal that is responsible to generate the source magnetic field without defining and inventing the best algorithms to process the induced signal scattered back from the target in the receiver of the sensor. The designer should build the sensor's geometry and coil design with a close connection to both sending and receiving of signals, thus excitation and post-processing at the same time. In general, it is an ill-posed inverse problem that should be solved. All the three

areas of investigation should be tackled equally. Any design change in one of these areas requires a change in the other ones.

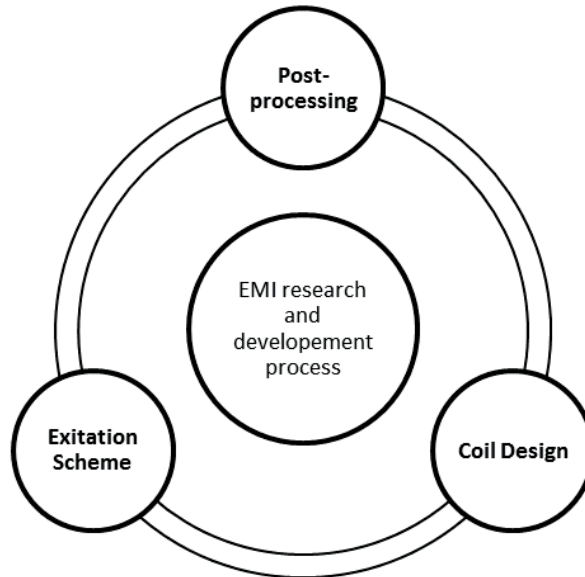


Figure 1:3 The main interconnected areas of study during the research and development of an EMI detection sensor.

Constructive research requires a validated logical approach to reach the aims that are usually set ahead. The first step in the current approach is to model the detection system described previously. The EMI detection system can be modeled either by an experimental approach or a computer simulation one. Analytical approaches of such systems are available only for simple geometries of the coils and very simple geometries of the targets to be detected. Simple target geometries mean geometries like a sphere or an infinitely long cylinder, which are rather too theoretical to be realized as industrial applications. On the other hand, an experimental approach, that relies purely on building a sensor hardware and performing trials and errors of some detection cases is nearly an impossible approach. It is difficult to reach the required aim due to the long time and high costs consumed for every setup. In addition to that, some effects cannot be quantified experimentally, for example, eddy current densities or flux flow in the targets. They also cannot be captured by the human eye and visualized. Another disadvantage of experimental approaches is their limitations due to noise at low signals and interferences. In other words, even a relative comparison between the results of two different experiments can be misleading, especially, at low induced signals, measurement errors related to manufacturing tolerances, and environmental changes. However, such non-ideal cases happen in the real devices, and here the virtual models play a big role in implementing imperfections and designing the best design that is valid for all target cases considering all deviations.

Computational methods help in modeling and simulating such detection systems, especially, when the experimental methods are expensive, less consistent and dominated by

noise in the case of low signals. The advances in computational techniques, like finite element method, have increased the ability to model sensors and improve them. Eddy currents are highly affected by geometry and material and, therefore, the model should include the highest dependency on space and not only on time. The advantage of the 3D simulation tools, especially finite element models is the ability to identify physical effects like mutual inductances. They provide visualization and realization of eddy currents in complex geometries and find new ideas to develop better detection devices. These simulation tools have disadvantages as well especially the computation time and the lack of robustness in cases where optimization is required for coil positions and geometries. The final design is only valid if a wide scan of target positions and sizes is performed, which requires a huge amount of computational time. Several improvements of simulation models have made virtual models that are more effective as published in [17], [18], [19], and [20]. A detailed overview is shown in the state-of-the-art section 1.2. It is necessary to use a simulation environment taking advantage of its 3D capability and still implement analytical models, where necessary, to preserve the accuracy required and provide the robustness needed. In the end, a modeling procedure for the EMI method is a major requirement for understanding, designing and optimizing a detection system leading to new features like material discrimination and distinguished feature detection. Moreover, fast (computationally efficient) forward models are mandatory for the inversion of the measured electromagnetic response for all target sizes, locations, and material identification.

During the research work on this method, every part is accomplished according to a workflow as the one represented in Figure 1:4 showing all building blocks and their interaction. It is an interconnected discipline that means they cannot be treated separately. It is necessary for the EMI system to define the coils' design and their optimum geometries and locations. The same importance should be given to choose the best excitation scheme that is relevant to that design. These two points are major parts of the detection system as shown in the 'System' block in Figure 1:4 on the left. Another main part is the post-processing technique, which is part of the 'Procedure' at the right side of the same workflow figure.

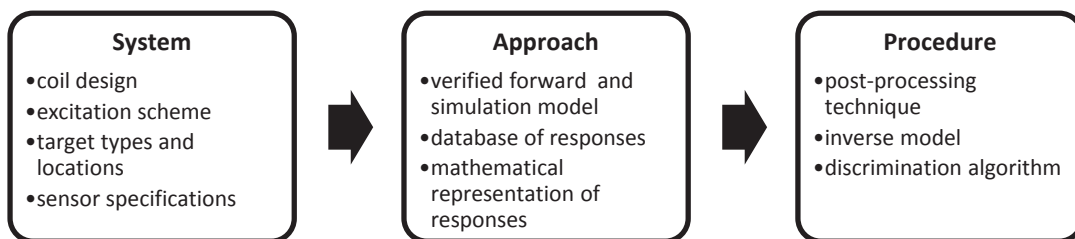


Figure 1:4 Workflow proposed for an EMI detection sensor starting with the detection system, then model approach, and ending in a discrimination procedure of the targets or objects.

Referring to the workflow of Figure 1:4, the first two blocks, 'System' and 'Approach', define the forward representation of a detection system. Forward model means that the

induced signals are calculated given the parameters of the target. The last block, 'Procedure' contains all the post-processing techniques of these responses and can process inverse information. Inverse problems are often formulated as optimization problems, i.e. finding the target parameters that best fit to the measured data. The inverse model is the final outcome of the EMI sensor workflow because only then it is possible to detect and discriminate a target feature (material, size, type, and location) by just processing a raw induced signal without knowing the target information ahead. That means a post-processed result of measured signals is needed by the inverse model to obtain the unknown features of the target. In addition to that a discrimination technique should be created to even distinguish between these features in the presence of other features, i.e. copper in the presence of steel for example.

## 1.1 Objective

The purpose of this work is to provide a technique depending on the specifications and features of a magnetic permeable and/or electric conductive targets to be not only detected by an Electromagnetic Induction (EMI) sensor but also discriminated and distinguished. Discrimination means identifying features like size, material, shape, and location of hidden targets based on their single response; while distinguished detection is the ability to distinctively identify these features of more than one type of targets and features present in the same place. All the parts mentioned in the blocks, 'System', 'Approach', and 'Procedure' of the workflow in Figure 1:4 contribute scientifically to the final aim of the current work. The present work contributes to special aspects of EMI technology that are briefly mentioned in this section. For a detailed identification of the novelty of this work, please refer to the 'Main Contributions' in section 5.1.

### 1.1.1 System

A system is to be built proposing a design of a set of coils with optimum placement and geometry, thus eliminating the mutual induction between the sender coil and the receiver coil. In addition to that, dissimilar kinds of excitations lead to dissimilar coil designs due to the interactions between the excitation and the physical design. Both pulse induction and harmonic induction schemes (see section 2.2) are to be investigated and implemented. Coupled targets cause mutual inductance between them and this should be considered in proposing verified solutions. Double target (closely lying targets) are decoupled with the help of a proposal that is experimentally validated and documented in a published paper and journal [21], [22]. Nearby targets present in the same magnetic field contribute to the induced voltage and thus a wrong estimation can occur. This work led to two patent applications, [23] and [24], claimed at the European Patent office, that are able to recognize complex composed targets and still estimate their position, depth, and material composition for single and multi-material grouped targets. This proposal was designed and verified for a specified range of target sizes and depths: for cylindrical rods of copper, steel, and combined copper-steel ones. When industrialized, it can solve many real-life applications especially in the construction industry where classical state-

of-the-art detection techniques fail if they use only EMI technology for such complex hidden metallic targets. An application example would be the detection of copper gas pipes near steel reinforcing bars but in the context of this work finite cylindrical rods were used for simplicity.

### 1.1.2 Approach

Two computational models are the main contribution in the 'Approach' block in Figure 1:4. One outcome is to generate an effective, robust, and validated simulation model where theoretical implementation should be implemented inside a finite element method (FEM) simulation environment (see section 3.1). One should also account for the correct boundary conditions and should achieve accurate results with the least computation time. In addition to that, a post-solve technique allows the calculation of the induced voltage anywhere in the domain using the vector potential formulation. These implemented scripts reduce the FEM matrix, which results in a faster inversion. The simulations show that the eddy currents are not only present at the skin as some publications claim. This is because the magnetic flux distribution is non-uniform, which is highly affected by finite shapes and locations of the targets. In other words, both transverse and axial excitations generate eddy currents even in cylindrical targets especially for non-uniform transient excitation currents. For that reason, a new theoretical Volumetric Estimation Method is needed as a prerequisite controller of the element mesh. This part is published in a paper [25] and a journal [26]. Considering the targets as pure cylinders with finite length is usual in building models of such systems but, on the other hand, one of the realistic applications is a complex shaped target that is cylinder-like. A suggested factor based system depending on the sender frequency and location to adapt the model with realistic inputs is detailed and published in a conference paper [27]. In addition to that a second model is developed with the help of this work. A dipole model was modified and implemented. It was verified against the FEM model and suited to finite length targets as discussed in section 3.2.

### 1.1.3 Procedure

In the 'Procedure' block of Figure 1:4, two important representations are verified for all possible target cases. The novel post-processing method based on the raw induced signals of the receivers in both transient (pulse induction in this case) and time harmonic excitation should be developed and used to identify targets with their size and location. This is still not defined as a discrimination procedure because it is relying on the forward model where the targets were already known when building a system database. The complexity increases when the target is composed of two or more materials as described in the work of [28] that analyzed the detection of UXO composed of different materials of bullets and shells. The post processing should also be adapted to different single materials and to grouped materials. Achieving the inverse model is a challenge but is mandatory to prove discrimination of targets in a unique, robust, and verified system by simulation and experimental hardware for two excitation modes. A distinctive detection design procedure is also filed for a patent application [23] showing the basis of a method in the time harmonic excitation field with a proposal for sensor design. This proposal



was implemented to distinctively detect at least three different material combinations and discriminate their target features at the same time according to a specified range and resolution.

Throughout the complete discipline that is described in this section a clear objective is to achieve a methodology following every part of the workflow of electromagnetic (medium frequency) detection by induction. It is important to discriminate single and multi-material (magnetic and non-magnetic) target features and not only size, depth, and transverse location. This is defined here as distinctive detection. It is easier to identify the new scientific contributions of this work by listing the state-of-the-art devices (conceptual or industrial), models, and publications in detection systems in general and in EMI in specific as briefly described in section 1.2 showing the implementation basis of these technologies.

## 1.2 State-of-the-art

Many published papers, journals, and patents describe methods of detecting hidden objects without the need to destroy the media that these objects are buried in. Media is referring to as soil, concrete, brick, wood, water, or even the material of the detected target itself. In many cases, these scientific articles and documents refer to detection methods as Nondestructive Testing (NDT). As mentioned in the introductory part of this chapter, the current work has identified the three-major basis of detection systems and categorized them according to the physical methods used like radar, induction, acoustic, ultrasonic, thermography, etc. It was also stated that each method (or a combination of methods) is suitable for a detection application. If a detection device is to be designed, it is important first to choose the physical method to be based upon. The method (or a combination of methods) is chosen according to the type of target that needs to be detected. Discriminating features of this target (or targets) for a quantity range, quality level, and/or resolution plays a role in evaluating and rating this detection method. Only then the sensor part is developed further. As an example, designing a device that finds any size of gold pieces hidden in soil uses a method completely different than a device that requires a high-resolution estimation of the crack size in steel pipes that transport gas. Another method would be needed to evaluate the corrosion level of steel rods in a nuclear plant, for example. For that reason, it is logical that all these devices can be categorized according to the physical method that governs them. A first study shows various state-of-the-art detection systems with different methods for different applications stated. These published papers and patents are using various models like analytical, experimental, numerical, or a combination of these models to verify the claimed ideas. For that reason, a first general description is conducted showing detection methods and then a specific section is dedicated to the state-of-the-art of Electromagnetic Induction (EMI) systems and models that are published and are mostly close related to the current work.

### 1.2.1 State-of-the-art in detection methods

Detection systems or nondestructive testing methods give their name to the industrialized devices that are based on them. A review on such methods is done, especially on radar, induction, ultrasonic, Neutron backscattering and electrochemical systems. High frequency radar method is used in detection applications like detecting steel reinforcing bars [29], mines [30], plastic pipes, location [31], shape [30], and material. This method has some advantages over other detection methods like shape discrimination [10], [30]. It can even give information about complex shapes of targets and to be relatively less affected by interferences [10], [32]. Moreover, its ability to discriminate wide material ranges from plastic to electrically conductive metals and magnetically permeable material is of utmost importance. It is also fast, i.e. the user can operate faster using such devices. On the other hand, it has a lot of disadvantages like environmental disturbances for example, moist [10], [32]. And since it uses high frequency, then a device certification is required in protected markets with specification norms against electromagnetic wave emissions. Due to the high frequency used in these devices the permittivity effect [12] results in design challenges. This method has also proven to be less effective, in some cases like precise size estimation, than other methods in the detection of metal objects, for example in [10], where a combination of two methods was essential for quality reasons.

Electromagnetic induction, on the contrary, has few advantages over radar and some other methods. It is relatively less affected by environmental disturbances like moist [10]. These devices are simpler and require less electronics [16] and can be produced and sold with low cost [15]. They don't require certifications or specialized end users. The main advantage is the potential to produce smart designs [33], [34] satisfying the end user demands and requirements for quality and introducing new features. Few disadvantages can be pointed out for this method, such as the restriction to low depth targets. However, its basic limitation is that the detected material has to be magnetically permeable and/or electrically conductive, as mentioned in [6], [20], [35], and [36]. And due to the inductivity effect under relatively low frequency the system has high time constants, which means the slower usage of the devices is required [37]. Such systems have a high potential of improvement to achieve a better-quality detection devices and fulfill the required aims. This method has a wide range of applications, such as detection of reinforcing bars, tension cables, corrosion, cracks, material (only metals), and land mines. It is known to be relatively precise by giving information about dimensions, and locations of metallic components, sub-components, and their features. The sender-receiver EMI detection system based on coils is not new, as in [38], [39], [40], and [41]. These systems also detect features of magnetic and non-magnetic targets as in [42], [43], and [44] finding voids or cracks in such single material targets. For example, evaluating steel decarburization from the permeability of single targets [45]. Some work was also done on discriminating composed targets of both non-magnetic and magnetic material as in [46] where steel inclusion inside copper rods was analyzed or vice versa but the target was simply placed between the sender and receiver and this does not apply for

hidden targets. The same coil configuration was studied in [47] but based only on ferromagnetic targets. The features of non-magnetic metallic targets, like copper, are difficult to identify precisely in the presence of ferromagnetic targets by using EMI only. Detection sensors based on the phase shift of signals like phase shift plots over a frequency range for copper, aluminum, and steel were documented in [48]. The phase angle plots in [46] are also showing differences between steel inclusions in copper rods or vice versa. The value of the phase angle or the tangent operator of this angle was used to show some differences in the inclusion size. Magnetic induction spectroscopy was implemented in [45] to find zero crossing frequencies. This spectrum analysis is typical in literature [49]. Frequency dependent phase shift was investigated in [50] to discriminate shape and orientation of targets but still a spectrum analysis is used. Designing a sensor by relying on a big range of frequency spectrum response is not practical. Live discrimination is difficult due to the huge amount of frequency excitation and their post processing, which takes a long time. The user must then scan slowly or process the data later by a separate fast processor, which is costly and time consuming. Several balanced configurations are known in literature and on the market, especially, the gradiometer [47], [51], [52] where two close receivers are used to produce a required balance and eliminate noise effects. But a gradiometer design alone is not enough to overcome the distinctive detection challenges (see Chapter 4).

Table 1:1 State-of-the-art methods compared to the proposed method showing the advantages,  $\oplus$ , and disadvantages,  $\ominus$ . The symbol,  $\odot$ , means it is neutral or not known.

General	Specific	Detection Methods			
		Proposed EMI	General EMI	Radar	Others
DESIGN	Simple electronics	$\oplus$	$\oplus$	$\ominus$	$\ominus$
	Low cost	$\oplus$	$\oplus$	$\ominus$	$\ominus$
	Smart design	$\oplus$	$\oplus$	$\odot$	$\ominus$
PERFORMANCE	Non-metallic targets	$\ominus$	$\ominus$	$\oplus$	$\ominus$
	Ferro-based media	$\odot$	$\ominus$	$\odot$	$\oplus$
	Distinctive detection	$\oplus$	$\odot$	$\oplus$	$\odot$
	size	$\oplus$	$\oplus$	$\odot$	$\odot$
	location	$\oplus$	$\oplus$	$\odot$	$\odot$
	shape	$\odot$	$\odot$	$\oplus$	$\odot$
	deep targets	$\odot$	$\ominus$	$\oplus$	$\oplus$
Handling	No moist effect	$\oplus$	$\oplus$	$\ominus$	$\odot$
	No certification	$\oplus$	$\oplus$	$\ominus$	$\ominus$
	No special handling	$\oplus$	$\oplus$	$\ominus$	$\ominus$
	No permission	$\oplus$	$\oplus$	$\odot$	$\ominus$

It is considered novel to be able to use one global sensor based only on EMI for discriminating target features of only non-magnetic (copper rod), or only magnetic (steel rod), or both present in the same place (copper and steel rods grouped). In addition to that, it

should estimate their diameter and depth using selective frequency responses rather than a whole spectrum analysis and post-processing. Such complex targets are numerous in the real industrial applications like:

- cables inside metal pipes
- stainless steel near reinforcing rods in bridges
- electric copper cables or gas pipes near ferromagnetic objects

Further challenges, in addition to the complexity mentioned above, are the mutual inductances between coils and mutual coupling of targets to each other. Distinctive detection is possible using the EMI method and when realized it contributes highly to end users who can 'distinguish' what material, shape, and size to detect in the presence of other materials, shapes and sizes. Material discrimination using EMI is popular in literature. It is already possible to identify the target metal type by using physical criteria like: electric resistivity and/or magnetic permeability [6], [13], [17], [35], [36], [37], [40], [53], [54], [55], [56], [57], [58]; but features like distinguished detection are rarely documented in literature. Theoretical derivations showing the different responses between metals due to conductivity and permeability dissimilarities are also shown in the "Electromagnetic Induction Spectroscopy" [28]. Even though it is not mentioned in the paper, it might be scientifically possible to separate responses based on the induction number as claimed in the mentioned paper, which did not state any practical sensor design suggestion. The current work, on the contrary, states that it is possible to identify material, shape and size by a response parameter, which may be unique for any combination of these features. Two patent applications [59], [34], mention a practical design that states the coupled problem between geometry and excitation but no theoretical modeling or verification of the physical effect behind. These patent applications perform signal amplitude modification on two phase shifted principle signals in the transmitter coils. These coils are, on purpose, geometrically unbalanced with the receiver coils. The signal amplitude manipulation constantly balances the induced signal to be able to select and/or calibrate on demand. They claim a material detection selectivity method.

Other detection methods also have been investigated and it is worth to mention the ultrasonic method, which has an advantage over the previous ones by being unaffected by a ferro-based media that covers detected targets [60]. On the other hand, it requires special handling [60], [61], it is expensive [60], it requires huge image reconstruction effort [62], it is affected by structural noise, when different materials are in the vicinity [63], it is slow and non-effective in isolation layers.

Special permission and user specialties are a requirement for using the following two methods: neutron backscattering [64] and electrochemical methods [65] and thus, they stay less attractive than the previous methods. The complexities of the devices and their cost are also major problems.

A summary of advantages and disadvantages of the main detection methods is illustrated in Table 1:1. The sign  $\odot$  is showing neutrality over other methods. The fields assigned with  $\oplus$  highlight the general advantages over other methods and the ones with  $\ominus$  have a disadvantage. The proposed method of this work has more advantages over other methods especially in distinctive detection.

### 1.2.2 State-of-the-art in electromagnetic induction models and systems

Electromagnetic induction models and systems are numerous in the literature. Models are highly linked to the development of such sensors. Sometimes it is almost impossible to design a sensor that achieves specified aims without developing first a representative model. This virtual model, when verified against experiments, is used as a basis to design and optimize a complete closed system with inverse detection. Inversions of models as well as computational time are the main challenges of such approaches.

Eddy current as a phenomenon that is used nowadays was first discovered by the French physicist Jean Bernard Léon Foucault (1819-1868) in 1851, and for this reason eddy currents are also known as Foucault currents [66]. Foucault built a device that used a copper disk moving in a strong magnetic field to show that magnetic fields are generated when a material moves within an applied magnetic field. Faraday discovered that when a magnetic field passes through a conductor or when a conductor passes through a magnetic field, electric current flows through the conductor in a closed path (circulates). Induction of currents and magnetic fields are the base of how detection devices work. For that reason, eddy current induction can be of advantage for applications such as non-destructive testing.

Table 1:2 State-of-the-art in computational models compared to the two proposed models showing the advantages,  $\oplus$ , and disadvantages,  $\ominus$ . The symbol,  $\odot$ , means it is neutral or not known.

General	Specific	Computational Models in Detection				
		Proposed Dipole Model	Proposed Modified FEM	Pure Analytical Models	Pure FEM Models	Others
Cost	Time	$\oplus$	$\odot$	$\oplus$	$\ominus$	$\odot$
	Software	$\oplus$	$\oplus$	$\oplus$	$\oplus$	$\ominus$
	Implementation	$\odot$	$\oplus$	$\ominus$	$\oplus$	$\odot$
Quality	Finite targets	$\oplus$	$\oplus$	$\ominus$	$\oplus$	$\odot$
	Complex targets	$\oplus$	$\oplus$	$\ominus$	$\oplus$	$\odot$
	Complex Coils	$\odot$	$\oplus$	$\ominus$	$\oplus$	$\odot$
	Accuracy	$\odot$	$\oplus$	$\odot$	$\oplus$	$\odot$
	Mutual inductance	$\odot$	$\oplus$	$\odot$	$\oplus$	$\odot$
Effectiveness	Practical	$\oplus$	$\oplus$	$\odot$	$\oplus$	$\ominus$
	Robust	$\oplus$	$\oplus$	$\odot$	$\odot$	$\oplus$
	Inverse model	$\oplus$	$\odot$	$\oplus$	$\odot$	$\odot$

Pure analytical models of electromagnetic induction with eddy currents induced in a conductive part have been used and published over the last decades. The general advantage of these models is the ability to compute fast when implemented, but the disadvantage is that it is nearly impossible to model complex geometries of coils and targets and get a high accuracy at the same time. The traditional classic way is to start from Maxwell's equations (Appendix A). After some derivations and assumptions, a set of equations needs to be solved. Some papers have solved the final set of equations by using Laplace transform, Bessel functions, or separation of variables [17], [40], [53], [54], [67]. The research potential of these methods is nearly saturated. Many publications in that direction are very old and considered to be too basic and limited. These methods are applied to model electrically conductive targets and not ferromagnetic permeable ones. Another method was found to solve the derived Maxwell's equations by performing a set of experiments and then doing a parametric identification based on these experiments to get the general results [68]. This method is not practical, because it requires, always, a set of defined experiments for every major design change. Also, a lot of physical information cannot be identified because they are mixed in the result and cannot be separated. Other approaches make some assumptions after the derived Maxwell's equations. Such assumptions are applied on coil shapes or on the targets as dipoles or representative spheres. This is a good approach to start modeling complex geometries, but in the literature [57], [58] it was found out that there are doubts about these assumptions and some physical effects, like capacitance, are neglected as well. Another approach is to perform mathematical engineering assumptions by representing the target, for example, by circuit elements like inductances and resistances [37]. These assumptions are easy to implement but can be highly time consuming. One of the approaches is to build up a geometry factor lookup table, which sometimes especially under the targets' mutual effects requires numerous tables to be generated for every design change. The reason behind that is that eddy currents are geometry dependent. But once this set of lookup table is built up then the system is considerably efficient in computational terms. This method is not recommended for complex geometries like finite rod or transversally oriented ones.

Computational or simulation models are relatively new and there is still a big potential in overcoming some challenges in modeling detection systems and improving these systems. The finite element method using the vector potential [9] as a degree of freedom has been available for quite a while to solve the Maxwell equations with the required assumptions and boundary conditions. It is the state-of-the-art FEM method that is used in commercial software already. The hardware and software advances in these 3D applications are still not on a level that allows these models to be solely used during system optimization phases. This method, when used as standalone, is relatively expensive in terms of computational time especially under high frequency transient simulations. An inverse problem based on finite element with an optimum coil setup approach that influences the accuracy and effectiveness is mentioned in [19]. Another finite element based approach that treats the skin depth using an approximation called "Thin Skin Approximation" (TSA) [20] can reduce the computation time by 30 times. This approach is needed for specific applications and similar ideas are developed as part of this work and

are described in section 3.1. Boundary integral equation method (BIEM) is a possibility for computational efficiency [35] due to a small matrix inversion. This method is attractive because it only requires one solution and, in addition to that, this solution is irrelevant to the coil position. This method provides the robustness needed for finding optimum solutions and similar approach has been followed in the context of the current work but it is based on FEM.

A summary of advantages and disadvantages of the main detection models is illustrated in Table 1:2. The sign  $\odot$  is showing neutrality over other models. The fields assigned with  $\oplus$  highlight the general advantages over other models and the ones with  $\ominus$  have a disadvantage for the specified features. The two proposed models, 'Modified Dipole' and 'Modified FEM' of this work have advantages over the other state-of-the-art ones depending on the usage and requirement.

### 1.3 Thesis outline

The three main interconnected foundations of an EMI sensor are explained in the first part of this chapter. As sketched in Figure 1:3, these are the main constitutions of the research done to design, analyze, optimize, and develop such sensors. They are pinpointed in the blocks of the workflow visible in Figure 1:4. The rest of the thesis follows the logic set in this workflow to satisfy the aims stated in section 1.1.

Chapter 2 starts with a description of feature discrimination and the challenges in detecting such features concerning signal strength, location, interference, noise, mutual inductance, and material properties. After that, three sections detail the detection system itself. The induction system relies on the generation of eddy currents in the hidden targets. This physical feature is highly dependent on the variation of the current with time. Usually, a current generator is executing this variation according to a predefined or controlled scheme. The current change in time produces a magnetic field that is also time variant and by that eddy currents are produced in electrically conductive and/or magnetically permeable objects located inside this field. Usually these objects are the targets that need to be detected. For that reason, the excitation scheme of the current is a deciding factor in the quality of the detection system. This generation of the field happens in source coils, which are named here as 'sender' coils. The back-scattering field due to the eddy currents produced in the target induces a voltage signal in other coils in the detection system. These coils are referred to as 'receiver' coils. The excitation field can be either transient or time harmonic and the choice also depends on the aim and specifications of the detection system including the features of the target to be detected. The electromagnetic field produced in the sender coils induces a voltage in the receiver coils due to mutual inductance. The perfect detection system can decouple the primary field of the sender from the secondary induced field in the receiver. This induced field contains the two parts, the mutual inductance by the sender and the induction due to the detected targets, when present. For that reason, geometrical optimization of the coils (both senders and receivers) and their design is crucial to decouple these effects or eliminate the primary effect at least. A simulation and experimental approach verifies and proves the

proposal in that direction. The last section deals with signal processing methods of such a system. The induced voltage signal is an array of voltage and time and that is all what the sensor detects. This induced signal should be analyzed to predict the features of the detected targets. Signal processing, here called post processing because it is executed after the voltage measurements, provides a parametric algorithm or procedure based on these signals to give information about the features of the targets hidden.

Chapter 3 focuses on all implementations done to get a robust and effective model of a detection system, which is described in Chapter 2. Without the model, the current work would not have been possible or at least not possible with the same outcome in the same time frame. As mentioned in the first part of this chapter, relying solely on experimental approaches can be misleading. The models developed or used here are based on the finite element method that solves Maxwell's equation. But theoretical implementations to the core model were performed at the pre-and-post processor levels so that the solver still gives accurate results in faster computational times. This model is also compared to a dipole based model for different setups. The dipole model is also considered in the current work. This model has limitations so its usage is only possible within these limitations that are also described. The ability to simulate 3D components in a reasonable time was a huge contribution. Frequency and time domain analysis were performed and verified against experimental results. The verification of the model was performed for different coil designs and excitation schemes as well as for different target positions, shapes, and materials. This model is not only used as a reference in this work, but also as a verification tool for the procedures proposed especially the distinctive detection part.

Chapter 4 proposes a procedure for discrimination and distinctive detection of targets. The main and final output of this work is explained in that chapter. The areas of focus, from the system representation to the model approach contribute mainly to this part of the work. The outcome is an efficient, robust and smart plan of using post-processed signals to identify targets and their features. The work continues further to propose a new concept on how to distinguish between captured information of more than one present feature. Application example is demonstrated and proved by simulation and experimental data.



## Chapter 2 EMI sensor

Electromagnetic induction (EMI) sensors are used to sense metallic objects buried or hidden in a base media. Usually, the base media is not sensitive to an electromagnetic wave while the objects themselves are. In general, the EMI sensor is effective mainly when the base media and the detected features have different responses to the electromagnetic wave. Additionally, some EMI sensors are used to sense voids or empty volumes in a metallic media. A different response is present when the user scans the device across a homogeneous media than a response over a local change in the material composition in the media. This change would be the targeted metal in a non-metal media or vice versa. An example of the first way of sensing is the detection of mines or buried objects in the soil [57], [58]. It is a nondestructive testing method as mentioned in Chapter 1 used to sense the buried objects without destroying the base material, which is the soil in this case. An example of the second way of testing is to detect cracks or voids in metal base material like steel pipes [35]. Usually, the response of compact steel is known and when some cracks are present then the response is different. Using EMI sensors allows optional application possibilities, for example the detection of corroded hidden steel [65]. Steel is ferromagnetic and when it is not corroded it gives a consistent response. But corrosion is paramagnetic and when it is present then the response is much different and can be analyzed and processed to even detect the amount of corrosion relative to the specifications set ahead. Other EMI sensor types are focused on detecting voids in soil-conducting media. Voids are neither permeable nor conductive and by that a conductive media always induces a consistent response but only in the presence of void the response is different. Therefore, it is important in the design of any EMI sensor to know first the specifications that must be set ahead. Some applications just should detect the transverse location of the targeted objects. For example, the answer of yes or no (one or zero) is sometimes sufficient in knowing if there is a landmine or not. The same applied to cracks in steel pipes in the gas and oil industry where the presence of any crack can be dangerous and needs to be repaired. The specifications can get more demanding if the depth of the landmine is also required to be evaluated from the induced signal. To disable a landmine different techniques are used depending on the depth of the mine. The detection industry exploits the EMI capability to the maximum, heading towards feature discrimination, which is one of the challenges for such technology. In the context of this thesis, feature means any specification of the targeted object to be detected that distinguishes it from another object. Size, location, shape, and material are examples of features that may induce electromagnetic scattering waves differently as mentioned in Chapter 1.

The level of feature discrimination, (section 2.1), defines the whole design of the sensor coils, (section 2.3) especially the sender coils and its excitation scheme, (section 2.2). The

sensor is improved and optimized accordingly. Signal processing (section 2.4) of the induced signals analyzes and delivers all the information required of these target features and this is the only source of proving the discriminated features.

## 2.1 Feature discrimination

EMI sensors are designed, optimized and developed according to the features of the objects or targets that need to be detected. Transverse location is a feature of most sensors. It is sometimes sufficient while moving the sensor in a transverse direction (scan direction in-plane of the sensor) to know if there is a change in the induced signal, which when analyzed and post-processed can define the existence of the object at that planar location of the sensor. Usually the sensor device is equipped with wheels so that the user moves it in the plane over the media to find target transverse locations. Many other features are required to be estimated and some of which are sketched in Figure 2:1. The depth is one of the regular features of such sensors. Many commercial devices implemented analysis schemes to provide the end user the depth of the object required, for example, finding the depth of a landmine under the surface of soil, or the depth of reinforcing steel bars inside the concrete walls or tunnels (section 1.2.1).

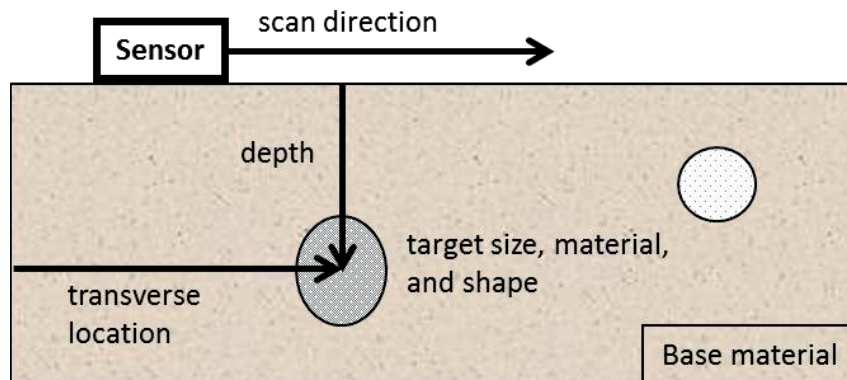


Figure 2:1 Target features to be detected, transverse location, depth, size, shape, and material.

EMI technology, as mentioned in section 1.2.2, has relatively strict limitations concerning depth. Induction, of the eddy current field in the target, should be high enough to overcome the noise level and interferences. And since the operating frequency of the sensor is relatively low ( $< 1$  MHz) then most induction sensors are not able to detect targets above 150 mm to 200 mm in general if the coil dimensions are in that range as well. EMI can be used to detect targets of several meters deep but the coil sizes should be in the meters range as well to get a strong signal from the target. One way to detect deep targets using EMI is to operate at higher source current intensity but the disadvantage is always the waiting time to post-process the induced signal, which makes the usage of the sensor relatively slow. When higher source currents are generated they need to be brought down to zero again in some excitation methods so that they don't dominate the response field which can be measured later. The waiting time is required because the source signal

dominates the receiver voltage and the device should wait until this is negligible and then induce the pure signal generated by the eddy currents of the target. This is the case in pulse induction. As for harmonic induction, the decoupling of the mutual inductance between the coils is even more difficult. This mutual inductance between the source sender coils and the receiver coils is mentioned earlier in Chapter 1 and is one of the main challenges in designing such sensor depending on the priority of the target features to be detected. One other challenge of such sensors is the discrimination of targets per material. It is highly demanded that the sensor can distinguish between ferromagnetic material like steel and purely electrically conductive material like copper or aluminum. Shape is one of the most difficult features of a target to be detected and visualized. Higher frequency sensors are able, to a certain extent, to highlight an estimation of the shape of the target even if it is complex in the form. The EMI sensors can be mainly used to discriminate between obvious shape features. The EMI method is able by using a sensor in a certain well designed way synchronizing between the excitation frequency and the correct signal processed, for example, to distinguish between full material cylinder and a pipe or tube. This is due the way eddy currents are dissipated on the skin of the target where the skin depth varies depending on the material and the excitation frequency (2.1). The advantage of EMI is that the permeability and conductivity of the target as well as the excitation frequency are all related and all influence the response that needs to be analyzed. That's why the material discrimination is possible for such sensors if the excitation scheme is smartly designed and this is explained in a section 2.2. But the eddy currents in the target should flow in the conducting space of the target material. If the space is limited, a thin hollow cylinder or a thin metal sheet, then the time constant for the induced signal to vanish differs from a geometrical shape to another even if they have the same material. It is well assumed that the eddy currents flowing in a conductive body only occupy a depth of  $\delta$  at the skin of this body as formulated in (2.1). Skin depth formula is related to the excitation frequency  $f$ , the electric conductivity  $\sigma$ , and the permeability  $\mu$ .

$$\delta = \sqrt{\frac{1}{\pi f \sigma \mu}} \quad (2.1)$$

Complying with the shape feature detection, the skin depth plays a big role in the detection of pipes versus full cylinders for example because it is also possible due to the defined skin depth to extend the flow of eddy currents in the target at a certain chosen frequency if the skin depth of this target is greater than the tube thickness. When a tube is detected rather than a cylinder, even the thickness of this tube can be estimated following this rule. Such examples, are numerous in real industrial application and the simple examples here just explain the relationship between target features and excitation scheme.

One of the biggest disadvantages is that the conductivity and the permeability are always present in the product  $f\sigma\mu$  which is the representation of the induction number  $k$  (see

sub-section 3.2.3). So, different targets may have the same induction number  $k$  and discrimination gets difficult. This skin depth formula is also used in computational models [25], [26] and is explained in the Chapter 3. So, for the same excitation frequency, for example, more conductive targets have smaller skin depths. Less permeable materials have bigger skin depths. And this is a clear prove that material discrimination is very difficult.

The size is another feature of targets. If the sensor is set up to detect cylinders, for example, then the diameter of these cylinders is a feature to be also estimated by post-processing. If the sensor is set up to detect metal sheets, then the thickness of these sheets is also a target feature.

To conclude, depending on the target features to be detected, specifications are set ahead. Only then it is preferred to design the coil geometry and the excitation scheme delivering, in the end, a procedure that satisfies these specifications. Such features are the transverse location, depth, material, size, and shape of the target to be detected.

## 2.2 Electrical excitation

The EMI sensor is based on the eddy currents induced in the target. They create, in turn, the back-scattering electromagnetic field. These eddy currents are only available if the source current in the sender is changing in time. It is therefore important to design an excitation scheme in the sender coils with well-defined variation in time to generate eddy currents in the targets that, in turn, create the back-scattering electromagnetic field to be induced in the receiver coils. The induced signal in the receiver coils is also expected in a certain form, which when processed in a planned way can give the information required of the features of this target and the difference to other features of other targets.

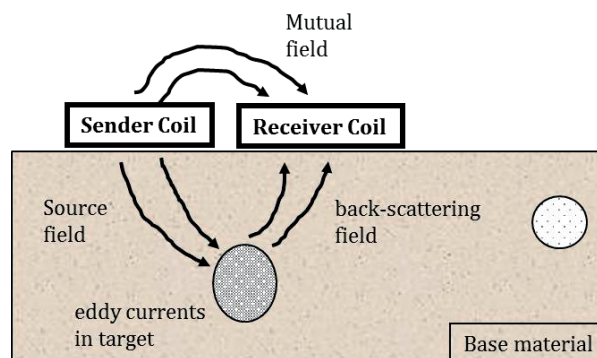


Figure 2:2 The three main fields in an EMI system: source field, eddy currents, and back-scattering.

The source field is a time variant electromagnetic field and to create such a field, a time variant source current should be circulating in a coil for example (sender coil). This coil

is made of few turns of electrically isolated copper wires. The design of such coils depends (geometrically) highly on the specification required and this is explained in the section 2.3. For now, the sender coil is represented as a block (see Figure 2:2). The position of the receiver coil is critical to the design especially because of the induction by the sender's dominant field. It is important to decouple the dominant mutual field of the sender from the back-scattering field of the target. Doing so allows induction of targets only and this is the goal. The receiver is presented also as another block (see Figure 2:2) for explanation reasons. The source time-varying field creates eddy currents in the target and this by itself generates a back-scattering time variant electromagnetic field that in the presence of a receiver coil induces a voltage that can be analyzed. Therefore, the source excitation scheme in the sender coil is the main driver of the detection system design.

Time-varying source current generated in the sender coils is not difficult to create. The current can be varying in any way. It can be harmonic in time at a certain frequency, or a series of harmonic signals each with a different frequency allowing the designer to reach the aim of the detection system (detect the specified features of the target). The current source can be a pulse. Pulse excitation is already used in detection systems because it decouples the sender and receiver coils in time. In contrast to harmonic excitation, pulse excitation is very broadband and therefore it is mathematically equivalent to measuring many frequencies. But it contains all the information of all these frequencies and by that it limits the flexibility of the feature discrimination. In the context of this thesis there is a focus on both pulse excitation and harmonic excitations with models, experiments, and verification. The placement of the sender coil relative to the receiver coil cannot be designed randomly. The sender coil position should be nearest to the target to generate the highest level of the eddy current field in this target. The receiver, as well, should be nearest to the target so that it senses the most intense signal. So, both coils are most effective when they are both nearest to the target. Simply they should be placed in the same place nearest to the base material. But a close lying sender and receiver will have the biggest mutual inductance. Therefore, the advantage in the increase in the amplitude will become a disadvantage in the cross talking between the coils. A perfect detection system allows zero induced voltage in the receiver due to the sender source field. The perfectly designed receiver should sense the back-scattering field from the target only. One idea is to place the sender far away from the receiver, which contradicts with the first criterion. As a conclusion of these two criteria it is important not only to design the excitation scheme but also the geometrical design of the coils. An optimum can be found to reach the specifications required with the supreme effectiveness and robustness. Coil design will be therefore described in more details in section 2.3. The first step in finding this optimum is to choose the excitation scheme. Both, pulse induction and harmonic induction are used in this thesis and an explanation of both follows. In every one of them the coil design should be different due to the interconnection described. Also, the post-processing and parametrization will be different. It is first important to explain the basics of excitations (pulse excitation in sub-section 2.2.1, and harmonic excitation in sub-section 2.2.2) and sensor design (section 2.3) with simple examples and engineering terms.

### 2.2.1 Pulse excitation

Pulse induction is a very effective excitation method since the source current decreases to zero very fast. The source sender coil is fed with a constant dc voltage to raise the current to a maximum level  $I_{max}$  as seen in Figure 2:3. After that the voltage is switched off and by that the voltage reduces directly to a very low negative value that brings the current to zero in a very short period  $\tau_{off}$ . The change in the source field induces eddy currents in the target, and with pulse induction the current changes rapidly to zero and after the zero level then the receiver should be independent on the mutual induction (if it exists) of the sender-receiver. After the current is zero, measurements of the induced voltage can be done on the receiver side. Because of this mutual inductance it is important to bring the current very fast to zero so that the receiver can measure only the target response. But this will limit the flexibility to have current changes in shorter times. The pulse induction will always have a predefined  $\tau_{off}$  and this will be limiting the excitation frequency to one value, usually one  $\mu s$  in time domain.

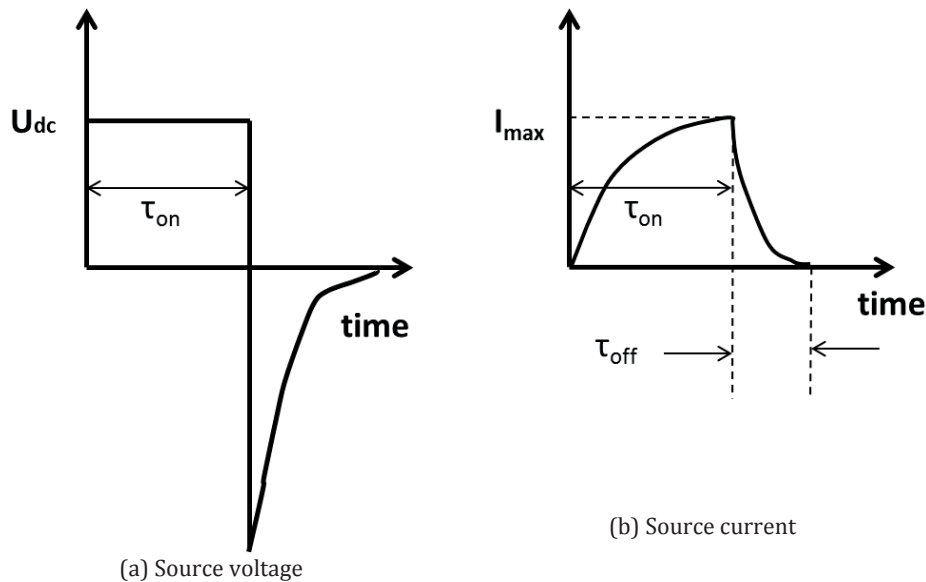


Figure 2:3 Pulse excitation on the sender source coil a) dc voltage applied and switched off, b) current rise and fall in the sender.

The electronic devices needed to produce a pulse are designed and fixed and therefore any changes in the time constants will not be possible after the design freeze. The rise time,  $\tau_{on}$ , of the current is required to raise the current to a fix value  $I_{max}$  before switching off. This time is depending on the resistance,  $R_s$ , and self-inductance,  $L_s$ , of the sender coil, that is why a sender coil should be also designed in connection of the excitation chosen because in theory  $\frac{L_s}{R_s}$  is the time constant of the coil if the capacitance is ignored. In the sensor design, sub-section later these parameters will be detailed. This time constant also affects the fall time,  $\tau_{off}$ , as sketched in Figure 2:3. The need for the lowest values of

the fall time requires the lowest values of  $\frac{L_s}{R_s}$  and by that the coil choice is important. In Figure 2:3 b,  $\tau_{off}$  is the waiting time for the current to diminish and after that there will be no mutually induced voltage between the sender and the receiver. The voltage induced in the receiver after that point in time is assumed to be the pure induction from the target. This induced voltage can be compared to other responses of other targets to distinguish the features of both targets.

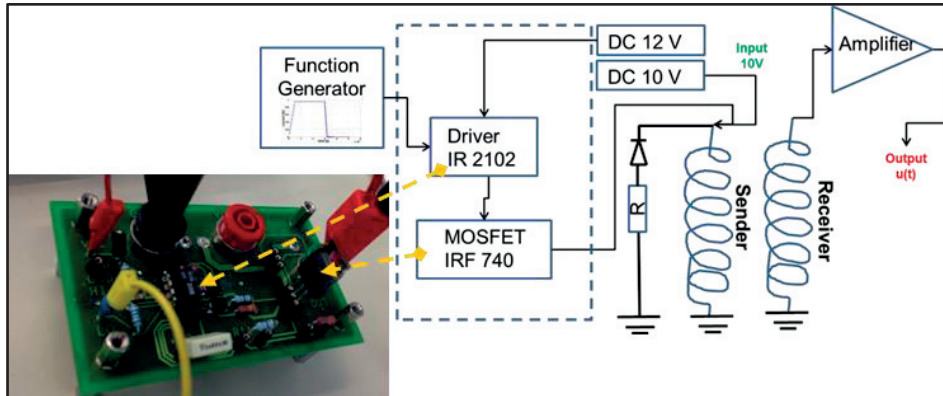


Figure 2:4 Pulse excitation electronic schematic, including a driver and a MOSFET that are timed according to an external function generator.

One way to generate a voltage pulse similar to Figure 2:3 (a), which will produce a current in the sender similar to Figure 2:3 (b), is by an electronic system hardware as sketched in Figure 2:4. A DC voltage of 10V from a power supply is connected to the sender. This will provide a first constant voltage  $U_{dc}$  to the sender. During this time the current will rise to a certain maximum  $I_{max}$ .

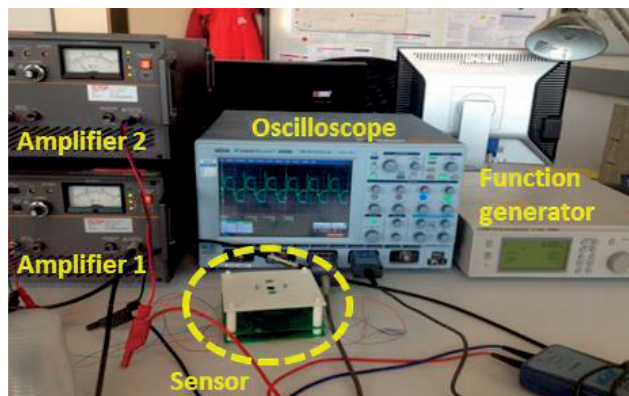


Figure 2:5 Experimental setup of a pulse induction scheme.

The other power supply of 12V is only needed on one terminal of the driver. Together with the function generator, they both define the timing of when to switch off and when

to switch on again. It is enough to have an asymmetric square signal with equal positive and negative amplitudes so that the MOSFET (metal oxide semiconductor field-effect transistor) switches off and then on again according to the timing of the function generator. If this square signal has low amplitude, then an amplifier should be used to amplify it to a desired level according to the driver requirements. Switching off will allow the current in the sender to reduce to zero and stay at zero level due to the diode in the schematic. This will repeat again and again periodically producing a desired pulse train in the sender. The resistor,  $R$ , is added in Figure 2:4 to be able to change the fall time,  $\tau_{off}$ , and would have importance in frequency manipulation for future work of distinctive detection by pulse induction. In the context of this work, the value of  $R$  is kept constant to reach a fall time of  $1 \mu\text{s}$ .

The receiver will experience a voltage due to the sender first and later due to the target response if any. The voltage in the receiver is relatively small and that is why it is amplified to get a clearer measurable signal.

All values can be measured using current probes and voltage differentiators and the signals can be visible and saved with the help of an oscilloscope like the one in the photo of Figure 2:5. The sensor prototype should be correctly wired according to the schematic. Additionally, two amplifiers and a function generator are also required.

In the context of this work pulse excitation has been used in experiments and in simulation models for validation and verification. The computational models are solved in time dependent domain. Harmonic excitation is also used and will be mentioned in the next sub-section.

### 2.2.2 Harmonic excitation

Harmonic excitation is simply feeding the sender coil by an alternating voltage usually a sine shape, which is continuous in time. The red curve in Figure 2:6 represent the voltage source at the terminals of the sender coil. The resulting current in the same coil will also be alternating but shifted in time with a phase angle  $\theta$ . Due to the inductance of the coil there will be a phase difference between the current and the voltage.

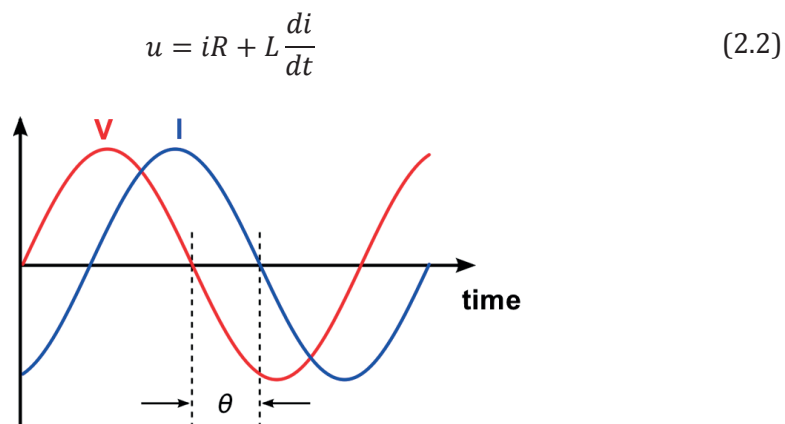


Figure 2:6 Source voltage (red) and current (blue) of the sender coil in a harmonic excitation.



The coil can be represented as a resistor and inductor in series (RL circuit). The voltage in the sender coil will be a function of these electrical properties as in (2.2). The phase angle  $\theta$  is the phase difference between the source voltage and the current. If the applied voltage is harmonic, then the current is as well and their values can be assumed as follows:

$$\begin{aligned}i &= I_{max} \sin(\omega t) \\u &= U_{max} \sin(\omega t + \theta)\end{aligned}\tag{2.3}$$

Where  $\omega$  is the angular frequency and  $t$  is the physical time.  $\theta$  is the phase shift of the voltage signal,  $u$ , relative to the current signal,  $i$ .

Taking the derivative of the current in (2.3) and inserting all variables in (2.2) will lead to the relationship in (2.4)

$$u_{max} = I_{max} \sqrt{R^2 + (\omega L)^2}\tag{2.4}$$

It is clear the total impedance is  $\sqrt{R^2 + (\omega L)^2}$  and depends on the frequency as well. The resistance of the coil is constant. The induced voltage is usually due to the self-inductance of the coil because the target induces a weaker signal. Also, the current in the receiver is usually negligible and its induction voltage in the sender is small compared to the source voltage in the sender. One can easily deduce that at high frequencies the impedance of the sender will increase and usually it is recommended to have a low impedance so that the same current is reached with lower voltages. This can be done by designing the coil to have a low inductance  $L$ . Another reason why  $L$  should be low is since it is responsible for the time constant of the source field and this will be explained in the section 2.3. Printing the coils on Printed Circuit Boards (PCB) will achieve a low  $\frac{L}{R}$  value and this would be optimum in using such coils in a relatively high frequency harmonic induction. The PCB coils will be detailed in the next section taking into account the capacitance and assuring that the resonant frequency would be much higher than the operating frequency.

The receiver will also experience a harmonic voltage part of which is induced due to the sender and the second part is induced from the target. This last part is the most useful in feature discrimination and is less intense than the one induced by the sender. A perfect receiver performance would be to eliminate the sender effect and measure pure target effects. This will be designed and described in the section 2.3. The induced voltage in the receiver due to the target is not easily quantified or put into known equations. It is due to the eddy currents in the target that are highly geometry related. Targets that are close to the receiver will induce higher signals. One must increase the frequency to get higher induced voltage from far targets. This increase is costly due to the increase of the total power and the heat generation in the coils. Therefore, optimum designs are required to achieve the detection aims of this work. The receiver voltage has a phase shift relative to the sender voltage but in the current work this phase shift will be relative to the sender

current instead. The current is responsible for the magnetic field and will be taken as a reference signal, i.e. it has a zero-phase angle.

## 2.3 Sensor design

The design of the sensor means here the geometrical design of the sender and receiver coils. Any trial and error approach in this kind of design can be misleading. The coil design and optimization are strongly linked to the excitation scheme described in section 2.2 and the post-processing procedure that is detailed in section 2.4. One cannot proceed in closing the loop of sensor design without including this three-major basis of optimum feature discrimination. To reach an optimum design that would deliver the aim in discriminating a set of defined features of a target, one should start in steps of eliminating challenging problems in such a system. It is difficult to have a complete automatic closed loop optimization procedure due to the quantity of free variables.

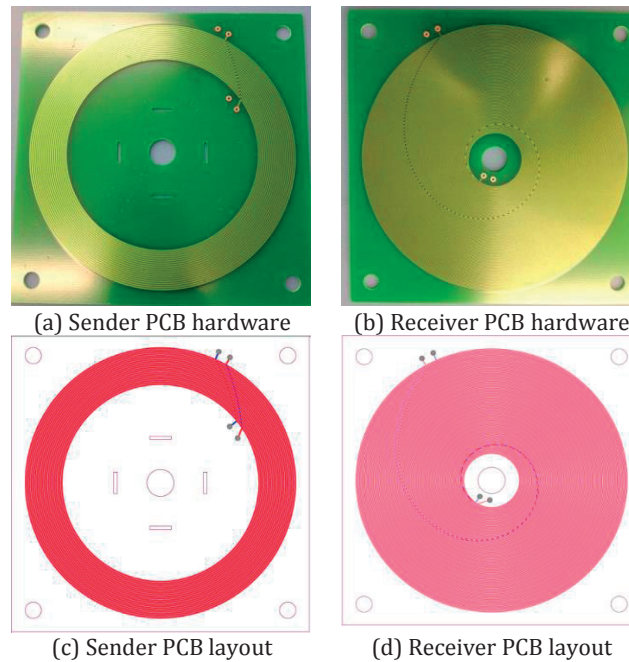


Figure 2:7 PCB hardware of the a) sender coil b) receiver coil with their PCB layout design done by Altium Designer c) and d).

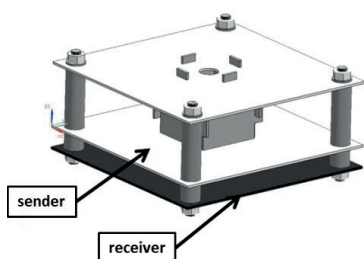
A design is only valid if it is applicable to all ranges of the combined variables. Some of these problems or challenges are the mutually induced voltage by the sender in the receiver, the signal strength to reach deep targets, the mutual or coupled field between nearby targets, the superposition of responses of targets, and the various challenges in feature discrimination according to the signal response. The choice of coils for such applications is not trivial. The coil is simply one wound wire (or printed pad on a PCB) with several turns. It has a resistance  $R$  and an inductance  $L$ . When a current is set to flow in

the coil a magnetic field is generated and the first rule of thumb for the induction applications is to have a low  $\frac{L}{R}$  ratio defined in the previous section as the time constant. Printed Circuit Board (PCB) coils were used in this work instead of classical wound coils due to the very low time constants they have. A first proposal of a sender and receiver PCB coils is shown in Figure 2:7. Optimum coil designs will not be introduced at this stage, but rather set the boundary conditions and functionality of such systems. The sender coil is responsible for the field and is fed by a voltage in the range of 10V so that the current is in the range of one Ampere. Its inductance should be low and resistance is in the range of 10  $\Omega$ . The need for low  $\frac{L}{R}$  is to have a fast rise time and fall time of the current. The sender coil in Figure 2:7 a) consists of 40 turns with a resistance of 11  $\Omega$ . The copper is printed on the 1.2 mm thick epoxy board with a gap of 0.5mm between the tracks. The outer diameter is 100 mm.

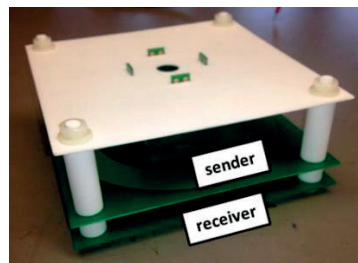
The track width is 0.5mm and the copper pad thickness is 35 $\mu$ m. The tracks are printed on the two sides so it is a double layer PCB. The receiver requires as many turns as possible to induce the highest possible voltage signal, which is proportional to the number of turns. The effective space should be filled up with copper pads, but the gap between the pads has manufacturing limitations and this will limit the number of turns. The first proposal for a concentric receiver as in Figure 2:7 b) is a total of 200 winding coil with the same copper height as the sender but the track width is 0.2mm and the gap between the tracks is 0.2mm. The gap here is less than the one in the sender because no current will flow in the receiver and there will be no cross coupling.

$$\omega_0 = \frac{1}{\sqrt{LC}} \quad (2.5)$$

It is important to calculate the voltage drop between the tracks that would produce a certain self-capacitance, which should be small enough to be ignored. In any case the coil will have a self-capacitance. No matter how small the capacitance is, it is mandatory to roughly calculate the resonant frequency of the system by (2.5). In the context of this work the coils are designed in such a way that the resonant frequency is always in the range of 2 MHz and more, because the maximum application frequency does not exceed a MHz in both harmonic or pulse excitation schemes.



(a) 3D sketch of the simple sender receiver



(b) hardware of the simple sender receiver

Figure 2:8 The simple sensor sketched first in a) CAD software then b) manufactured by rapid prototyping and assembled with the PCBs.

The coils should be placed precisely concentric to each other. With rapid prototyping and assembly, the first simple prototype can be used for testing as shown in Figure 2:5. The receiver is at the bottom. This means that the target is below the sensor in this case. This first simple configuration is tested for both excitation schemes because it is the simplest design (see DESIGN I in Appendix B) that can be used for validating simulation models. Verifications and comparisons to experiments are shown in Chapter 3 as well as simulations using two different computational models for a better understanding and later for optimization and case studies. Some configurations are then added to prove their validity.

### 2.3.1 Neutral sensor inductance

The mutual inductance between the sender coil and the receiver coil is a challenge during sensor design because the best placement of both sensors is where they are both close to the target. Theoretically, and if there were no mutually induced voltage between them, the best case would be to place them concentric inside each other. The receiver would get the maximum signal from the target after the sender has excited the target. But on the other hand, this placement would produce the highest mutual inductance in the receiver, thus the highest voltage induced by the sender coil. This would dominate the induced voltage by the target. The first approach is to find a neutral inductance position of the receiver. Neutral means here that the sender coil, theoretically, induces no voltage in the receiver coil. Looking at the field lines generated by one winding of the sender coil where a current ( $I$ ) flows, flux density lines (blue) are generated around the wire as in Figure 2:9. The magnetic flux  $\varphi$  normal to an area  $A_{coil}$ , which is a surface area of the receiver is calculated simply by  $\varphi = B_{axial} \times A_{coil}$  where  $B_{axial}$  is the flux density axial to the coil or perpendicular to the surface its area. The flux lines in Figure 2:9 cross through the receiver (green coil) in two directions. They create a positive flux on the left side and a negative one on the right side.

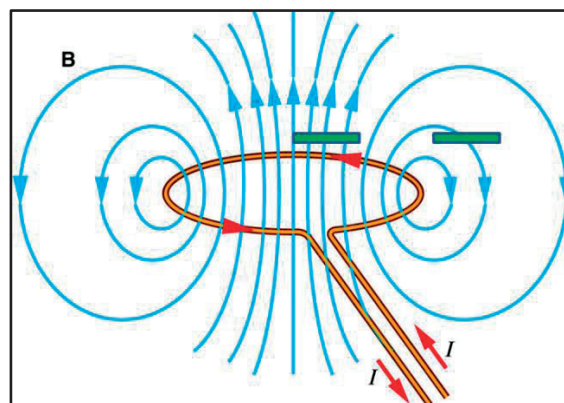


Figure 2:9 Magnetic field lines generated by a coil wire, and the general placement of a receiver (green rectangle).

If the sender and receiver are concentric then all the flux lines are in the positive axial direction resulting in a positive flux while for the green rectangle on the right side the flux would be negative. So, if the complete receiver coil is placed in the middle of the sender coil a positive flux is generated. Consequently, if it is placed on the right side then a negative flux is generated.

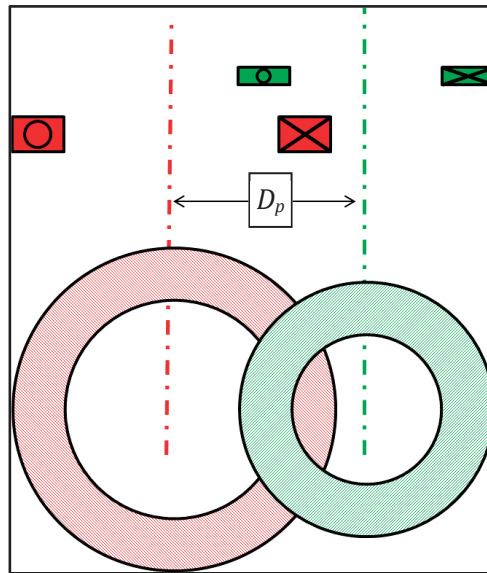


Figure 2:10 Geometrical balance of the receiver coil against the sender coil by a shift of  $D_p$ .

The first approach, after this observation, is to design a receiver with the best area distribution placed in a way that part of it induces a positive flux while the other part induces an equal negative flux to achieve a total sum of zero flux. This balances the receiver and generates zero inductance voltage in the coil. A simple first proposal is to have a receiver coil similar to the sender coil placed in a way shifted in the radial direction until the flux is zero. If this is achieved, then the receiver will only induce a response from the target and no longer from the sender. This is called neutral inductance as well. For simplicity and understanding the way to reach neutral inductance, consider a perfectly round sender and receiver coils set as in Figure 2:10, which are displaced radially by a distance  $D_p$ . The red coil is the sender that creates the magnetic field while the green receiver is displaced to reach induction neutrality.

In the next chapters, examples and verifications will be demonstrated starting from this coil design concept. In the rest of this chapter some highlights on the flexibility of this concept are shown. One advantage is the frequency effect and its relevance to the geometrical setup and target feature discrimination.

### 2.3.2 Frequency and geometrical relevance

The sender when excited with a harmonic signal generates a harmonic field, which interferes with both the receiver and the target. The receiver experiences both fields of the

sender and of the target. It was shown in sub-section 2.3.1 that the receiver position plays a big role in the induced flux. At one displaced position the response is zero but is this valid for all operating frequencies? A parametric study was performed to the configuration in Figure 2:10 where the frequency is varied from 20 kHz to 300 kHz. The displacement  $D_p$  is also changed from being concentric ( $D_p = 0$ ) to a displaced relative position of both coils. The maximum displacement here was  $D_p = 75$  mm. The induced voltage is represented, in the harmonic case, by a real part and an imaginary part. Both voltages are plotted in Figure 2:11 a) and b) respectively.

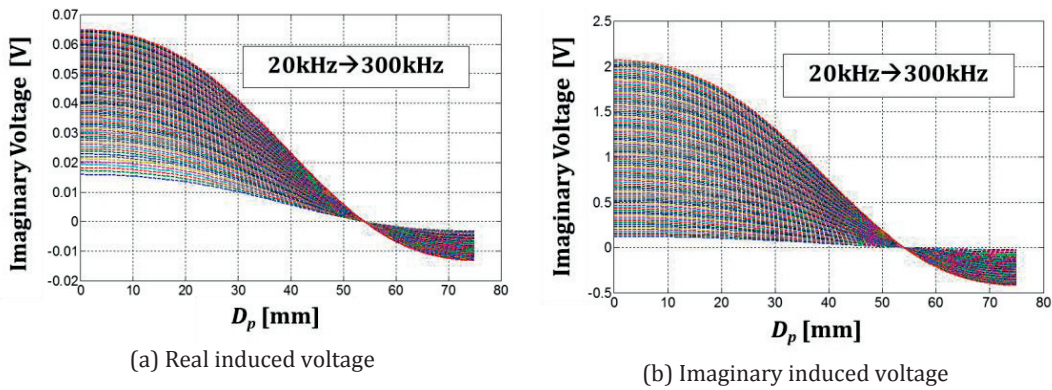


Figure 2:11 The effect of the sender frequency and the receiver displacement ( $D_p$ ) on the induced a) real voltage and b) imaginary voltage.

The plots of Figure 2:11 prove that the real and imaginary voltages in the receiver will vanish for a displacement of the receiver near  $D_p = 54$  mm for all frequencies. This phenomenon is useful in some cases depending on the feature discrimination set. The choice of circular coils is conducted in this example but a study of elliptical and square shapes leads to different displacements,  $D_p$ , canceling the induced voltage at all the operating frequencies. For that reason, it is free to use any coil shape if the displacement,  $D_p$ , is computed similarly afterwards.

The first advantage of such a system is the ability to have a zero or near zero response when the target is not present. By that the induced voltage in the receiver by the sender is eliminated and only additional response by a target will be sensed. The target response may be relatively smaller than the response in the classical way but when amplified it will be the pure target response, which is more reliable in the discrimination procedure done by post-processing later. There would be no need to calibrate the sensor by electronic means or by subtraction of responses. In addition to that and when designed in a smart flexible way, some features can be eliminated while others would be highlighted and this leads to distinctive detection technique described in details in Chapter 4. The induced voltage has information about target features and this has to be processed. Signal processing description is done in section 2.4.

## 2.4 Signal processing

The induced signals have to be processed. In any excitation scheme, harmonic or transient, and with any coil configuration the only output signal from the receiver is a voltage signal. In a transient pulse induction scheme, the voltage signal would be a voltage decay signal in time. The challenge here is to relate this decay to some features of the target that needs to be analyzed. In harmonic excitation methods, the induced voltage can also be assumed harmonic and the output is reduced to only two parameters: amplitude and phase shift or real and imaginary parts. The amplitude and phase shift when compared to a pre-defined database can give information about the location, size, and even material of the target. The processing is not trivial and there are challenges like environmental variances, like temperature for example.

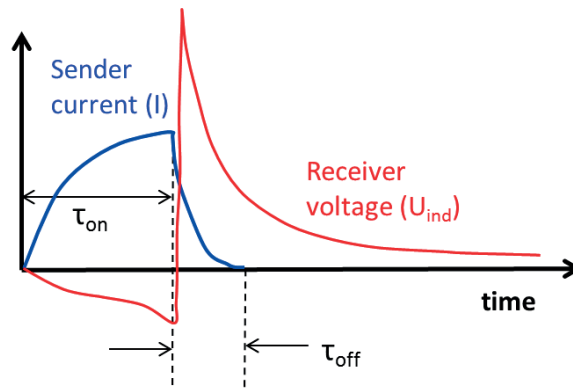


Figure 2:12 Pulse excitation done by producing a current (blue) in the sender which induces a voltage (red) in the receiver.

Very different amplitude responses could be generated for the same coil and target setup but at different ambient temperatures. This means the sensor is not considered robust if it only relies on amplitudes. The signal's phase angle may not vary with the temperature and a smart sensor design plays a role in eliminating such effects as well.

Another challenging aspect is the similarity in response of different features. For example, a small shallow target may give a very similar response to a bigger but deeper target. Again, the sensor design has to be adapted to be able to find clever ways to discriminate these differences. The amplitude of the induced voltage signal is easy to extract because it has a repetition of maximum values every period. The phase angle is always compared to the phase of the current. The current in the sender is always considered as a reference (zero phase shift).

Any induced voltage will have a phase shift to the sender current. In a transient scheme a pulse train (repetitive pulse) can also be designed inducing a repetitive set of decays to be averaged for resolution reasons. A small example is required to explain that. This example will be used also in the next chapters. In any random placement of the sender and receiver coils as in Figure 2:2 the pulse induction can be done by exciting a current in the

sender and measuring the voltage in the receiver. In the presence of a target the induced voltage would be different than in its absence. An example of such a current and voltage behavior is sketched in Figure 2:12. The current has to rise to a maximum using a dc voltage then the voltage is switched off allowing the current to drop to zero in a time period of  $\tau_{off}$  as described in section 2.2.1. This drop is the most important player in inducing eddy currents in the target. As mentioned in section 2.2, eddy currents are produced because of the change in the current, thus the change in the field in time. As long as the current in the sender is not zero there will always be an induced voltage in the receiver even if there was no target. This is due to the mutual inductance between the sender and the receiver. During these time frames,  $\tau_{on}$  and  $\tau_{off}$ , there is a dominant voltage due to the sender current. Only after the current in the sender is diminished, the recorded voltage in the receiver would be reliable. For that reason, it only makes sense to measure the voltage starting from that point in time.

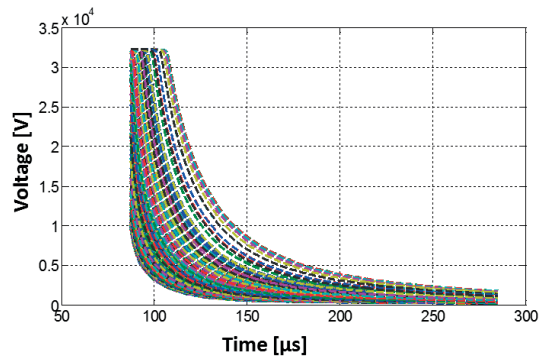


Figure 2:13 Typical induced voltage decays of different target sizes, depths, and transverse locations.

The induced signal will be nothing but a series of voltage decay in time. This voltage decay will be different in the presence of different target features like location, material, size and shape. Typical measured decays by experiments on a simple sensor are shown in Figure 2:13. These voltage decays show clearly that they are much different in the starting point as well as the ending level. Many considerations have to be taken into account for such an example and it is worth to mention a few:

- One extra challenge in this pulse excitation scheme is to be able to quantify the series of decaying voltage in time using few parameters rather than the complete points in time. In harmonic excitation, as mentioned earlier, the parameters can be maximum two, real and imaginary components of the induced voltage, or amplitude and phase angle. In a non-periodic response like the pulse induction response the voltage is a set of voltage values in time similar to any curve or decay in Figure 2:13.
- These voltages were already amplified and the amplifier has an upper bound limitation clearly visible at the early stage of the decay. At that early time, some



signals are stronger than others. The response of a bigger, but shallow, target is stronger than the response of small deep targets. The amplifier usually is hardware fixed for the whole range of signals that is why stronger signals get limited at the starting time. Referring to Figure 2:13, some of the signals stay constant at the left side because of the limitation of the over amplification while other signals are starting to directly decay. Having this constant level for a longer time interval will make the signal difficult to parameterize or analyze. Usually, the constant part is skipped and only the decay part is considered. If signals have to be fairly compared at the same starting point in time, which is usually the classical case then the starting point will be much later in time in order to cover all ranges of responses and this is a disadvantage.

- Interferences induce additional voltage in the receiver. Eddy currents are also generated in the electronic parts or metal parts of the whole sensor package and this is included in the measured signal in the receiver coil. The response due to a target has to be subtracted from the response without a target. This is called calibration. This eliminates the sender mutual inductance as well if superposition principle applies. In building the experimental database for a developed device, calibration has to be done often in order to ensure that a pure target signal is deduced. Calibrated signals have to be saved before the post-processing step.
- The low signals generated due to small targets at deep locations will have a certain amount of noise that cannot be avoided. Filtering and fitting techniques have to be included so that they are fairly compared with well-constructed signals.
- In order to differentiate between the signals, each signal has to be represented by two or three parameters. The first step is usually to represent these parameters in look-up tables as a function of features to be differentiated. If the features are depth and diameter of steel targets, for example, then a database is constructed by saving all the decays for different depths and diameters. It is possible to apply a post-processing procedure representing new parameters in a 2D lookup table (2D because in this example there are two dimensions: diameter and depth). Just few parameters represent a decay as a function of the unknown features. Of course, one lookup table with two variable features is not enough to solve the inverse problem and therefore, additional techniques have to be used as described mainly in Chapter 4.
- The decays may also be fitted to an equation with a physical correspondence to induction methods. But in the actual device a micro-controller is performing the calculation. It is a big challenge to do fewer operations to ensure a fast way of feature discrimination. Nevertheless, a compromise between computation time of the fit and accuracy can be done to deliver two ways of signal processing: live discrimination and post-scan discrimination. In the live discrimination, a very fast method should give a rough estimation of hidden objects where the end user demands some plots and values on the device screen immediately. Post-scan, on

the other hand, is used by more professional users who need a very precise estimation or even 3D plots of the targets and can wait a few hours to analyze, on a separate computer, all sets of decays that have been saved after the measurements were taken.

### 2.4.1 Signal processing example

A simple example is demonstrated here in order to clarify some challenges in signal processing. Both experiments and simulations of an actual hardware are conducted using pulse induction. A post-processing method is evaluated to inversely find an unknown target with a certain allowable tolerance or error. The detection system analyzed in this section consists of a sender PCB coil with 40 printed copper turns and a receiver with 64 turns. Both sender and receiver cross-sections are sketched in Figure 2:14 together with the target to be detected. The target is a steel cylinder long enough to avoid end effects. The target features of interest here are the diameter,  $d$ , cover,  $c$ , and horizontal displacement,  $x$ . A pulse induction scheme as in Figure 2:12 with a current rise time of  $80\mu\text{s}$  ( $\tau_{on}$ ), and a fall time of  $1\mu\text{s}$  ( $\tau_{off}$ ) is being generated. The maximum current reached is  $0.9\text{A}$ . This system is used to evaluate the voltage response in the receiver for all the following combinations of features:

- $d = 6, 8, 10, 12, 14, 16, 20, 25, \text{ and } 28\text{ mm}$
- $c = 5\text{ to } 155\text{ mm, measured every } 5\text{ mm}$
- $x = -150\text{ to } 150\text{ mm, measured every } 5\text{ mm}$

The voltage responses are saved as only decay signals after switch off. The measurement starts in the receiver just after the current in the sender is zero. The receiver will have a strong signal when  $x=0$  for any case of  $c$  and  $d$ .

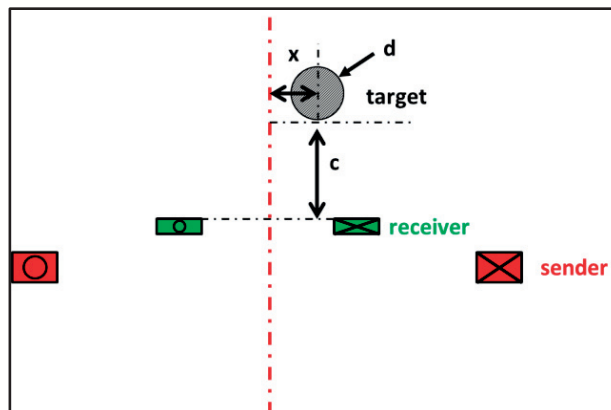


Figure 2:14 A detection system with some target features  $x$  (horizontal position),  $c$  (cover depth), and  $d$  (target diameter).

The strength of the response is proportional to  $d$  and inversely proportional to  $c$ . The response in this case is highly non-linear and has to be measured in an experiment for every combination of values of  $d$ ,  $c$ , and  $x$ . A typical decay response in the receiver is similar to the red line in Figure 2:15, which is simply a voltage decaying with time for one diameter, cover, and transverse location. During an experiment, these variables are known because they are set before the measurement. It is essential to represent this curve in few parameters that have a physical meaning. The points in the curve are nothing but voltage values every  $\mu\text{s}$  time sample. The points A and C are the start and end of the measurement respectively (Figure 2:15). The time interval between them is set to  $200 \mu\text{s}$ .

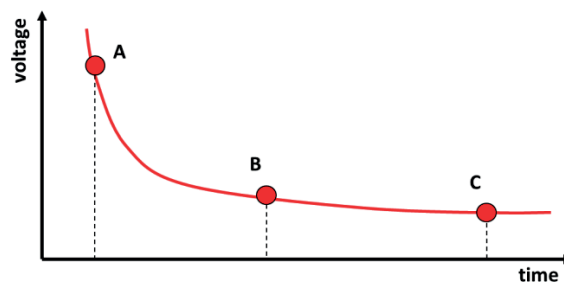


Figure 2:15 A classical parameterization of induced signal decay.

One simple classical way to represent this curve is to subtract  $U_C$  from  $U_A$ , i.e. the voltage at C from the voltage at A. This is one value that can represent this curve and if the first part of the curve is saturated, as described before, the same is done by subtracting  $U_C$  from  $U_B$ . The evaluation  $U_A - U_C$  is quick and simple but it will not capture all the information in the curve. Some state-of-the-art applications use this as a way to discriminate the features. This is not effective in diameter discrimination that is why this simple coil configuration and excitation mode will not be enough. In the context of this section it is important to have the simplest system for explanation. For that reason, the analyzed results are concentrated only on systems with the configuration in Figure 2:15.

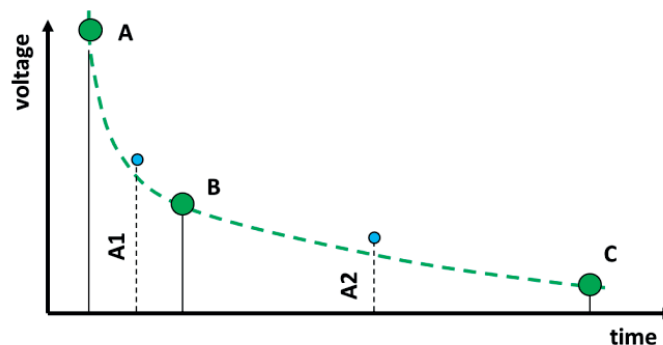


Figure 2:16 A new parameterization proposal of an induced signal decay.

It was observed from the measured signals of all the cases that two different responses of two different cases can have the same starting and ending values but different curvature of the decay between these points. That means the expression  $U_A - U_C$  may not be unique for these different features. As an example, a bigger and deeper steel cylinder can have the similar  $U_A - U_C$  value to a smaller and shallow one. A novel effective way to avoid the disadvantage of the previous evaluation is to represent a voltage decay with parameters of physical meaning. The curvature of the decay can be evaluated also by a new representation as sketched in Figure 2:16. The start and end points in the curve can remain the same. But point B has to be chosen so that the area under the curve from A to B is equal to the area under the curve from B to C. For every measurement, point B is to be calculated and this equality in area is a simple representation of some features of the target. Eddy currents diffusing in steel depend on the geometry. The response strength depends on the depth. If the diameter of the cylinder is small the eddy currents in the target decay slower than if the diameter is big due to limited space. That's why the curve from B to C may be less steep. On the other hand, if two targets of the same diameter have different depths then the one nearer to the sensor will have a higher start between the point A and the end-point B. The idea here is to assume that the generated flux can be represented as the area between A and C. Point B is found at the time when half of this flux is already reached. After finding point B that splits the decay into two parts, a new expression  $A1-A2$  is evaluated.  $A1$  is the average of the first part and  $A2$  is the average of the second part of this decay. This expression is equivalent to a kind of frequency difference. It is giving more information about the time needed to generate half of the flux compared to the time needed to generate the rest.

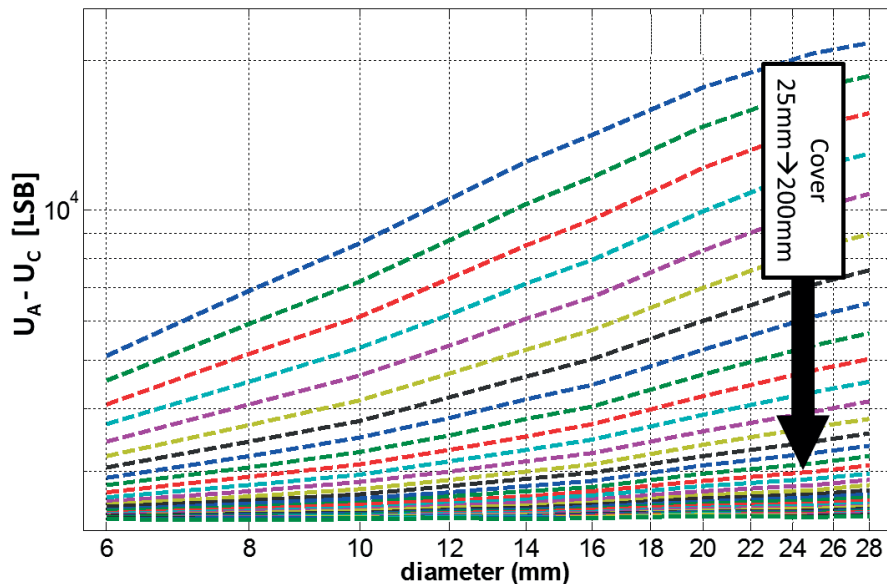


Figure 2:17 State-of-the-art evaluation of the induced signals by experiments for different diameters and covers but at  $x=0$ .

The two evaluation expressions were performed on the experimental measurements for all the cases of  $d$ ,  $c$ , and  $x$  and compared. For a 2D visualization of the difference between

the two methods, only the diameter,  $d$ , and cover,  $c$ , are varied while the horizontal position  $x$  is kept zero. It means that the sensor is centralized under the steel cylinder, which can change diameter and cover. The expression  $U_A - U_C$  is evaluated for the following cases:

- $d = 6, 8, 10, 12, 14, 16, 20, 25,$  and  $28$  mm
- $c = 25$  mm to  $200$  mm, measured every  $5$  mm
- $x = 0$  mm

The result is a 2D table that can be plotted in Figure 2:17, where the x-axis is the diameter and every line represents a cover value. It is expected that the value of this function for smaller cover is bigger than the one for larger covers or deeper targets. The top first blue line is representing the values at 25mm cover. The rest of the lines represent the values of higher covers up to a 200mm covers in steps of 5mm each.

The graph is in logarithmic scale and nevertheless the difference is non-uniform and the values at larger covers are extremely near each other, so differentiating between them would be difficult. On the other hand, evaluating the new function  $A_1 - A_2$  described in Figure 2:16 for the same cylinder diameters and covers yields a linear uniform unique differentiated curves as in Figure 2:18.

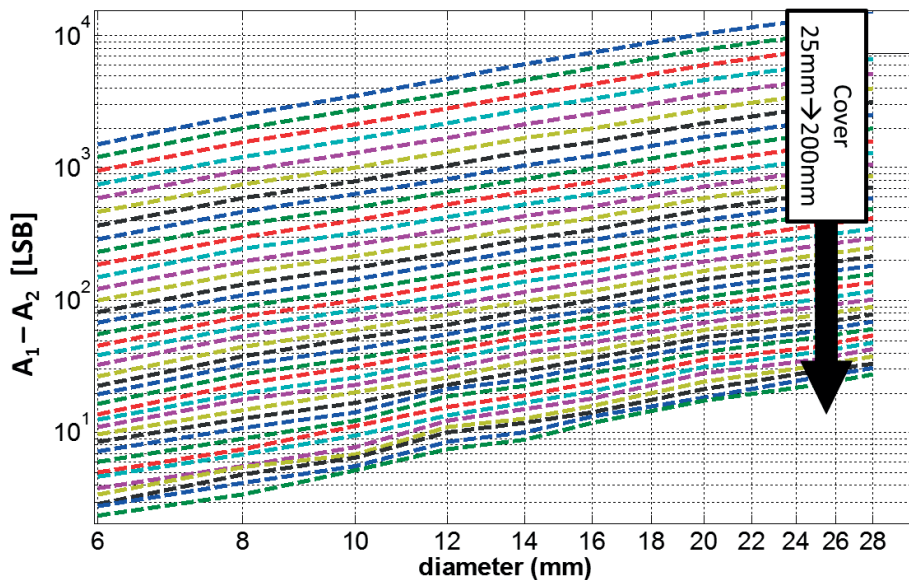


Figure 2:18 Alternative evaluation of the induced signals experiments for different diameters and covers but at  $x=0$ .

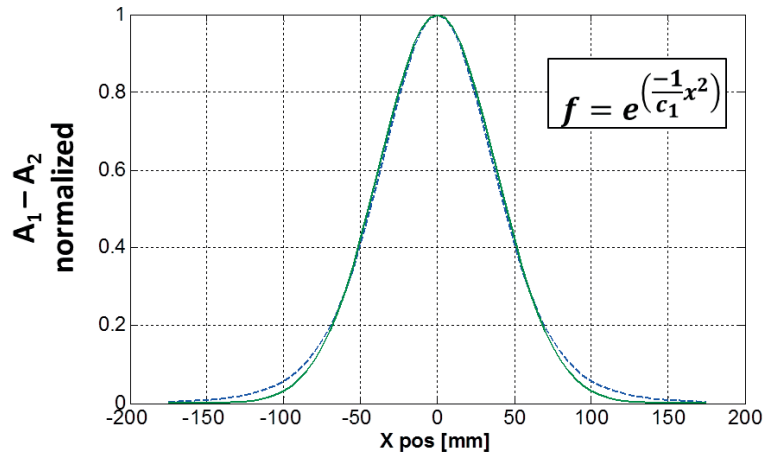


Figure 2:19 Alternative evaluation of the induced signals experiment of one diameter and cover, normalized about  $x=0$ .

The two functions can be compared now because they represent the two different post-processing techniques on the same experimental data. This new function shows the effectivity of the new idea and produces a 2D lookup table as a function of diameter and cover. The values shown in the figure have a unit of LSB (Least Significant Bit) instead of volts because the decays were imported in LSB due to the digital-to-analog converter. A constant factor should be applied to convert it back to volts but it is not necessary for this work due to the consistency in the evaluation. With only one 2D lookup table and two variables, it is not enough to find the solution that inversely predicts the two variables. In the inverse case, it is supposed that the target diameter and cover are not known. The user in real application of the sensor performs a scan in the  $x$ -direction that sends pulses continuously and saves the corresponding decays.

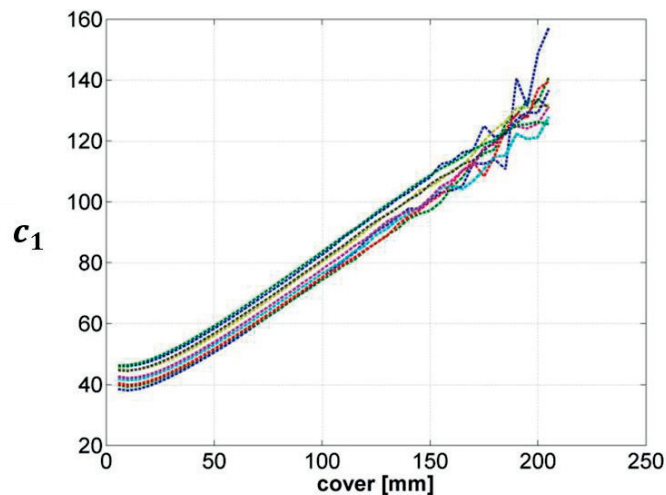


Figure 2:20 Fitting parameter  $c_1$  of the gauss fit as a function of cover; every line is for a specified diameter.

Every decay can be represented by one value of  $A1-A2$  and by looking at the graph in Figure 2:18 a value of 100 LSB, for example, yields more than one unique solution of cover and diameter values. Up to now, advances have been made to come up with a more reliable lookup table that is also effective for deep targets or low signals but still additional post-processing techniques are required. The comparison so far in this example was done when the center of the steel cylinder and the sensor center are coinciding in the  $x$ -direction ( $x=0$ ). If the same evaluation is done for all the values of  $x$  (scan response) and after normalizing them about the value at  $x=0$ , then the normalized  $A1-A2$  for one cover,  $c$ , and one diameter,  $d$  would be a curve with maximum value in the middle as in Figure 2:19. The dotted blue line is the normalized evaluation of the measurement. A gauss fit (solid green line) is fitted to it in order to find the parameter  $c_1$  in the fitting equation:

$$f = e^{\frac{-1}{c_1}x^2} \quad (2.6)$$

The same gauss fit over the  $x$ -position scan should be done for all the covers and diameters to find out that the parameter  $c_1$  is a linear function of the cover plotted in Figure 2:19. Every line in the figure is representing a diameter value of the steel cylinder. This is a useful information besides the new function defined before in order to easily find the unknown diameter and cover in an inverse method. This is helpful because for any value of  $c_1$  of a scan, a small range of possible covers,  $c$ , can be predicted.

So far a horizontal scan in the  $x$  direction is required together with an evaluation of a new function, which when normalized leads to another parameter  $c_1$ . This is important to narrow the discrimination procedure but is still not enough to find the exact cover and diameter. In sub-section 2.4.2, a fit equation to the decay itself will be explained, which will be then used in Chapter 4 to propose a global post-processing method.

#### 2.4.2 Advanced decay parametrization

A novel method in post-processing of the signals is presented here using a four-parameter fitting function on the induced decay signal. This technique is another representation of the system and is essential to be used in the forward and inverse models.

An advanced and more reliable method starts with the fitting equation of all the decays of all the features measured as shown in Figure 2:13. The fitting equation (2.7) uses the measured values,  $y(t)$ , of the voltage decay in time,  $t$  and finds these unknown parameters  $a$ ,  $t_0$ ,  $n$ , and  $a_0$ , that best fit every decay measurement.

$$y(t) = a(t - t_0 + 1)^{-n} + a_0 \quad (2.7)$$

Decaying exponential functions were explored but they did not fit the induced decays of all the ranges of diameters and covers. Equation (2.7) is more realistic to represent the physical meaning of the parameter,  $t_0$ , which should be only diameter dependent and at the same time flexible in defining the decay parameter,  $n$ . A major criterion should be

that this should apply to copper and steel. For comparison reasons, a measured experimental signal for a specific diameter and cover is chosen and fitted by a general exponential function represented in (2.8). The two equations, (2.7) and (2.8) both have four unknown parameters set in a condition that  $y(t_0) = a + a_0$  and  $y(\infty) = a_0$ .

$$y(t) = \frac{a}{e^0} e^{-n(t-t_0)} + a_0 \quad (2.8)$$

The resulting  $t_0$  for all diameters and covers should be only diameter dependent which is not the case for the general exponential case, (2.8). In addition to that, the proposed fit, (2.7), is more accurate than the general exponential one. Figure 2:22 shows the comparison between the two fits.

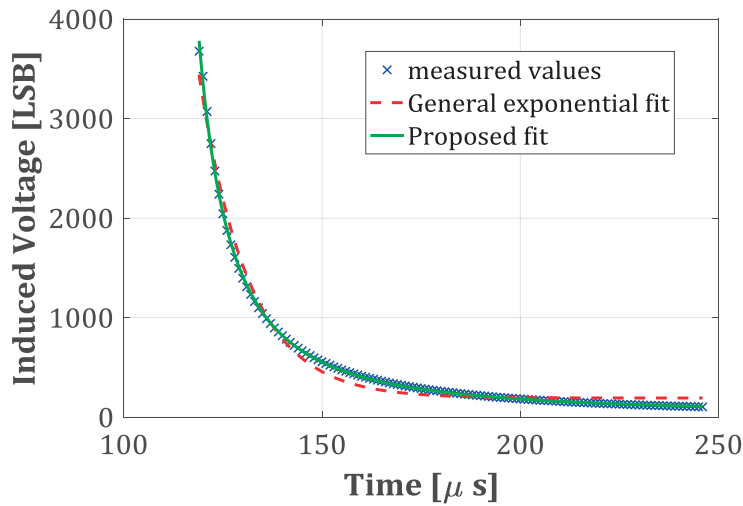


Figure 2:21 a comparison between the general exponential fit and the proposed fit on one experimental case.

Quantifying the goodness of the fits, equations (2.9) to (2.11) should be calculated resulting in one value  $R_{square}$  which is the square of the correlation between the response values and the predicted response values

$$R_{square} = 1 - \frac{SSE}{SST} \quad (2.9)$$

$$SSE = \sum_{i=1:m} (y_i - \check{y}_i)^2 \quad (2.10)$$



$$SST = \sum_{i=1:m}^m (y_i - \bar{y})^2 \tag{2.11}$$

Where:

$y_i$  are the experimental response values in time.

$\check{y}_i$  are the fitted values in time.

$\bar{y}$  is the time average of the experimental response values of all  $m$  points.

$R_{square}$  is a statistic measures how successful the fit is in explaining the variation of the data.

A perfect fit will yield to a value of one. For the General exponential fit,  $R_{square} = 0.9864$  and for the proposed fit,  $R_{square} = 0.9995$ . The proposed fit of (2.7) had a higher  $R_{square}$  for all responses of all covers and diameters which means it is a better-quality fit than the general exponential one (2.8). The four fitting parameters of both fits are shown in Table 2:1.

Table 2:1 the coefficients of the fits of (2.7) and (2.8) with the corresponding goodness of fit.

	$a$	$a_0$	$t_0$	$n$	$R_{square}$
<b>General exponential fit</b>	2.010e+05	192.6	67.96	0.08081	0.9861
<b>Proposed fit</b>	2.056e+05	25.47	107.4	1.58	0.9995

Every measured signal or response of a target diameter, cover, and transverse location should be fitted using (2.7) to calculate the four unknown parameters of that fit. The same measurement data of the previous subsection can be used. One measured signal plotted as blue dotted line in Figure 2:22, has a starting time  $t_s$  and an ending at time  $t_f$ .

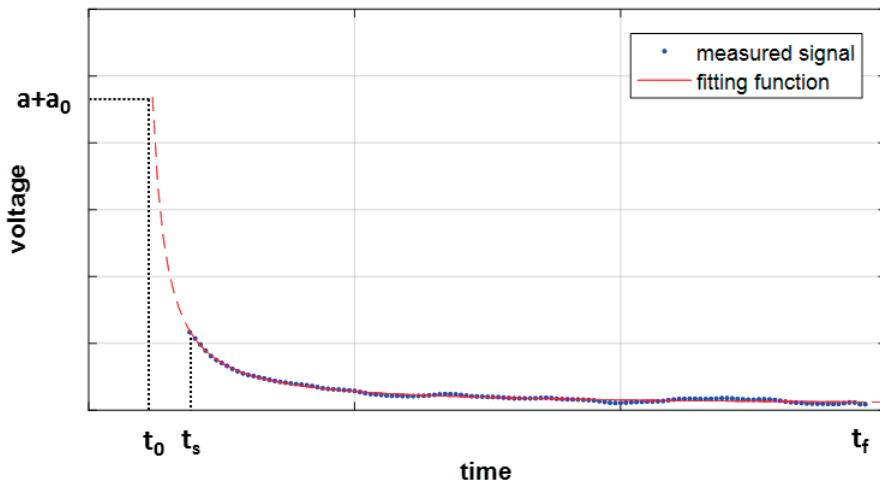


Figure 2:22 A measured voltage decay and its fitting function that can reconstruct the signal especially at the predicted current switch at time.

The fitting function (dashed red line) can be plotted for any time interval after extracting its parameters. One parameter,  $t_0$ , lies always behind the switching-off time of the pulse or the starting time  $t_s$ . The explanation of the parameter  $t_0$  is that there was an amount of flux induced by the target during the rise time of the current and earlier than the switching-off time. If the voltage signal can be extrapolated back in time to represent this virtual induction, then it is assumed that the voltage starts at a high value of  $a + a_0$  and at an early time  $t_0$ . This means the larger the diameter of the target, the earlier the time  $t_0$  should be because induction requires more time to dissipate and therefore it should start earlier. This early time can be represented by a virtual value  $t_0$ .

It was found out after some analyses that  $t_0$  is only dependent on the diameter and not on the cover for steel cylinders using the example of Figure 2:14. The switching-off time for that example was set to  $t_s=80 \mu\text{s}$ , and  $t_0$  was found to vary from about  $t_0=72 \mu\text{s}$  (for the maximum diameter) to about  $t_0=80 \mu\text{s}$  (for the minimum diameter). The parameter  $t_0$  was represented in an equation that is only dependent on the diameter of the cylindrical steel target for that specific sensor design and excitation method. If another sensor design and excitation scheme were used, or another material of the target is to be detected, then a new function of  $t_0$  should be determined. This can be done using a variety of measured or simulated signals and performing a semi-automatic fitting technique. But for the actual sensor the parameter  $t_0$  is defined by the following equation:

$$t_0 = a_1(d - a_2)^2 + a_3 \quad (2.12)$$

The parameter  $t_0$  is a function of the target diameter,  $d$ ; where the other parameters  $a_1$ ,  $a_2$ , and  $a_3$ , are fixed for every sensor design. The unknowns in (2.12) should be determined once and for all for a finalized frozen design of the sensor. The parameter  $a_1$  is always negative which means that the parameter  $t_0$  gets larger with a smaller diameter  $d$  as expected. When the diameter is small enough to a lower limit of  $d = a_2$ , then the value of  $t_0$  will be the highest possible ( $t_0 = a_3$ ), which is close to the device switching-off time, which is in this case  $a_3 = 80 \mu\text{s}$  for such a system.

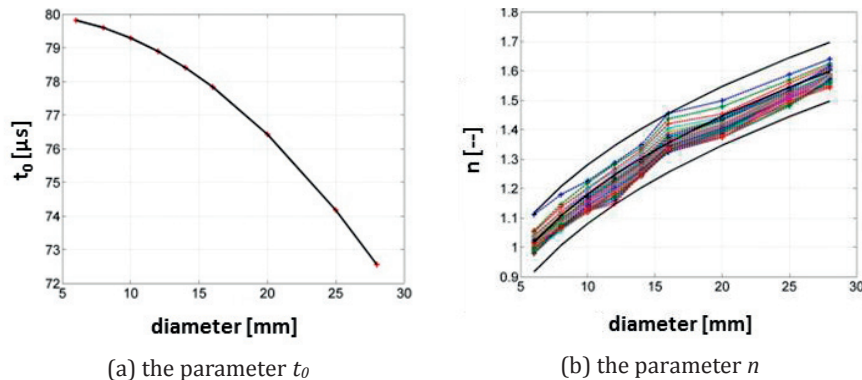


Figure 2:23 The two main parameters of the decay fit varying with the diameter and cover.

Another important parameter in the fitting function of (2.7) is the parameter  $n$ . This parameter is the negative power of the decay and it increases with the increase of the diameter. It depends on the diameter as in (2.13) for this system.

$$n = b_1(d)^{b_2} \pm tol \quad (2.13)$$

In (2.13) the unknown values of  $b_1$  and  $b_2$  are determined for the specified sensor and are kept constant for all diameters, covers, and transverse locations during the fitting of the decay signal. The tolerance value in the equation of  $n$  is the range allowed for  $n$  to vary depending on the cover. Every line in Figure 2:23-b represents the values of  $n$  for a fixed cover. The tolerance in the example of interest was found to be  $\pm 0.1$ . A sensor can be designed in a way to eliminate this tolerance and make  $n$  only diameter dependent.

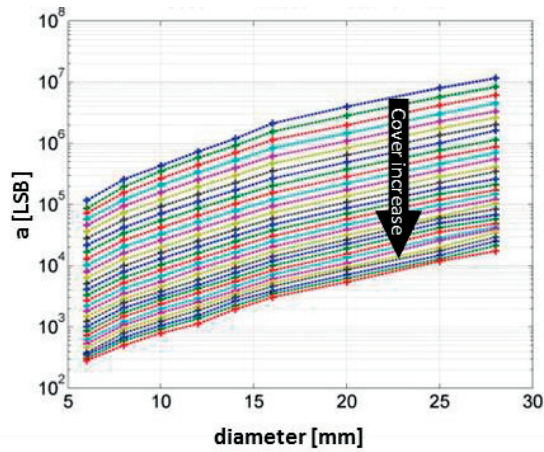


Figure 2:24 The parameter  $a$  as function of the target diameter; every line represents a cover value.

The parameter  $a_0$  in (2.7) is not of importance during the fit because it is very small compared to  $a$  but its existence is important because it filters the error in measurement. If the fitting function is correct, then theoretically, there should not be any induced voltage in the receivers as  $t$  tends to infinity. The decay should vanish to zero when time passes if the source field is inactive. If  $t$  is replaced by infinity in (2.7) then an induction of  $a_0$  volts is left which, theoretically, should be zero but it is not the case due to experimental errors. This equation has the advantage of splitting the amplitude  $a$  from the error  $a_0$ . At  $t = t_0$  the result is  $a + a_0$  and this is the highest induction which happens at the start of the decay even before the switching-off time.

The geometrical sketch of it is shown in Figure 2:22. Finally, the parameter  $a$  is one of the most important parameters that will help in the discrimination of features in section 4.1. This parameter produces another look up table as a function of the two features: diameter and cover. At the first step, only the values of the case where  $x=0$  are taken. Every  $x$ -position will have a different lookup table. This lookup table of the parameter  $a$

can be used besides the previous lookup table (Figure 2:18) in the previous sub-section example. This will be explained in Chapter 4. The parameter  $a$  increases with the diameter and decreases with the cover, which is logical because  $a$  represents the strength of the signal.

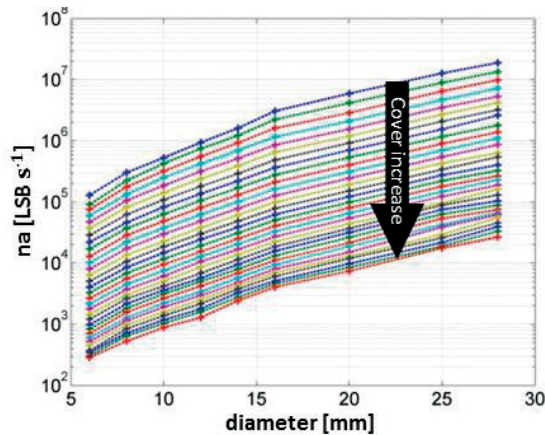


Figure 2:25 The parameter  $na$  as function of the target diameter; it is the time derivative of the voltage at time  $= t_0$ .

Every line in Figure 2:24 is representing a fixed cover starting from the lowest values of cover (top line) to the deepest targets (bottom line) with an increment of 5 mm. The plot in the logarithmic scale shows a uniform distribution, which is also helpful in the discrimination procedure. After the fits are done, different other lookup tables can be deduced from these parameters and still represent a physical meaning. One of the possibilities is done by taking the time derivative of the fitting function (2.7) and evaluate it at  $t=t_0$ . The result is another lookup table, which is the multiplication of  $n$  by  $a$  or simply  $na$ . Figure 2:25 shows this lookup table which has a similar tendency as the table of the parameter  $a$ .

Other forms and lookup tables are done by integrals and other evaluations of the signals are also helpful in the processes of target feature discrimination and will be introduced in a Chapter 4.

## 2.5 Summary

The chapter concentrated on the main parts of EMI sensor design. The explanation of feature discrimination defines the sensor specifications. Accordingly, the excitation and signal processing techniques were defined. Two main excitation methods were applied here, pulse and harmonic induction. Each of these methods has an advantage and will be extended in Chapter 4. New ways to build a system of variables is being introduced by lookup tables of physical parameters for a pulse induction example. The new methods were more effective for deep targets and their evaluation response is better differentiating between different features. These small and simple examples are meant to introduce

the sensor and show the workflow with real examples. The need for sensor optimization and optimum response is required in the feature distinctive detection and decimation covered by Chapter 4. For that reason, modeling the system is essential in capturing variations, which are difficult to do efficiently just by relying on experiments. These computational models will be introduced in Chapter 3.

## Chapter 3 Computational models

The choice of computational models in the context of this work is very important in the sense of understanding, validating and optimizing EMI detection systems. The need for fast computation is always a requirement but also accuracy is demanded especially for complex target detection by electromagnetic induction systems. Electromagnetic induction models are numerous, and a few are mentioned in the state-of-the-art section 1.2. Some of these models are categorized in terms of accuracy and computational time in Figure 3:1. As mentioned before, pure analytical models have advantage in fast computation, but are not accurate enough for real industrial applications especially when modelling complex geometries of coils and targets. The finite element method (see FEM in Figure 3:1) is one of the well-developed numerical methods as mentioned before using vector potential as a degree of freedom and already implemented in commercial software like ANSYS®, COMSOL Multiphysics®, Opera®, Flux®, etc. Using commercial software out of the box is still considered to be expensive and time consuming.

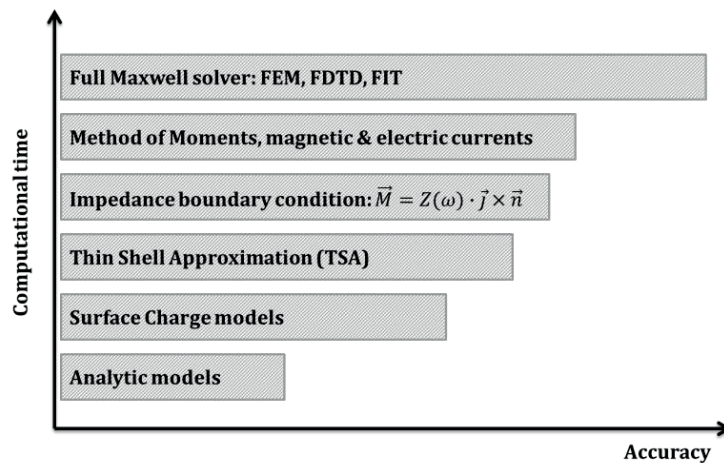


Figure 3:1 Comparison in accuracy and computational time for the current work applications of EMI using different models

In Addition to The FEM method, several key electromagnetic simulation technologies have emerged over recent years include the Method of Moments (MoM), and Finite Difference Time Domain (FDTD) solutions. Although in principal these technologies could be used to solve the same problems as the FEM does and can be in some cases as accurate and even more efficient, there are often good practical reasons why one simulator is better suited to solving a specific problem type. Driven largely by high levels of circuit integration and complexity, the use of electromagnetic (EM) field solvers is becoming increasingly important to many RF/Microwave designers and high speed digital designers. The purpose is to find an approximate solution to Maxwell's equations (Appendix A) that

satisfy a given set of boundary conditions and initial conditions. Addressing this requirement, it is not surprising that a ‘micro scale’ parasitic inductance requires a different solution method than a ‘macro scale’ radar cross-section of a fighter aircraft, for example.

In recent years three key solution technologies have found favor in commercial CAD tools, these are based upon Method of Moments (MoM), Finite Element Method (FEM) and Finite Difference Time Domain (FDTD) techniques. In general, simulation methods use a similar approach to solving a particular problem [69]. The key steps in the simulation process include:

- Creation of the Physical Model: this step involves the creation of the geometry together with the assignment of material properties to objects.
- EM Simulation Setup: defining the extents of the simulation and the boundary conditions, and specific simulation settings.
- Performing the EM Simulation: discretizing the physical model (meshing). The field/current across the mesh approximated using a local function. The boundary conditions should be satisfied in the solution
- Post-processing: calculation of quantities as a function of the solution parameters.

Even though these three key solvers (MoM, FEM and FDTD) are similar in general, there are some important differences which ultimately lead to certain solvers being better suited to certain applications.

The MoM simulation method is often referred to a ‘3D planar’ solver. It is one of the most difficult to implement because it requires the careful evaluation of Green’s functions and coupling integrals. The advantage of the MoM technique is that it is only necessary to discretize (mesh) the metal interconnects in the structure being simulated since the current distribution on the metal surfaces emerge as the core unknowns. This contrasts with other techniques which typically have the electric/magnetic fields everywhere in the solution space. The direct consequence of this is that the ‘planar’ MoM mesh is much simpler and smaller than the equivalent ‘3D volume’ mesh required for FEM/FDTD simulation. An efficient MoM mesh will be conformal (mesh cells are only created on the metal interconnects) and will typically consist of rectangles, triangles and quadrilateral shaped mesh cells. This is relatively computationally efficient. This makes MoM well suited for the analysis of layered structures. MoM is not applicable for general 3-dimensional structures. As already stated MoM relies upon the computation of Greens functions which are only available for free space or for structures that fit in a layered stack up. This in turn means that the structures being simulated must be ‘planar’ in nature and fit within the layered stack up. Fortunately for many RF/Microwave technologies this limitation is not significant because the technology is often planar in nature but not practical for the current application.

The FEM simulation method is a true 3D field solver which has the advantage over MoM in that it can be used to analyze arbitrary shaped 3D structures and is not confined to a layered stack up. FEM simulation requires that the objects being simulated are placed into a 'box' which truncates space and defines the simulation domain. The entire volume of the simulation domain is discretized, usually using tetrahedral mesh cells with a denser mesh being created around the geometric model being simulated.

The FDTD simulation method is also a true 3D field solver which can be used to analyze arbitrary shaped 3D structures. FDTD algorithms solve Maxwell's equations in a fully explicit way, in contrast to MoM and FEM. FDTD analysis requires that the objects being simulated are placed into a 'box' which truncates space and defines the simulation domain. The entire volume of the simulation domain is discretized, usually using hexahedral mesh cells (often referred to as 'Yee' cells [70]). These hexa-cells are often not applicable to arbitrary complex 3D shapes.

One of the significant benefits over the FEM method is that FDTD technique does not require a matrix solve and thus very large problems can often be addressed using surprisingly small amounts of computer memory. FDTD performs well with parallelization taking advantage of the capabilities of modern GPU's (graphics processors).

For 'planar' structures, MoM provides the most efficient simulation method and for that reason generally MoM would be recommended for the analysis of PCB interconnects, on-chip passives and interconnects and planar antenna's. FEM or FDTD are more appropriate for true '3D' structures. Another important consideration is the circuit response type. Both MoM and FEM solve natively in the frequency domain, this makes them more appropriate than FDTD. On the other hand, FDTD solves natively in the time domain which means that it can be very useful for highly time dependent applications. The complexity of the geometry and the problem size favor the FEM method to be the most efficient solution. On the other hand, FDTD provides the most memory efficient simulations for electrically large problems. Applications better suited to FDTD simulation include antenna placement on vehicles/aircraft and the analysis of antenna performance in the presence of detailed human body models.

For the reasons mentioned above, the FEM method is the most suitable than many other methods within the specifications of the applications of the current work. The frequency used here is in the quasi-static regime. Problems should be solved in time and frequency domains. The detection depth is not more than double the maximum dimension of the sender coil. The targets are finite cylindrical rods but the models should be extended to real industrial applications with complex arbitrary shapes. And the coils are not needed to be multi layered. Nevertheless, the FEM method is one of the most expensive in computational time. Many published papers and journals implemented several modified methods to reduce the computational time and still keep the accuracy needed as listed in sub-section 1.2.2. In the context of this work a similar modification have been done and will be shown in the coming section.



The finite element computational model implemented here contributes to this work in many cases especially in the understanding of the system and its coupled parts. Such implementations are mentioned in section 3.1. This FEM model played an important role in the comparison, modification, and implementation of the dipole model, which was mainly developed and improved together with Prof. Christoph Würsch [71]. The Dipole model, which is mainly explained in section 3.2, is also used and validated against the finite element model. The dipole model is not considered a mere analytical model because after deriving the dipole moment equations, space discretization is required as well as the numerical solution of the Bessel functions. Still it is much faster than the FEM model and was used in this work to make parametric variations and optimization performances few of which are described in Chapter 4. Both models will be detailed in this chapter and compared with experiments showing their advantage and their limitations. Section 3.3 contains the experimental verifications of several sensor designs, excitation schemes, and target configurations. The main prerequisite to distinguished detection methods is that these experimental results are compared to both FEM and dipole models that are the most effective virtual tools for this work.

### 3.1 Finite element modified model

The need for 3D computation and system comprehension is a requirement to develop and optimize such devices nowadays. Pure theoretical models are mostly limited to special geometrical cases as mentioned previously. Due to the advances in computer hardware and software, especially parallel computing and cluster computation and distribution, the realization of accurate 3D models with complete space discretization is becoming more practical than ten years ago. Nevertheless, commercial software using finite element solvers are still not able to compete concerning computational time. The classical use of commercial finite element electromagnetic 3D models is not computationally efficient and lacks modeling flexibility or robustness. The proposed approach focuses on:

- Implementing theoretical formulations in 3D finite element model of a detection device, such as the line receiver model.
- An automatic Volumetric Estimation Method (VEM) developed to selectively model the target finite elements.

Due to these two approaches, this model is suitable for parametric studies and optimization of the number, location, shape, and size of PCB receivers in order to get the desired target discrimination information preserving high accuracy with tenfold reduction in computation time compared to commercial finite element software. The basic components of a detection system, as sketched in Figure 1:2, are the *physical method*, *targets* and *sensor*. The magnetically permeable and electrically conductive targets, like steel and copper, should be modelled geometrically and meshed with finite elements. Material properties and boundary conditions are applied. A coil sender, excited with time varying current, creates a magnetic field that in turn creates eddy currents in hidden targets. The eddy currents, in turn, create a magnetic field that induces a voltage signal in the receiver

coil or sensor. This induced voltage, when analyzed, can provide the required information about the target. Higher precision, greater accuracy and more information about hidden targets like their material, shape, and orientation [7] are basic industrial requirements. To be able to meet these requirements, a verified practical system model is needed. Experiments have limitations due to noise at low signals and interferences as well as the difficulty of capturing physical effects, such as mutual inductance and eddy currents. Eddy currents cannot be measured or captured. In contrast to experimental systems, 3D simulation models don't have such limitations, but rather other disadvantages like model flexibility and huge computation times. Theoretical models, on the other hand, exist only for the simplest shapes such as a permeable conductive spheroid or a sphere [40], [54]. Some papers [18], [19], [20] contributed to modeling of such systems by using the advantage of the computational 3D capability and still implementing theoretical models where necessary to preserve the accuracy required and provide the robustness and fast computational time needed. Similarly, the current approach focuses on modeling a detection sensor, in this case, made of PCB sender and receiver coils. The final model is fast, robust and accurate enough to be used in parametric variation studies.

### 3.1.1 Complete 3D simulation model

Eddy currents or Foucault currents, as explained in sub-section 1.2.2 are the physical basis of EMI detection system. In order to understand, simulate, and improve detection systems based on eddy current evaluation, it is important to describe it in differential equation formulation and then solve these formulations.

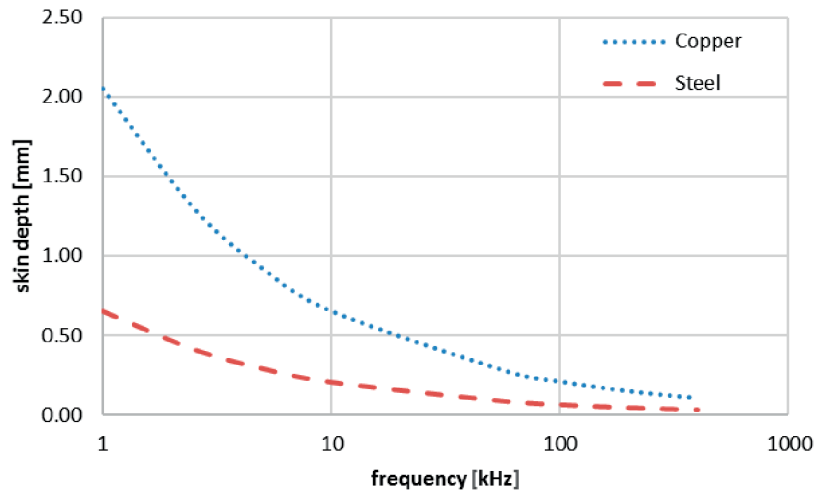


Figure 3:2 Skin depth for copper and steel targets depending of the frequency.

The well-known Maxwell equations in differential form, can be used as the starting point of the derivation (see Appendix A). One of the most accurate methods to solve these sets of differential equations is the finite element method (FEM) or finite element analysis (FEA) as referred to in computational references. The assumptions further for the actual work and applications are that the displacement current  $\frac{\partial \mathbf{D}}{\partial t}$  is zero and that there is no

free charge  $\rho$ . Equating these two terms to zero in Ampere's law and electric Gauss' law (see Appendix A) reduces the complexity of the model. Furthermore, a great care has to be done in the space discretization or meshing (with finite elements) of the geometry where eddy-currents are present. Eddy currents are mainly present in the target that should be detected. At least three elements should be present in the complete thickness of the skin depth in order to model precisely the current density distribution along this thickness. The surface elements have the highest concentration of current and the third elements in the depth direction have the least one. So a gradient is present and three elements are the minimum number of elements required for that in the depth direction as a rule of thumb. The skin depth is formulated in (3.4). The skin depth is dependent on the target permeability  $\mu$ , target electric conductivity  $\sigma$ , and the frequency  $f$  of the excitation coil. To get an idea how the material and frequency affect the skin depth, Figure 3:2 shows how it is changing for copper and steel for example. The detection sensor's highest active frequency, for pulse induction excitation for example, is in the last end of the range plotted in Figure 3:2 (greater than 100 kHz). In that range, the eddy currents all flow at a skin depth of a tenth of a millimeter on the copper target while for a steel target it is about some tens of a micro-meter. Therefore, it is mandatory to adapt the mesh size to the lowest calculated skin depth in the system, i.e. the highest permeability, conductivity, and frequency. For transient simulations, the frequency is not constant and for that one has to choose the maximum inverse of the time step. As for the permeability, which can be nonlinear with the magnetic flux intensity following the constitutive law of Maxwell's equations (see Appendix A), the maximum active permeability has to be chosen. For the simulations in the current work, the edge-based magnetic vector potential is used by the solver of ANSYS (a commercial finite element software) to solve the electromagnetic problem. The theoretical description is in chapter 5 of the ANSYS theoretical manual especially section '5.1.5 Edge-Based Magnetic Vector Potential' explaining this formulation as well as the use of SOLID236 element formulation [72]. *"SOLID236 is a 3D 20-node element capable of modeling electromagnetic fields. The element has magnetic and electric degrees of freedom. Magnetic degrees of freedom are based on the edge-flux formulation. The edge-flux (AZ) degrees of freedoms are the line integrals of the magnetic vector potential along the element edges. They are defined at the mid-side nodes only, and there are no magnetic degrees of freedom associated with the corner nodes. The edge-flux formulation uses tree gauging to produce a unique solution. In an electromagnetic analysis, the electric degree of freedom is the electric potential (VOLT) defined at each node"* [72].

A Complete 3D simulation model using the commercial finite element software, ANSYS, has been built up. A first step verification has been performed to check if the sender and receivers are modeled correctly. Figure 3:3 shows the experiment versus simulation results without any targets involved. The sender is excited by a harmonic current signal. Harmonic voltage signals in time are measured in all coils and the amplitudes are extracted. The two receivers were connected in anti-series and are identical in all means. The total induced voltage in the receivers is therefore the difference of both receiver voltages. Theoretically, and if the receiver coils are identical, a total induced voltage  $U_r = U_{r1} - U_{r2} = 0$  is equivalent to a gain of  $-\infty$  dB if the target is absent. This is the case

at any operating frequency. But when a target is present, the gain in dB units is calculated by (3.1) :

$$Gain = 20 \log_{10} \left( \frac{U_{r1} - U_{r2}}{U_s} \right) \quad (3.1)$$

where  $U_s$  is the source sender voltage.  $U_{r1}$  and  $U_{r2}$  are the receiver voltages respectively.

In order to create non-symmetry in the system, for verification reasons, some turns of *only one* of the two receiver coils are then deactivated. The last turns of the coil are cut mechanically to reduce the impedance of one coil. Figure 3:3 plots the results of both experiment and simulation for three wire eliminations one at a time. The simulation gives reasonable results, still in the absence of the target. Well planned simulation model verifications with experiments are described in section 3.3.

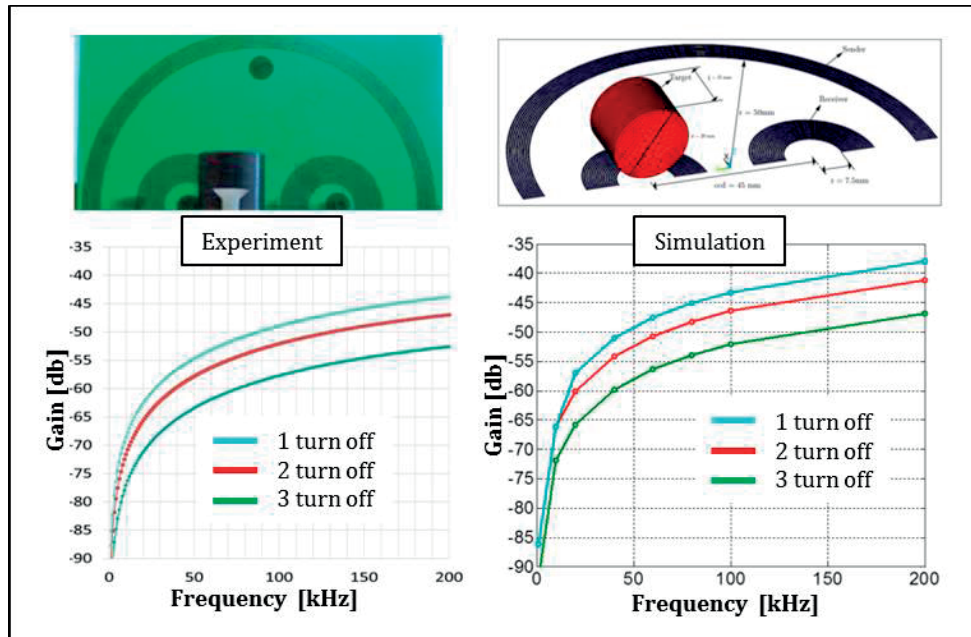


Figure 3:3 Experiment (left) and simulation (right) of the amplitude ratio of the receiver and sender.

This complete and verified, 3D simulation model is used as a reference in order to compare it to modified models described in the next sections. The only disadvantage of this model is the computational time. Two main modifications have been implemented in this work to make a strict cut in computation time. These new modifications are possible to implement on a commercial software as a tool for FEM simulation and are detailed in sub-sections 3.1.2, and 3.1.3, and 3.1.4 to reach a modified efficient 3D FEM model using methods stated in [25]. The two main contributions in this direction are the 'line receiver model' and the 'volumetric estimation method'.

### 3.1.2 Line receiver model

Theoretical implementation on the receivers by integrating the flux vector potential of the element edges across a specified contour using (3.2) is first performed inside the scripting language of the 3D FEM solver. This contour, as in Figure 3:4, needs to be pre-defined before meshing the air in the software tool so that the postprocessor can find the nodes path and perform the integration.

$$\Phi = \oint \vec{A} dl \quad (3.2)$$

$$u = -\frac{d\Phi}{dt} \quad (3.3)$$

The flux derivative in time is nothing more than the induced voltage (3.3) and when multiplied by the number of turns, the result is the total induced voltage in the coil. The accuracy of this modified model is around 1% after signal amplification while the computational time has been nearly halved (see *case 1* in Figure 3:6). This case used the line receiver model and can be directly compared to the complete FEM model (*case 0*). The accuracy error is valid for the whole range of frequencies (the errors for 100 kHz and 200 kHz are shown in Table 3:1). The investigated coils that led to this error have an inside diameter not less than one third of the outer diameter.

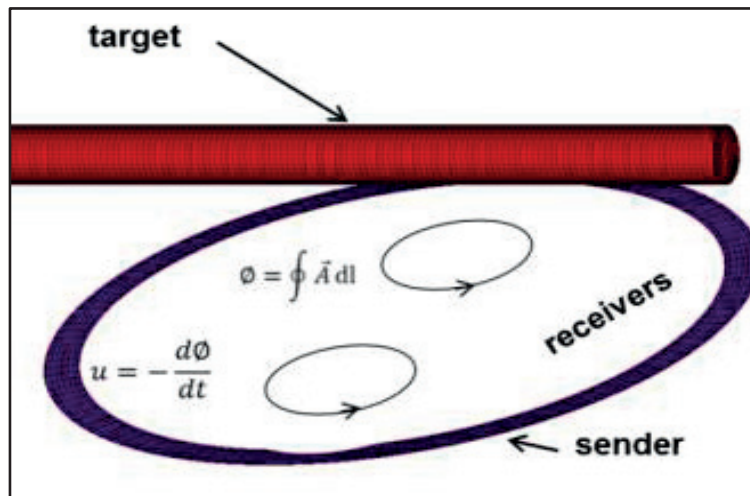


Figure 3:4 Line receiver model.

Modeling the receivers is no longer required and the advantage here is not only the reduction of computational time but the flexibility of the model to provide, with one computation, all the induced voltages of all possible combinations of receiver(s) at all position(s), shape(s), and orientation(s). All possible line receivers can be sketched prior to the solution to provide a variety of results after only one solution command.

### 3.1.3 Volumetric Estimation Method

This method modifies the target volume and not the coils. Several checks are performed to see the accuracy versus computational time of several skin modification cases as in Figure 3:5. If the magnetic flux is uniform and axial to a cylindrical target, for example, then it is assumed that eddy currents induced in the target are only circulating around the surface of this cylinder up to a depth of  $\delta$ , which is evaluated by (3.4), [28]. The target has an electrical conductivity  $\sigma$  and a magnetic permeability  $\mu$ . The sender is excited with a harmonic current with a frequency  $f$ . The target is placed 22.5 mm in lateral direction, which should be above the center of one of the receiver coils giving highest response in the lateral direction. The target diameter was 20 mm and placed at a depth of 50 mm.

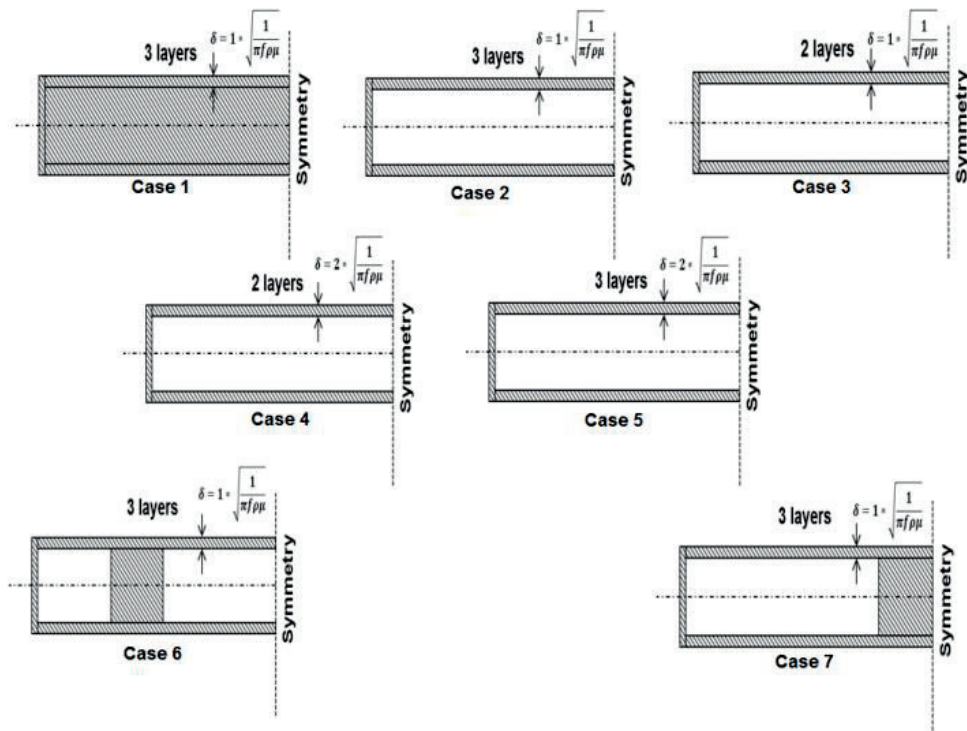


Figure 3:5 Seven different skin designs to be compared to the complete model.

Some published models [20] perform a target skin estimation, such as the *Thin Skin Approximation* (TSA), which has a relatively good balance between accuracy and computation time (see Figure 3:1). In the current work, and in order to check the skin influence, seven cases (Figure 3:5) were checked and compared to a full complete model (complete model means complete coils and a complete target as *case 0*). That means all other cases from *case 1* to *case 7* use the *Line Receiver Model* described in the previous section for the calculation of the induced voltage of the receivers. *Case 1* has the same target model as *Case 0* and the comparison between them shows the effect of the line receiver model

only. *Case 2* models only the skin, with three layers of total height  $\delta$ , which is computed from (3.4).

$$\delta = \sqrt{\frac{1}{\pi f \sigma \mu}} \quad (3.4)$$

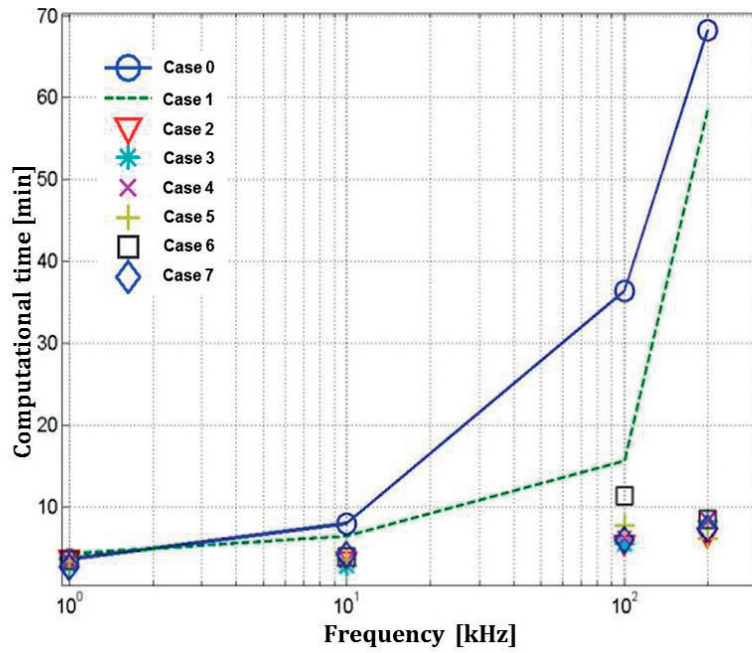
*Case 3* models the skin depth with only two layers. *Case 4* and *Case 5*, model twice the skin depth with two and three layers respectively.

*Case 6* and *Case 7* are the same as *case 2* but a small part of the core (10 mm axially) is kept because the eddy current distribution is not uniform in the target and the flux is not always axial to the target. For that reason, the most accurate approximation (referring to Table 3:1) relative to the complete model (*case 0*) is *case 7*, which is also one of the most efficient concerning computational time as shown in Figure 3:6. So far, a computational harmonic model about ten times faster and with up to 1.5 % accuracy relative to the complete model has been realized. As a conclusion, modeling only the skin, as in TSA [20] for example is sometimes not very accurate because of the finite target shape and its relative position to the sensor, which allows a change in the flux flow direction. Not only that eddy currents may flow locally in the core part of the cylinder but also the inductance of the system may not be preserved by the skin part alone.

Table 3:1 Response of the seven cases compared to the complete model (*case 0*).

Case	Amplitude [dB]		Relative accuracy to <i>case 0</i> [%]	
	100 kHz	200 kHz	100 kHz	200 kHz
<b>0</b>	61.63	55.25	0.00	0.00
<b>1</b>	62.30	55.88	1.09	1.14
<b>2</b>	62.91	56.49	2.08	2.24
<b>3</b>	58.45	52.7	-5.16	-4.62
<b>4</b>	58.04	52.18	-5.83	-5.56
<b>5</b>	59.03	53.16	-4.22	-3.78
<b>6</b>	62.93	56.49	2.11	2.24
<b>7</b>	62.52	56.06	1.44	1.47

The transient systems experience low and high effective frequencies during the excitation, which force the eddy currents to flow in a variable skin depth and in a non-uniform manner inside the target. For that reason, a volumetric approximation method is needed to automatically predict the current density distribution in the target from the time derivative of the vector potential, thus preparing the exact mesh requirement before finalizing the simulation procedure of all system parameters. According to Figure 3:6 the most efficient cases in reduction of computational time were the ones with less target elements. The target elements have additional electric degrees of freedom (Volt DOF) and any reduction in these elements would contribute highly to having fast computations. When models are computed in transient 3D solvers, the computational time may be unbearable.


 Figure 3:6 Computational time of all cases relative to *Case 0*.

One part of the current work is an instantaneous prediction of high current densities in the target at time step  $\{n+1\}$  from known values of vector potential derivatives at time step  $\{n\}$ . Deriving the second Maxwell's equation (see Appendix A) as in [73], (3.5) states that a change in the magnetic field leads to an electric field in a conductive target.

$$\nabla \times \vec{E} = -\frac{\partial \vec{B}}{\partial t} \quad (3.5)$$

$\vec{E}$  = electric field intensity vector

$\vec{B}$  = magnetic flux density vector

And rewriting it in terms of magnetic vector potential  $\vec{A}$  leads to (3.6)

$$\vec{J}_e = -\frac{1}{\rho} \frac{\partial \vec{A}}{\partial t} \quad (3.6)$$

$\vec{J}_e$  = induced eddy current density vector

$\vec{A}$  = magnetic vector potential

$\rho$  = electric resistivity

The induced eddy current density can be estimated from the time derivative of the vector potential, which in turn is a degree of freedom in the transient finite element solver. Mak-



ing use of (3.6) one already has information where the possible locations of eddy currents are in a conductive target in the next time step. In order to realize this, a simple pulse induction of a metallic sphere is setup.

### 3.1.4 Pulse induction of a metallic sphere

A simple experimental and simulation setup of a pulse excited coil with a metallic sphere is being verified and checked as in Figure 3:7. Three different sphere materials are simulated with linear relative permeability because the signal is small and the magnetic field does not lead to magnetic saturation. Table 3:2 shows the three different materials as well as the estimated skin depth when applying (3.4) for the range of frequencies used in the transient simulation. Between 1 kHz and 100 kHz, it is classically known that the eddy currents flow at a steel skin, which is three times less than the copper skin. This cannot be quantified in an experiment but current-voltage verification was first done between experiment and simulation before proceeding.

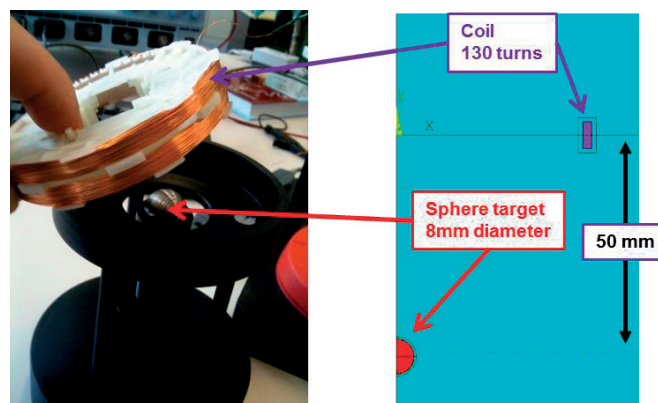


Figure 3:7 Pulse induction of a sphere, 2D axisymmetric FEM simulation with experimental verification.

Table 3:2 Skin depth for different target materials and excitation frequencies.

Name	Target resistivity [ $\Omega \cdot m$ ]	Relative permeability [--]	Skin depth [mm]	
			1 kHz	100 kHz
<b>copper</b>	1.66e-8	1	2	0.20
<b>steel 1</b>	16.6e-8	100	0.65	0.065
<b>steel 2</b>	16.6e-8	400	0.32	0.032

The coil is excited with a constant voltage to reach a steady state and then switched off to let the current in the coil diminish to zero very fast in time. The same coil is used here as a sender and receiver. The sphere radius is 4mm and a simple check of the two quantities of (3.6) for the three different materials confirms that *steel1* and *steel2* do not need

the complete radial space. As for the case of *copper*, Figure 3:8 shows that 2  $\mu$ s after the pulse is activated, the current density  $J$  can be neglected between the center (0 mm) and 3mm distance from the center. After 25  $\mu$ s the complete sphere is active and thus the core radial limit is 0 mm as shown.

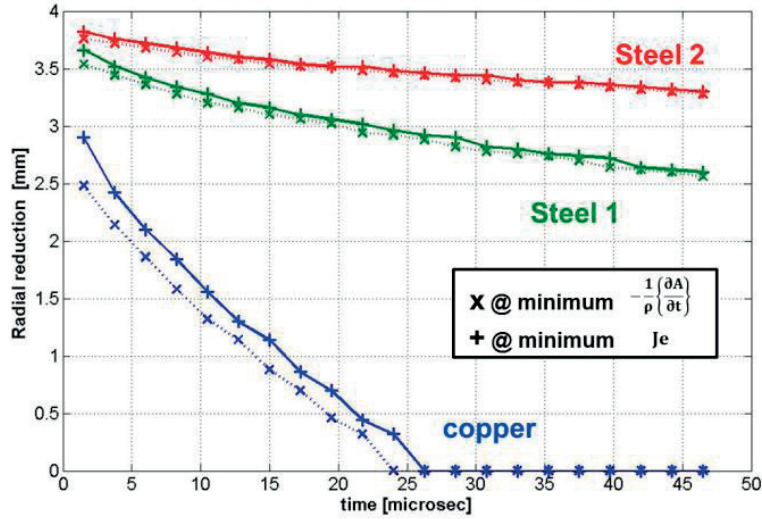


Figure 3:8 Space reduction check using the two components of (3.6).

While for steel the inner core of the sphere (0 mm to ~2.5mm) is still not active even after 45  $\mu$ s *steel2* is four times more permeable than *steel1*; that's why the active skin depth is nearly always about two times thinner than the skin depth of *steel1*. This means that at 25  $\mu$ s, for example, the *steel1* inactive core is 3 mm (skin depth =1 mm) while *steel2* is 3.5 mm (skin depth = 0.5 mm), which matches the skin depth equation (3.6).

The main observation of Figure 3:8 is that for each of the three materials the radial limit of  $-\frac{1}{\rho} \frac{\partial \vec{A}}{\partial t}$  is always lower than the limit of  $\vec{J}_e$  at any given time. In other words, the radial limit of the inactive sphere core predicted by  $-\frac{1}{\rho} \frac{\partial \vec{A}}{\partial t}$  at time  $t$  is the same as  $\vec{J}_e$  at time  $t+\Delta t$ . This was possible by making use of the time discretization knowing the spatial current densities in the future time step. These criteria allow predicting the future space limit of the current density derived from the actual vector potentials present in the database history of an FEM simulation solver. Quantifying what is described above, Figure 3:9 and Figure 3:10 both show the difference between copper and steel by plotting the term  $-\frac{1}{\rho} \frac{\partial \vec{A}}{\partial t}$  across the sphere radius. Directly after the pulse (at the first few microseconds) there is a jump in the current density at the skin. But afterwards the field diffuses to the inner core of the sphere.

In the case of steel, this diffusion is limited and even after 50  $\mu$ s (black curve in Figure 3:10) the limit of 3 mm (skin depth =1 mm) is reached in contrast to copper where the whole sphere is occupied. That's why, when applying a space reduction procedure, the

unnecessary finite elements that can be eliminated at around 41  $\mu\text{s}$  (see Table 3:3) are more than the ones for copper.

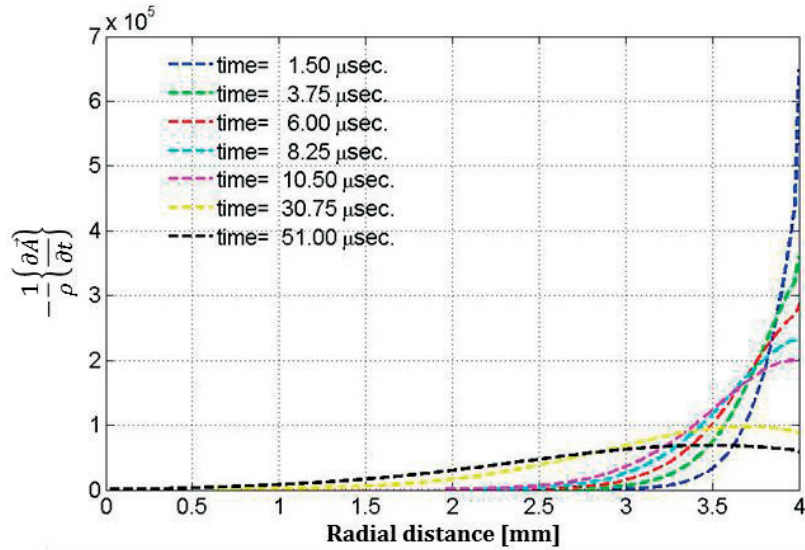


Figure 3:9 Instantaneous plots of vector potential derivative across the radius of the copper sphere.

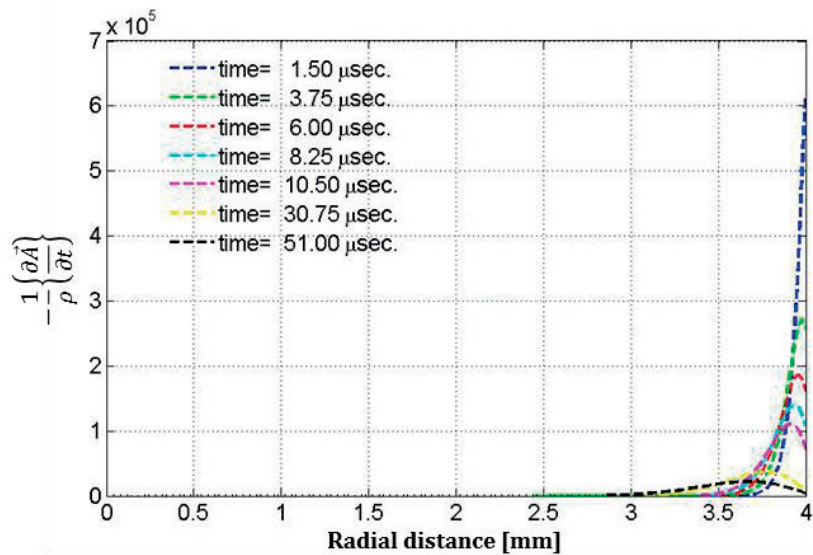


Figure 3:10 Instantaneous plots of vector potential derivative across the radius of the steel sphere.













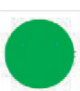

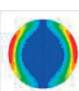
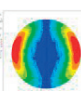
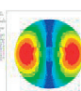
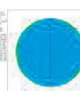


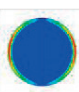
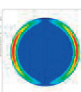
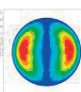
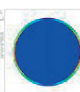
Referring to the current density plots between copper and steel in Table 3:3 one notices clearly the instantaneous distribution and its transient reduction of elements. This kind

of automatic moving skin depth has one drawback, which is when the core limit is over-estimated, or the skin is underestimated, the border current density may not be low and needs to be corrected before the next time step is solved. For that reason, a slight modification is implemented by using (3.6) again and taking the derivative of both sides. And since the sphere is assumed to be fixed in space the only variable is time then this leads to (3.7).

$$\frac{d\vec{J}_e}{dt} = -\frac{1}{\rho} \frac{d^2\vec{A}}{dt^2} \quad (3.7)$$

Equation (3.7) is helpful by doing a numerical integration to estimate  $-\frac{1}{\rho} \frac{\partial \vec{A}}{\partial t}$  at a certain location in space and at time  $t+\Delta t$  from values at time  $t$  or simply suggest the speed of the diffusion of current density inside the core of the sphere and thus the next corrected border limit. As a summary of the results one can state that modeling a permanently fixed skin depth is not always accurate during a transient simulation.

Table 3:3 FEM mesh and current density.

	0 μs	7 μs	21 μs	41 μs	200 μs	400 μs
<i>copper</i> mesh						
<i>steel 1</i> mesh						
<i>copper</i> $J_z$						
<i>steel 1</i> $J_z$						

On the contrary, the proposed *moving skin depth* procedure allows a future prediction of the possible current density location. The disadvantage of finite element elimination from the target core is a sudden change in the effective inductivity of the system in the case of ferromagnetic material which is magnetically permeable. Even if no electric current flows in the ferromagnetic parts, they lead to an induction only by being present in the magnetic field. On the contrary, induction in pure electric materials, like copper, relies on a current flow in them.

For purely conductive materials, like copper, that have low relative permeability this may not be a problem. In the case of steel this can affect the accuracy of the results. If the aim of the simulation is to estimate the instantaneous joule heat generated in the target,

then just eliminating the elements during the computational transient run is not enough. It would be more suitable in this case to replace these elements by a material, which has the same permeability but no resistivity.

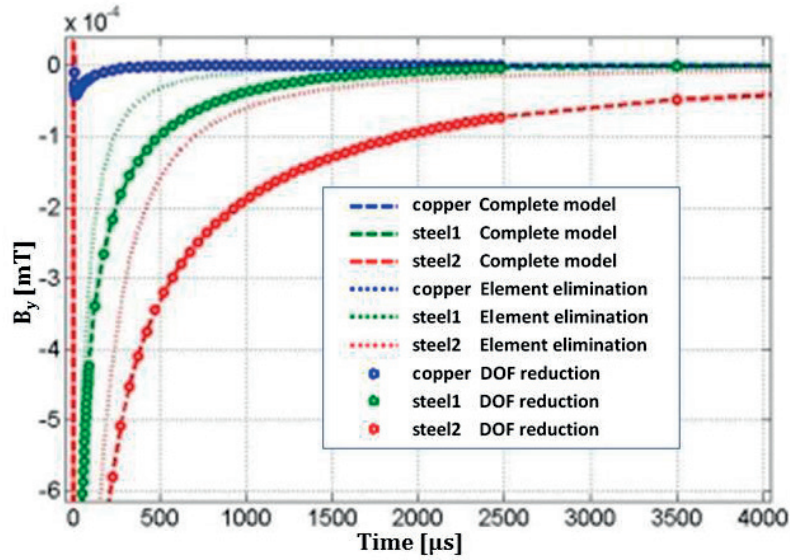


Figure 3:11 Flux Density at the surface of the sphere with different material using different methods.

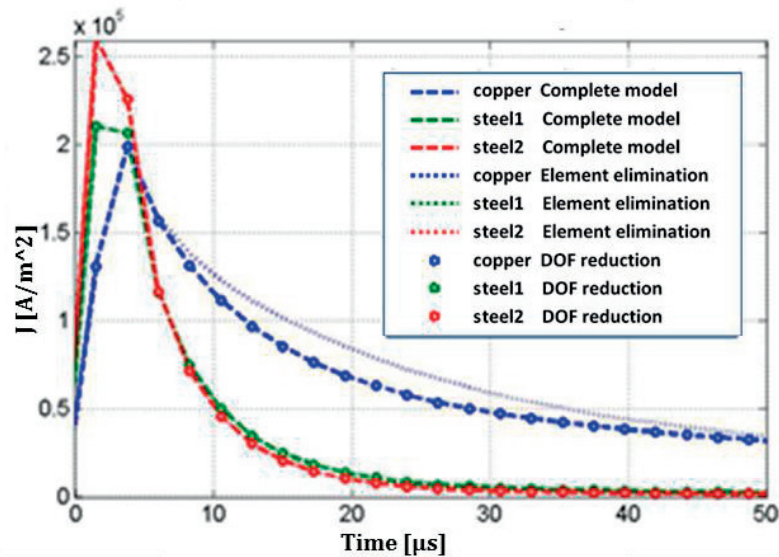


Figure 3:12 Current density at the surface of the sphere with different material using different methods.

Calculation time becomes slightly higher than ‘mesh elimination’ but it is less than having both degrees of freedom, electric and magnetic, in these elements. Figure 3:11 plots the flux density at the sphere surface for the three different materials. The element reduction method is not acceptable while the DOF method is matching exactly with the complete model. If the aim of the simulation is just to estimate the current density, then Figure 3:12 shows that even the element reduction method is not that far from the complete model. 2D planar simulations (infinitely long coils and cylinder target) were also checked and the same conclusions were drawn.

The effect of these two methods may not be that high on the reduction of computational time in 2D cases because the post processing of every time step is required to apply material change or element reduction and this may take the same time as the time saved in computation, but in 3D this is proven to be a bigger advantage.

## 3.2 Dipole model

*ScanSim* is a dipole model implemented in MATLAB discretizing the relevant bodies in 3D space and solving basically harmonic responses of eddy currents generated in permeable and electric conductive objects. *ScanSim* is the user interface developed in the phase of a CTI (Commission for Technology and Innovation) project under the number *CTI-Nr. 14469.1 PFIW-IW* in Switzerland. The collaboration done together with the team members of the mentioned project has resulted in a report where the dipolar model is documented [71]. The final aim of this project was to build an industrial EMI sensor that detects reinforcing steel bars hidden in concrete and also estimate the location, and size of these targets. In principle, the scattering of objects can be modeled by means of the quasi-stationary solution of the Maxwell equations in 3D using finite element tools like Maxwell, COMSOL, and ANSYS, or FIT or Boundary Element Solver. The *ScanSim* is meant to be a scanner simulator, which means that it should simulate a real scan over a 60 cm by 60 cm area and for that reason it is not practical to use any commercial finite element solvers in space and time especially for pulse induction schemes. *ScanSim* can calculate the required scan area in few minutes and not hours. This makes it possible, in principle, for *ScanSim* as a forward model to be combined with an optimization method. *ScanSim* is not based on a complete solution of the quasi-stationary Maxwell's equations in 3D, but on the dipole approximation of stray fields for the quasi-stationary case. Part of the development and use of the dipole model developed here was also published in some articles [21], [22], [27], and [74] as a part of the current work.

### 3.2.1 Introduction to the theory

The theory behind *ScanSim* was developed by Burrows [75] to model eddy currents and is based on analytical solutions for the magnetic susceptibility of objects in the underground. The first geophysical problems were developed (search of mineral deposits and mapping of the subsurface) through Wait [76], Grant and West [77]. After geophysics and material testing by eddy current method the theory was forward implemented in the development of inductive sensors for detecting objects in the subsoil, in particular for

the detection of unexploded ordnance (UXO) and for mine detection [58], [13], [78]. For some permeable, conductive objects such as cylinder, sphere, ellipsoid, or cylindrical shell, conductor loop analytical dipole are approximated and the calculation of dipole stray fields present is assumed. The dipole approximation limits the applicability of *ScanSim* to geometries that are either very far or very close to the scanner. *ScanSim* does not calculate the exact field distributions of the excitation, but rather the stray fields of the objects themselves. A metallic plate, for example, cannot simply be approximated as a simple superposition of dipole fields. In such cases of complex targets, it would be necessary, to integrate distributed models, i.e., to discretize the plate, either by volume (FEM) or by surface (BEM) and to solve the eddy current response of the coupled system. For elongated objects, on the other hand, such as reinforcing bars, the induced magnetization is calculated as a superposition of individual elementary dipoles, and assumed at large distances, to be a one-dimensional object.

### 3.2.2 Dipole model implementation

The induced voltage  $U_{ind}$  in a coil that covers a flat area  $\partial S$  placed transverse to an external field can be calculated either via the vector potential  $\vec{A}(\vec{r})$  or directly via the magnetic flux density  $\vec{B}(\vec{r})$ , which is derived from the flow of the magnetic flux,  $\varphi$ , through the coil. For a harmonic excitation of angular frequency  $\omega$  the induced voltage (imaginary part) is derived as follows:

$$U_{ind} = -i \frac{d\varphi}{dt} = -i\omega \iint_S \vec{B}(\vec{r}) \cdot d\vec{S} = -i\omega \oint_{\partial S} \vec{A}(\vec{s}) \cdot d\vec{s} \quad (3.8)$$

Formulating the induced voltage as a function of vector potential is an advantage where the coil surface  $S$  is defined by line segments  $d\vec{s}$ . The magnetic flux density can be calculated from the Biot-Savart law written in (3.9) or derived from the vector potential as in (3.10) and (3.11).

$$\vec{B}(\vec{r}) = \frac{\mu_0}{4\pi} \oint_{\partial S} \vec{j}(\vec{r}') \times \frac{\vec{r} - \vec{r}'}{|\vec{r} - \vec{r}'|^3} d\vec{r}' \quad (3.9)$$

$$\vec{A}(\vec{r}) = \frac{\mu_0}{4\pi} \oint_{\partial S} \frac{\vec{j}(\vec{r}')}{|\vec{r} - \vec{r}'|} d\vec{r}' \quad (3.10)$$

$$\vec{B}(\vec{r}) = \nabla \times \vec{A}(\vec{r}) \quad (3.11)$$

Following the procedure in [71], the resulting dipole magnetic flux density is written as follows:

$$\vec{B}(\vec{r}) = \frac{\mu_0 \vec{m}}{4\pi r^3} \cdot (3(\vec{a}_r \cdot \vec{a}_r) - \mathbf{1}) \quad (3.12)$$

Where:  $\vec{a}_r = \frac{\vec{r}}{|\vec{r}|}$  and the dipole moment is written as a function of the polarizability tensor  $\mathbf{M}$  and the transmitter coil field as follows:

$$\vec{m} = \mathbf{M} \cdot \vec{H}_{TX} = \mathbf{M} \cdot \frac{\vec{B}_{TX}}{\mu_0} \quad (3.13)$$

When replacing the dipole moment of (3.13) in (3.14) the final result of the scattering field in the receiver coil as a result of the transmitter field and the polarizability tensor is as follows:

$$\vec{B}_S = \frac{\mu_0}{4\pi r^3} \cdot (3(\vec{a}_r \cdot \vec{a}_r) - \mathbf{1}) \cdot \mathbf{M} \cdot \vec{H}_{TX} \quad (3.14)$$

By using the reciprocity theorem and (3.13) and (3.14) to formulate the induced voltage in the receiver coil starting from (3.8) the final result for a harmonic excitation is rewritten as:

$$U_{ind} = \frac{i\omega\mu}{I_{TX}} \vec{H}_{RX} \cdot \mathbf{M} \cdot \vec{H}_{TX} \quad (3.15)$$

Where the nominations  $RX$  and  $TX$  in (3.15) correspond to receiver coil and transmitter coil respectively.

### 3.2.3 Cylinder target formulation

The most important detected target shape in the simulation here is the cylinder. A reinforcing rod, for example, is approximated as a linear array of dipoles. The discretization of the reinforcing rod is chosen depending on the sensor dimensions and for most of the cases in this work it is 15 mm. The magnetic susceptibility  $\chi$  relates the magnetic moment  $\mathbf{M}$  to the magnetic field intensity  $\mathbf{H}$  as in (3.16). For an infinitely long, conductive, and permeable cylinder, the axial magnetic susceptibility,  $\chi_{\parallel}$ , and transverse magnetic susceptibility,  $\chi_{\perp}$ , are calculated from Braunisch et al [13], Shubitidze [78], Verma [79], Kertz [80], and Wait [76].  $\chi_{\parallel}$  is parallel to an external homogeneous magnetic field while  $\chi_{\perp}$  is perpendicular to it. Both calculated quantities are per unit length.

$$\mathbf{M} = \chi \mathbf{H} \quad (3.16)$$

The axial and transverse polarizabilities of a cylinder target are represented in (3.17) and (3.18).

$$\chi_{\parallel}(ka) = 2\pi a^2 \left\{ \frac{J_2(ka)}{J_0(ka)} + (\mu_r - 1) \frac{J_1(ka)}{ka J_0(ka)} \right\} \quad (3.17)$$

$$\chi_{\perp}(ka) = a^2 \left\{ \frac{ka J_0(ka) - (\mu_r + 1) J_1(ka)}{ka J_0(ka) + (\mu_r - 1) J_1(ka)} \right\} \quad (3.18)$$

Here,  $\mu_r$  is the relative magnetic permeability of the cylinder.  $J_0$ ,  $J_1$ , and  $J_2$  are Bessel functions of the first kind (Appendix G) of the argument  $ka$ , which is the product of the



radius  $a$  of the cylinder and the induction number  $k = \sqrt{-i\sigma\mu\omega}$ . The polarizabilities  $\chi$  are complex functions of one single parameter  $\gamma = ka$  that contains all relevant material properties for discrimination. The transmitter and receiver fields  $\vec{H}_{TX}$  and  $\vec{H}_{RX}$  are strongly depth and orientation dependent.

This formulation of the induced voltage and the chosen polarizabilities is the basis of some publications [21], [22], [27], and [74] where modifications have been implemented depending on the application. The dipole model, *ScanSim*, has some advantages like the computation time and the ability to be linked to MATLAB based optimization scripts and parameter studies.

### 3.2.4 Time domain transformation

The dipole model is solved in the frequency domain. The main result is the induced voltage in the receivers, which is derived first from the time derivative of the flux crossing the receiver as in (3.8). The final result is a frequency dependent induced voltage (3.15) that takes into account the axial (3.17) and transverse (3.18) polarizabilities that are also frequency dependent. Transient responses are required especially in pulse induction. The transformation from frequency domain to time domain is done after the solver has computed a wide range of frequency responses and evaluated  $\Phi(\omega)$  for an expected active range saving all the results as done already in the previous sub-section. The next step is to perform the cosine transformation to solve for  $\Phi(t)$  from  $\Phi(\omega)$  as described in (3.19), which is a step response.

$$\Phi(t) = \frac{2}{\pi} \int_0^{\infty} \frac{Im \Phi(\omega)}{\omega} \cos(\omega t) d\omega \quad (3.19)$$

The polarizabilities should be adapted accordingly and an example of a simple sphere would have one polarizability because axial and transverse ones are the same and therefore the sphere polarizability is defined in frequency domain as in (3.20).

$$\chi(\omega) = \frac{(2\mu_r + 1)ka - (2\mu_r + 1 + (ka)^2)\tanh(ka)}{(\mu_r - 1)ka - (\mu_r - 1 - (ka)^2)\tanh(ka)} \quad (3.20)$$

Where  $a$  is the radius of the sphere in this case. Similarly, the time domain polarizability can be deduced by the work done by Wait [76] and Smith et al [81] for the sphere case (3.21) and (3.22).

$$\chi(t) = \frac{2\mu_r - 2}{\mu_r + 2} - \sum_n \frac{e^{-\delta_n^2 t / \sigma\mu a^2}}{(\mu_r + 2)(\mu_r - 1) + \delta_n^2} \quad (3.21)$$

$$\tan \delta_n = \frac{(\mu_r - 1)\delta_n}{\mu_r - 1 + \delta_n^2} \text{ where } n\pi \leq \delta_n \leq (n + 1/2)\pi \quad (3.22)$$

The rest of the equations are trivial in the time domain as the target dipole moment in (3.23).

$$\vec{m}(t) = \chi(t) \cdot \vec{H}_{TX} \quad (3.23)$$

This transformation is essential for the pulse induction responses for simulating different coil design setup and the response of any transient current after a range of frequency responses are calculated.

### 3.3 Experimental verification

Using computational models in the current work is essential to consider the advantages of every model. As described in the previous chapter, the modified FEM computational model has advantages in the accuracy and the ability to model complex 3D objects and coupled coils for the EMI sensor technology. This modified FEM model, as a contribution of this work, provides a compromise in computation time and was able to keep the complexity and accuracy while the computation time was reduced to an acceptable level. Even after the modifications, it is still not suitable for huge designs, for scans, and in the transient excitation, when optimization methods are needed. It suits to be a reference and also performing parametric studies of few variables. On the other hand, the dipolar model is very fast and is suitable for scan responses but has limitations concerning complexity.

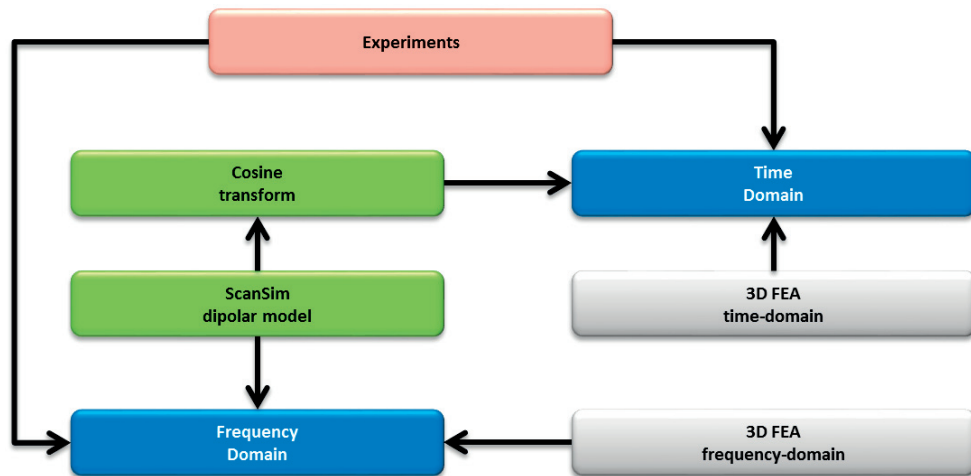


Figure 3:13 Experimental verification procedure for different models under frequency and time domain.

Both models need a verification procedure with experiments. Regardless of the model used, verification with experiments should be done in both frequency and time domain. The dipolar model, as mentioned in section 3.2, is based on the frequency domain but it can compute a transient response using cosine transformation to the time domain. The FEM model is solved by ANSYS solver in both frequency and time domains. Many aspects have been adapted in the dipole model when compared with the FEM model so that the implementation is as accurate as possible. In the end, this fast dipole model is suitable to perform optimizations and variations of the sensor parameters of both models and both

domains leading to a comparison with each other and with experimental data of more than one sensor design. Figure 3:13 shows the verification procedure of the models with experiments for both domains, different targets, and any sensor design.

### 3.3.1 Harmonic excitation validation

The first part of the verification is the model validation between the modified FEM model and the dipolar model. The simplest step is to do a frequency span for a defined design of coils and a defined setup of a target then compare the induced voltage in the receivers. The first design named here DESIGN II is sketched in Figure 3:14.

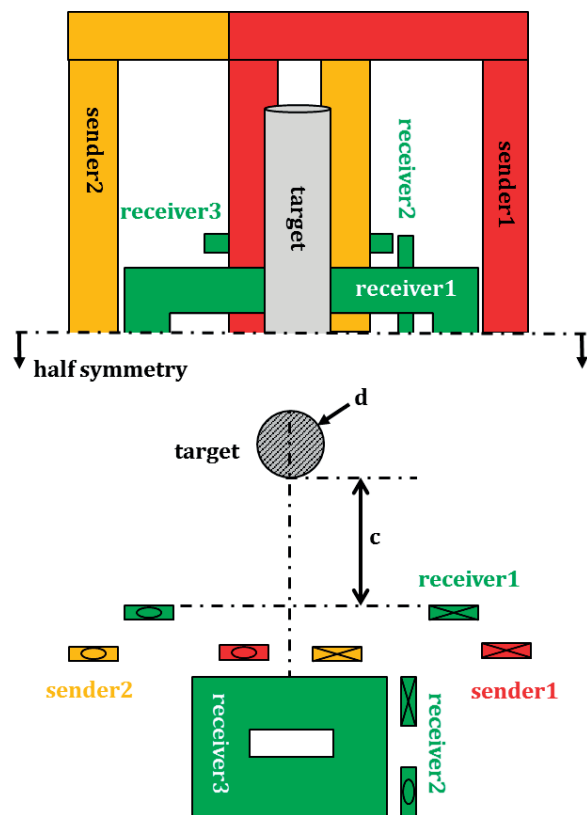
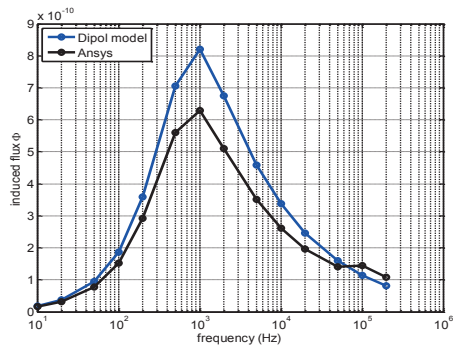
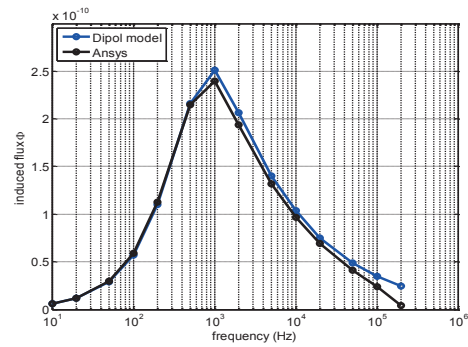


Figure 3:14 Sensor DESIGN II (Appendix D) including senders and receivers and the position of the target defined by  $c$  and  $d$ .

A harmonic current of 1A amplitude and a frequency range between 10-Hz and 200 kHz is input in the senders. The current flows anti-clockwise in both senders. The resulting harmonic flux amplitude in the receivers is compared for verification reason. More information about the coil geometry, dimensions, and specifications is found in Appendix D. The target is defined by material (copper or steel) and by the dimensions:  $c$  and  $d$  as in Figure 3:14. Different target setups are performed by varying these two dimensions.

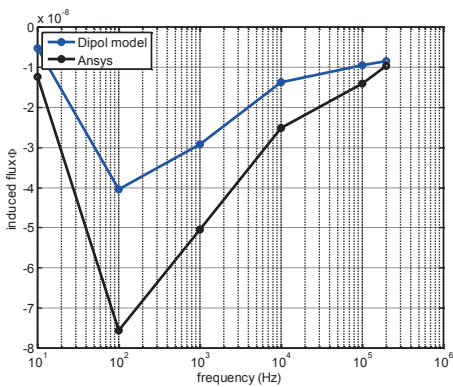


(a) induced flux in receiver 2

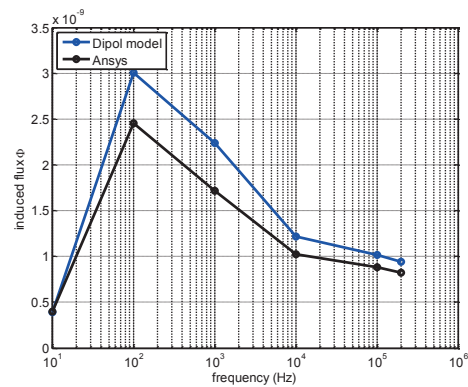


(b) induced flux in receiver 3

Figure 3:15 The simulated induced flux in receiver 2 and receiver 3 of DESIGN II (Appendix D), 'setup 1', and a copper cylindrical target.

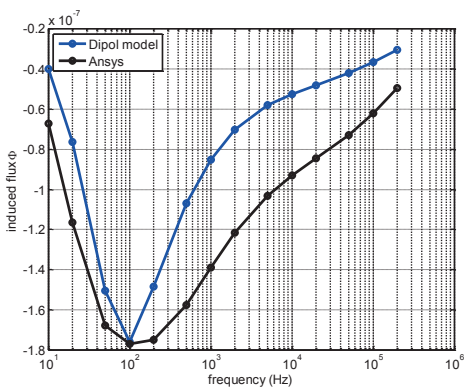


(a) induced flux in receiver 1

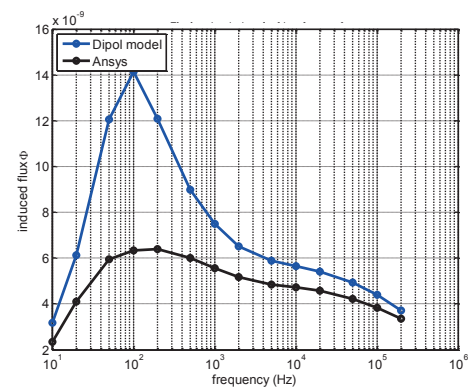


(b) induced flux in receiver 2

Figure 3:16 The simulated induced flux in receiver 1 and receiver 2 of DESIGN II (Appendix D), 'setup 1', and a steel cylindrical target.



(a) induced flux in receiver 1



(b) induced flux in receiver 2

Figure 3:17 The simulated induced flux in receiver 1 and receiver 2 of DESIGN II (Appendix D), 'setup 2', and a steel cylindrical target.

For this design two setups of targets are simulated by the modified FEM model and the dipole model. *Setup 1* and *Setup 2* have the following target dimensions:

- Setup 1,  $c = 46$  mm,  $d = 8$  mm
- Setup 2,  $c = 38$  mm,  $d = 16$  mm

The target for both setups is simulated with copper first and then steel. The material properties are as follows:

- Copper, relative permeability  $\mu_r = 1$  and electric conductivity  $\sigma = 5.5e^7$  S.m<sup>-1</sup>
- Steel, relative permeability  $\mu_r = 100$  and electric conductivity  $\sigma = 1e^7$  S.m<sup>-1</sup>

The targets are 30 cm long cylindrical rods. The sender coils are excited harmonically with a span of frequencies while their responses are sets of fluxes induced in all three receivers of the design sketched in Figure 3:14. Copper, as a cylindrical target being placed as defined in ‘setup 1’, yields an induced flux that matches very well between both models: FEM ANSYS model and dipolar model. This is clearly visible for the whole frequency span in Figure 3:15 a) *receiver 2* and Figure 3:15 b) *receiver 3*. In both vertical receivers, and for all the frequency range, the two models give the same results. If a steel target is used instead of copper, then the interpretation of the results should be done with care.

The permeable steel target required modifications on the dipole model. The demagnetization factor for the permeability of the axial component of the magnetic polarizability tensor helped to improve the dipolar model for the low frequency regime. This brought an acceptable comparison between the models for steel targets. The EMI sensor anyway is used at high frequencies but still this modification was needed for completion purpose. The horizontal receiver, *receiver 1*, and the vertical receiver, *receiver 2*, induced similar flux profiles when two different setups of steel targets were simulated. The results of the steel targets are plotted in Figure 3:16 (‘setup 1’) and Figure 3:17 (‘setup 2’). The FEM model is assumed to be a reference and therefore the modifications on the dipole model were done so that later a time dependent pulse induction excitation can be performed. The harmonic excitation validation was performed to align the dipole model to the FEM model under different materials and positions of cylindrical targets for all working frequencies so that when pulse induction is performed next, it would have a full validation.

The harmonic excitation validation is part of the whole computation validation flow described in Figure 3:13 where the lower left corner shows the frequency domain verification between the two computational models. On the other hand, time domain validation and experimental validation are necessary to close the verification flow chart. The top right part of Figure 3:13 is labeled by ‘Time domain’ and an example of such an excitation is pulse induction and is described in sub-section 3.3.2.

### 3.3.2 Pulse excitation verification

Pulse induction is described in subsection 2.2.1 as an excitation scheme that creates a pulse of current in the sender inducing a decaying voltage in the receivers. The procedure is performed in both computational models: FEM ANSYS solver and the dipole model. Experimental results are also compared to both models for DESIGN II and for both setups 1 and 2. In addition to that copper and steel targets are also used making the a total of six results to be compared. The currents in the senders have the same direction (anti-clockwise) as in the harmonic case before. The current profile in pulse induction is exactly like in Figure 2:3 b) with:

- $\tau_{on} = 80 \mu\text{s}$ ,  $\tau_{off} = 1 \mu\text{s}$ , and  $I_{max} = 0.9 \text{ A}$ .

The induced voltage decays in *receiver 1* are plotted in Figure 3:18 and Figure 3:19 for 'setup 1' and 'setup 2' respectively. The red curves are for steel and the green ones are for copper. In addition to that, both computational models as well as the experimental results are plotted. Only the decay part after the cutoff time ( $\tau_{on} = 80 \mu\text{s}$ ) is important to compare to. During this transient time of the decay all the information of the target is preserved. Due to experimental limitations, the voltage decays can only be saved after  $87 \mu\text{s}$  that is why the experimental decays do not start at  $80 \mu\text{s}$ . On the contrary, the simulation results can be plotted for any time interval.

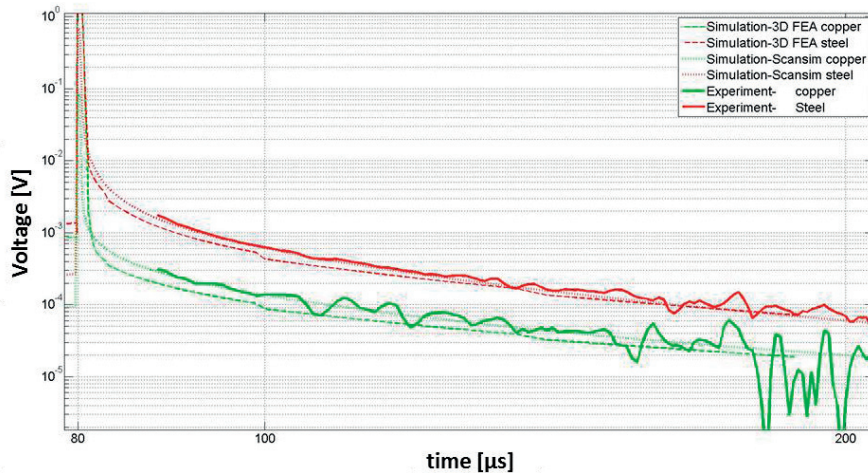


Figure 3:18 Transient induced voltage in *receiver 1* for DESIGN II (Appendix D) for 'setup 1' of copper and steel targets. Experiments and both simulation models are compared.

Some important observations are stated for these first results:

- Both computational models (3D FEM and *ScanSim* dipolar) have good compliance with the experimental results for copper and steel and for both 'setup1' and 'setup2'.

- Copper voltage response curves are lower than the steel ones for the same setup even though copper is more electrically conductive but it is less magnetically permeable.
- Responses of ‘setup 1’ are generally lower than the ones of ‘setup 2’ for the same material because the target in ‘setup 1’ is smaller and deeper than the one on ‘setup 2’.

In order to perform a size, depth, and material discrimination at the same time based on pulse induction, it is important to notice from the verifications done already that relying solely on the induced voltage values in time is not enough. Output decays of different setups may look similar and new features in these decays should be extracted to help in discrimination of material as well as of the size and location.

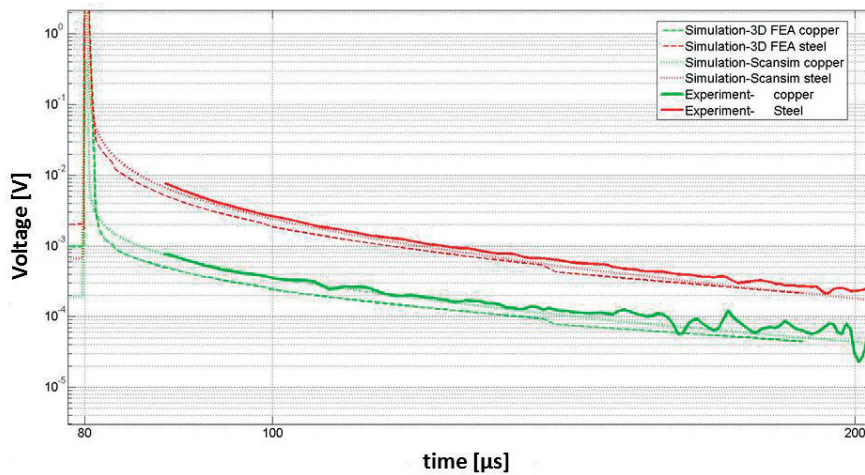


Figure 3:19 Transient induced voltage in *receiver 1* for DESIGN II (Appendix D) for ‘setup 2’ of copper and steel targets. Experiments and both simulation models are compared.

Chapter 4 widens the topic of discrimination taking material, size, and location into account. The comparisons done so far are for one sensor: DESIGN II (Appendix D). Another transient pulse induction scheme is performed on another sensor design that is named DESIGN I (Appendix B). This is the same simple exact design of one sender and one receiver coils as in Figure 2:7. The assembly shown in Figure 2:8 and the testing electronics hardware are exactly as in Figure 2:4 for pulse induction. This design has one sender and one receiver and the current profile for pulse induction is similar to the one in Figure 2:3 b) with the following current specifications:

- $\tau_{on} = 80 \mu s$ ,  $\tau_{off} = 1 \mu s$ , and  $I_{max} = 1 A$

The target, in this case (‘setup 3’), has the following dimensions:

- setup 3,  $c = 6$  mm,  $d = 8$  mm

Simulation results of the two simulation models mentioned earlier result in voltage decays for both copper and steel and are plotted in Figure 3:20 for comparison.

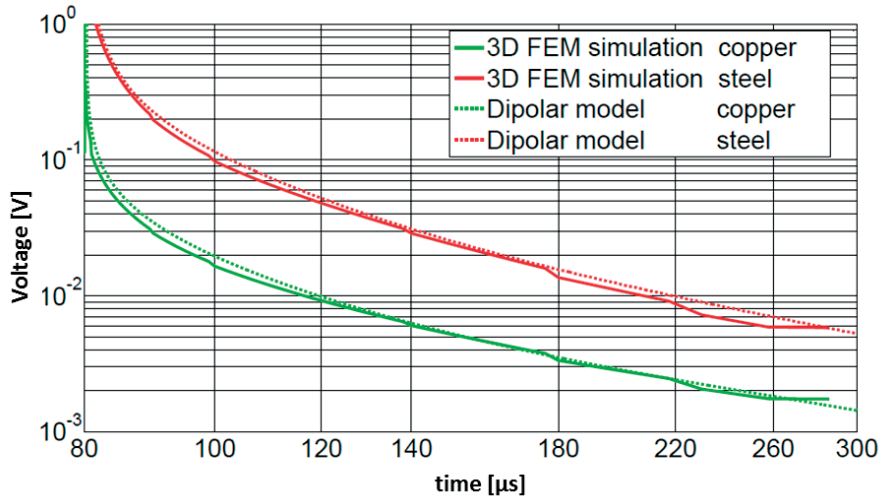


Figure 3:20 Transient induced voltage in the receiver for DESIGN I (Appendix B) of copper and steel targets at 'setup 3'. Both simulation models are compared.

Up to this point, the two simulation models are comparable with each other, and with the experiments, for two different target materials and with three different target geometrical setups using two different sensor designs. In the time domain (pulse induction) the validation is more reliable. In the frequency domain (harmonic induction) the match is good at high frequencies. This is acceptable because the very low frequencies can be ignored in the context of this work.

After this validation procedure by harmonic and pulse induction excitations, the next simulations and experiments consider complex targets like double cylinders. Such work includes a coupled effect of targets and is detailed in the sub-section 3.3.3.

### 3.3.3 Mutual inductance

For efficient inversion of the model of nearby targets, the superposition principle is required. To check the general validity of this principle, the dipole model was compared with the reference 3D finite element method (FEM) model for a frequency span. For the investigated targets, the coupling effect can be neglected only for high frequency range but a huge error can be made at low frequencies. Computational models for single targets have been implemented and verified so far. But for close lying targets, electromagnetic coupling can play an important role for accurate inversion of target parameters. The aim is to develop the dipolar model further so that it is valid for close target separations and excited at a wide frequency range [22]. In order to compare the induced flux of a double cylinder (two nearby cylinders) to the superposition of two separate induced fluxes of



each of the two single cylinders, experiments and simulations were performed with harmonic excitation input signals.

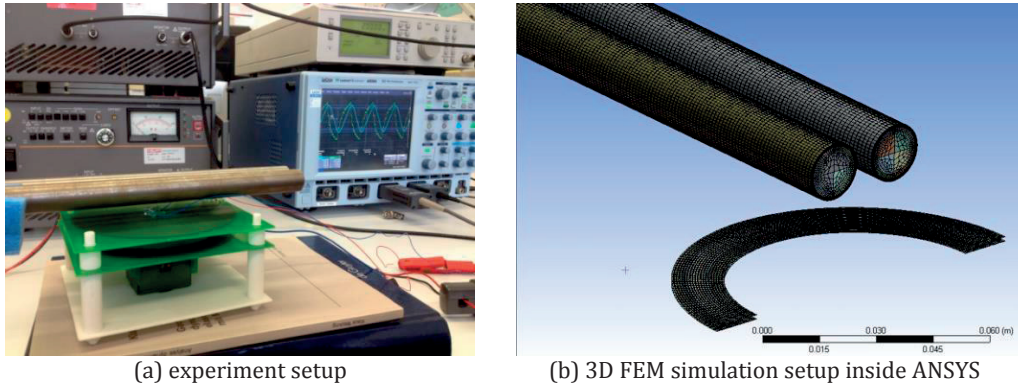


Figure 3:21 Setup of DESIGN I (Appendix B) with two steel cylindrical targets.

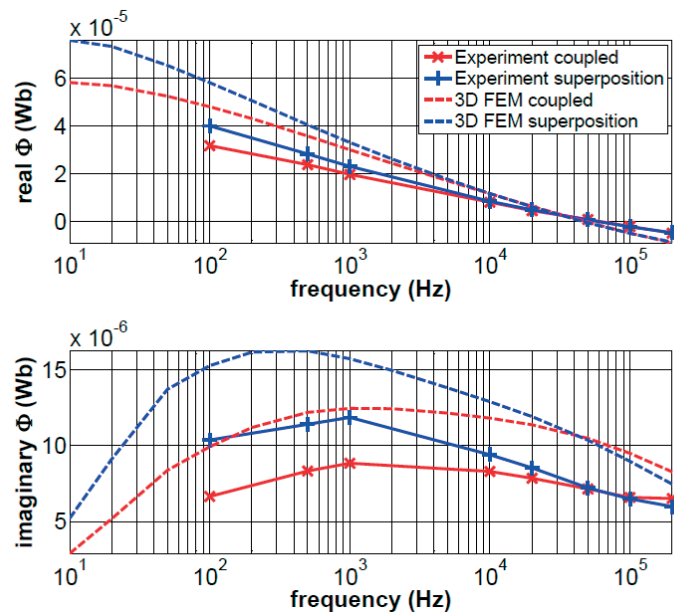


Figure 3:22 The real (upper) and imaginary (lower) flux response of a double cylinder versus the addition of single response. The sensor used is DESIGN I (Appendix B).

The experimental setup is shown in Figure 3:21 a). The sensor design is the DESIGN I (Appendix B) sensor mentioned previously in this chapter and shown in Figure 2:7 and Figure 2:8. The two steel cylinders are 16 mm diameter each with a distance 10 mm from

the upper PCB receiver coil ( $c = 10$  mm). these cylinders are separated by a transverse distance of 5 mm. A function generator of a periodic sine wave with the required frequency is generating a voltage signal that is amplified before being fed to the sender to make sure a current of 1A amplitude is set at any operating frequency. The induced voltage in the receiver is then amplified and measured in the oscilloscope.

Three outcomes are needed to proceed:

- outcome 1: no target is present
- outcome 2: a single cylinder target is present
- outcome 3: a double cylinder target is present

The last two outcomes are subtracted from the first case to get the pure induced results of the cylinder(s) to eliminate the mutual inductance of the sender, which is very high for this design. Finally, two quantities are compared:

- $quantity\ 1 = 2 \times (outcome\ 2 - outcome\ 1)$
- $quantity\ 2 = (outcome\ 3 - outcome\ 1)$

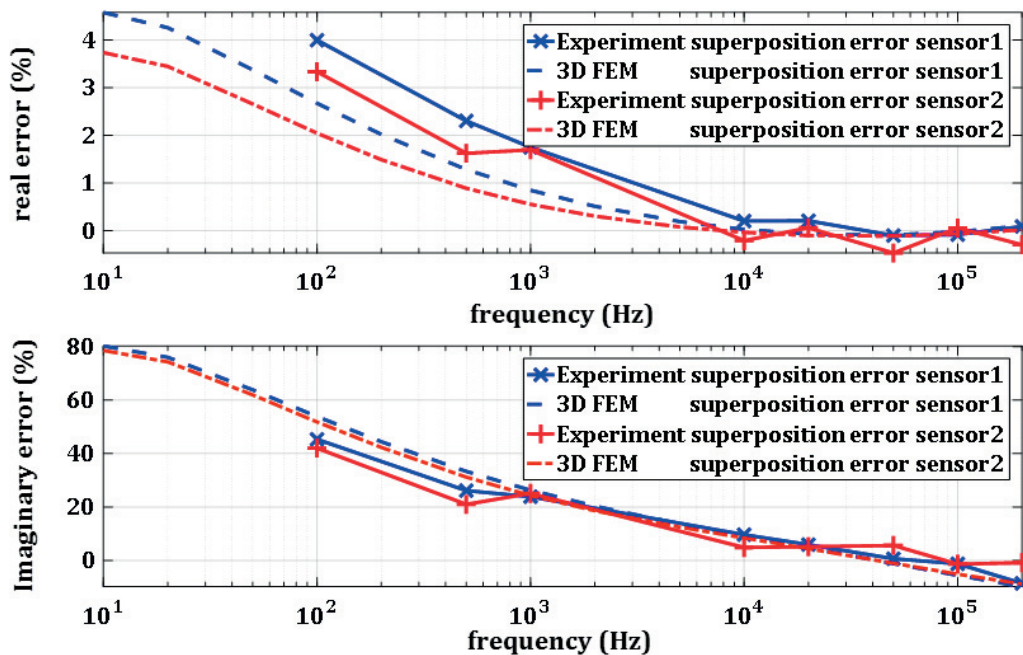


Figure 3:23 Measured and calculated superposition error relative to double cylinder response for both sensors are evaluated: the real and imaginary fluxes in the receiver coil using DESIGN I-sensor 1 (Appendix B) and DESIGN I-sensor 2 (Appendix C) for steel targets.

The first quantity represents the superposition of two non-interacting cylinders (superposition principle). The second quantity represents the response of a double cylinder

target. The voltage results are integrated to get the induced flux. This procedure is applied to the 3D FEM simulation results as well as the experimental results and compared in Figure 3:22. It shows the real and the imaginary part of the induced flux for the combination of the two parallel steel cylinders and the superposition of the response of two single steel bars.

The receiver can easily be replaced with another coil, and so a PCB receiver coil with 40 turns is also checked to be sure that the winding capacitance does not have an effect in the investigated frequency band. In order to differentiate here between the two sensors, which are based actually on the same design, they are named:

- DESIGN I-sensor 1 (Appendix B)
- DESIGN I-sensor 2 (Appendix C)

The difference between the two sensors is just the number of turns of the receiver.

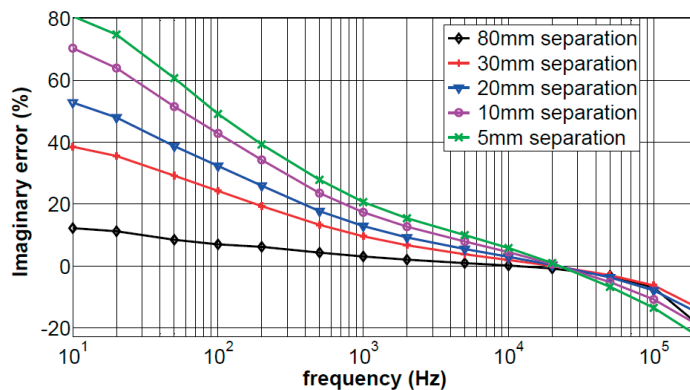


Figure 3:24 Relative difference between the coupled and the single target superposition of the induced imaginary flux for two close lying 20 mm diameter steel cylinders for several separation distances. The sensor used is DESIGN I-sensor 1 (Appendix B).

For these steel responses, which are close to each other (5 mm separation), and referring to Figure 3:22, below 20 kHz, the superposition signals give much higher response than the coupled signals. This tendency is the same for experiment and simulation. This means, the coupling strength is dominant in the frequency range below 20 kHz, so that the simple dipole approach without additional coupling can only be used as forward model for high frequency sensors. The signal amplitudes differ between simulations and experiments. A reason could be the input impedance of the amplifier used. However, the relative error defined as the difference of the superposition and the coupling flux divided by the coupling flux and plotted in Figure 3:23 matches perfectly with experiment. Around 20 kHz, the coupling is not present (or probably cancelled) for this target separation of 5 mm. This happens when the coupled and superposition lines meet (see Figure 3:22), or when the relative error of the two is zero (see Figure 3:23). In Figure 3:23, the

results of sensor 2 are also included showing that the behavior of both sensors is the same.

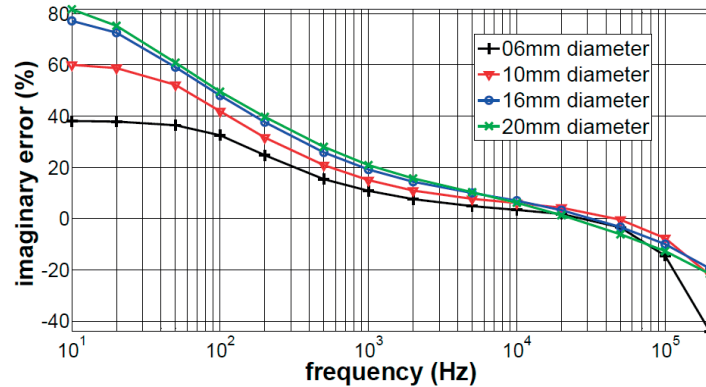


Figure 3:25 Relative difference between the coupled and the single target superposition of the induced imaginary flux for two close lying steel cylinders with several diameters and a fixed separation of 20 mm. The sensor used is DESIGN I-sensor 1 (Appendix B).

So far only one case (fixed separation = 5 mm and fixed diameter = 16 mm) has been analyzed. The 3D FEM model is now used to check more general cases like separation and diameter variations. Figure 3:24 shows the superposition relative error when the diameter is kept constant at 20 mm and the separation is varied from 5 mm to 80 mm. The coupling strength decreases with separation as expected. All curves cross at a small range of frequency averaged to 20 kHz for the current application and specifications of diameters and separations.

The coupling is zero or cancelled around this frequency range between 15 kHz and 40 kHz. This special frequency range is mainly material dependent. Figure 3:25 shows the superposition relative error when the separation is kept constant to 5 mm (surface to surface) and the diameter is varied from 6 mm to 20 mm. The relative error (i.e. the coupling strength between the targets) increases with the diameter as expected. Again, all curves cross at a small range of frequency around 20 kHz. The coupling is zero or cancelled around this frequency. It has also been proven that this error is independent of the target depth. This proves a new phenomenon that the frequency of around 20 kHz is allowing decoupling of double steel cylindrical targets regardless of their diameter, depth, and separation. If the targets are copper instead of steel, then the relative error is proportional to the increase of the frequency. This is a different characteristic than the one of steel. The frequency ranges up to 1 kHz are showing no superposition error of copper. The error simply increases with the frequency. The diameter and separation range required for this study show that the decoupling frequencies fall in the range of 15 kHz to 40 kHz as represented in Figure 3:26.

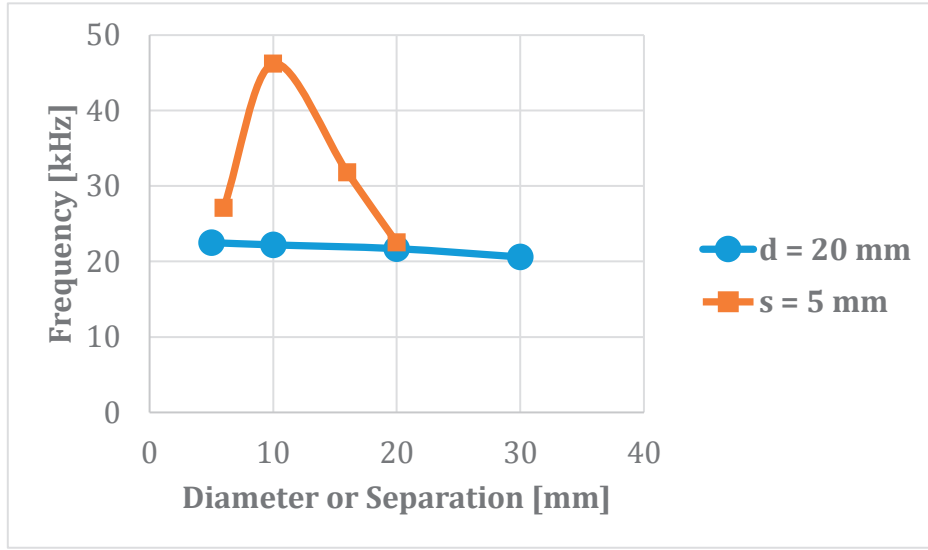


Figure 3:26 The decoupling frequencies for fixed diameter ( $d = 20$  mm) and variable separation, as well as the ones for fixed separation ( $s = 5$  mm) and variable diameter.

Until this point of the current work, a 3D FEM electromagnetic simulation and some experimental setups were used to analyze the effect of the coupling between ferromagnetic cylindrical objects. These results have to be compared to the dipole model. It has been proven already that both the dipole model and the 3D FEM model give close results for high frequencies and non-interacting i.e. largely separated objects. The 3D FEM model as well as the experiments show, that for parallel steel cylinders in transverse excitation, the coupling strength is large at low frequencies (less than 20 kHz). The coupling is also large at smaller separation and large diameters. There is a narrow frequency interval where coupling is cancelled totally, nearly independent on diameter, depth and separation. The importance of this decoupling frequency for steel target presence will be explained and used in distinctive detection Chapter 4.

The dipolar model shows the same behavior if the secondary field of the neighboring dipoles is taken into account for the calculation of the total field at the dipole position. To model the coupling, the suggestions of Braunisch et al [13] are followed, where the total field is calculated at a certain dipole position as the sum of the primary excitation field and the secondary field caused by all other dipoles at this position. The dipole field at position  $\vec{r}_j$  caused by the induced magnetization  $\vec{m}_i$  is given by:

$$\vec{D}(\vec{r}_j, \vec{m}_i) = \frac{1}{4\pi} \left( \frac{3\vec{r}_{ij}(\vec{r}_{ij} \cdot \vec{m}_i)}{r_{ij}^5} - \frac{\vec{m}_i}{r_{ij}^3} \right) \quad (3.24)$$

Where  $\vec{r}_{ij} = \vec{r}_j - \vec{r}_i$ .

The total magnetic field at the dipole position  $\vec{r}_j$  is then the superposition of the transmitting field  $\vec{H}_{TX}$  and the secondary fields of all other dipole moments  $\vec{m}_i$  and written in the form:

$$\vec{H}_{tot}(\vec{r}_j) = \vec{H}_{TX}(\vec{r}_j) + \sum_{i \neq j} \vec{D}(\vec{r}_j, \vec{m}_i) \quad (3.25)$$

The dipole moments can be calculated by  $\vec{m}_j = M(\omega)\vec{H}_{tot}(\vec{r}_j)$

And this leads to a set of linear system of equations in  $\vec{m}_j$  that can be calculated explicitly:

$$\vec{m}_j = M(\omega) \left[ \vec{H}_{TX}(\vec{r}_j) + \sum_{i \neq j} \vec{D}(\vec{r}_j, \vec{m}_i) \right] \quad (3.26)$$

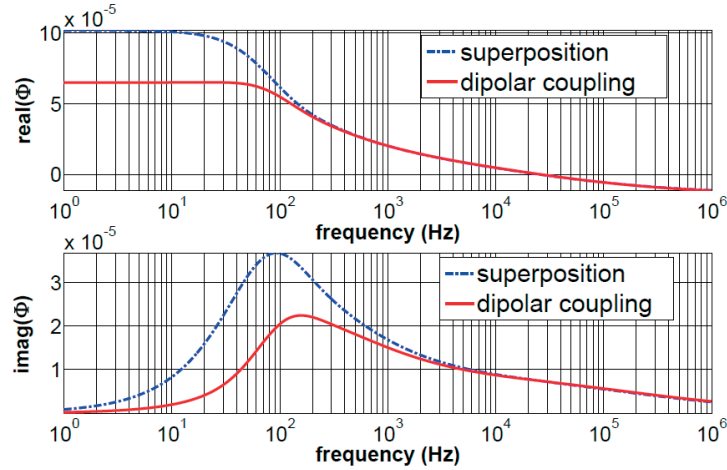


Figure 3:27 Magnetic flux  $\phi$  as function of frequency above two cylindrical targets with (dotted) and without (solid) considering the dipolar coupling between the targets in the quasi-static dipolar approximation. The sensor used is DESIGN I-sensor 1 (Appendix B).

In this approach, this system of linear equations is not solved explicitly, but by considering the change of the magnetic field strength at the location of the dipole  $\vec{m}_j$  due to all the other primarily induced dipoles  $\vec{m}_k$  ( $k \neq j$ ) and superimposing this secondary field to the primary field in the frequency domain. The simulated results of the setup using two steel cylinders in 5 mm separation at 10 mm from the receiver coil are displayed in Figure 3:27. A decrease in the imaginary (i.e. secondary) flux for low frequencies ( $f$  less than 1 kHz) compared to the superposition of two independent steel cylinders is observed. At higher frequencies ( $f$  greater than 20 kHz), the situation changes. The coupled model gives a slightly higher response compared to the superposition of two independent targets. The results of the coupled model match well with the experiments and the 3D FEM

simulation. This simple dipolar model can still be improved with more realistic coupling mechanisms for cylinders and pipes based on an approach proposed by [77].

These verified and validated models, with all their modifications and adaptations are the main tools of design and optimization in the context of this work. These computational models are mainly used to reach a concept plan of an EMI sensor that can distinguish detected features of targets as well as being able to identify materials of composed targets (detailed in Chapter 4).

## Chapter 4 EMI distinctive detection

The research and development of a detection system based on electromagnetic induction should cover all three parts of experience or knowhow: the coil design, the excitation scheme, and the post processing technique. These three fields must be equally valued in any work in this domain as proposed in the introduction Chapter 1. These basic contributors are sketched in Figure 1:3 and are equally important to the work to be done in this domain. If any point is omitted or given less value, the aims are not easily reached or at least they are not reached in a logical scientific approach. Trial and error ways in such a domain are common but costly and mainly misleading. The procedure is drawn by starting at the system level, continuing at the model approach, and ending in the inverse model, which is difficult to achieve without a well programmed forward post-processing procedure. This complete workflow was summarized in Figure 1:4. So far the previous chapters have introduced the system and sensor design including the possible coil design, and coil excitation choices as pulse induction or harmonic induction. The mathematical, theoretical, and numerical models explained, verified with experiments, and used as a forward model as seen in Chapter 3 are the main virtual tools for understanding and improving this detection system. Post processing ways in the form of signal analysis and processing are introduced in section 2.4 where parametrization is being done on the sensor responses of already known target features. But in a real-life application, these features are usually not known. Detection devices should be programmed to identify unknown targets, which are supposed to be hidden. The features of the hidden targets are usually not known. That is why an inverse model is required. Inverse approach is the final goal in designing and developing a detection sensor. It is highly linked to the excitation method (section 2.2) and the sensor design (section 2.3). An inverse problem is possible only when the basic constitutions of a sensor are clear and known. Having reached this stage of knowledge the next step is to setup a procedure that estimates features of hidden metallic (magnetic or nonmagnetic) targets from the measurement of one induced signal (or the response of at most one transversal scan) in the receiver coils. This relies on all database tables that define the system as described in Chapter 2. Then numerically inverting the forward approach leads to feature discrimination of targets. It is also important to mention that targets can be classified as pure electrically conductive (copper) or ferromagnetic (steel). This chapter highlights on ways to distinguish both and apply different methods in both cases. On top of that, wherever targets are located close to each other, some suggestions are proposed to distinguish between single material and double material ones. This is named in the context of this work as 'distinctive detection'. The complete chain of information to reach this stage are all necessary and equally important. This chapter shows different approaches for detection procedures and feature discrimination, firstly by pulse induction and secondly by harmonic induction. Feature discrimination was discussed previously in section 2.1. The meaning of feature can be the material, size, and location of the target to be detected. A



complete way of distinctively detecting different targets placed near each other, composed of different materials (magnetic and nonmagnetic), and still able to characterize their size, location, and depth is also described here in details.

## 4.1 Pulse induction

The choice of pulse induction together with the coil design as mentioned in Chapter 2 has an important influence on the post processing method. The signal processing on the decay fits is detailed in section 2.4 for the receiver coil voltage response of a pulsed current in the sender coil. This decay parametrization is a novel contribution to the induction methods. The ability to find parameters of that decay that are dependent on certain features made the inverse approach simpler. Estimating diameter and depth (or cover) of targets at the same time and using one excitation direction and one receiver response has never been implemented in any known commercial devices so far. In all investigated methods and sensor designs, including industrial and commercial ones, quality is matched with:

- additional excitation modes
- additional receivers relatively placed in several orientation angles to the target

Precise size discrimination is possible by doing the above additions. In contrast, the decay parametrization, proposed here, allows the full estimation of the target features with only one sender coil and only one receiver coil without any special orientation (simply placed parallel to each other). Some pulse induction sensor hardware (Design II in Appendix D and Design III in Appendix E) used in this work are made of more than one receiver in order to show the difference between state-of-the-art designs and the proposed single receiver method. The same multi-receiver hardware can be experimentally used but postprocessing only one of its receivers. Additionally, multi-senders are shown in some hardware designs (Design II in Appendix D and Design III in Appendix E) because the original classic hardware uses more than one excitation modes. The current direction in each sender may not be the same for a certain mode. The actual proposed method uses one excitation mode and by that the same classical hardware can be used by keeping the same current direction of two nearby senders. This can be considered one sender. The proposed method has many advantages over classical pulse induction detection methods like:

- Cost reduction since less coils are needed and therefore the design can be more compact especially that geometrically oriented coils relative to each other are not required. There are fewer electronic devices like drivers, transistors, amplifiers because of the reduced number of coils.
- Less interferences especially on PCB boards, which have less copper paths and less layers in the proposed solution. Thus, there would be less routing pads interconnecting printed coils, which reduces cross talking at high frequencies and self-capacitance.

- Less data from the voltage response are required. Since these voltage decays are parametrized and therefore the complete raw signal is not needed. For example, the limitation due to amplifiers limits the amplified induced voltage to an upper value until it starts to decay. This first constant part can be skipped, in the presented method, while in other post-processing classical methods it would be a problem. Furthermore, the long decays are not required, so 150  $\mu\text{s}$  effective measured time interval is enough for the actual application. The direct raw induced signal is small and amplifiers are required in order to get a better resolution. The targets with low cover and large diameters have higher response than the high cover and small diameter ones. But once an amplifier is chosen then it should be unique and valid for all cases. That's why the low signals should be at least readable but the highly amplified signals saturate at the first 10  $\mu\text{s}$  or even 20  $\mu\text{s}$  time interval and using the proposed method eliminates this problem. Such measured signals are plotted in Figure 2:13 where the saturation can last up to 107  $\mu\text{s}$  (27  $\mu\text{s}$  after switch off) mainly for large and shallow targets.
- Less effect from coils' mutual inductances because it requires a smaller number of coils to do the same task. There is more space separating them.
- More time allowed for post-processing or even live processing (during a scan). The reduction of the excitation modes of the sender coils saves excitation time as well as receiving, post-processing, and data storing time. On top of that, the reduction of receiver coils, requires less signal processing times. Due to all this, rough characterization of targets can be even possible during a scan with live results on the device screens under a limited scan speed (along the x-direction). The short measuring time contributes to the device speed significantly.
- Quality increases for slow scan speeds. The device can be set by the user to do more accurate scans by allowing the sender to send several redundant signals while the responses are averaged. This is achievable only because the sending and receiving time intervals are shorter for the same detection quality, leaving more time for signal saving and signal processing.

The database produced in the example mentioned in section 2.4 contains tables of mainly three decay parameters  $t_0$ ,  $n$ , and  $a$  that are either a function of target diameter  $d$  only or both diameter and cover  $c$ . Additional parameters like  $c_1$ , the one in the Gaussian fit of (2.6) gives a first estimation of the cover range by the linear relationship it has to the cover as in Figure 2:20 for the specified detection example. Based on these parameters that represent a forward relationship (target features  $\rightarrow$  measured response), an inverse approach is possible (measured response  $\rightarrow$  target features) and is described in details in the following subsection.

#### 4.1.1 Inverse problem as fast estimator

The detection process is an inverse problem in the end. Usually the target features are unknown, i.e. the target diameter, cover, and location are not known because the target

is hidden. What is first available, is a set of voltage decays in time (for pulse induction methods) and each decay is an induced voltage at a certain transverse location (sensor scan direction).

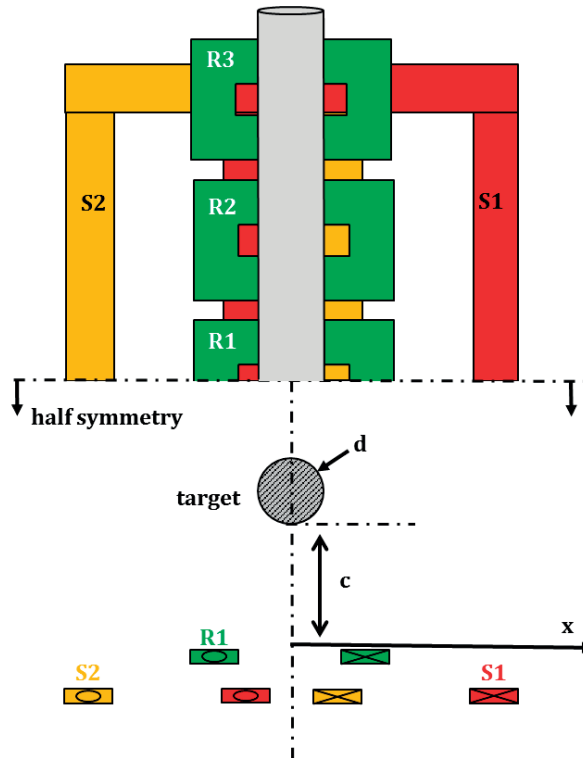


Figure 4:1: Detection sensor DESIGN III (Appendix E) for pulse induction using one excitation mode and one receiver direction. The target features  $d$ , and  $c$  are unknown as well as the  $x$  location.

A pulse induction example is taken here with real experimental results explaining the inverse procedure step by step. The aim is to estimate the target diameter, cover, and transverse location using only the voltage decays of the scan. The terms: *scan*, *transverse*, and  $x$ -direction all have the same meaning in this work and are simply the direction of the  $x$ -axis in Figure 4:1. It is representing the movement of the sensor from right to left relative to the target, which is supposed to be fixed and hidden. In all experiments and simulations done in this work, the opposite was performed: The scanning device was fixed but the target is moved from left to right instead (positive  $x$ -direction). This was done on purpose in order to be consistent in characterizing all variables and quantities as a function of  $x$ -position. At every target  $x$ -location during the scan, the sender generates current pulses that in turn generate magnetic fields and then each receiver experiences an induced voltage decay signal. Every decay is associated with an  $x$ -location. For every sensor design and excitation scheme, responses of all possible known target cases

are performed in a similar way to the pulse induction procedure described in section 2.4 where all quantities and tables are representing a forward database model. Regardless if this system representation is done experimentally or by simulation, the complete representation requires saving these database tables of responses of all target feature combinations. Thus, all target sizes and depths (covers) are scanned leading to sets of lookup tables and equations as a function of  $x$ ,  $c$ , and  $d$ , which are variables sketched in the new example of Figure 4:1. This concept is named here DESIGN III and more information about the coil design of this hardware is found in Appendix E.

In this example two senders,  $S1$  and  $S2$ , have the exact same currents generated in them flowing in the same direction (anti clockwise) so that the same field in the same direction out of the plane of the coils. Five receivers are placed just above the senders and parallel to them. It was mentioned before that one receiver and one sender are enough for this method and this is still true. The two senders here can be replaced by one sender because the current direction is the same and both senders are in the same plane printed on a multi-layered circuit board. The field generated is nearly the same. Concerning the lateral overlapping of the receivers, a good transverse target localization can be achieved by cancelling the stray fields on the intersection because the currents of both senders are opposite in direction at the middle of the sensor. This is not a priority design issue for achieving the aims of this work. Overlapping senders and non-overlapping senders would reach the same goals. Also, the middle receiver,  $R1$ , is enough, and one can consider the other four receivers as redundant (two and a half receivers only are shown in the figure due to symmetry). One can also take the sum of responses of all five receivers and consider them as one response. It is also possible to replace all five receivers with only one big receiver. The five receivers are simply an array meant to increase the resolution. Also, averaging the decay voltage responses of these receivers is even more robust and less liable to measurement error. Redundancy here is just made as an industrialized solution of such a sensor to avoid measurement errors, signal storing errors, and manufacturing tolerances. If the coils are manufactured and assembled with high quality and very low tolerances, then redundancy can be avoided. The coil design to be used here is the one in Figure 4:1. That is a similar concept to the one in Figure 3:14 except that the vertical receivers are skipped. The vertical receivers of DESIGN II in Chapter 3 were used for simulation verification reasons. In addition to that, these receivers were used while activating the senders differently (different excitation modes) but this is not documented here because it is irrelevant. If the current in *sender 1* is clockwise while the other in *sender 2* is anti-clockwise then the magnetic field penetrates the target horizontally (parallel to the  $x$ -direction). It also penetrates these vertical receivers horizontally (perpendicular to them). These receivers' induced voltages have better information about target sizes. However, this excitation mode is not needed any more and is not used throughout this work, and therefore vertical receivers can be skipped. As mentioned in this section, the detection sensor should be able to discriminate all features by using horizontal compact coils only and one excitation mode only. For that reason, DESIGN III (Figure 4:1) is created to prove this concept. Referring to the definition of a current pulse in Figure 2:3 a pulse induction scheme with a rise time of  $110 \mu\text{s}$  ( $\tau_{on}$ ), and a fall time of  $1 \mu\text{s}$  ( $\tau_{off}$ ) is

being used in this example. The maximum current reached is 1 A. The three variables in the system are:

- $d = 6, 8, 10, 12, 14, 16, 20, 25, 28,$  and  $32$  mm
- $c = 5, 10, 20, 30, 40, 50, 60, 70, 80, 90, 100, 110, 120, 130, 140, 150, 160, 170$  mm
- $x = -120\text{mm}$  to  $120\text{mm}$ , in steps of  $3$  mm

For every combination of variable values there is a measured voltage decay in time in every receiver. An experimental setup was done where the target-scanner relative position was atomized by a robot and all voltage decays were saved and analyzed. The variable  $d$  has 10 possibilities whereas  $c$  and  $x$  have 18 and 81 possibilities respectively. The total number of decays in time measured are simply  $10 \times 18 \times 81 = 14580$  decays, which when plotted versus time would look like the ones in Figure 2:13. Some of the receiver strong voltage signals have an upper bound value due to the amplifier limits. The data are saved for all decays starting at  $117 \mu\text{s}$ , which is  $7 \mu\text{s}$  after the sender's switch off time to make sure that the sender coil has no influence on the receivers' response. All decays are measured till  $250 \mu\text{s}$ . As stated before there is no real loss of information if measurement started late or ended early because parametrizing these decays builds the missing data in time. The advantage of decay parametrization especially for this saturation in the voltage signals is also clearly visible in Figure 2:13 where some signals are limited to a constant value before the decay is known and saved.

The coils in Figure 4:1 are printed on PCB and have characteristics shown in Table 4:1 for each coil. The copper wires printed on the board for each coil are dimensioned as  $p_w$ ,  $p_h$ , and  $p_s$  corresponding to the wire width, height, and spacing of the printed copper pads. The spacing here is the lateral distance separating each pad from the other. This spacing is chosen carefully not to have a high self-capacitance and should be greater than  $0.1$  mm. These pads are printed in layers on each board and adding up to  $N$  number of turns for every coil.

Table 4:1 Coils characteristics including dimensions of copper pads on the board.

Coil Name	$N$ turns [-]	$W$ Width [mm]	$L$ Length [mm]	$p_w$ pad width [mm]	$p_h$ pad height [mm]	$p_s$ pad spacing [mm]
<b>S1, S2</b>	28	110	209	0.8	0.03	0.2
<b>R1-R5</b>	300	29.5	29.5	0.1	0.03	0.1

The outer width ( $W$ ) and length ( $L$ ) of the coils are also dimensioned in the table. The sender coils overlap in width direction and therefore the center of  $S1$  in the x-axis is located at  $x = -24$  mm and the one of  $S2$  is at  $x = +24$  mm. From that it is easy to deduce the outer width of the biggest PCB board (in this case the one containing  $S1$  and  $S2$ ) to be  $158$  mm while the length is  $209$  mm (same as  $L$  of the senders). Additional clearances and electronics also need to be installed on the board and thus the area required is even bigger. The five receivers are separated by  $1$  mm from each other and are printed next

to each other on one separate board fixed just above the sender board. After freezing the coil design and defining the pulse induction excitation scheme, the post processing method is a signal analysis of the induced voltage decays in the receivers that is applied to all 14580 measured or simulated cases by varying the variables  $d$ ,  $c$ , and  $x$  mentioned above. The result is a representation of this system. It is saved to be used in the inverse model.

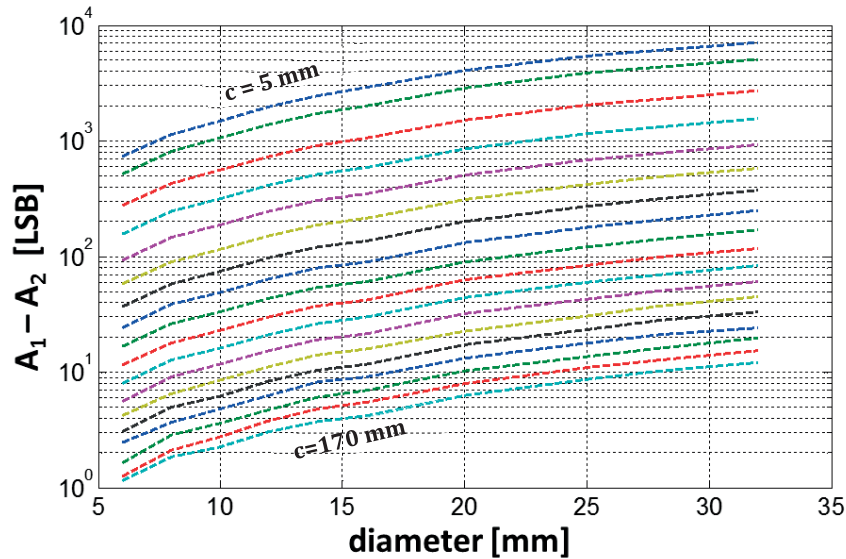


Figure 4:2: Lookup table of the function  $f = A_1 - A_2$  plotted versus the diameter  $d$  of the targets. Every line corresponds to a cover  $c$ . This table corresponds to the value of  $x$  equals zero. The sensor used is DESIGN III (Appendix E).

By evaluating the function  $f(d, c, x) = A_1 - A_2$  ( $A_1$  and  $A_2$  are described in section 2.4.1 and sketched in Figure 2:16), the first effective lookup table after saving all these experimental decays is generated. The function  $f(d, c, x)$  is represented as a 2D lookup table dependent on the first two variables ( $d$  and  $c$ ). Along the scan positions, for every value of  $x$  there is a unique 2D lookup table. Each lookup table has 180 points. If the scanner is located just below the center of the target rod, then  $x=0$  and should have the highest relative responses. A plot of one lookup table at  $x=0$  is shown in Figure 4:2. Every transient voltage is now represented by one point as a discrete function of three variables,  $d$ ,  $c$ , and  $x$  and for illustration reasons the 2D table in Figure 4:2 is generated at  $x = 0$ . Similar tables are generated for every  $x$ -position. These values are based on real experiments of single steel cylindrical targets and they show a good differentiation between cover values in the logarithmic scale and nearly linearly dependent on the target diameter. Each curve is plotted for a constant cover value, which means the highest curve corresponds to  $c = 5$  mm and the lowest curve corresponds to  $c = 170$  mm. Small cover values mean that the target is near the sensor that is why the response is higher. These tables are still not sufficient to find the unknown variables.

The values of  $f(d, c, x)$  in the  $x$ -direction have a maximum at  $x = 0$ . This is the transversal location where the target and the sensor are aligned. If the variables,  $d$  and  $c$  are fixed, the plot of  $f$  along  $x$  is like the one in Figure 2:19, which is normalized about  $x=0$  where it exhibits a maximum. The data are then fitted to a gauss equation of the form (2.6) to evaluate the parameter  $c_1$ , which when evaluated for all diameter and cover values leads to a plot like Figure 2:20.

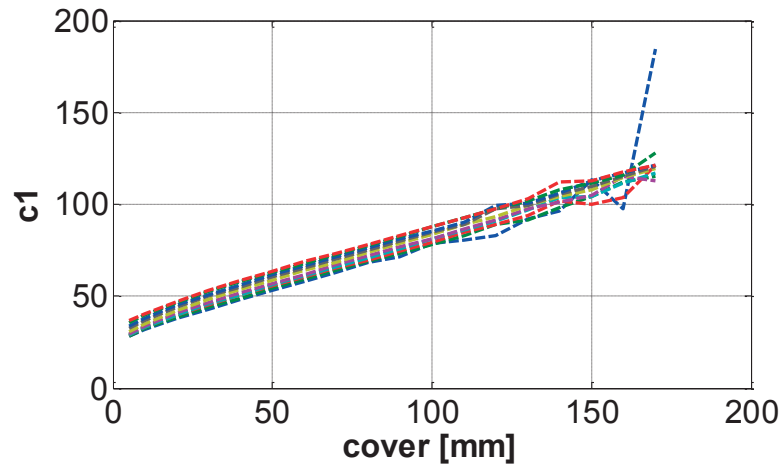


Figure 4:3: Parameter  $c_1$  evaluated for 180  $x$ -scans and plotted versus cover  $c$ . Every line corresponds to a diameter  $d$ . The sensor used is DESIGN III (Appendix E).

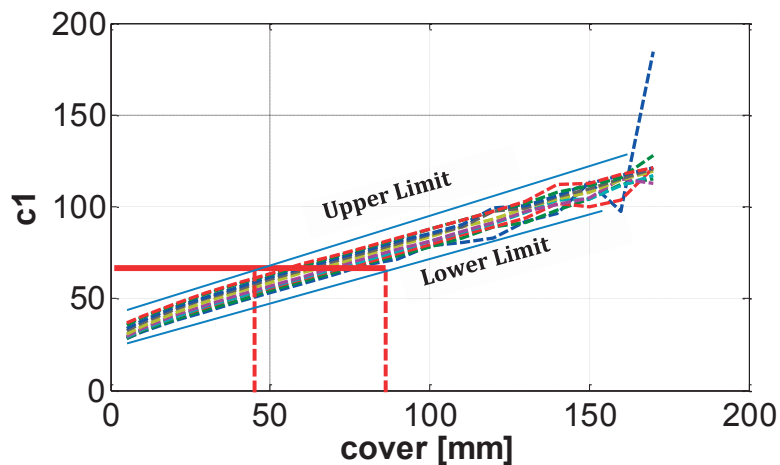


Figure 4:4: Illustration of the first estimation of the cover interval by knowing  $c_1$  from one scan in  $x$ -direction. The sensor used is DESIGN III (Appendix E).

For all the experimental results of the example in current section, the parameter  $c_1$  was extracted from all the fits over every scan, and plotted versus the cover  $c$  for every diameter  $d$  in Figure 4:3. This graph helps to find the first cover interval. The solution must lie in this interval. In the detection process in a real device a scan in the  $x$ -direction is performed resulting in one unique value of  $c_1$ . And then simply by looking at Figure 4:3, the

cover solution can only be in a certain interval. If  $c_1$  is found to be equal to 65 after performing a scan, for example, a direct horizontal line at the value of 65 cuts the database in Figure 4:4 for all the diameter lines and states that the target has a depth or base media cover between  $c = 45$  mm and  $c = 85$  mm.

The base media covering the target is assumed to be clean concrete or even air, which means that it has no effect on the electromagnetic field in this example. Finding this cover interval is the first step in the estimation processes because it helps in narrowing the possible solutions. Additional techniques are still needed to find one unique value of  $d$  and one value of  $c$  by just performing this same one scan only once. It is also important to mention that the location,  $x=0$ , is directly determined by the maximum value of  $f$  along the scan. That is an easy process because the maximum always occurs at  $x=0$  for single targets and so the focus should be on finding the exact value of the two unknowns ( $d$  and  $c$ ) so that the inverse problem is complete.

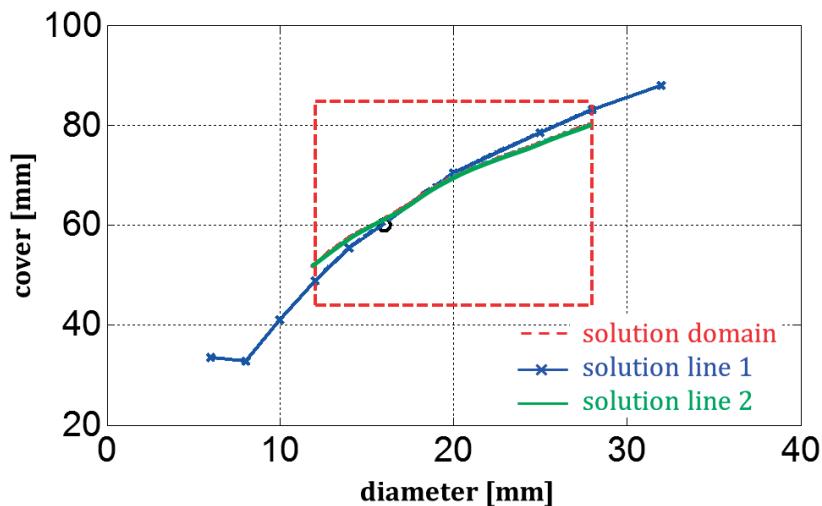


Figure 4:5 Solution domain bound by the red dashed box by  $c_1$ . The *line solution 1* is found from known  $f$  values. The *line solution 2* is found from parametrized decay estimation. The sensor used is DESIGN III (Appendix E).

As explained so far, when a scan is performed, then a direct calculation of  $f$  should be first done for every point in the  $x$ -direction, which is the scan direction. The parameter  $c_1$  is extracted leading to a cover interval solution. Immediately the  $x=0$  location is known, which is exactly the target transverse location. The value of  $f$  by itself delivers more than one unique solution, if a line is cut in the 2D table of Figure 4:2. It cuts horizontally the cover lines. Taking the value of  $f$  at the location  $x = 0$  and searching for solutions in Figure 4:2, yields a set of solution points ( $d, c$ ). These can be plotted in a cover versus diameter graph as a line of points (see the blue line in Figure 4:5). Every point on the line is a potential solution. This blue line (*solution line 1*) was extracted from the matching of the measured  $f$  to the lookup table of  $f$ . The red dashed box then would be the one limited by the cover interval found by  $c_1$ . Therefore, the equivalent solution set is successfully



reduced to all points on the line but lying within the box and not outside it. These potential points can be either  $[d = 12 \text{ mm}, c = 45 \text{ mm}]$ ,  $[d = 28 \text{ mm}, c = 85 \text{ mm}]$ , or any point on the line between them. For such a strength of a signal it is logical to have several solutions because the response of a small diameter and low cover is nearly equivalent to the one of a large diameter and high cover (deep target).

Relying only on techniques that depend on signal strength is not enough. The value of  $f$  can be equivalent to more than one combination of  $c$  and  $d$ , which are found out to be any of the six  $(d, c)$  solution points plotted as a blue marked line in Figure 4:5 within the red box. For every chosen diameter  $d$  there is an equivalent cover  $c$ . Therefore, an additional fast estimator is needed to explicitly find the diameter and, thus, the cover can be known. The function  $f$  versus  $x$ , when normalized about  $x = 0$ , makes a clear distinguished tendency for diameters rather than covers. It is also symmetric about  $x = 0$  and therefore one can average the response corresponding to the positive and negative values of  $x$  and plot the normalized values for only the negative  $x$ -values as in Figure 4:6. This has to be done for the measured single response (marked “+” dashed blue line) and the six found solution responses from the database corresponding to the points found in Figure 4:5. In this example the six possibilities of  $(d, c)$  are  $(6, 41)$ ,  $(8, 48)$ ,  $(10, 55)$ ,  $(16, 61)$ ,  $(20, 70)$ ,  $(26, 78)$ , and  $(28, 83)$ ; their normalized  $f$  responses taken from the database are plotted as solid lines in Figure 4:5.

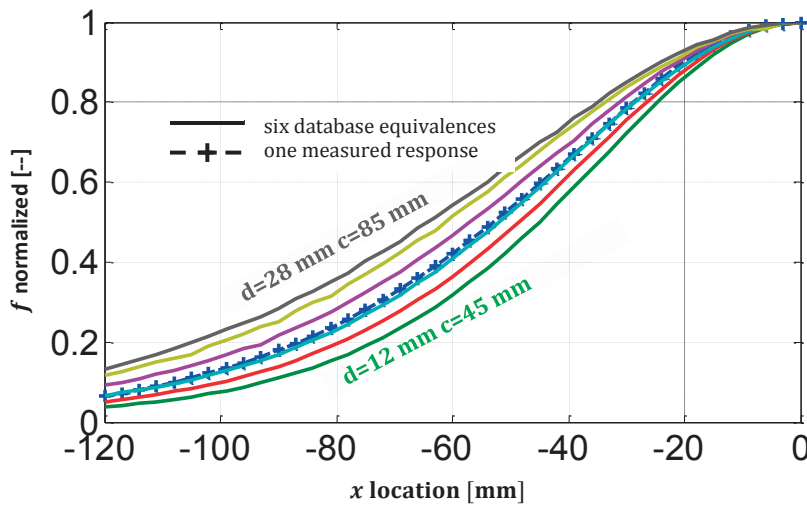


Figure 4:6 All possible  $f$  database equivalences (solid lines corresponding to six different  $(d, c)$  possible solutions) and plotted against the  $x$ -direction (symmetry averaged and normalized), the marked dashed line is the measured response. The sensor used is DESIGN III (Appendix E).

Relying on one value of  $f$  (at  $x=0$  for example) can have many solutions but a scan response can determine the diameter directly by executing the following procedure:

Out of the six possible solutions that are plotted in Figure 4:6 by finding their equivalence from the saved database, the measured response matches obviously the third database

response (16, 61) and the program when scripted using equations (4.1) can directly give the nearest solution or even perform an interpolation to find a nonstandard target. Even by observation the solution for diameter and cover are explicitly  $d=16$  mm and  $c=61$  mm, which is correct because the measured signal was exactly the response of [16, 60].

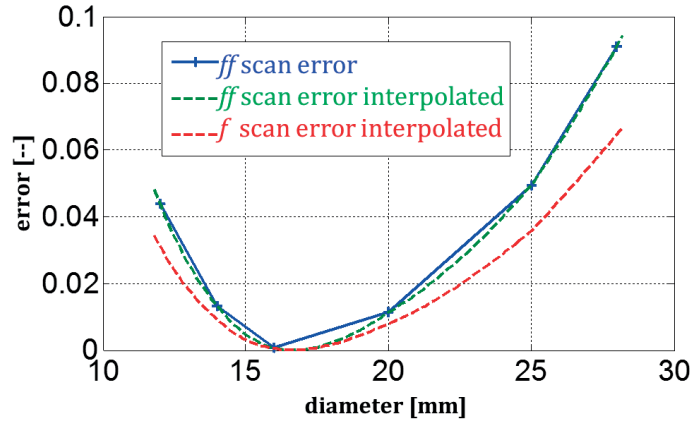


Figure 4:7 Error evaluated between the measured response and the six suggested responses by the database; the letter  $ff$  in the legend refers to normalized  $f$ . The sensor used is DESIGN III (Appendix E).

An error of 1 mm in cover should be discussed later due to specifications of the device and fast scripting implementation with limited electronics on real industrialized sensors.

$$SSE = \sum_{i=1}^6 ((f_{measured} - f_i))^2$$

$$SST = \sum_{x=-120}^{x=0} (f_{measured} - average(f_{measured}))^2 \quad (4.1)$$

$$f_{error} = \frac{SSE}{SST}$$

But to finalize this method, the error formula defined in (4.1) can be applied to all proposed solutions or even an interpolation of these solutions to find the global minimum error that represents the solution of the inverse problem. The error statement in (4.1) is plotted in Figure 4:7 for the six possible solutions and always shows a curve of a global minimum, either for a fitted spline between the specified database diameters, or the interpolated one, or even the error on a non-normalized  $f$ . They all lead to the suggestion of one unique diameter, 16 mm, and the corresponding cover of 61 mm. The same task should be done for all signals that are measured assuming that the target is unknown, and then predicting the target unknown features with a certain error in diameter and cover.

Every device should be calibrated first against air signals. That means that a signal in the air (without target) is measured and then it is subtracted from the measured signal to get a pure target response. This should be done for the measured signal as well as for the stored database responses. In addition to that it is important that the measured signal should be compatible to the database signal.

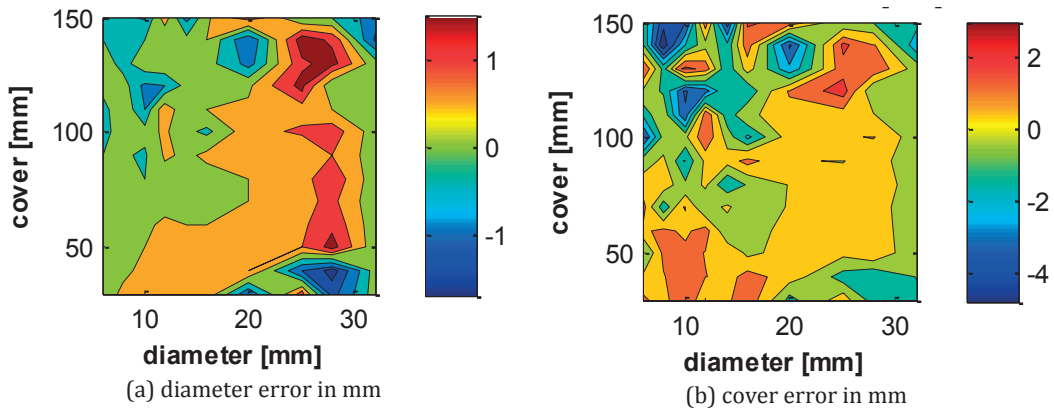


Figure 4:8 The corresponding errors in a) diameter and b) cover using only one receiver  $R1$ , the targets investigated are between 6 mm and 32 mm in diameter placed up to 150 mm away from the sensor. The estimation of  $d$  and  $c$  features is based on real experiments. The sensor used is DESIGN III (Appendix E).

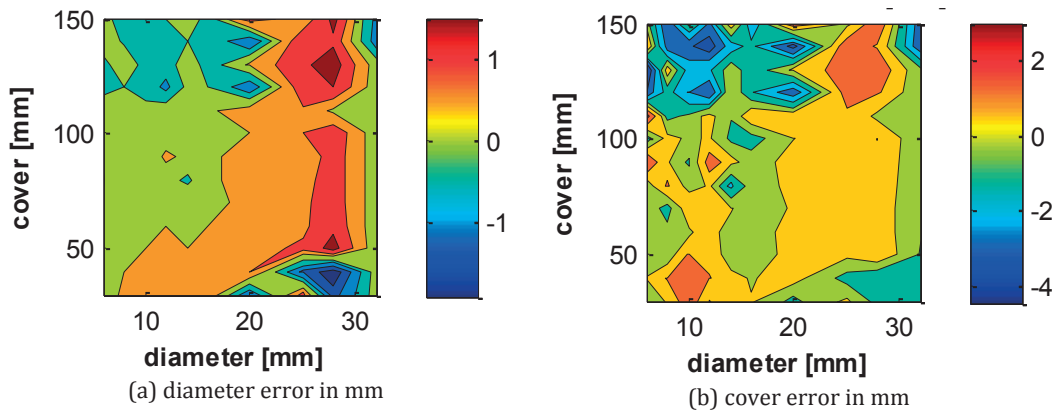


Figure 4:9 The corresponding errors in a) diameter and b) cover using the average of responses of all five receivers  $R1-R5$ , the targets investigated are between 6 mm and 32 mm in diameter placed up to 150 mm away from the sensor. The estimation of  $d$  and  $c$  features is based on real experiments. The sensor used is DESIGN III (Appendix E).

Consistency between the database and the measured responses is important. If the database tables and responses are based on induced voltages from one receiver ( $R1$  for example), then only responses from this receiver are post-processed to have an estimation.

For better performance, it is also possible to average the responses of all the five receivers and build a database accordingly. It is then required from the measured scan procedure to average the responses as well.

In the two cases, of using only receiver R1 (Figure 4:8) or using all receivers (Figure 4:9), the results are similar and acceptable. For all ranges of diameters, the error in diameter estimation does not exceed 1 mm in absolute value. The maximum diameter error happens for the large diameters and this is reasonable. As for the cover estimation, the error can be up to 4 mm less than the reality mainly for the deep covers of 130 mm to 150mm.

In this fast post-processing method, the error is within the specification and can be implemented to be industrialized especially that it is based on real hardware and experimental results. An extended estimator with additional advantages is described in subsection 4.1.2 that leads to material discrimination in subsection 4.1.3.

#### 4.1.2 Inverse problem by decay parametrization

In the real industrial applications, the user of such detection sensors can make several scans and save the results allowing the user to use them on a separate computer. Professional and precise post-processing software can be used and perform estimations that require more computational time to process. The method proposed here needs more calculation effort but has more advantages concerning accuracy and is more feature effective. It is also less dependent on just signal strength because it extracts parameters on the voltage decay that are physically meaningful concerning diameter size. These parameters are also classifying the material of the target as described in subsection 4.1.3.

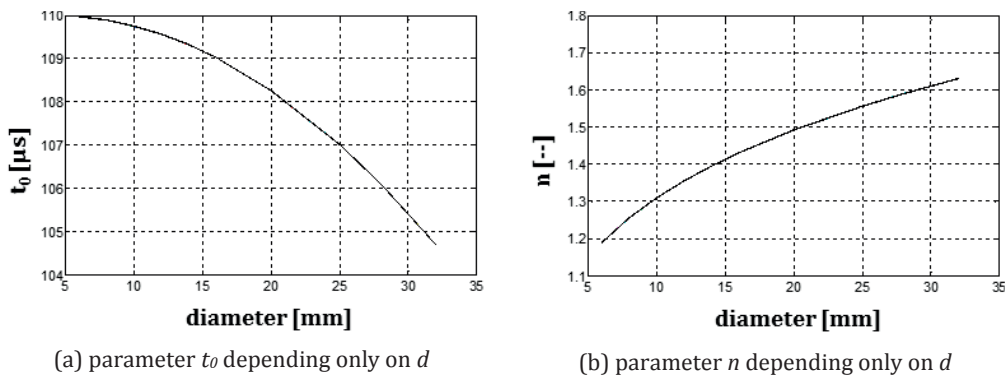


Figure 4:10 The two parameters of the experimental voltage fit depending only on the diameter of steel cylindrical targets. The sensor used is DESIGN III (Appendix E).

Temperature and environmental conditions can have a big effect on the signal strength and since the previous fast estimating method relies on the height of the signal it can be less precise. The previous method is still regulated if the complete decay suddenly shifts in height due to temperature change because it is calibrated before measurement. So the

shift is always subtracted. And the idea of the function  $f(d, c, x) = A_1 - A_2$  made the response nearly linear with the diameter size in the logarithmic scale but if a change in the temperature happens after calibration then it can be a disadvantage. For that reason, the method proposed in the current sub-section requires more time but focuses on decay tendencies rather than decay heights. It was also proven that calibration can be omitted in this decay parametrizing method due to the parameter  $a_0$  that considers the shift due to environmental effects and measurement errors.

The following method starts by fitting (2.7) for every voltage decay that is measured as plotted in Figure 2:22 and extracting the parameters  $a$ ,  $t_0$ ,  $n$ , and  $a_0$  for all database tests and later for the measured signals doing the same as done for the fast estimator method in the previous subsection. The previous design in Figure 4:1 is used here as well together with all the saved voltage responses. The micro controller in the sensor starts by defining the allowed space by doing the same as sketched in Figure 4:5. The next step is to parametrize the measured decays and start the inverse problem based on already saved databases for such parameters. The database can be different from a sensor design to another, and that's why when a sensor is designed and manufactured, a complete database should be performed but only once and for all. The parameters  $t_0$  and  $n$  are only diameter dependent for this design. No matter how far the target is from the sensor, every voltage relationship in time is following (2.7) where two out of four unknowns are diameter dependent only. This make the inverse problem easier.

The two main parameters of the decay fit are physically representing the tendency of the decay and are dependent on the diameter size only. This is represented in Figure 4:10 and equation (4.2) for DESIGN III (Appendix E). The parameter  $t_0$  can be evaluated for the specified diameter range. A lowest diameter value of about 4 mm is allowed just because the smaller diameters dissipate the magnetic field at later times than the larger targets so the upper limit of  $t_0$  would be the switch off time of the pulse (110  $\mu$ s in this case). With such constraints, the strength of the signal can be represented by the parameter  $a+a_0$  as described in sub-section 2.4.2. A similar procedure is done here for DESIGN III (Appendix E) and a database can be generated starting by the parameter  $a$ , which depends on both diameter and cover and is plotted in logarithmic scale in Figure 4:11.

$$t_0 = -\frac{6.72(d - 3.92)^2}{1000} + 110 \quad (4.2)$$

$$n = 0.85d^{0.188}$$

Additional redundant 2D lookup tables can be created based on the parameters of the decay fit. The parameter  $a$  plotted in Figure 4:11 is shown for  $x=0$  where the strength of the signals is maximum. The physical meaning of this parameter as discussed in section 2.4.2 is the virtual peak voltage of the receiver at a virtual time  $t_0$  that occurs before switch off time. Virtual here means that the decay is virtually extrapolated backward in time assuming that it starts at a voltage peak of  $a+a_0$  at time  $t_0$  then this would be equivalent to an amount of induced voltage generated by the target even before switch off

time. Measurements start at a later time ( $7\mu\text{s}$  after switch off time as mentioned before) that is why it is an assumed virtual quantity that has a physical quantity equivalence.

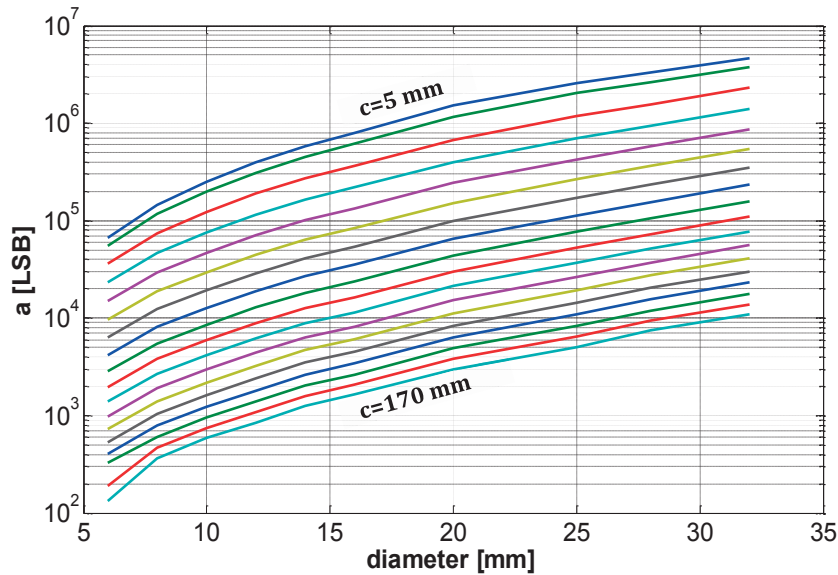


Figure 4:11 The parameter  $a$  of the fitted equation representing the intensity of the signal. The sensor used is DESIGN III (Appendix E).

This 2D lookup table (Figure 4:11) is well differentiating between every value of the cover value,  $c$ . Every line (plotted versus diameter) corresponds to a cover value. Again, following the same technique in evaluating the solutions by using the  $f$  lookup table in the previous sub-section, the same is to be done by using the  $a$  lookup table instead. This can be also done by using a lookup for the multiplication of  $a$  and  $n$ . The result is again a lookup table like the one of  $a$ . The product  $n \times a$  or simply  $na$  has a physical meaning here as well. Taking the time derivative of the voltage fit (2.7) and evaluating this derivative at  $t=t_0$  leads to the value  $na$ . It represents the rate of decay at the earliest stage of the constructed decay signal and it is dependent on both diameter and cover. By referring to Figure 4:5, the marked blue curve (*solution line 1*) in that figure represents the possible solutions extracted from the lookup table of  $f$  (Figure 4:2). But when cover values of these six diameter values are derived from the lookup table of parameter  $a$  (Figure 4:11) then the result for that example is the green dashed curve (*solution line 2*) in Figure 4:5 that intersects the blue one (*solution line 1*). The intersection point is the solution of the problem. It gives a clear one solution ( $d, c$ ). When applying this to all 180-possible diameter and cover combinations it was realized that in some cases this may not lead to a unique solution especially at weak signals. The solution for that is discussed in the coming text and by that a robust stable result is achieved and is described by a relationship between the decays and diameters and again independent of the cover. The discovery here made a great leap in the effectivity of the inverse method. It also reduced iterative time, and mainly avoided any trial and error tasks. The post-processing quantity is given

a symbol  $t_{drop}$  which represents a time quantity. It can be described as a time delay or a time constant. It is the time needed for the induced voltage to drop to zero only if this voltage has a fixed rate of  $na$ .

$$t_{drop} = \frac{U_A - U_C}{na} \quad (4.3)$$

Going back to the classical post-processing way of the induced voltage signal in Figure 2:15, the term  $U_A - U_C$  is effective as a 2D lookup table when used solely because it does not show a clear differentiation between deep cover responses even in the logarithmic scale. But when this term is divided by  $na$ , which is a voltage time derivative, it would lead to a time quantity,  $t_{drop}$ , represented in (4.3) and is dependent only on the target diameter regardless how far away the object is from the sensor as seen in Figure 4:12.

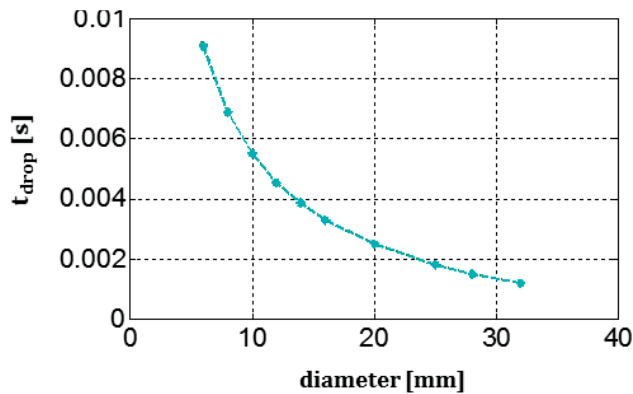


Figure 4:12 The time quantity  $t_{drop}$  depending only on the target diameter regardless of the cover value. The sensor used is DESIGN III (Appendix E).

The post-processing parameter should be extracted from the measured signal especially at the maximum response in the scan direction, which would be  $x=0$ . The importance of this quantity  $t_{drop}$  is that it is not affected by the x-position much. Its value is only dependent on the diameter and for that reason many decay signals along the scan are used to evaluate it. When compared to the relationship plotted in Figure 4:12 it gives a nearest estimate of the target diameter and closes the loop. The small diameters need longer time to dissipate, even though their response would have less intensity but the rate ( $na$ ) – rate of decay of the voltage in time at time  $t_0$  – is relatively lower for such small sizes, which makes the time delay higher.

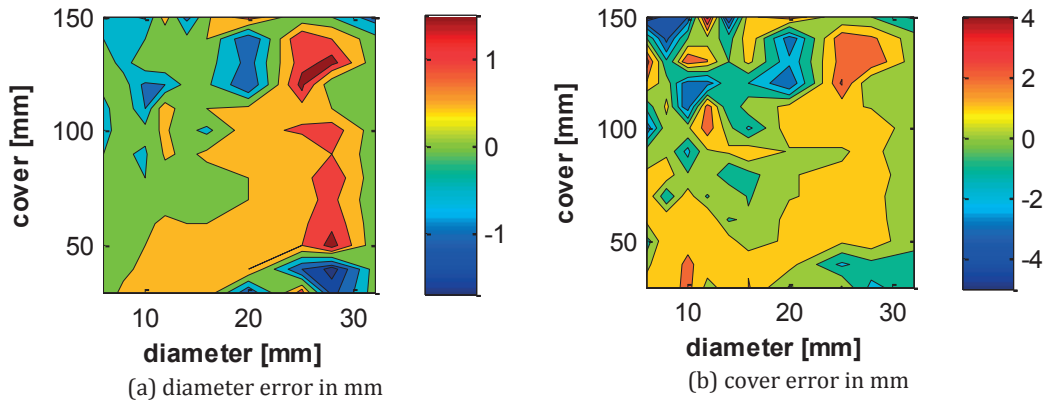


Figure 4:13 The corresponding errors in a) diameter and b) cover using only one receiver  $R1$ , the targets investigated are between 6 mm and 32 mm in diameter placed up to 150 mm away from the sensor. The sensor used is DESIGN III (Appendix E).

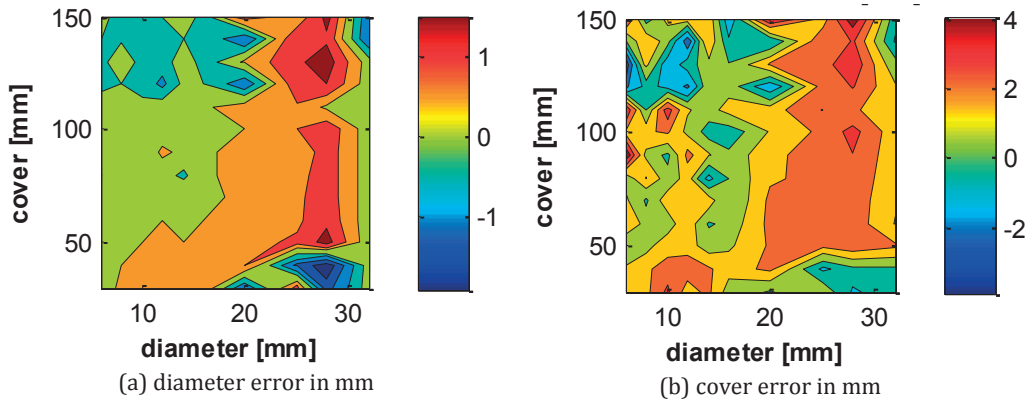


Figure 4:14 The corresponding errors in a) diameter and b) cover using the average of responses of all five receivers  $R1-R5$ , the targets investigated are between 6 mm and 32 mm in diameter placed up to 150 mm away from the sensor. The sensor used is DESIGN III (Appendix E).

The application of the *decay parametrization* method is more effective in size discrimination. It is not based mainly on amplitudes. It is also effective when the signal contains noise because extracting the parameters  $n$  and  $t_0$  are showing signal tendencies rather than signal strength. The extraction of parameters that only depend on the diameter is a huge advantage in discrimination. It reduces the iteration effort in material discrimination as described in sub-section 4.1.3. Such parameters are  $t_0$ ,  $n$ , and  $t_{drop}$ . These parameters are not affected by the distance to the target: even the  $x$  position does not affect the responses (up to about 60 mm range in the  $x$ -direction). This is another clear advantage since they are not dependent on the scan location. In the case of robustness, the first method (*fast estimator*), based on  $f(d, c, x) = A_1 - A_2$  (see sub-section 4.1.1), is more robust for cover estimation because it uses many signals in the scan direction. Therefore, a failure in one would still have less error in the estimation rather than relying only on one signal.



The combination of both methods: '*fast estimator*' and '*decay parametrization*' can provide a discrimination method having all advantages of both methods. This combination is tested for estimating the 180 variations using the same sensor as previously (DESIGN III (Appendix E)). The results are shown in Figure 4:13 (using *R1* only) and Figure 4:14 (using the average of *R1* to *R5*). These results are slightly improved compared to using only the '*fast estimator*'. They require more computation time but this method is needed in material discrimination based on pulse induction as detailed in the next sub-section due to the feature dependent parameters rather than amplitude dependencies. It is also more effective for weak signals and noise dominant ones and does not require device calibration. Both estimators are new to the pulse induction detection device industry. They are recommended for getting high quality using less complicated coil design of these scanners.

#### 4.1.3 Material discrimination by pulse induction

The application of pulse induction method in this section has proven its effectivity for ferromagnetic targets like steel. Applying it to purely conductive metals like copper and aluminum with no modifications would be difficult and misleading. The reason behind that is the limitation of the frequency in the excitation scheme. A pulsed current in the sender already contains limited and relatively high frequencies and allows no flexibility for frequency manipulation. As discussed in the 'feature discrimination' section 2.1, the dissipation of eddy currents in the target space is dependent on a combination of frequency and material properties and for that reason flexibility in the excitation frequency provides better information about the material when the target size is known. That is why the skin depth in (2.1) is a spatial parameter that is affected by the excitations frequency and material properties together. A smart design for material discrimination requires frequency selections and an effective post-processing method accordingly. But due to the physical limitation of the pulse, it would be considered not effective. Nevertheless, the feature dependent parameters described in the previous sub-sections allowed a simplification in this sense. The parameters  $t_0$  and  $n$  already are correlated to steel diameters and the same can be done for copper diameters. This new idea of decay parametrization can distinguish, even by the same usual pulse induction scheme, between copper and steel targets for example. In the end of any design, after the geometry is finalized and specifications are fixed, a set of scans for all diameters and covers has to be performed. The parametrization leads to relations and databases that represent the system. So for a new design, the parameters,  $t_0$ , and  $n$  would be surely different according to a new geometry of the sensor or a new pulse excitation scheme. The design in Figure 2:14 was experimented by real hardware and all decays were extracted and plotted in Figure 2:13. The parameter  $t_0$ , and  $n$  were found out to be the ones in Figure 2:23 with some more tolerance allowed for  $n$ . They are in the form of the ones in (2.12) and (2.13). The resulted parameter  $a$  from these experiments was a 2D lookup table plotted in Figure 2:24 with a corresponding  $na$  table in Figure 2:25. For the sake of investigating this design for copper rods, it was convenient to simulate it using the "dipole model" that is described in Chapter 3 (section 3.2) under steel targets as well as copper targets. Every-

thing should be performed exactly as done in the experiment. The simulation of the voltage decay should fit to the parametrized equation (2.7) for the following range of diameters and cover as:

- $d = 6, 8, 10, 12, 14, 16, 20, 25,$  and  $28$  mm
- $c = 5$  mm to  $150$  mm, measured every  $5$  mm

Based on the simulation of the sensor and the steel targets of different diameters and covers the parameters were extracted and represented in equation (4.4) where  $t_0$  is diameter dependent and  $n$  follows a diameter relationship but can have a tolerance. These parameters based on simulation results are plotted in Figure 4:15 and are matching well with the experimental results of Figure 2:23. The same simulation model can be used to check the case of copper targets. The difference between simulated steel and simulated copper parameter in this case can be observed by comparing Figure 4:15 to Figure 4:16 respectively. The parameters  $t_0$  and  $n$  for copper are linear with the diameter of the target and are independent completely from the cover. These parameters classify the material constitution and this step is a huge leap in material discrimination by pulse induction techniques.

$$t_0 = -\frac{11(d-2)^2}{1000} + 80 \quad (4.4)$$

$$n = 0.602d^{0.2928} \pm 0.1$$

The parameter  $a$ , in cases of the simulated steel and copper targets, is as expected, a 2D lookup table representing the strength of the voltage signal. It shows the same tendency between steel and copper. On the other hand, copper rods have responses that their two main fitting parameters ( $t_0$  and  $n$ ) make a big difference in tendency and value concerning their relationship to target size.

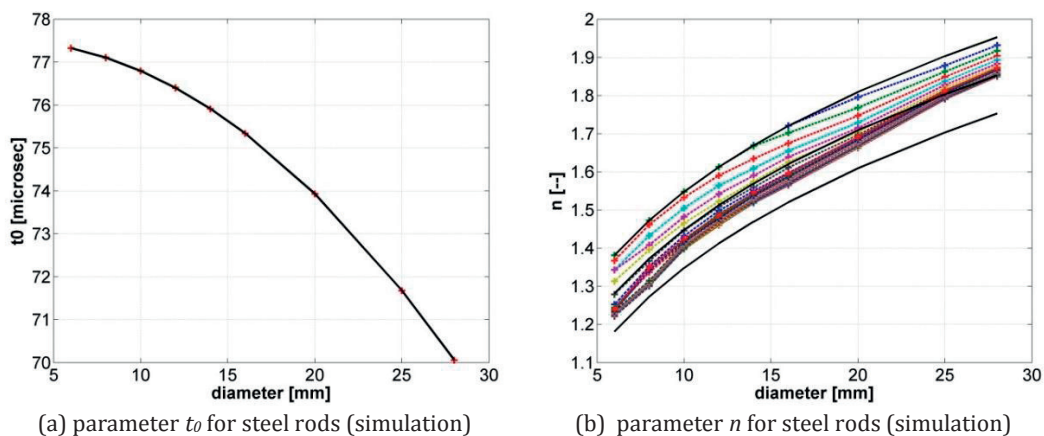


Figure 4:15 The two parameters,  $t_0$ , and  $n$  extracted from the simulation results of the voltage induced by steel cylindrical targets.

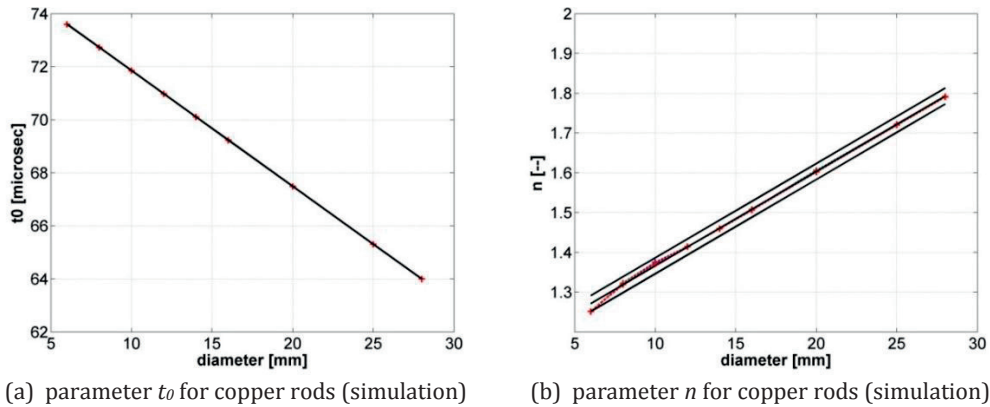


Figure 4:16 The two parameters,  $t_0$ , and  $n$  extracted from the simulation results of the voltage induced by copper cylindrical targets.

The discrimination of copper rods is an inverse model like the one for steel. If the device is programmed to detect either steel or copper and should do that automatically then the decay fitting parameters for the selected diameters proposes cover values also based on  $na$  lookup tables. This must be done for both copper and steel lookup tables. The least error in fitting should be included to help indicating the final solution.

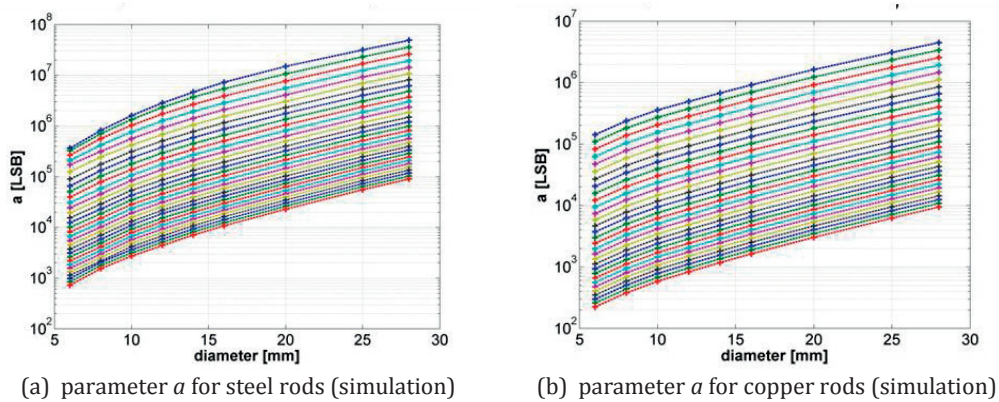


Figure 4:17 The 2D lookup table of the parameter  $a$  differs in value between a) steel and b) copper based on simulated results.

The parameter  $t_{drop}$  has also a role in localizing the diameter of the target. As mentioned in sub-section 4.1.2, the size and material features influence these main parameters.

Building up an inverse model to discriminate materials is now possible but requires more iteration due to the increase in the number of unknowns. Nevertheless, this finding is a good contribution to the pulse induction method and can be used for material detection of nonmagnetic metals. But the idea of distinctively detect copper and steel for ex-

ample, placed in the same place hidden underground would require more effort in frequency manipulation and by that this method reaches its limits. Harmonic excitation, on the other hand, allows this frequency planned excitation schemes and delivers results both in simulation and experiments.

## 4.2 Harmonic induction

Using harmonic excitation signals in detection devices allows the flexibility needed to code the induced signals that can be de-coded in the signal processing phase. Pulse induction has limitations in the frequency range and thus the electronics limit target material discrimination. As described in Chapter 2, the material properties, together with the frequency, influence the eddy current skin depth in the target of a certain size. One induced voltage signal contains all these effects. This combines material, size, and frequency. An electromagnetic detection system is not just an arbitrary collection of sender coils and receiver coils. One of the main aims of this work is to show that detection devices are designed according to the features to be discriminated and this would be lost in trial and error unless there is a focus on the complete chain of excitation scheme (section 2.2), coil design (section 2.3), and post-processing methods (section 2.4). These main fields of sensor development are introduced in Chapter 2. On the other hand, harmonic excitation schemes have disadvantages in electric power, efficiency, and strength. Mainly deep targets require high excitation currents. The best design choice requires an optimum performance versus requirements and that is an important goal of this work.

Many detection devices or non-destructive testing devices also known as electromagnetic induction (EMI) sensors are used to sense metallic objects buried or hidden in a base media as introduced in Chapter 1. It is important before designing any EMI sensor to set ahead its requirements (section 2.1). These requirements are classified as detected features (e.g. target, size, and location) within a defined resolution and must be known ahead of the design phase. According to these requirements the designer can then define the geometry of the coils, the excitation scheme, and the post-processing method. Some applications just need to detect the transverse location of the targeted objects. Many industries exploit the EMI capability to the maximum, heading towards precise feature discrimination (see feature discrimination in section 2.1). The work here insists that EMI sensors are designed, optimized and developed according to the features of the objects or targets that need to be detected. The sensor is designed differently (according to the workflow of Figure 1:4) if one feature is considered the main priority and others are not or vice versa. Concerning material discrimination, feature is not only copper and steel material discrimination but also copper-steel grouped as one target feature. Non-ferromagnetic targets, like copper, are more difficult to detected by induction at medium frequencies than permeable ones, or at least it is difficult to rely only on EMI to discriminate features of non-magnetic metals. As mentioned in section 1.2, many applications aim to detect features in a single material (find voids or cracks). Others can discriminate composed targets that are required to be placed between the sender and receiver. This does

not apply to hidden or buried targets. In addition to that, designing a sensor by EMI technology to discriminate these features of non-magnetic material especially in the presence of other magnetic material is a very challenging task when EMI solely. EMI is easy and cheap compared to other detection techniques like ultrasonic, radar, and thermography as described in the 'State-of-the-art' section 1.2. It is considered novel to be able to use one sensor at the same time based only on EMI for discriminating target features of only non-magnetic (copper rod), or only magnetic (steel rod), or a complex target i.e. both present in the same place (copper and steel rods grouped together) under challenging conditions of manufacturing tolerance, environmental conditions, and buried hidden target locations where the sensor cannot reach the targeted object physically. In addition to all of that, to be able to discriminate size, location, and depth of such targets is considered a complete functional discriminator and distinctive detection sensor at the same time.

The feature referred to here as 'complex target' is an additional challenge due to discriminating it (copper rod grouped together with a steel rod) from a copper rod or a steel rod. This is not material discrimination only; it is rather more complex. Such complex target features are numerous and challenging in the real industrial applications. The current work can be extended and used as a basis for additional discrimination of complex target features like cables inside metal pipes, stainless steel near reinforcing rods in bridges, electric copper cables near ferromagnetic objects, metallic plates, or even corroded steel. Such complex objects have always been an engineering challenge in the manufacturing of nondestructive testing devices. The common challenges, in addition to the complexity mentioned above, are spotted in the published paper [74] and journal [82] as well as the claimed patents [23], [24]. One challenge is to minimize the dominance of the sender coil on the receiver coil as briefly explained in section 2.3 where a suggestion to calibrate the receiver relative the sender was first mentioned as a solution. The second challenge is the induction of nearby targets, which was analyzed experimentally and simulated for same material (steel) double rods in section 3.3 and published in [22]. It was shown that smart selection of frequencies can eliminate coupled effects of nearby targets or at least cancel their effect on induced voltages in the receivers. In addition to that, since the target is hidden, it makes the design more challenging because the sender and receiver coils have to be placed on the same side, i.e. the receiver has to be placed close to the target to get its maximum response. As mentioned in section 1.2 many detection devices for many applications are stated and referenced ([53], [37], [17], [40], [54], [6], [35], [36], [55], [13], [56], [57], [58]) but none of them tackled the distinctive detection of multiple material hidden target using induction only as a physical method. For that reason, creative ways need to be implemented in order to achieve the discrimination of these specified complex and simple target features in the same device at the same time.

An example of one of the complex object discrimination (mainly a double material target from single material ones) is presented in an example in this chapter. This example is simulated and experimentally validated showing the use of the 'spatial phase profile' method. This simulation model (dipolar model detailed in section 3.2) is the main tool to verify this discrimination for a range of target sizes and depth. The next section describes

this extension of the dipolar model and its effectiveness in reaching a geometrically calibrated sensor for the feature discrimination set ahead. As for the size and depth discrimination, a set of database using all the receiver coils' amplitudes in different modes to estimate the target diameters and depth is described in the inverse model section in order to complete a functional sensor and prove the validity under all variations of size and depth.

#### 4.2.1 Design methodology

The geometrical design of the coil configuration of an EMI detector suitable for material discrimination can be developed using a dipolar approximation of the targets (see section 3.2). This approach is valid, as long as the targets and coils are sufficiently separated from each other. In the dipolar approximation, the induced voltage  $U_{ind}$  in the receiver coil at a radial frequency  $\omega$  was written in (3.15) and is rewritten in the matrix form in (4.5) as a tensor product of the magnetic polarizability tensor  $\chi$  with  $\vec{H}_{TX}$  and  $\vec{H}_{RX}$ , the magnetic field intensity of the transmitter (TX) and the receiver (RX) at the dipole position [13], [38]. The scalar,  $I$ , is the transmitter current,  $R$  is a rotation matrix,  $A$  is a constant that considers the gain transfer function of the amplifiers, and  $\mu_0$  is the magnetic flux constant.

$$U_{ind}(\omega) = A \cdot \frac{i\omega\mu_0}{I} \vec{H}_{RX}^T \cdot [R \chi(\omega) R^T] \cdot \vec{H}_{TX} \quad (4.5)$$

Exact magnetic axial  $\chi_{||}$  and transverse polarizabilities  $\chi_{\perp}$  are available for simple shapes in frequency domain [76] for a homogenous or for a dipolar primary excitation field. Both are written in equations (3.17) and (3.18) respectively. It is first important to highlight again the induction number  $k = \sqrt{-i\sigma\mu\omega}$  that is part of  $\gamma = ka$  to be solved for using the Bessel function as mentioned in section 3.2. The axial and transverse polarizabilities are the diagonal components of the polarizability tensor. They are complex functions of this single parameter  $\gamma = ka$  that contains all relevant material properties for discrimination. In the actual case, the realistic targets are cylinders of *finite* length that are modelled in this work using a linear chain of infinitely small dipoles as described in the publication [22]. This approach has many assumptions, but it gives sufficiently good results if the effect of the finiteness of the cylindrical segments has been taken into account by the demagnetization factor of the finite cylinder itself [22]. Further assumption here is that the primary excitation field is homogeneous at the position of this cylindrical element so that the calculated polarizabilities in a homogeneous excitation field can be used. The rotation matrix  $R$  projects the field to the local transverse and axial coordinate system of the cylindrical element. The model gives accurate amplitude and phase information for long ferromagnetic and non-ferromagnetic conductive cylindrical targets or pipes that are separated sufficiently away from the TX and RX coils. As soon as the diameter of the target is smaller than the radius  $r_0$  of the smaller coil of a coil configuration TX-RX and the distance of the target to the coil is larger than this radius  $r_0$ , the predicted induced voltage of the model is within a small error to measurements. It can therefore be used

for the optimum coil design for given performance parameters such as separation performance (i.e. discrimination of two close lying separate objects), material discrimination, and detection range for targets that are not too close to the coils.

The transmitter and receiver fields  $\vec{H}_{TX}$  and  $\vec{H}_{RX}$  are strongly depth and orientation dependent. For a robust estimation of the parameter  $ka$  and for target discrimination, it makes sense to get rid of the orientation and depth dependence of  $U_{ind}$  in (4.5). For a *single* target, this can be achieved by either one of the following ways:

- Frequency domain, by measuring the phase shift of the induced voltage  $U_{ind}(\omega)$  relative to the excitation current  $I$  as function of frequency  $\omega$ , which is proportional to the quotient of imaginary and real part of the polarizability and almost independent on the signal strength
- Time domain, by evaluation of the time decay of the induced voltage  $U_{ind}(t)$  when using pulse induction. Fitting a second order polynomial  $p(t) = a_1 t^2 + a_2 t + a_3$  to the normalized logarithm of the induced voltage  $\ln [U(t)/U_0]$  delivers parameters  $a_1, a_2$  and  $a_3$  that allow discrimination between a *single* ferromagnetic and non-magnetic target as well as between pipes and full cylinders.

However, if there are *multiple* different close-lying targets to be discriminated, the situation becomes more complex and experimentally expensive. For this case, the dipolar model is a sufficiently accurate approximation to design the sensor coils, to develop a classification algorithm, and to test the limits of what is possible. In the current section, three different target cases using the dipolar model and validation experiments: steel, copper, and both together are analyzed.

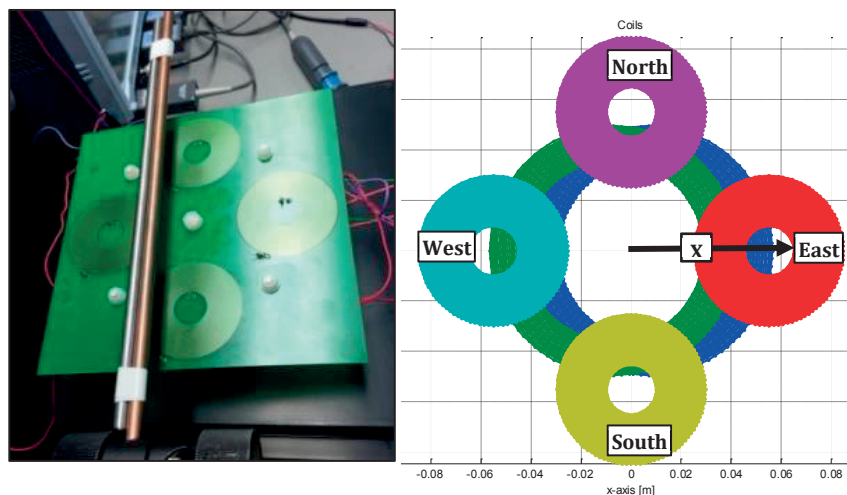


Figure 4:18 The four receivers placed relative to two senders as an outcome of an optimized sensor named DESIGN IV (Appendix F).

As already mentioned in section 3.3, it was evident that nearby rods of steel, for example, are decoupled at a frequency around 25 kHz regardless of depth, separation, and diameter of the targets. The current work makes use of that to distinguish copper from steel and from copper-steel combinations since the copper material-frequency combination is much different than steel ones. Detection sensors based on the phase shift of signals rather than on amplitudes are not new in literature. Phase shift plots over a frequency range for copper, aluminum, and steel were documented in [48]. The phase angle plots in [46] are also showing differences between steel inclusions in copper rods or vice versa. The value of the phase angle or the tangent operator of this angle was used to show some differences in the inclusion size. In the current work, the '*spatial phase profile*' rather than the phase value is being used as a material flag because a combined target (copper-steel) configuration is required to be distinguished from single material response. In addition to that, many scientists and engineers have already published frequency spectrum responses, as in [48] for example, to show material differences. In the current work, selected frequencies are used rather than a spectrum or range. A wider overview of the state-of-the-art detection by induction ideas, designs, and publications are detailed in sub-section 1.2.1.

The new proposed concept by harmonic induction excitation is an outcome tested and simulated after combining several design methods. This design is presented in Figure 4:18 where the two sender coils printed at the bottom board and the four receiver coils printed on the top board. Transverse harmonic magnetization of the targets is used here. This configuration has the advantage, that also tilted configurations with respect to the scan direction can correctly be discriminated, whereas in the axial magnetization case, this would be difficult, because the symmetry is destroyed and every tilt angle would give different results.

The design reached in Figure 4:18 is the outcome of many parameter variations (geometrical and electrical). Dimensions and coil characteristics of this design are documented as DESIGN IV (Appendix F).

A detailed methodology is used by introducing the different design concepts logically and in steps, by first showing the cover independence ratios of transverse excitation (sub-section 4.2.2), followed by the optimization done on a simple sender-receiver mathematical model to define ratios suitable for single copper or single steel rods diameter discrimination (sub-section 4.2.3). After that, an explanation of the 'double balanced' system of coils (sub-section 4.2.4) shows the importance of the geometrical balance of coils. The '*spatial phase profile*' method (sub-section 4.2.5) shows the use of phase profiles instead of values and its effectivity in distinguished detection. After this is implemented, a set of post-processing techniques are used to reach a complete inverse problem using harmonic induction (sub-section 4.2.6). A sensor is complete only if the inverse solution is possible from all database and relationship defined. The complete set of features should be detected using a complete forward database.



### 4.2.2 Cover independence

The fields  $\vec{H}_{TX}$  and  $\vec{H}_{RX}$  in (4.5) are strongly depth and orientation dependent. For a robust estimation of the parameter  $ka$ , a depth independent estimation is required. Starting by a simplified special case as shown in Figure 4:19. The simulation model based on the dipole model is used having the sender and the receiver coils to be exactly in the same place and having the same dimensions.

The induced voltage amplitude  $U_f$  is the final result and written in equation (4.11) after deriving it from (4.5) and (3.18) for such a case and for one single target with diameter  $d$  covered by air media with a cover  $c$ .  $R_0$  represents the effective radius of the coil. The radius  $a$  of the target is replaced by  $\frac{d}{2}$  and  $k$  by the induction number  $\sqrt{-2\pi f \sigma \mu} \cdot i$ . It is important to mention that only transverse polarizability is used here because the excitation field is transverse mainly to the target as mentioned before. That is why only the transverse polarizability of cylinders is used i.e. equation (3.18).

The voltage  $U_f$  is a function of  $c$ ,  $d$ ,  $f$  as well as of the material of the target. Taking the ratio of the responses  $U_f$  of two different frequencies leads to a *cover independent* ratio because the middle term in the right-hand side of (4.11) always cancels for this ratio for any fixed target material.

For example, taking the ratio of two responses  $U_{f_1}$  and  $U_{f_2}$  corresponding to any two frequencies  $f_1$  and  $f_2$  yields to a cover independent relationship (4.7). The parameter  $c$  has been canceled from this ratio.

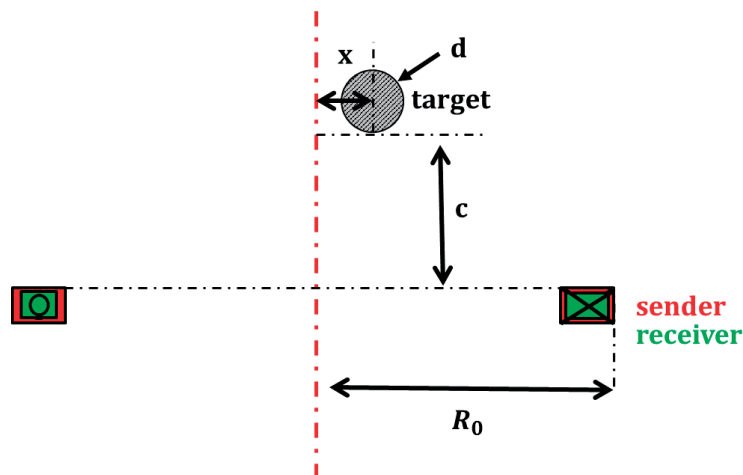


Figure 4:19 A simple sender-receiver coil is considered one coil used for sending and receiving, this is done for simple simulation concept.

$$U_f = 2\pi f \cdot \frac{\left(\frac{d}{2}\right)^2 \cdot R_0}{\left(\left(c + \frac{d}{2}\right)^2 + R_0^2\right)^{\frac{3}{2}}} \cdot \chi_{\perp} \left( \sqrt{-2\pi f \sigma \mu \cdot i} \frac{d}{2} \right) \quad (4.6)$$

$$ratio = \frac{f_1 \cdot \chi_{\perp} \left( \sqrt{-2\pi f_1 \sigma \mu \cdot i} \frac{d}{2} \right)}{f_2 \cdot \chi_{\perp} \left( \sqrt{-2\pi f_2 \sigma \mu \cdot i} \frac{d}{2} \right)} \quad (4.7)$$

Some published articles used effective ratios of transverse and axial polarizabilities because the phase shift was frequency dependent [50]. They used their work to classify target shape using a frequency spectrum. But the current work uses only a few specified frequency responses processed in dimensionless smart ratios to have the highest diameter dependency if the material is provided ahead.

#### 4.2.3 Dimensionless ratios of selective frequencies

Following the concept of cover independence ratios, of the previous sub-section, by dividing any sum of responses of different frequencies by another one, the ratio is always cover independent, i.e. the parameter  $c$  disappears. Two kinds of ratios are investigated here for single steel rods and single copper rods. The forms of the ratios  $R_1$  and  $R_2$  in (4.8) and (4.9) respectively are chosen in a way to achieve a maximum dependency on the diameter only using three different frequencies  $f_1$ ,  $f_2$ , and  $f_3$ .

$$R_1 = \frac{\ln(U_{f_3}) - \ln(U_{f_2})}{\ln(U_{f_2}) - \ln(U_{f_1})} \quad (4.8)$$

$$R_2 = \frac{U_{f_3} - U_{f_2}}{U_{f_2} - U_{f_1}} \cdot \frac{U_{f_3}}{U_{f_2}} \quad (4.9)$$

The first ratio (4.8) has a difference of the natural logarithm of responses in the numerator. This equates to the logarithm of their ratio, which is still cover independent. The same applies to the denominator and thus the whole ratio is cover independent. Similarly, the second ratio is theoretically cover independent as well. The two ratios are made so different in order to find out, which one is better for copper single rods and, which is better for steel ones. This is then extended in a practical demonstrator to also discriminate a grouped steel and copper single rods simulated and experimentally validated (see sub-section 4.2.5).

A gradient optimization is performed using the Sequential Quadratic Programming (SQP) method where the frequencies  $f_1$ ,  $f_2$ , and  $f_3$  are design variables. Starting with the ratio  $R_1$  and taking the setup in Figure 4:19, the target is a single steel rod of diameter  $d_i$ . The ratio  $R_1(d_i)$  is evaluated for every diameter,  $d_i$ , resulting in a diameter dependent response curve. The objective of the optimization is the inverse of the steepness of this response to be minimized as in (4.10). The objective (*Obj*) is a single evaluated value for the complete set of diameters  $d_1 = 10 \text{ mm}$  to  $d_n = 22 \text{ mm}$  and for every combination of

frequencies. This is the same for any cover value (since it is cover independent). The optimization starts from an initial guess of frequencies and finds out the best variation over the diameters using  $R_1$ . The optimization is calculated again from different initial guesses to assure a global optimum. The constraints are set on the frequencies to be monotonically increasing. The frequencies are bounded between 1 kHz and 75 kHz (highest frequency limit set for this coil design).

$$Obj = \left( \frac{\sum_{i=1}^n \|R_1(d_i) - \text{mean}\{R_1(d_{1 \rightarrow n})\}\|}{\text{mean}\{R_1(d_{1 \rightarrow n})\}} \right)^{-1} \quad (4.10)$$

The same optimization is performed for copper and steel separately using  $R_1$  and then  $R_2$ . It was found out that the ratio  $R_1$  is suitable for steel rods while  $R_2$  is better for copper rods. And the corresponding optimums are listed in Table 4:2. The steepest ratio over a diameter set is an objective to be maximized to get a better resolution. The lower bound was always set to 1 kHz because a minimum induction is required for both metals. In the case of copper using  $R_2$ , the optimizer was always minimizing  $f_1$  and  $f_2$ , therefore an additional constraint to separate them by 9 kHz difference was needed in order to have distinguished responses. As for steel and using  $R_1$ , the middle frequency  $f_2$  was found to be near 20 kHz, which has a significant meaning in previous work done [22]. This frequency is larger for double rods.

Table 4:2 The optimum frequencies that generate the steepest ratios.

	$f_1$	$f_2$	$f_3$
<b><math>R_1</math> (steel)</b>	1 kHz	17.62 kHz	45.78 kHz
<b><math>R_2</math> (copper)</b>	1 kHz	9.99 kHz	74.26 kHz

The analysis in this section was done for  $x=0$  (see Figure 4:19) but full discrimination requires scanning in the  $x$ -direction and double rods have to be introduced as well and this is explained in the inverse model in sub-section 4.2.6 where, as a result, the optimum frequencies differ slightly.

#### 4.2.4 Double balanced configuration

The best placement of the sender and receiver coils in a detection system is where they are concentric inside each other and both closest to the target exactly like the design in Figure 4:19. This would be ideal in case of no mutual inductance. For a high sensitivity of the sensor, a balanced coil configuration is favorable in order to eliminate or cancel this induced voltage. This however demands a high mechanical stability or active means for calibration or compensation, such as additional compensation coils or a manual calibration at the start of the measurement. As has been explained in section 2.3 a sender-receiver setup like the one in Figure 2:10 is done by taking a set of one sender and one receiver coils with the same dimensions and number of turns as in Figure 4:18 but checking the placement of the receiver radially would find a neutral position. Eliminating the induced voltage in the receiver is done by performing a displacement  $D_p$  of this receiver

relative to the sender (red coil) as in Figure 2:10. Exciting the sender with the range of frequencies up to 300 kHz results in zero induced voltage at a displacement  $D_p = 54$  mm for this example. The plots are visible in Figure 2:11. Several configurations are known in literature and on the market, especially the gradiometer [47], [51], [52] that describes balanced induction. In the current work, a novel ‘double-balanced’ coil configuration designed for material discrimination is proposed. ‘Double-balanced’ here means that every receiver is separately balanced relative to the two displaced senders. In addition to that the senders are also displaced against each other so that in some excitation modes and according to defined specifications and requirements, it also possible to balance the sender response to each other. The final ideal design for two senders and four receivers is shown in Figure 4:18. The balancing is done without the presence of targets.

The next step is to follow the same methodology but now for targets well separated from each other. When the targets are near each other, they also exhibit a mutual coupling that affects the total induced voltage in the receiver. Such coupled effects are detailed e.g. in [22], leading to the selection of frequencies in this work as a continuation. The careful selection of active frequencies allows the sensor to be effective even for nearby targets as shown in sub-section 4.2.6.

#### 4.2.5 Spatial phase profile method

The phase shift (shifted from the sender current) of a differential signal  $U_{east} - U_{west}$ , which is the subtraction of the voltage in receiver west from the one in receiver east (see Figure 4:18 for naming) can now be used to determine whether the target is a copper rod, steel rod, or both copper and steel at the same time. A simple explanation of these target cases is sketched in the respective boxes in Figure 4:20 from left to right. The ‘spatial phase profile’ for every scan in the x-direction is unique.

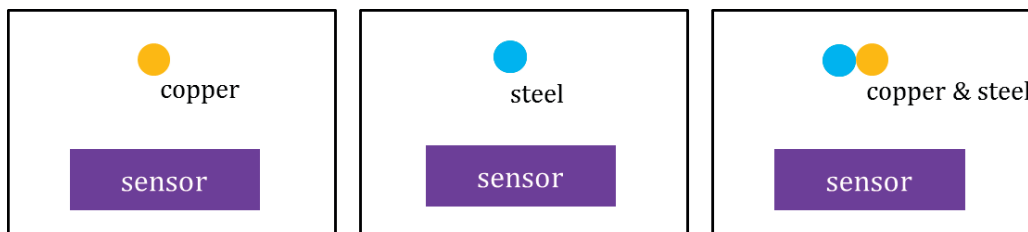


Figure 4:20 The three cases of discrimination and distinctive detection: single copper rod, single steel rod, and double copper-steel rods.

Scan means moving the sensor in the opposite  $x$  direction (east to west) or moving the target rods in the  $x$ -direction (west to east). After freezing the design, which was reached by using the dipole model and experimentally verified for several excitation frequencies and depths of targets, a 10 kHz and 20 kHz examples are being shown here for illustration. The best placement of the receivers (four distributed receivers) as in Figure 4:18 induces nearly no signals in the absence of targets. This was found using a parametric

study by varying the geometrical lengths and positions of the coils based on the method described in the previous sub-section ‘Double balanced configuration’. The two big sender coils sketched from the dipole model as seen in Figure 4:18 (right) are excited with the set of frequencies. These, blue and green sender coils when excited with a harmonic current induce voltage signals in the east and west receivers, which when subtracted should be very small in the absence of any target. This is an advantage because in the presence of any target the receivers sense induced signals mostly by target responses rather than the sender’s effect.

The measured signal is weak due to this placement. But in the presence of a target the signal is dominated by target response. Nevertheless, at  $x=0$  it is a symmetry, i.e. equal voltages are induced in the receivers and this differential signal is negligible. As a solution to this problem, discrimination relies on the spatial phase profile overcoming amplitude problems and making the system more reliable and robust.

The phase measurement relative to the source current can be extracted even out of the weakest periodic signals. Measuring the phase of the differential signal (phase angle of  $U_{east} - U_{west}$ ) at every x-location (scan direction) leads to the graphs as in Figure 4:21 a) at 10 kHz and b) at 20 kHz, for example, where all rods were 8 mm in diameter. When signals are detected due to the scan over an 8 mm copper rod, a constant response in phase is achieved over the scan in the x-direction (green simulation and experimental lines) as shown in Figure 4:21. One can also now determine that either copper is present or nothing at all because the north and south coils sense a voltage change versus the scan, which indicates the presence of a target anyway and this can be used here as a flag as well. The post processing of the north and south voltage responses is used for cover estimation as a redundant database in case of an industrialized sensor. The blue parabolic profiles are the responses of an 8 mm steel rod and the opposite parabolic red profiles determine explicitly that both copper and steel (both are 8 mm in diameter) are present. This is done using ‘east’ and ‘west’ signals. The ‘north’ and ‘south’ signals are used later for size and depth detection.

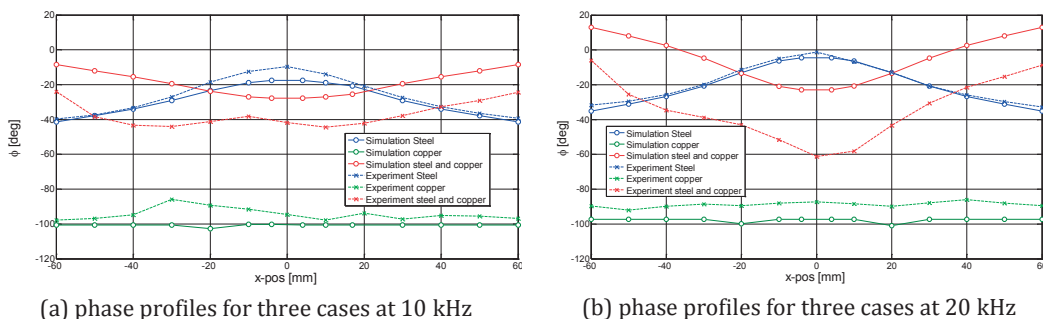


Figure 4:21 Simulation versus experiment for three cases of material discrimination using 10 kHz (left) and 20 kHz (right) sender frequencies. The response is the phase angle of the differential voltage signal relative to the sender current. The sensor used is DESIGN IV (Appendix F).

Observing the curves in Figure 4:21, the red curves (responses of copper-steel targets) do not fit well between simulation and experiments as the other curves (single copper and single steel targets). The curvature of the curves is what matters for this method and this matches well but it is worth to mention that the mutual effects between nearby rods were not considered yet in these simulations. In addition to that, the experimental measure of the phase of the signal is relying on the zero crossing of the harmonic voltage signal which contains some noise. This may make a shift to the whole phase profile positively or negatively.

In the current work, the sender coils are excited with the same frequency at the same time during an application scan this means the two senders are excited with the same signal of a certain frequency. Several frequencies are used during the scan and the corresponding responses are saved as well but at any instance in time both senders have the same frequency. Nevertheless, this design is meant to apply different frequencies on the two senders respectively for a smarter and faster detection system. This system will be presented in future work. For that reason, the two-sender design instead of one-sender is kept here and treated with the same frequency at a time.

#### 4.2.6 Inverse problem by harmonic induction

The designed device in Figure 4:18 showed the ability to distinguish between a copper rod, steel rod and copper-steel rods (referring to Figure 4:20 for the target cases). This was so far valid for one depth and one diameter and many frequency variations. In order to approve the idea, it has to be simulated using the dipole model for many other possibilities of target diameters and depths. If the diameter is fixed and the rods are just moved away from the sensor from 10 mm to 40 mm in 5 mm steps, then steel leads to responses of the phase along the scan direction seen in Figure 4:22 a). If the same is done using a group of two rods one made of copper while the other is steel, then the spatial phase profile is the opposite of the steel as expected. Figure 4:22 b) shows the response of this complex grouped copper-steel rods also for the investigated depths. These results are outcomes of the simulation model described previously after its validation. Fitting a parabola of the form (4.11), the unknown  $a_1$  for all variations of diameters and depths is a clear indicator of the target composition.

$$y = a_1 x^2 + a_0 \quad (4.11)$$

The parameter  $a_1$  is simply distinguishing whether the target is steel (positive values) or copper-steel (negative values). Figure 4:22 illustrates the 'spatial phase profile' for several depths of the target and for a fixed 8 mm diameter. From each profile,  $a_1$  is evaluated and the same can be done for all diameter variations as well. Figure 4:23 shows the value of  $a_1$  for several diameters and depths at the same time. The values are all negative for steel rods (Figure 4:23 a)) and all positive for copper-steel rods (Figure 4:23 b)). This is all what is needed from 'spatial phase profile' of the voltages in the coils 'east' and 'west' of this device.

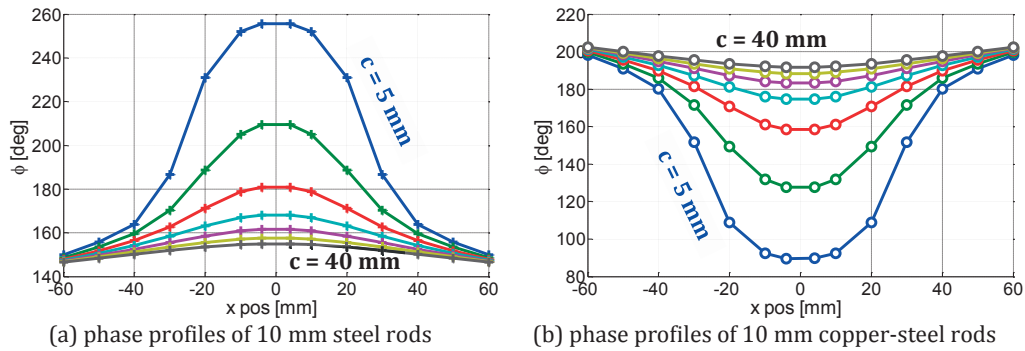


Figure 4:22 The phase response of steel (left) and copper-steel (right) rods of a fixed diameter of 8 mm and depths variation from 10mm (blue) to 40 mm (black) in 5 mm steps with an active frequency of 25 kHz in the sender coils.

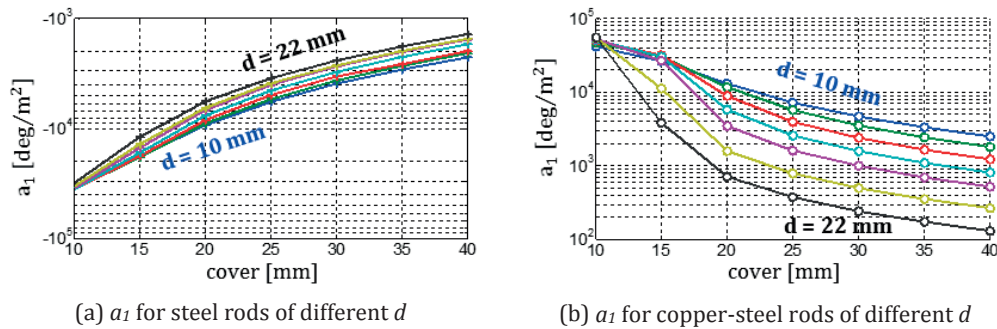


Figure 4:23 The parameter  $a_1$  of the parabolic fits of the phase response of every scan over a steel rod (left) and steel-copper rods (right) for all diameters starting from 10mm (blue) to 22 mm (black) in steps of 2 mm, all plotted versus the depth of the target with an active sender frequency of 25 kHz.

More database checks of amplitudes of coils ‘north’ and ‘south’ lead to exact estimation of the diameters and depths, which is described later. The copper responses are not needed to be fitted simply because copper phase response is found to be a straight horizontal line along the scan  $x$ -direction rather than a parabola therefore  $a_1$  is always equal to zero for any diameter and depth.

In order to distinguish copper rods from ‘no rods’ (or simply air) then the aid of the ‘north’ and ‘south’ amplitude responses are needed. And this is completed in this section. It is also important to note here that the variable  $a_1$  is extracted from the phase of the differential voltage signal  $U_{east} - U_{west}$  during a transversal scan from ‘east’ to ‘west’. It is also proven that the same can be done for the same scan but extracting  $a_1$  from the phase of the summed signal  $U_{north} + U_{south}$ . The outcome would be reversed relative to the one in Figure 4:23 that means  $a_1$  is positive for steel rods and negative for copper-steel rods. It is also zero for copper rods alone. This is a redundant way to check the material composition of target rods and therefore the plots are skipped in this context. But redundancy is important in industrialization due to measurement and geometrical tolerances but it

is not required her to prove the idea. After identifying the material of the target(s), the next step would be size, and depth discrimination.

The ability to identify these features are required to complete the use of such sensor. Relying only on the  $a_1$  fitting parameter of the differential signal phase would so far not even be used as lookup tables for depth and diameter, for sure not for copper because  $a_1$  is always zero. The plots in Figure 4:23 are also not linear even in a logarithmic scale plot as seen. The variations between the diameter curves is also narrow and makes the resolution not useful for an industrial device. On the other hand, and due to experience, amplitudes are better used as lookup tables. But in this design the amplitude of the differential signal is found out to be very effective. The 'Root Mean Square' (RMS) of this differential voltage signal should results in a zero value for  $x=0$  as in Figure 4:24 a). But the whole scan values exhibit a sine shape or form. As an example, which is plotted in Figure 4:24 a), a steel rod of 8 mm diameter is scanned in the transversal direction ( $x$ -direction) leading to sine shapes for every depth of this rod. The sine function fitted to the RMS profiles of  $U_{east} - U_{west}$  has four parameters as in (4.12) and only  $A_1$  parameter is used here. This parameter is plotted across all depths and all diameters in Figure 4:24 b). This can be used as a 2D lookup table for steel rods but it leads to several solution combinations of diameters and depths. For that reason, another lookup table is required to identify, which one of the features is the correct one and will be the next step mentioned in this sub-section.

$$RMS = A_1 \sin(a_2 x + a_3) + a_4 \quad (4.12)$$

The same fitting procedure is done for the copper-steel combined rods as well as the pure copper rods. Both 2D lookup tables are plotted in Figure 4:24 c) and d) respectively. The lookup tables for all three target cases can be also done using the RMS of the summed signal  $U_{north} + U_{south}$ , which should have a maximum at  $x=0$ . The fit to such curves is an exponential one in the form of (4.13).

$$RMS = c_0 e^{-\frac{1}{c_1} x^2} \quad (4.13)$$

The parameter  $c_0$  produces three lookup tables linear in the logarithmic scale and well separated between each diameter of interest. These lookup tables are not plotted here and are considered redundant for this procedure. Redundant lookup tables are useful when disturbances in measurement or electromagnetic interferences are present. Also when environmental changes are extreme these tables would be effective to minimize the error in matching parameters. But another technique is still required to explicitly identify the diameter and depth of each of the materials of the target by just performing one scan in the  $x$ -direction. Here it is important to note that the  $x$ -location of any target is easy to locate from the minimum of the  $RMS$  of a sine profile when a scan is done referring to Figure 4:24 a). As soon as the composition of the target is identified by the parameter  $a_1$  the device uses simple lookup scripts to search in the corresponding tables of  $A_1$  and the result is then still not unique. For that reason, other post processing equations based on selective frequency responses are proposed here to create functions of



the diameter regardless of any depth. These equations complete the inverse problem and result in a direct unique (one solution of diameter and depth) characterization of the target. For the 'spatial phase profile' and *RMS* of the differential signal done so far it was enough to use the responses of a 25 kHz excitation for this design. It was found out that this is also effective for any frequency in the range of 20 kHz to 30 kHz as proven in [22]. It is the range of the decoupling of mutual induction of nearby steel targets. The 25 kHz central frequency was proven to be one of the frequencies resulting from an optimization done on the complete sensor like the work done in sub-section 4.2.3. According to that, and for the application of this work, two post-processing formulae are introduced where the sender at every scan position is excited by few chosen frequencies including the 25 kHz. The responses of the frequencies are then saved to be used for feature discrimination.

$$ratio1 = \frac{\ln(A_1(50)) - \ln(A_1(25))}{\ln(A_1(25)) - \ln(A_1(1))} \quad (4.14)$$

$$ratio2 = \frac{A_1(75) - A_1(10)}{A_1(10) - A_1(1)} \times \frac{A_1(75)}{A_1(10)} \quad (4.15)$$

The first ratio, *ratio1* is a dimensionless function of the natural logarithm of the amplitude  $A_1$  (renamed here as  $A_1(f)$ ) of the RMS profile of a scan response when the sender coils are excited with frequency  $f$ . For example,  $A_1(25)$  means the fitting parameter  $A_1$  for a 25 kHz frequency exactly the same as the plots in Figure 4:24. This *ratio1* in (4.14) is using three frequency responses; the 25 kHz is essential here and was as expected but it is anyway an outcome of an optimization. The other two frequencies are 50 kHz and 1 kHz. When these responses are put in (4.14) they lead to a ratio that is nearly independent on depth but only dependent on diameter. This is effective for steel and copper-steel targets as in Figure 4:25 a). The term *ratio1* for copper rods is nearly constant for all diameters and depths as seen from the graph. The dashed line in the graph is the average of all depths of these rods. The exact responses of these rods are plotted as standalone markers  $\ast$ ,  $o$ , and  $x$  for steel, copper-steel, and copper respectively. Using this ratio, it is easy first to estimate the diameter and then go back to the 2D lookup tables (Figure 4:24 b) or c)) to extract the depth as well. This is valid for steel and copper-steel targets only while in the case of copper, another ratio is required if the sensor has already assumed that the target is a pure copper rod. The copper rods need to be analyzed similarly but with a different combination of frequencies, which were found to be 75 kHz, 10 kHz, and 1 kHz.

The first term *ratio1* (4.14) was more effective in the presence of steel due to the combined operations done on the specific amplitude response of  $\ln(A_1(50)) - \ln(A_1(25))$  and  $\ln(A_1(25)) - \ln(A_1(1))$ . The responses in the logarithmic scale for frequencies around 25 kHz are linear with depth and diameter. Subtracting this from a higher and then from a lower frequency response gives terms with coupled target effects. But when taking their ratio, the result is affected mainly by the diameter and is nearly independent of the depth.

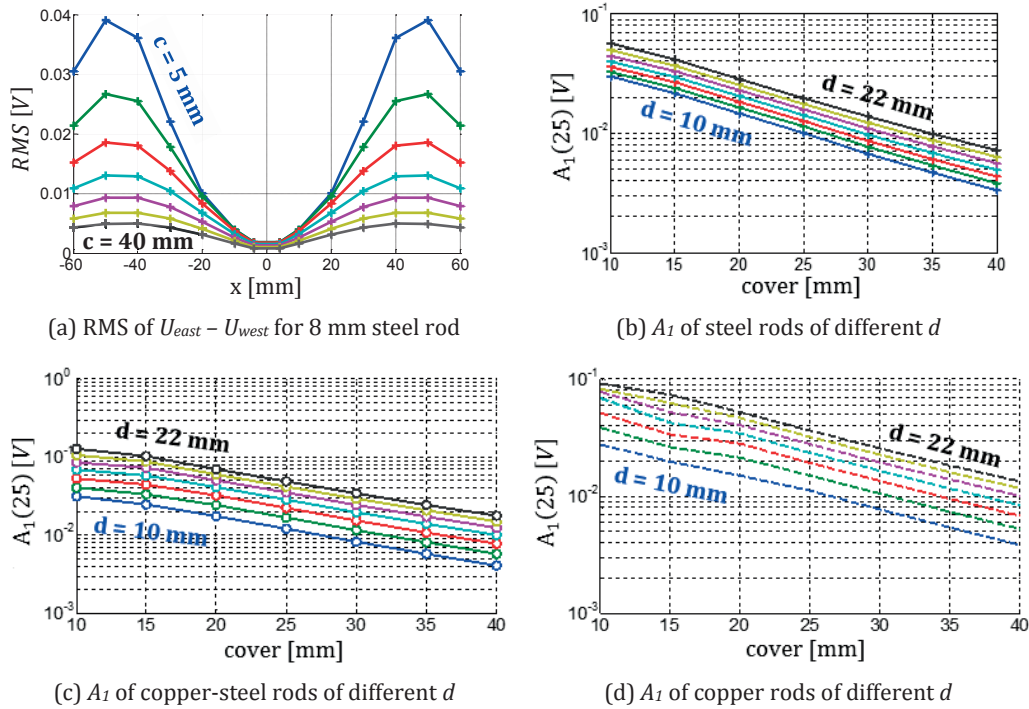


Figure 4:24 a) The plot of the RMS of the differential voltage signal ( $U_{east} - U_{west}$ ) across a transversal scan for an 8 mm steel rod with a variation in depth from 10 mm (blue) to 40 mm (black) in steps of 5 mm. b), c), and d) correspond to the plot of the parameter  $A_1$  (the amplitude of the sine fit of the RMS across the scan at frequency  $f = 25$  kHz),  $A_1$  is plotted versus the depth of the three cases targets for all diameters 10 mm (blue) to 22 mm (black) in steps of 2 mm.

In the absence of steel, a different approach is required. The term *ratio2* is the most effective for single copper rods only and is written in (4.15). It is plotted in Figure 4:25 b) with nearly no dependence on depth as seen but only on the diameter. Copper as a pure conductive material had proven that a ratio between a higher frequency difference and a lower frequency one leads to a depth independent behavior and a good differentiation between diameters. These frequencies were the optimum frequencies results from an SQP gradient optimization done on the complete sensor with all the target feature combinations, similar to the work in sub-section 4.2.3. It is important to clarify the reason why some values mainly in *ratio1* are not on the averages dashes lines in Figure 4:25-a even though it was stated before that this ratio is cover independent. These discrete points correspond to different cover values and they differ for every fixed diameter because the system is including the whole coil designs with all senders and receivers. The simulated signals also include random noise added. In addition to that, the center of a double rod target is not the center of any of the rods. This means for  $x=0$  (see Figure 4:19) one rod is located at  $x=d/2$  and the other rod is at  $x=-d/2$  in case of a double rod target. Nevertheless, the resolution of both *ratio1* and *ratio2* are acceptable to be used as diameter estimator.

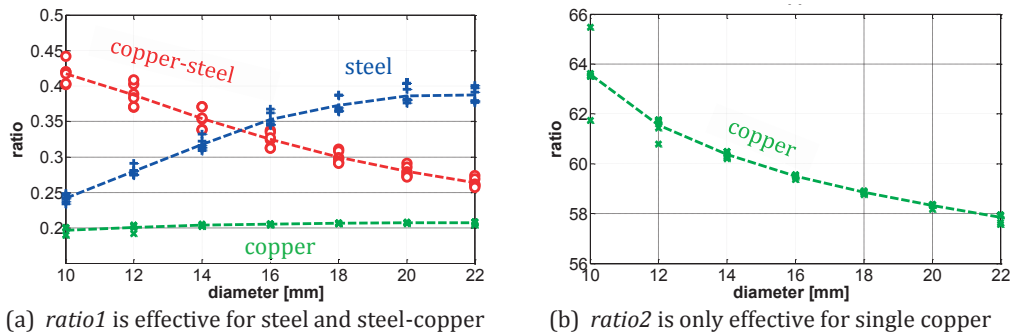


Figure 4:25 a) left is the plot of the  $ratio1$  in (4.14) which is effective to find diameters of steel or copper-steel rods, b) right is the plot of the  $ratio2$  in (4.15) which is effective to find diameters of copper rods.

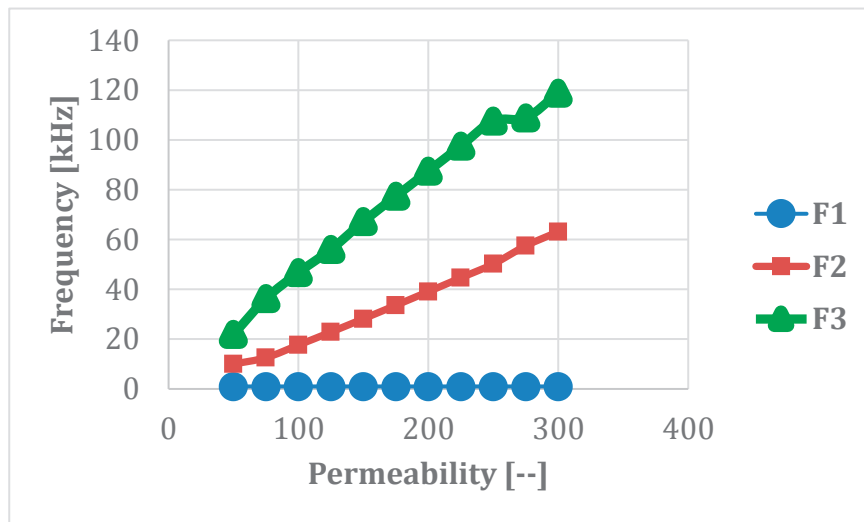


Figure 4:26 The effect of the permeability on the optimum selective frequencies to be used in  $ratio1$

The optimum frequencies found for  $ratio1$  in (4.14) are results of a setup with steel rods having a relative permeability of about 100. Because of the linear behavior of steel at low currents, the permeability of steel is assumed to be between 100 and 125. For that reason, the frequencies 1 kHz, 25 kHz, and 50 kHz are applicable to be used in  $ratio1$ . These optimum frequencies are material dependent and therefore the relative permeability is effective in defining these frequencies. Figure 4:27 shows the permeability effect on the optimum frequencies to be used in  $ratio1$ . If other materials with different permeability should be distinctively detected, then different optimum frequencies should be used.

In order to apply this idea for an industrial device, many tests have to be done on real applications like copper cables instead of rods and also maybe reinforcing steel bars instead of simple round rods. This will be open for future work and further verification of the novel idea.

#### 4.2.7 Robustness and reliability

One claimed advantage in this work is the robustness of the proposed method under environmental, manufacturing, and measuring errors. Noise signals are one of the usual and frequent physical aspects of such sensors. Due to the accuracy and efficient tools developed here, it is able to prove the acceptance of the resulting error in feature discrimination for the whole specified target feature range. Proving that the method is reliable and robust requires an analysis of not only one case and one measurement but rather an outcome of several random error analysis of the complete diameter and cover ranges. This should also be done for all target material cases sketched in Figure 4:20.

$$U_{real}^{new} + iU_{imag}^{new} = (U_{real}^{old} + Z_{real}) + i(U_{imag}^{old} + Z_{imag}) \quad (4.16)$$

Using the model developed in this section for harmonic induction discrimination and distinctive detection, a random complex noise signal is added to the pure voltage response. The added noise in complex form,  $(Z_{real} + iZ_{imag})$ , is chosen randomly to vary between noise level limits and added to the old voltage signals resulting in a new voltage signal as in (4.16).

For all the variations of  $c$ ,  $d$ , and  $x$  there is a corresponding induced voltage  $U^{old}$  that is maximum in amplitude at minimum  $c$ , maximum  $d$ , and  $x=0$ . This maximum response is defined as  $U_{max}^{old}$  and is a complex number.

white noise to all the responses of all covers, diameters, and transverse positions means the same noise,  $Z$ , is a percentage of the maximum signal and added later to all signals. This noise is defined in (4.17) where  $p$  is a noise part varying randomly 20 times within a lower limit  $-pU_{max}^{old}$  and an upper limit  $+pU_{max}^{old}$ . As an example, when a 0.5% white noise is added, then  $p=0.005$ . Therefore, 20 different random noise signals are added to every old signal. This additional signal,  $Z$ , may vary as in (4.18) where  $p=0.5\%$ .

A final statistical mean and standard deviation are evaluated according to this addition of white noise to every case of material, size, and depth of the target.

Adding a white noise of 0.5% is not a small amount because it is constant noise 0.5% of the highest signal added to the weak signals as well. In general, strong signals are responses of shallow targets (small cover) and low signals are responses of deep targets (large cover).

$$Z = \pm pU_{max}^{old} \quad (4.17)$$

$$-pU_{max}^{old} \leq Z \leq +pU_{max}^{old} \quad (4.18)$$

The signal strength is not linear with the distance and it nearly inversely proportional to the 6<sup>th</sup> power of the distance. Adding 0.5% of the shallow signals to the deep signals

makes a big noise. The amount of 0.5% white noise is used here due to industrial experience for such hand-held devices and their measuring imperfections. The electronic hardware quality and tolerance play a role in this amount of noise as well. A study with double this noise value is also conducted to analyze extreme cases.

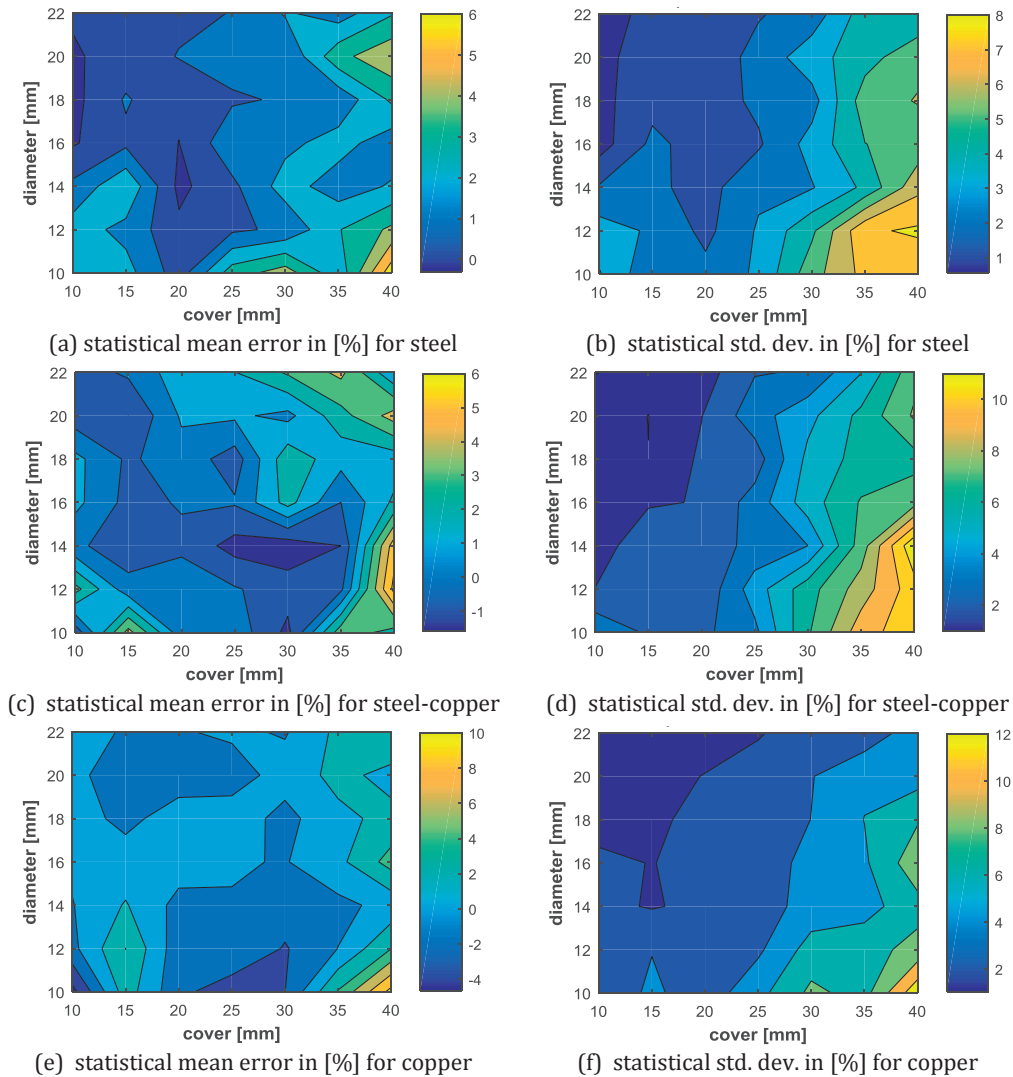


Figure 4:27 The mean and standard deviation error in percentage of cover values. This is a statistical analysis of 20 random white noise levels ranging between -0.5% and +0.5% of the maximum signal induced added to all responses of all cover and diameter values performed at 25 kHz excitation frequency.

The final cover estimation error done by this noise addition using 25 kHz frequency is plotted in Figure 4:27. The error is in cover percentage and is acceptable for the specified resolution of the sensor. The mean of the cover error for steel is found out to be between 0% and 6% of the cover value as in Figure 4:27a. The average of the 20-random noise

added to the original signal is maximum +6% but mainly for cover values of 40 mm, which means a +2.4 mm error. So, for all 20 noisy signals the average cover estimation is 42.4 mm instead of 40 mm for that case and mainly for the 10 mm diameters and 20 mm diameters.

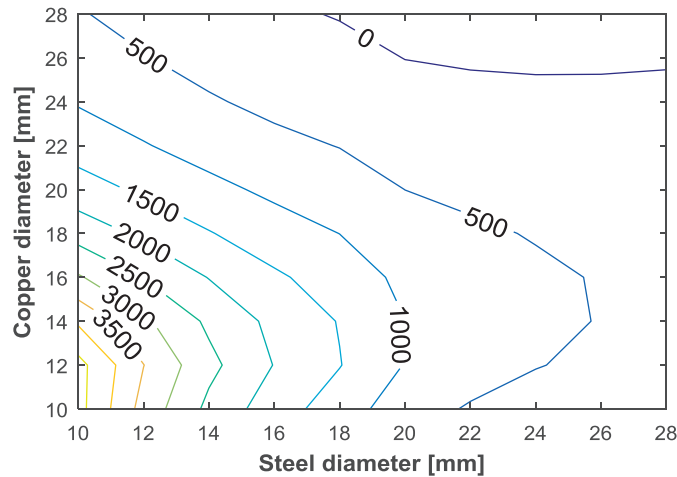


Figure 4:28 The value of  $a_1$  simulated for double rod case where the diameters of steel and copper are different. The operating frequency is 25 kHz and the rods were placed at  $c = 30$  mm.

The average standard deviation of this error and that special case would be around 5%. For all other steel diameters and cover cases the errors are much less. Figure 4:27c and Figure 4:27d show the same results for the steel-copper case. The last two figures show the cover error for the single copper rods case. If a higher frequency is used the results are much better. Even for the same amount of white noise the error in cover estimation becomes much less. If the noise level is increased to  $\pm 1\%$  instead of  $\pm 0.5\%$  the error gets higher but this is a big amount of noise. Nevertheless, the error is still acceptable in general. When the diameter is small and the cover is big then the error is at its maximum and is still relatively acceptable except for the highest noise level ( $\pm 1\%$ ) and low frequency of 25 kHz. The results of  $\pm 0.5\%$  and  $\pm 1\%$  noise corresponding to 25 kHz and 75 kHz frequencies are all documented in Appendix H.

Another study is conducted here checking the cases of double material target that would have different diameters. The 'spatial phase profile' described in sub-section 4.2.5 can identify that the target is composed of two rods each having different materials (steel and copper) from single material target (steel or copper). But so far the double material case was considering that the two rods placed next to each other have the same diameter.

If the volume of copper to steel is not equal, then probably the parameter  $a_1$  would reach its limits. To find these limits, new scan responses are evaluated and their corresponding parameter  $a_1$  is extracted to show if its sign is still a flag of material discrimination. It was assumed in the previous sub-sections that if  $a_1$  is zero then the target is pure copper.

Negative values of  $a_1$  indicate steel rods, while positive values indicate a double rod target of copper and steel at the same time. So, by taking the third case in Figure 4:20 (right) and varying the diameters of both rods, simulation results show the corresponding values of  $a_1$ , which is supposed to be positive to indicate the presence of two materials (Figure 4:28). The zero-value contour line indicates the limit of this method. It shows that the steel and copper rods having any combination of diameters between 10 mm and 22 mm (the range set for this work) lead to a positive parameter value of  $a_1$ . This is a clear indication that two different materials are present rather than one. Further on, the diameter discrimination and depth estimation should be worked on in future work for such cases. The example in Figure 4:28 was performed for a cover value  $c = 30$  mm. This method has a tighter range if the depth is increased and for that reason more calculations are presented for deeper targets up to  $c = 50$  mm in Appendix F. This method reaches its limits for deeper targets that are out of the specifications of this work and should be treated differently using different design settings in the future (higher current values for example).

Another robustness and reliability advantage of the double balanced coil system is the ability to adjust it for oriented scan directions. If the scan is not perfectly perpendicular to a rod target, then the usage of all four receivers (Figure 4:18) becomes effective by postprocessing the single amplitudes of the receivers showing unsymmetrical response across the scan. In details, the north and south signals can be extra used together with the east and west signals to estimate the orientation angle of the target rod to the scan direction.

### 4.3 Summary

Distinctive detection is a highly challenging task even after a forward system is created to define a relationship between target features and induced voltages (both in frequency or time domain). Inverse models were successfully verified and applied for both harmonic and pulse induction systems, which allowed the reverse relation between the voltage and the target features of single material with an acceptable error in diameter and depth (cover) for a big range of these variables. Material discrimination is also possible by parametrizing the voltage decay responses of pulsed currents and it was shown that depth independent parameters can decide if the target is steel or copper, for example. This method reaches its limits when both targets of different materials are placed together to be distinctively detected as they are including their depth and size. This is referred to as 'complex target' and would be the highest challenge of detection by EMI.

On the other hand, the harmonic induction method showed flexibility and is effective in such cases. Again, a forward system using harmonic induction has been created but this time material discrimination is done as first step in this procedure. Being able to detect by induction of complex target combination (nearby copper and steel cylindrical rods) is implemented using a 'double-balanced' geometrical coil layout adapted to a 'spatial phase profile' proposed discriminator. The combination of those two concepts led to a

proposed design of an electromagnetic detection system, which was designed and simulated using a dipole model. Both, simulation and experimental results could identify whether the detected target is copper, or steel, or both steel and copper in the same place. The experimental validation of the dipole model for many cases was important to rely on such a tool. A promising concept of distinguished detection of such complex target combination was then completed and verified. This is valid for low to medium frequency (up to one MHz) ranges of detection by induction devices. Thus, a complete robust and geometrically calibrated detection sensor to discriminate features of finite length rods of steel, copper, or both copper-steel combined.

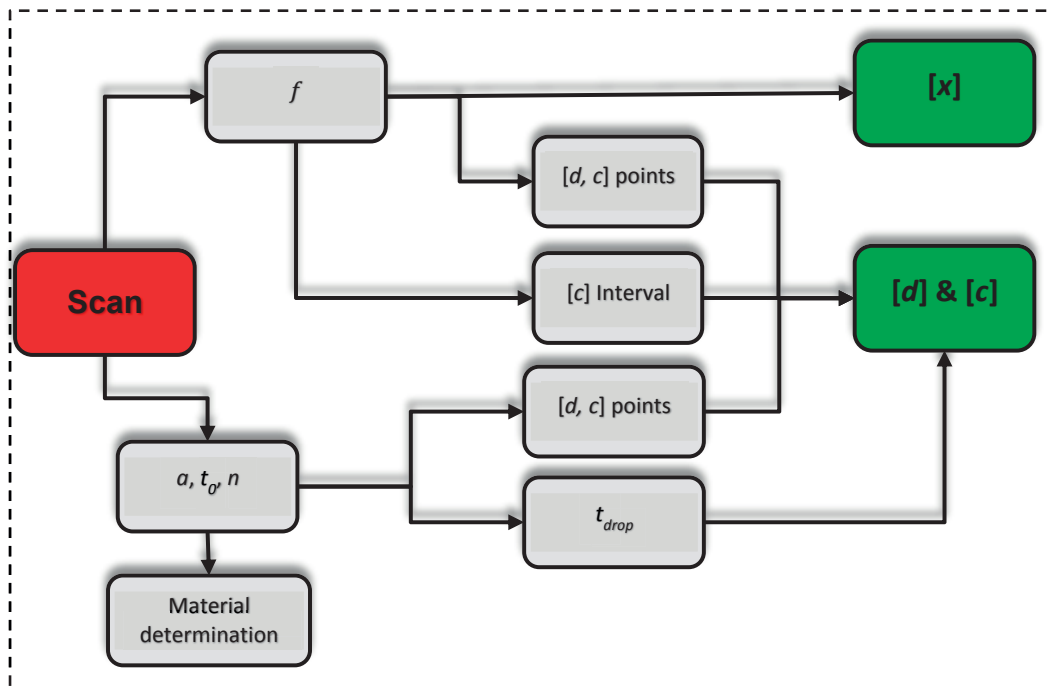


Figure 4:29 The workflow of the inverse model by pulse induction to estimate the unknowns  $[x, d, c]$  from a single scan.

The sensor can identify the material composition between all three material combinations using a 'spatial phase profile' method rather than just single phase or amplitude values. The sign of the first parameter ' $a_1$ ' (as in Figure 4:23) can estimate whether a steel rod or a combination of copper and steel rods are present. The parameter  $a_1$  is zero in the case of copper. The main characterization of the diameters is then achieved by a diameter dependent post processing procedure, which is nearly independent on the depth of the targets. This is done by calculating the dimensionless ratio of (4.15) if the target is identified as a copper rod or (4.14) if the target is a steel rod or two rods of steel and copper. After that the depth is post processed using lookup tables of amplitude based profiles depending on the composition of the target(s) found. These tables are not local amplitude based. They are based on amplitudes of the whole response across the scan, which makes it more robust. Such tables have to be originated newly if the design



changed and examples are found in Figure 4:24 for all cases investigated. The transverse location in the scan direction is easy to find based on the minimum of the RSM profile (Figure 4:24 a)).

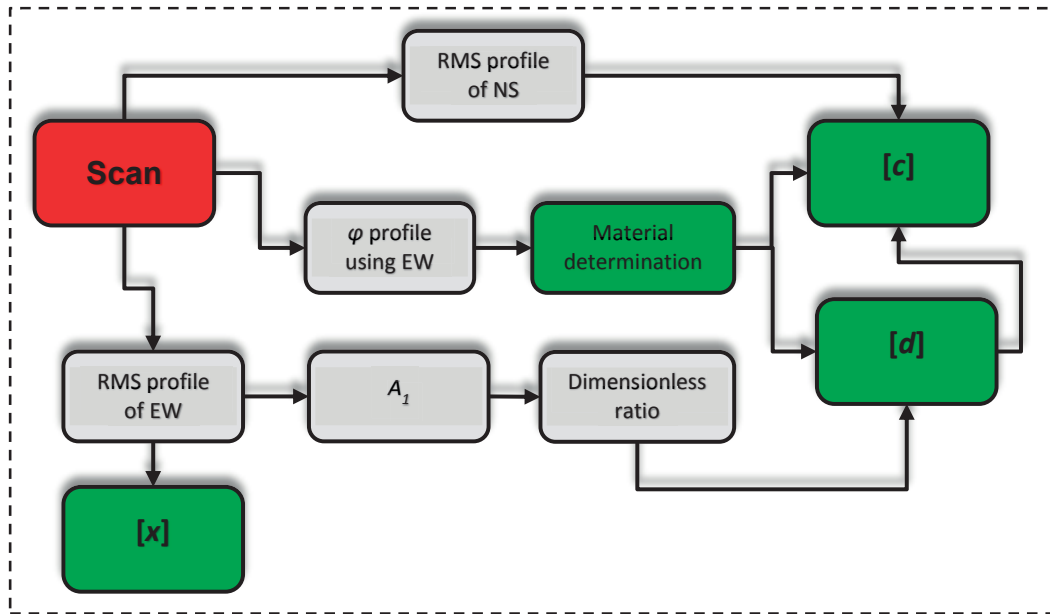


Figure 4:30 The workflow of the inverse model by harmonic induction to estimate the unknowns  $[x, d, c]$  from a single scan.

This complete procedure is possible due to the placement of six coils ('double balanced' configuration) together with the 'spatial phase profile' method. It provides a versatile and robust configuration for an inductive sensor for depth and diameter determination of metallic rods including material discrimination. It can be used to discriminate non-permeable conductors from permeable conductors or even mixed configurations. The dipole model used to simulate such a system delivers this final concept with an acceptable experimental verification.

The simplified sketch of the inverse model using pulse induction is drawn in Figure 4:29 where the unknown variables  $x, d,$  and  $c$  referring to  $x$ -location, diameter, and cover respectively are estimated from one scan in the  $x$ -direction relative to the target, which is supposed to be hidden and unknown.

A similar sketch of the inverse model using harmonic induction this time is drawn in Figure 4:30 where the unknown variables  $x, d,$  and  $c$  are estimated from one scan in the  $x$ -direction relative to the target. This procedure has an additional feature: it can, not only specify if the target is a single copper rod or a single steel rod, but also a combined copper-steel rods and still estimate their sizes.

Transverse magnetization of the targets is used here with an advantage: tilted configurations with respect to the scan direction can correctly be discriminated as well. The sensitivity of the sensor is sufficient such as Printed Circuit Board (PCB) coils can be used, which have a low time constant due to the low ( $L/R$ ) specification.

In order to apply this idea for an industrial device, many tests have to be done on real applications like copper cables instead of rods and also maybe reinforcing steel bars instead of simple round rods. This will be open for future work and further verification of the novel idea.

Combining both harmonic and pulse induction would lead to a multi-task device that is effective in all feature selectivity and detection.

## Chapter 5 Conclusion

A detection system based on EMI technology to recognize hidden metallic objects being either magnetic or non-magnetic (or both at the same place) and still estimating their features (location, size, depth, and material) is achieved with contributions on the following levels: system, approach, and procedure.

These points are detailed in section 5.1. The design procedure proposed here depends on the features to be detected and the quality or resolution required. The focus is on three research areas: excitation scheme, coil design, and post processing. These fields are interconnected and should be tackled equally using a workflow starting by the system (coils, detected target, specifications, and excitation method whether harmonic or time periodic). Further on, the system should be represented by forward models using both, simulations and experiments. The result of the forward representation is a set of detailed steps in the post-processing of the responses of many target cases. The final aim of discrimination is to inversely estimate all target features for any case. Forward representation means the responses are achieved by known target features. Inverse representation means that the features are deduced from one scan response. This is accomplished efficiently using computational models:

- modified 3D finite element model (see section 3.1)
- modified dipolar model (see section 3.2)

Both models are verified against experiments for different designs and excitation schemes. If the aim of the sensor is to detect material composition only, then harmonic excitation is proven to be more effective and many of the post processing techniques of estimating other features, such as position and size, can be neglected.

The detector depends on one transverse scan across hidden metallic targets and is independent on signal amplitudes. This helps in the detection of deep targets due to weak signals or bad efficiency even for small/medium sized objects.

The design does not need additional coils and thus no additional lookup tables for other feature detection (mainly size). This can be simply done by one sender and two receivers where their differential signal is required to find 'spatial phase profiles' rather than phase values or any amplitude values. This simple design can distinguish between magnetic targets and nonmagnetic targets and even a combination of both located at the same place.

In case other features are required, like depth and size, then additional coils can be printed on the same PCB, which when post-processed in a defined way depending on the material can estimate these features more accurately. On the other hand, a pulse induc-

tion excitation method is also proposed requiring a completely different coil design, excitation, and signal processing. This method is robust, more precise, and can also be implemented to discriminate features whether they are copper or steel single targets. Unfortunately, it requires more computational effort when processing an inverse model because the unknown parameters double in quantity.

These methods are verified and validated against experiments. Real applications on several hardware designs are performed to reach the desired specification and are just one step before the phase of industrialization or automated production. Copyright of the distinctive detection idea was already filed through two patent applications ([23] and [24]) at the 'European Patent Office'. Separate and interconnected contributions of this work in methodology, modeling, design, signal processing, discrimination, and distinctive detection are listed in section 5.1.

## 5.1 Main contributions

The aim of this work, as mentioned in section 1.1, is to achieve a method for distinctive detection of magnetic and nonmagnetic hidden metallic objects. Novel contributions in feature discrimination and distinctive detection were accomplished on the level of:

- System

The coils and their design are the main part of the system. The '**double balanced**' coil design is new and not a gradiometer. In this design the receivers are balanced against the senders which are also balanced against each other in an optimized relative distance to the target. It brings a robust system that is flexible for frequency manipulation and free from any coil dominance. It captures the dominant eddy current response of the targets and has a very high resolution when amplified. This is referred to in sub-section 4.2.4 as well as the published paper [74]. In addition to that, the limitation of the coil design to '**one receiver and one sender**' parallel to each other in pulse induction is sufficient for feature discrimination. It diverts from state-of-the-art detection devices where additional excitation modes and additional coils are required for high quality size feature discrimination (see section 4.1). This simple design achieves acceptable quality with the least post-processing time without additional excitation modes and without additional oriented coils.

- Approach

At the approach level the models (mathematical representation of responses) are the basic tools required in achieving the aims of the current work. One contribution is the modified FEM model to reduce computational time but sufficiently accurate as the full commercial model. Robustness is an added value especially due to the implementation of the '**line receiver model**' as well as the '**volumetric estimation method**' as described in section 3.1 and published mainly in [26].

This modified FEM model is used to help in implementing adjustments in the dipolar model that contributed to achieving a very fast simulation tool for detection sensor design. The computation efficiency allowed the use of optimization techniques like parametric variations and gradient based optimizations. This dipolar model is described in details in section 3.2. This implementation which is applied to finite cylindrical rods has been published in [22]. It highlights a '**decoupled frequency**' finding for double rods. It is verified by experiments described in sub-section 3.3.3. Representing the responses by fitting the voltage decay response is novel and effective. Some of these '**decay parameters**' are found to depend on one feature only, the diameter in this case. This made the size discrimination easier and the inverse problem faster and effective. Using both simulations and experiments, the result is validated by pulse induction on several hardware applications at least two of which were demonstrated. This method made a complete reduction in number of coils and their orientation, thus the volume as well. It also made the excitation time and post-processing time faster. These parameterizations are applied to magnetic and nonmagnetic materials with a distinguished behavior allowing material discrimination procedures to be implemented as well. The first introduction to that is mentioned in the signal processing section 2.4 and the '**material discrimination by parametrization**' is a contribution described in sub-section 3.3.3.

- Procedure

The final detection procedure is an inverse problem where features of hidden targets must be determined from scan responses. The forward model generated relationship and lookup tables representing the whole sensor functionality. This means that all the responses would be generated from known target features. On the contrary, the inverse model is the end aim because usually targets are hidden and unknown. This method is not new in the scientific community but the methods in inverse models like '**spatial phase profile**' allowed composed material discrimination even for double targets of different materials (magnetic and non-magnetic) located in the same place. This method was also published in a paper [74] and a patent application [23]. It is detailed in sub-section 4.2.5. This method is very effective by using the '**harmonic inverse model**' referring to a published journal [82] and another patent application, which is part of this work [24]. Additionally, a complete feature discrimination is completed as described in sub-section 4.2.6 where a diameter dependent relation is newly introduced based on '**frequency selectivity**'. It allowed explicit diameter discrimination. The spatial phase profile method is a prerequisite in this case because target classification is first required.

Summarizing the main contributions for each level in Table 5:1 shows the referenced documents and text as well.

Table 5:1 Summary of the main contributions and their references.

Level	#	name	thesis	public	description
System	1	<i>double balanced</i>	4.2.4	[74]	Achieving neutral inductivity by balancing sender and receiver coils against each other
	2	<i>one receiver and one sender</i>	4.1		Complete feature discrimination especially the target size without additional excitation modes or coils
Approach	3	<i>line receiver model</i>	3.1	[26]	Induced voltage calculation at any closed line implemented in a FEM solver
	4	<i>volumetric estimation method</i>	3.1	[26]	Achieving the optimum computation time and quality of eddy current evaluation by doing an element based elimination inside the target volume (not only on the skin)
	5	<i>decoupled frequency</i>	3.2, 3.3.3	[22]	The excitation frequency that decouples the response of two nearby steel rods
	6	<i>decay parameters</i>	2.4, 4.1.2		Achieving a forward model of the pulse excitation by parametrizing the voltage response
	7	<i>material discrimination by parametrization</i>	2.4, 4.1.3		Using the decay parameters to distinguish between steel and copper in the case of pulse induction excitation
Procedure	8	<i>spatial phase profile</i>	4.2.5	[74], [23]	Spatial profile, independent on amplitudes, that can distinguish single from double material targets using one frequency response rather than a spectrum analysis
	9	<i>harmonic inverse model</i>	4.2.6	[82], [24]	A complete feature discrimination and distinctive detection method using harmonic excitation
	10	<i>frequency selectivity</i>	4.2.6	[82], [24]	Selective set of frequency excitation suggested for every distinctive detection application. It is size dependent only.

## 5.2 Future scope

This work contributes to new ideas in discrimination and detection, adding the following potential advantages: detection speed, less interference, less cost, and high quality. The main goal in distinctive detection is also reached. But industrializing these methods requires the same work to be done on real applications like detection of reinforced rods, stainless steel cables, electric copper wires besides steel rods, and cables inside aluminum pipes. There is no real difference in the procedure if reinforcing steel rods are the real targets instead of rods, this was investigated and published in a paper [27]. A factor based system can be added. In the context of this thesis work reinforcing rebar were also experimentally used and tested, which proves its validity. But for detecting a multi-rebar mesh hidden in concrete, for example, additional post-processing scripts need to split the responses and solve for a bigger number of unknown variables. This should be implemented in the decay parametrization method for pulse induction. The coefficients of the fit equation can be linearized in the logarithmic scale. This requires the solution of a linear system of unknowns and is a straightforward procedure that is recommended for such applications. In addition to that, distinctive detection in real applications should be

implemented on real targets rather than simple cylindrical rods. The use of the 'spatial phase profile' is not yet proven to be effective on real complex targets. This method would might require the generation of lookup tables under different excitation frequencies. The newly invented ratios are expected to be merely size dependent but the current work has not proven that for copper litz wire cable near steel reinforcing steel bars, as an industrial real example.

The finding in this work are the basis to design, model, optimize, and develop EMI sensors per specifications. Industrializing the ideas requires a big effort.

# Appendix A

## Maxwell's equations in differential form

James Clerk Maxwell (1831-1879) formulated in 1865 the classical electromagnetic theory. He joined both electricity and magnetism into a consistent theory through a set of partial differential equations known as Maxwell's equations that are referred to in many books and publications [73]. The Ampere's Law (0.1) in differential form represents the generation of magnetic fields caused by currents in conductors and time-varying electric fields. The first term of the right-hand side is the source current density and the eddy currents inside conducting material. The second term is the displacement current in dielectric media caused by time-varying electric fields where  $D$  stands for the density of the electric flux. In the left-hand side the intensity of the magnetic field  $\mathbf{H}$  shows. Faraday's Law (0.2) states that a time varying magnetic field induces an electric field  $\mathbf{E}$ . The magnetic Gauss' law (0.3) states that the magnetic field is divergence free while the electric Gauss' law (0.4) states that the electric flux out of any closed surface is proportional to the total charge enclosed within the surface. Maxwell has combined all these laws together represented by (0.1) to (0.4) as a set of partial differential equations to be solved in space and time. Additional constitutive equations are needed still to solve these equations and are represented in (0.5) to (0.7).

$$\nabla \times \mathbf{H} = \mathbf{J} + \frac{\partial \mathbf{D}}{\partial t} \quad (0.1)$$

$$\nabla \times \mathbf{E} = -\frac{\partial \mathbf{B}}{\partial t} \quad (0.2)$$

$$\nabla \cdot \mathbf{B} = 0 \quad (0.3)$$

$$\nabla \cdot \mathbf{D} = \rho \quad (0.4)$$

$$\mathbf{B} = \mu[\mathbf{H} + \mathbf{M}] \quad (0.5)$$

$$\mathbf{J} = \sigma[\mathbf{E} + \mathbf{E}_i] \quad (0.6)$$

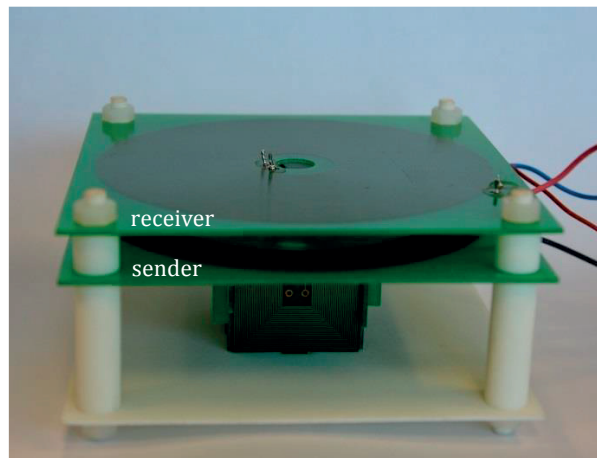
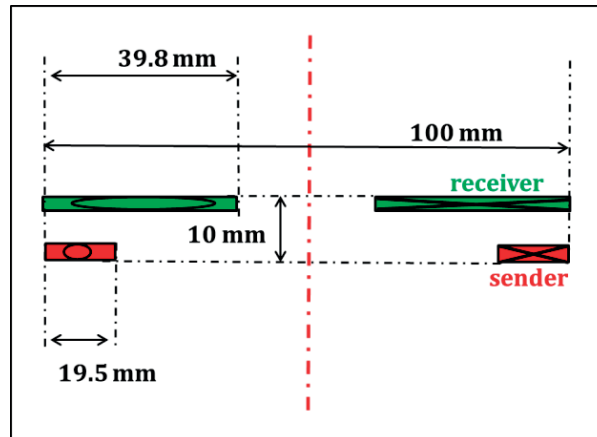
$$\mathbf{D} = \varepsilon[\mathbf{E} + \mathbf{P}] \quad (0.7)$$

Symbol	Quantity	Units
$\mathbf{H}$	Magnetic flux intensity	A/m
$\mathbf{J}$	Current density	A/m <sup>2</sup>
$\mathbf{M}$	Magnetic moment	A/m
$\mathbf{D}$	Electric flux density	C/m <sup>2</sup>
$\mathbf{E}$	Electric field	V/m
$\mathbf{B}$	Magnetic flux density	T
$\rho$	Electric charge density	C/m <sup>3</sup>



# Appendix B

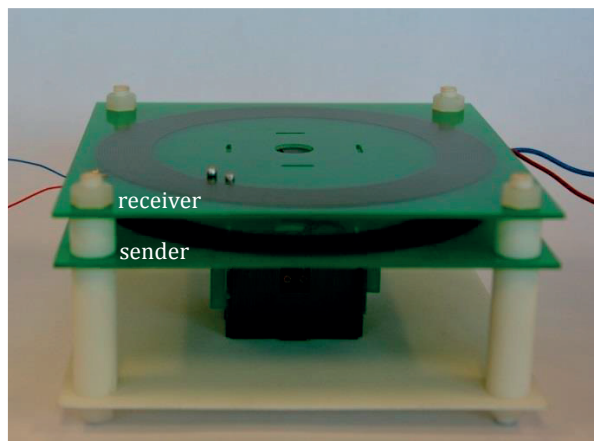
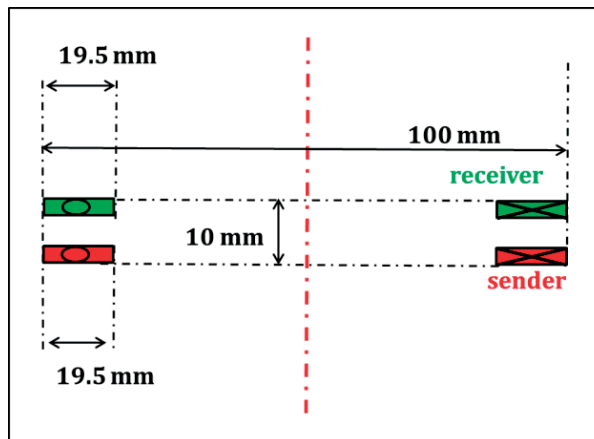
## Design I: sensor 1



	total number of turns	number of layers	copper pad height	copper pad width	pad gap	total coil resistance
sender	40	2	35 $\mu\text{m}$	0.5 mm	0.5 mm	11.04 $\Omega$
receiver	200	2	35 $\mu\text{m}$	0.2 mm	0.2 mm	97.2 $\Omega$

# Appendix C

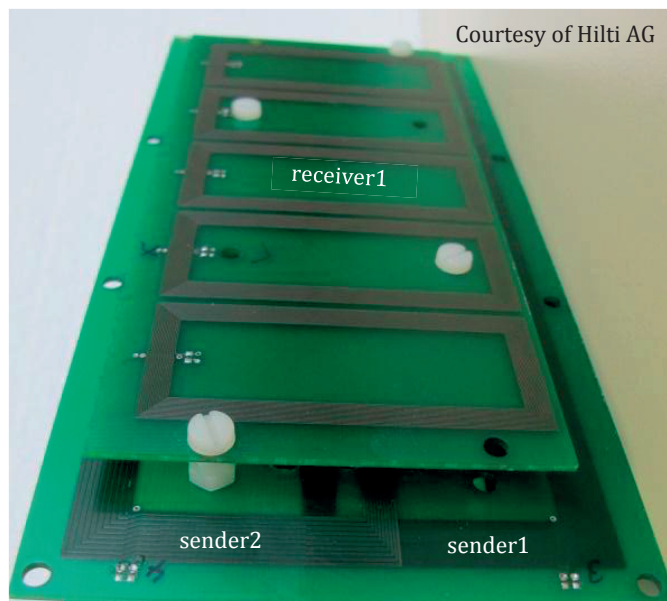
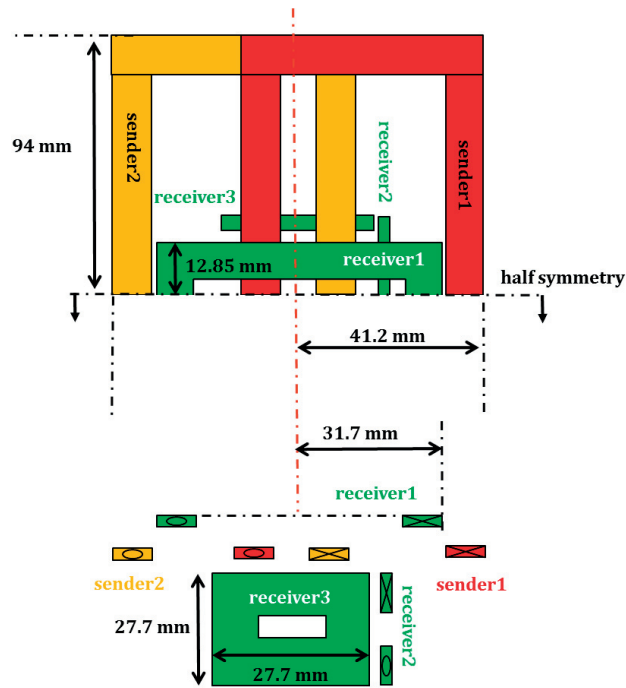
## Design I: sensor 2



	total number of turns	number of layers	copper pad height	copper pad width	pad gap	total coil resistance
sender	40	2	35 $\mu\text{m}$	0.5 mm	0.5 mm	11.04 $\Omega$
receiver	40	2	35 $\mu\text{m}$	0.5 mm	0.5 mm	11.04 $\Omega$

# Appendix D

## Design II



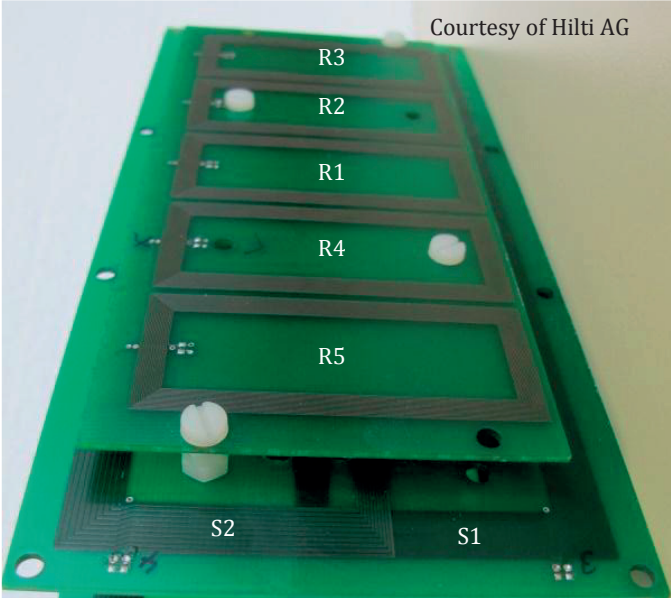
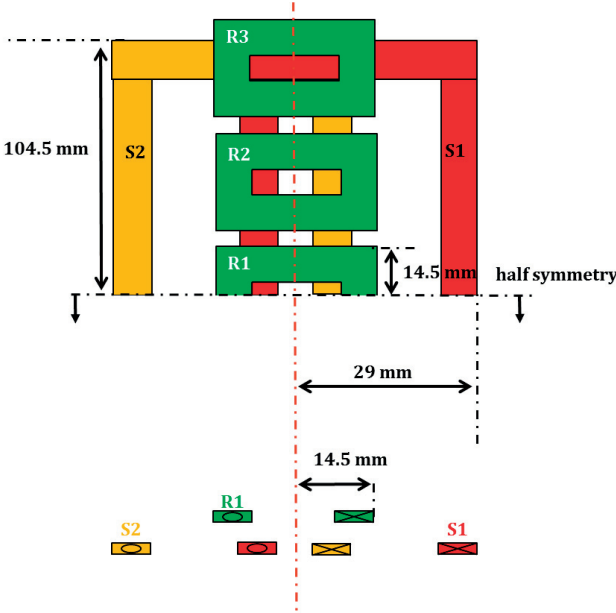
Appendix D

---

	<b>total number of turns</b>	<b>number of layers</b>	<b>copper pad height</b>	<b>copper pad width</b>	<b>pad gap</b>	<b>total coil resistance</b>
<b>sender1</b>	20	2	30 $\mu\text{m}$	0.75 mm	0.15 mm	8.5 $\Omega$
<b>sender2</b>	20	2	30 $\mu\text{m}$	0.75 mm	0.15 mm	8.5 $\Omega$
<b>receiver1</b>	64	4	30 $\mu\text{m}$	0.15 mm	0.15 mm	23.1 $\Omega$
<b>receiver2</b>	136	4	30 $\mu\text{m}$	0.15 mm	0.15 mm	6.1 $\Omega$
<b>receiver3</b>	136	4	30 $\mu\text{m}$	0.15 mm	0.15 mm	6.1 $\Omega$

# Appendix E

## Design III



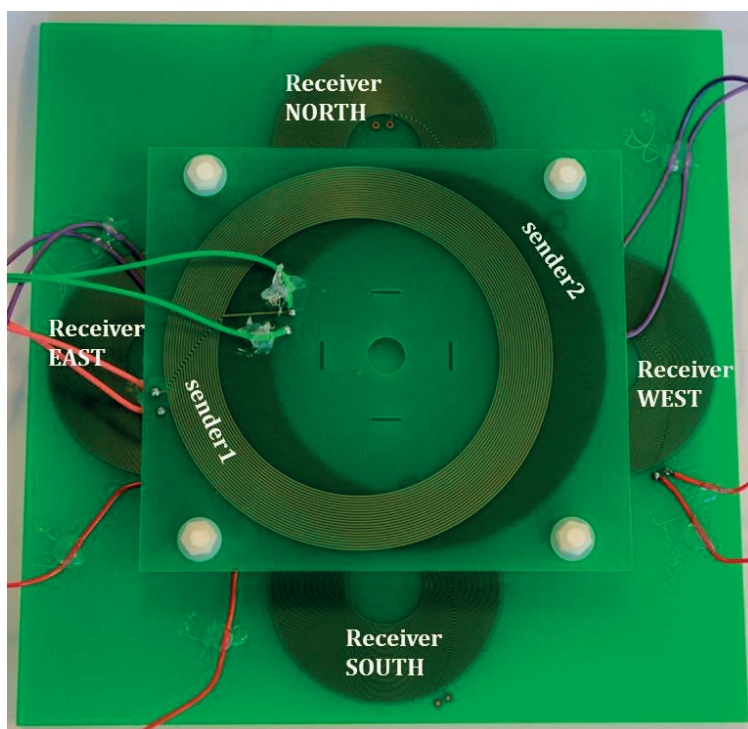
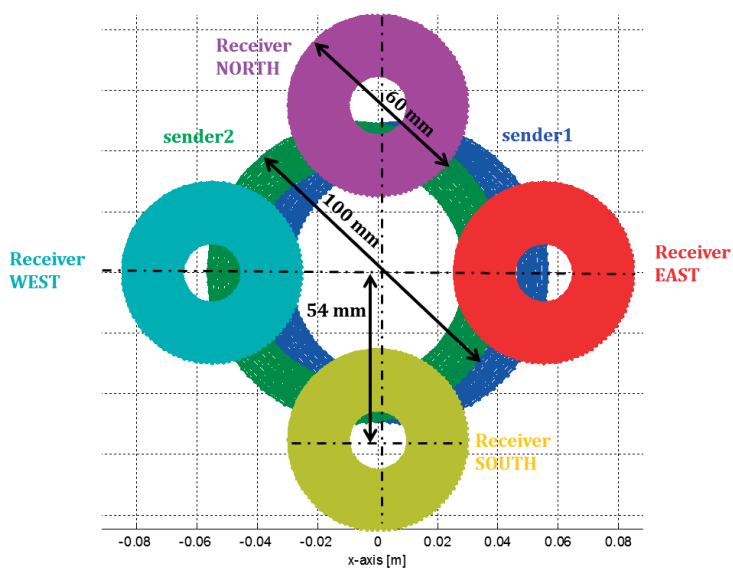
Appendix E

---

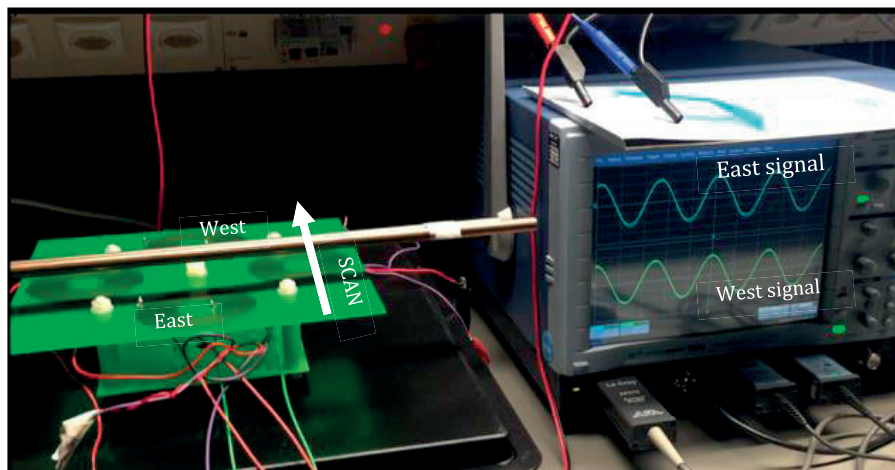
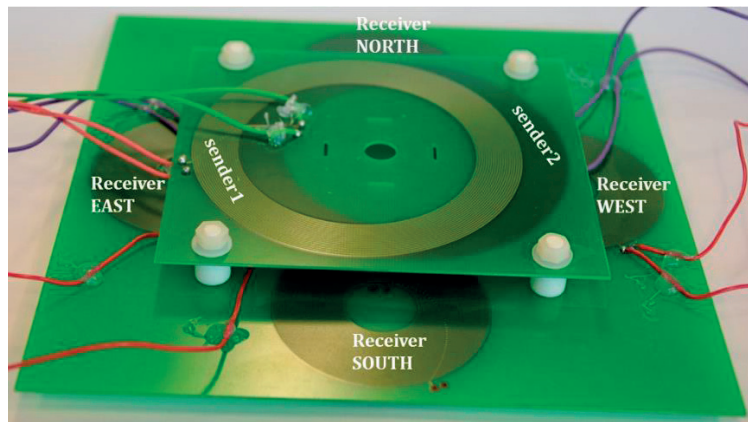
	<b>total number of turns</b>	<b>number of layers</b>	<b>copper pad height</b>	<b>copper pad width</b>	<b>pad gap</b>	<b>total coil resistance</b>
<b>sender S1</b>	28	2	30 $\mu\text{m}$	0.8 mm	0.2 mm	10.5 $\Omega$
<b>sender S2</b>	28	2	30 $\mu\text{m}$	0.8 mm	0.2 mm	10.5 $\Omega$
<b>receiver R1</b>	300	4	30 $\mu\text{m}$	0.1 mm	0.1 mm	10.1 $\Omega$
<b>receiver R2</b>	300	4	30 $\mu\text{m}$	0.1 mm	0.1 mm	10.1 $\Omega$
<b>receiver R3</b>	300	4	30 $\mu\text{m}$	0.1 mm	0.1 mm	10.1 $\Omega$

# Appendix F

## Design IV



Appendix F



	total number of turns	number of layers	copper pad height	copper pad width	pad gap	total coil resistance
sender1	20	2	35 $\mu\text{m}$	0.5 mm	0.5 mm	5.5 $\Omega$
sender2	20	2	35 $\mu\text{m}$	0.5 mm	0.5 mm	5.5 $\Omega$
receiver E	100	2	35 $\mu\text{m}$	0.2 mm	0.2 mm	32 $\Omega$
receiver W	100	2	35 $\mu\text{m}$	0.2 mm	0.2 mm	32 $\Omega$
receiver N	100	2	35 $\mu\text{m}$	0.2 mm	0.2 mm	32 $\Omega$
receiver S	100	2	35 $\mu\text{m}$	0.2 mm	0.2 mm	32 $\Omega$



# Appendix G

Bessel function of the first kind:

$$J_\nu(z) = \left(\frac{z}{2}\right) \sum_{k=0}^{\infty} \frac{\left(\frac{-z^2}{4}\right)^k}{k! \Gamma(\nu + k + 1)}$$

$J_\nu(z)$  is the solution of the differential equation:

$$z^2 \frac{d^2 y}{dz^2} + z \frac{dy}{dz} + (z^2 - \nu^2)y = 0$$

Where  $\nu$  is a real constant and  $\Gamma(a)$  is the gamma function:

$$\Gamma(x) = \int_0^{\infty} e^{-t} t^{x-1} dt$$

And for an integer  $x$  the gamma function is defined as:

$$\Gamma(n) = (n - 1)!$$

# Appendix H

The addition of white noise to the raw signals using harmonic induction and performing cover estimation after evaluating the diameter of the hidden targets is shown below for  $\pm 0.5\%$  and  $\pm 1\%$  of the maximum signal of all variations. This is also presented for 25 kHz and 75 kHz.

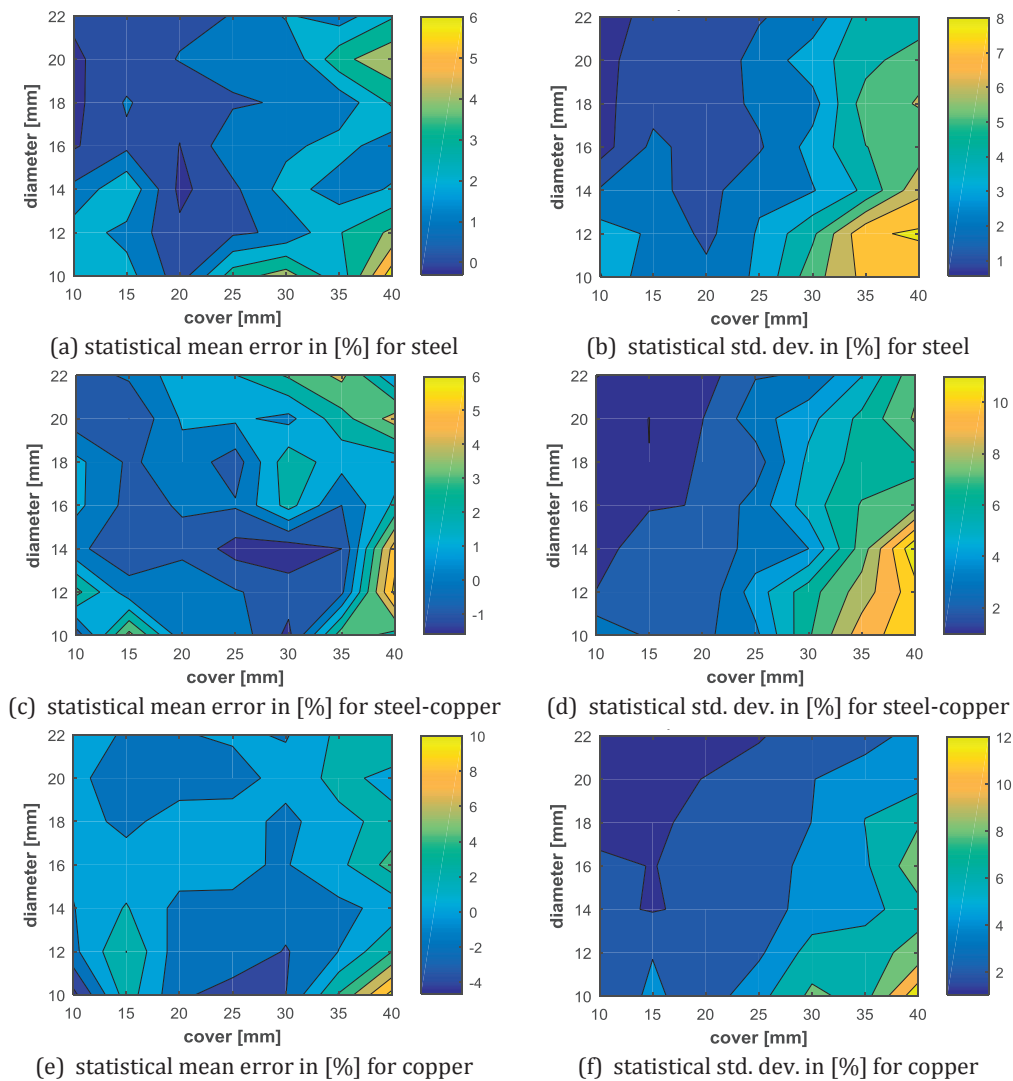


Figure H: 1 The mean and standard deviation error in percentage of cover values. This is a statistical analysis of 20 random white noise levels ranging between -0.5% and +0.5% of the maximum signal induced added to all responses of all cover and diameter values performed at 25 kHz excitation frequency.

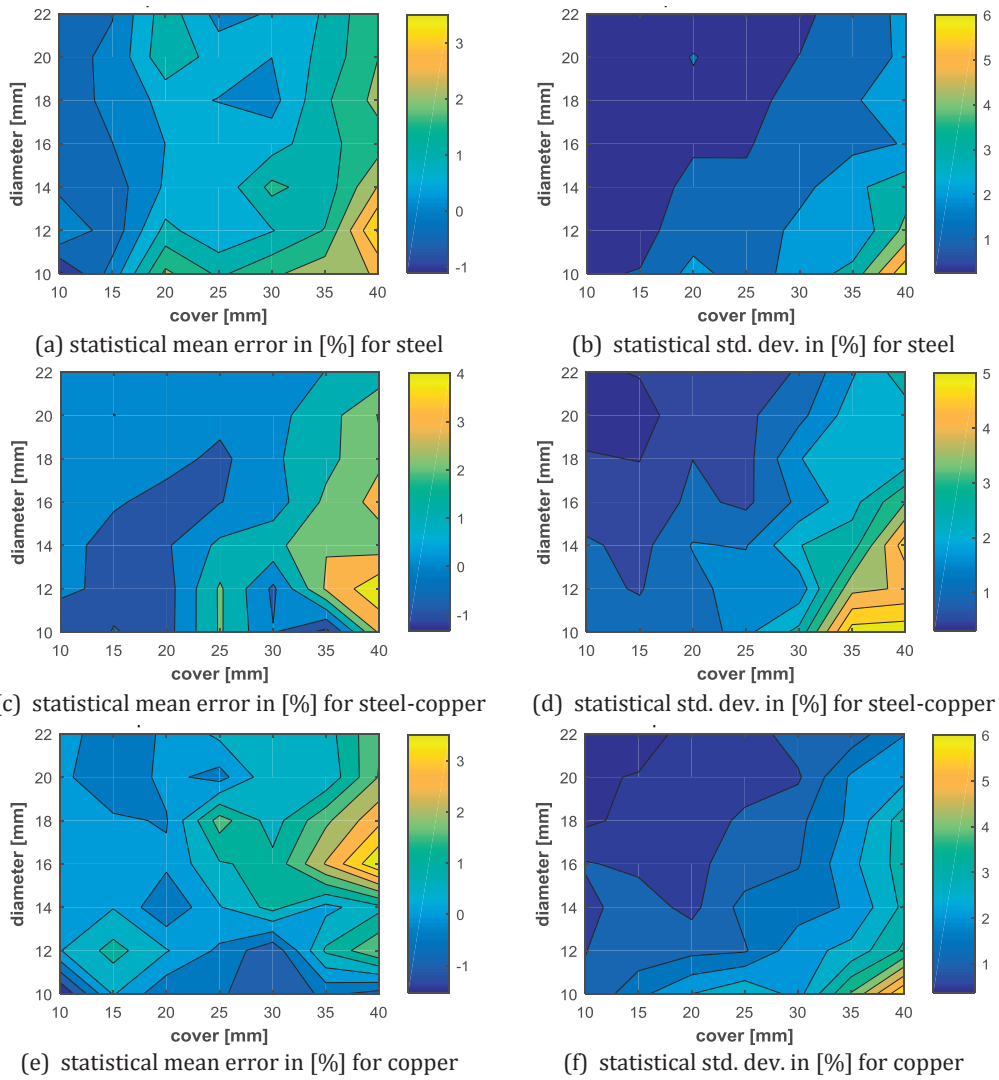


Figure H: 2 The mean and standard deviation error in percentage of cover values. This is a statistical analysis of 20 random white noise levels ranging between -0.5% and +0.5% of the maximum signal induced added to all responses of all cover and diameter values performed at 75 kHz excitation frequency.

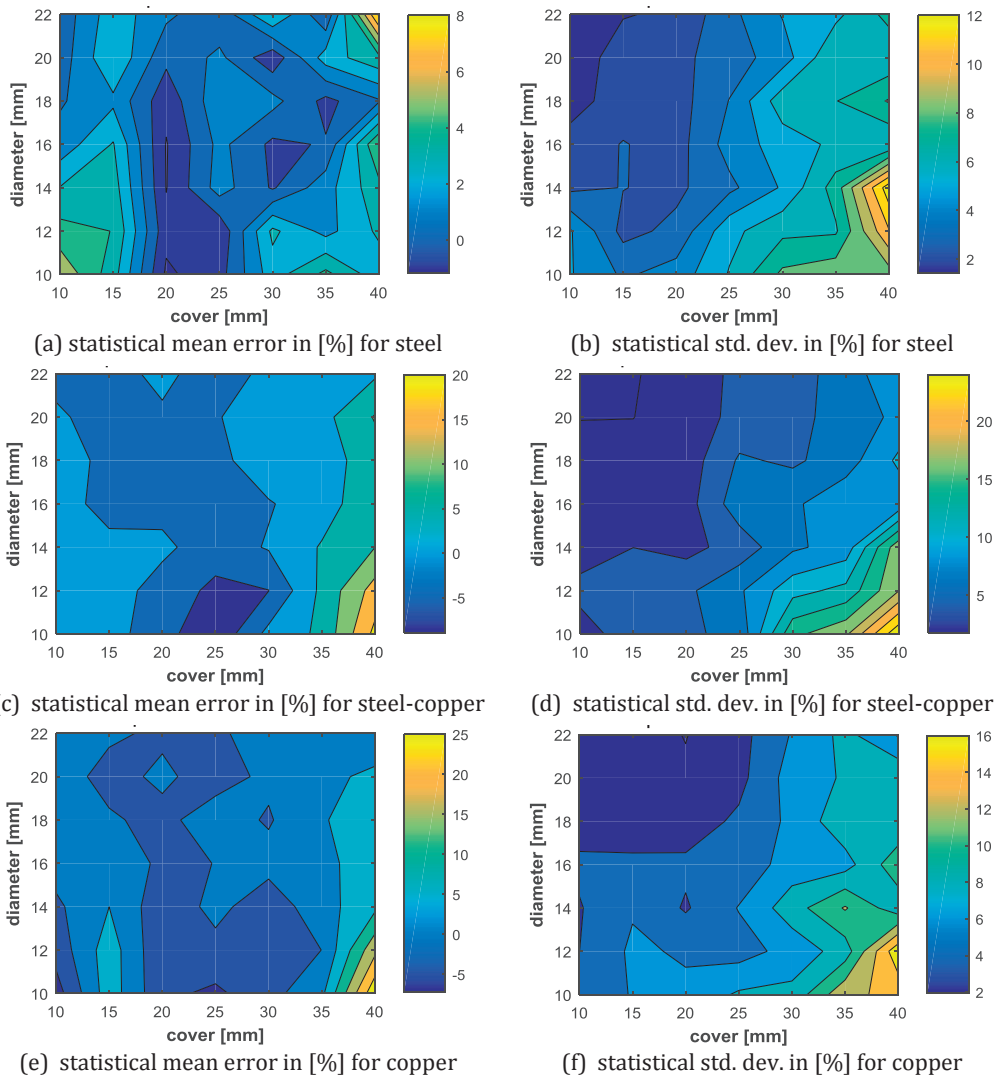


Figure H: 3 The mean and standard deviation error in percentage of cover values. This is a statistical analysis of 20 random white noise levels ranging between -1% and +1% of the maximum signal induced added to all responses of all cover and diameter values performed at 25 kHz excitation frequency.

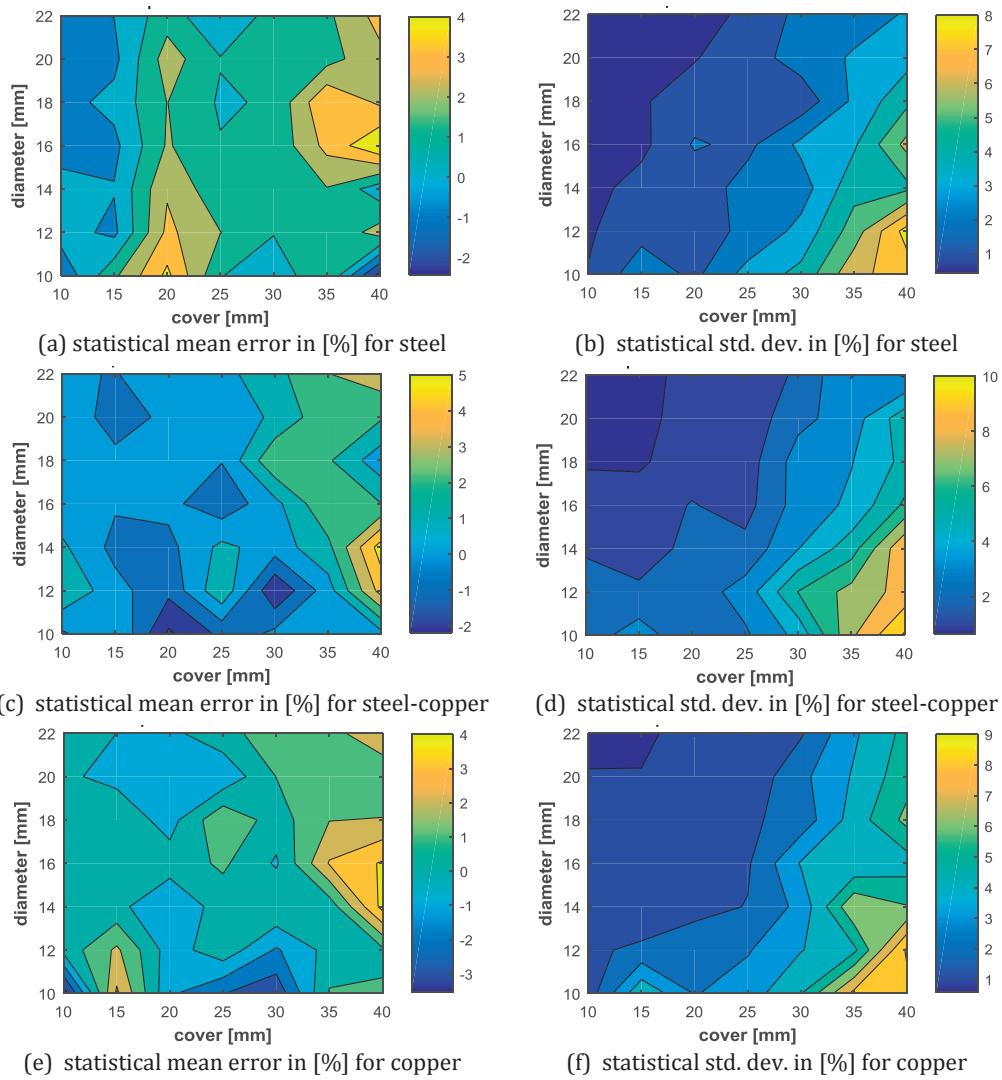


Figure H: 4 The mean and standard deviation error in percentage of cover values. This is a statistical analysis of 20 random white noise levels ranging between -1% and +1% of the maximum signal induced added to all responses of all cover and diameter values performed at 75 kHz excitation frequency.

## Appendix F

Investigating the value of the parameter  $a_1$ , which is fitted to the 'spatial phase response' and should be positive in the case of double material (copper and steel rods placed at the same place). Performing the simulation of all combinations of diameters of copper and steel from 10 mm to 28 mm at 25 kHz leads to 2D results of this parameter. All positive values mean the method is feasible at the corresponding diameter values. The following figure are the results of  $c=30$  mm,  $c=40$  mm, and  $c=50$  mm respectively. In the last figure, the zero-contour line defines the limit of this method.

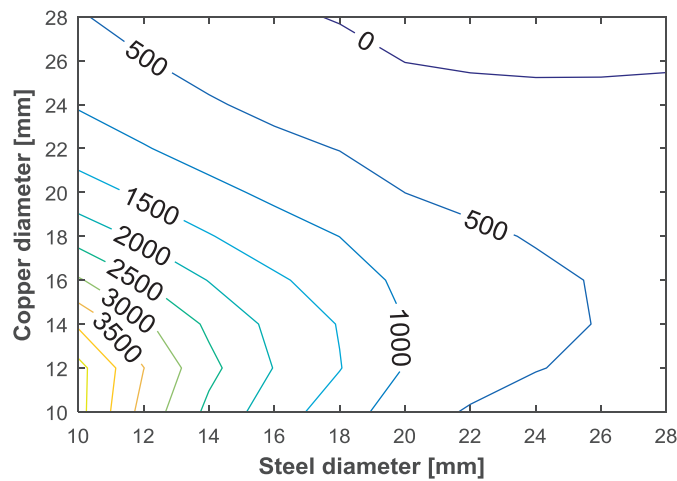


Figure F: 1 The value of  $a_1$  simulated for double rod case where the diameters of steel and copper are different. The operating frequency is 25 kHz and the rods were placed at  $c = 30$  mm.

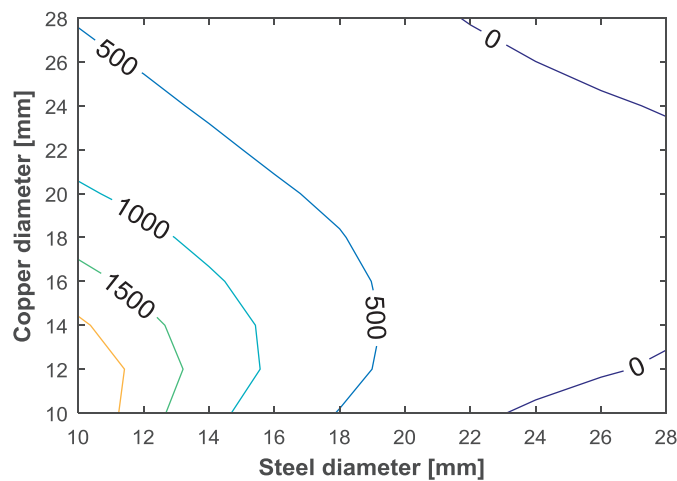


Figure F: 2 The value of  $a_1$  simulated for double rod case where the diameters of steel and copper are different. The operating frequency is 25 kHz and the rods were placed at  $c = 40$  mm.

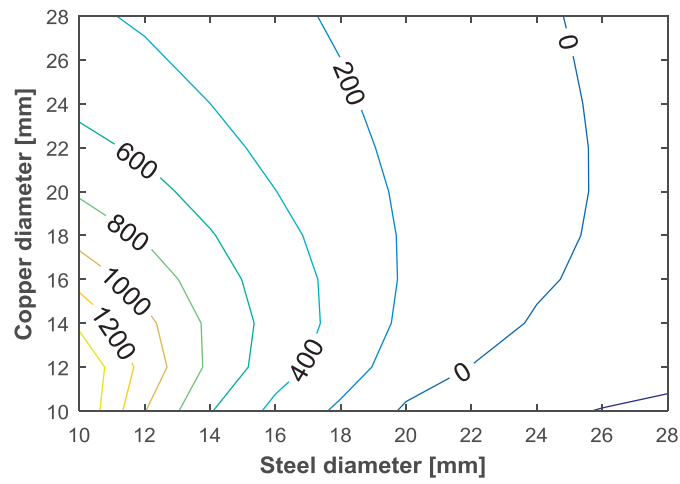


Figure F: 3 The value of  $a_1$  simulated for double rod case where the diameters of steel and copper are different. The operating frequency is 25 kHz and the rods were placed at  $c = 50$  mm.

# Nomenclature

Symbol	Units	Description
$A$	$[m^2]$	area
$A1$ and $A2$	$[V]$ or $[LSB]$	voltage average over a time interval
$A_1(f)$	$[V]$	amplitude of a spatial voltage response at frequency $f$
$a_1$	$[deg\ m^{-2}]$	parameter fit of the spatial phase response
$a$ and $a_0$	$[LSB]$	amplitude parameters of the voltage decay
$a$	$[m]$	radius of the cylinder in the dipole model
$\vec{A}$	$[T\ m]$	magnetic vector potential
$B$	$[T]$	magnetic flux density
$c$	$[m]$	cover distance between the target and sensor
$C$	$[F]$	capacitance
$c_0$	$[V]$	Gaussian fitting parameter
$c_1$	$[mm^2]$	Gaussian fitting parameter
$d$	$[m]$	target cylinder diameter
$D$	$[C\ m^{-2}]$	electric flux density
$D_p$	$[m]$	displacement of the receiver coil to the sender coil
$\delta$	$[m]$	skin depth
$\vec{D}$	$[H\ m^{-1}]$	magnetic dipole field
$f$	$[Hz]$	frequency
$E$	$[V\ m^{-1}]$	electric field
$\varphi$	$[Wb]$	magnetic flux
$\mu$	$[H\ m^{-1}]$	magnetic permeability
$\mu_0$	$[H\ m^{-1}]$	magnetic permeability of free space
$\mu_r$	$[-]$	relative magnetic permeability
$H$	$[A\ m^{-1}]$	magnetic field intensity
$I$ and $i$	$[A]$	electric current
$J$	$[A\ m^{-2}]$	electric current density
$k$	$[complex]$	induction number
$J_0, J_1, \text{ and } J_2$	$[function]$	Bessel functions of the first kind
$L$	$[H]$	inductance
$L$	$[m]$	length of a coil
$\vec{m}$	$[A\ m^{-1}]$	magnetic dipole moment
$M$	$[A\ m^{-1}]$	magnetic moment
$\mathbf{M}$	$[H\ m^{-1}]$	polarizability tensor
$n$	$[-]$	power parameter of the voltage decay
$N$	$[-]$	number of turns of a coil
$p$	$[\%]$	percentage of white noise
$p_w$	$[m]$	copper pad width on a printed circuit board
$p_h$	$[m]$	copper pad height on a printed circuit board
$p_s$	$[m]$	copper pad spacing on a printed circuit board
$R$	$[\Omega]$	resistance
$R$	$[-]$	rotation matrix
$R_0$	$[m]$	effective coil radius
$R_1$ and $R_2$	$[-]$	dimensional ratio of voltage responses
$ratio1$ and $ratio2$	$[-]$	dimensional ratio of voltage responses
$\rho$	$[C\ m^{-3}]$	electric charge density
$\rho$	$[\Omega\ m]$	electric resistivity
$\vec{r}$	$[m]$	position vector
$\vec{s}$	$[m]$	Line segment vector
$S$	$[m^2]$	surface
$\sigma$	$[S\ m^{-1}]$	electric conductivity
$t$	$[s]$	time
$t_0$	$[s]$	time parameter of the voltage decay



## Nomenclature

---

$t_{drop}$	[s]	time constant quantity
$\tau$	[s]	time interval
$\theta$	[deg]	electric phase angle
$U$ and $u$	[V] or [LSB]	voltage
$w$	[rad s <sup>-1</sup> ]	angular frequency
$W$	[m]	width of a coil
$x$	[m]	target location in lateral, transverse, or scan direction
$\chi$	[--]	magnetic polarizability
$\chi_{\parallel}$ and $\chi_{\perp}$	[--]	parallel and transverse magnetic polarizabilities
$Z$	Complex [V]	white noise

---

# References

- [1] "The American Society for Nondestructive Testing," [Online]. Available: [www.asnt.org](http://www.asnt.org).
- [2] "European Federation of Non-Destructive Testing," [Online]. Available: [www.efndt.org](http://www.efndt.org).
- [3] «The British Institute of Non-Destructive Testing,» [En ligne]. Available: <http://www.bindt.org/>.
- [4] "Australian Institute for Non-Destructive Testing," [Online]. Available: [www.aindt.com.au](http://www.aindt.com.au).
- [5] "Indian Society for Non-Destructive Testing," [Online]. Available: [www.isnt.org.in](http://www.isnt.org.in).
- [6] E. E. Kriezis, T. D. Tsiboukis, S. M. Panas and J. A. Tegopoulos, "Eddy Currents Theory and Applications," *IEEE*, 1992.
- [7] A. Langman and M. Inggs, "A Stepped Frequency CW Polarimetric Radar for Mine Detection," *IEEE*, 1996.
- [8] J. Philip, C. Rao, T. Jayakumar and B. Raj, "A new optical technique for detection of defects in ferromagnetic materials and components," *NDT&E International*, vol. 33, pp. 287-295, 2000.
- [9] N. Ida and W. Lord, "A Finite Element Model for Three-Dimensional Eddy Current NDT Phenomena," *IEEE TRANSACTIONS ON MAGNETICS*, 1985.
- [10] K. O'Neill, K. Sun, C. Chen, F. Shubitidze and K.D.Paulsen, "Combining GPR And EMI Data for Discrimination of Multiple Subsurface Metallic Objects," *IEEE*, 2003.
- [11] P. Jagerbro, B. Brusmark, A.-L. Christiansen and A. Lauberts, "Combination Of GPR and Metal Detector for Mine Detection," FOA Defence Research Establishment, Sweden, 1999.
- [12] K. Mayer, A. Zimmer, K. J. Langenberg, C. Kohl and C. Maierhofer, "Nondestructive Evaluation of Embedded Structures in Concrete Modeling and Imaging," *NDT In Civil Engineering*, 2003.
- [13] C. O. Ao, H. Braunisch, K. O'Neill and J. A. Kong, "Quasi-Magnetostatic Solution for a Conducting and Permeable Spheroid with Arbitrary Excitation," *IEEE Transactions on Geoscience and Remote Sensing*, 2002.
- [14] T. P. Montoya and G. S. Smith, "Land Mine Detection Using a Ground-Penetrating Radar Based on Resistively Loaded Vee Dipoles," *IEEE Transactions on Antennas and Propagation*, 1999.
- [15] A. Bernieri and L. F. G. Betta, "Characterization of a Magnetic measurement system for NDT," *IEEE Transaction on Instrumentation and Measurement*, 2002.
- [16] D. Vasic, V. Bilas and D. Ambrus, "Pulsed Eddy-Current Nondestructive Testing of Ferromagnetic Tubes," *IEEE Transactions on Instrumentation and Measurement*, vol. 53, no. 4, pp. 1289 - 1294 , 2004.
- [17] R. Callarotti and M. Alfonzo, "Measurement of the Conductivity of Metallic Cylinders by Means of an Inductive Method," *Journal of Applied Physics*, 1972.
- [18] W. Chen, G. Zhang, Y. Sun and M. Chen, "Integrated Third Kind Boundary Condition for 2D Eddy Current Problems and Its Application in NDT," *Proceedings of the IEEE*, Oct 1993.
- [19] W. Renhart and C. Magele, "Optimal Design of a Coil Arrangement for the Identification of Hidden Ferrous Objects," *IEEE Transaction on Magnetics*, 2002.
- [20] C. D. Moss, K. O'Neill, T. M. Grzegorzczuk and J. A. Kong, "A Hybrid Time Domain Method to Calculate Electromagnetic Induction Scattering from Targets with Arbitrary Skin Depths," --.

## References

---

- [21] C. Abu Antoun, C. Würsch, C. Köchli and Y. Perriard, "Validity Tests of Superposition Principle Based on Forward Model for Electromagnetic Induction Scattering," in *Conference on Electromagnetic Field Computation (CEFC)*, Annecy, France, 2014.
- [22] C. Abu Antoun, C. Würsch, C. Köchli and Y. Perriard, "Validity Tests of Superposition Principle Based on Forward Model for Electromagnetic Induction Scattering," *IEEE Transactions on Magnetics*, vol. 51, no. 3, pp. 1-4, 2015.
- [23] C. Abu Antoun, "Scanning Detector and Control Method". Switzerland Patent EP16158912.2, 7 March 2016.
- [24] C. Abu Antoun, "Detection Method for a Scanning Detector". European Patent Office Patent EP17155094.0, 8 February 2017.
- [25] C. Abu Antoun and Y. Perriard, "Robust and efficient 3D model of an electromagnetic induction (EMI) sensor," in *International Conference on Electrical Machines and Systems (ICEMS)*, Busan, South Korea, 2013.
- [26] C. Abu Antoun and Y. Perriard, "Robust and Efficient 3D Model of an Electromagnetic Induction (EMI) Sensor," *Journal of International Conference on Electrical Machines and Systems*, vol. 3, no. 3, 2014.
- [27] C. Abu Antoun, C. Würsch, C. Köchli and Y. Perriard, "Frequency Analysis of Finite Steel Cylinders and their Comparison to Complex Cylinder-like Targets using an Electromagnetic Induction Sensor," in *International Conference on Electromagnetics in Advanced Applications (ICEAA)*, Torino, 2015.
- [28] I. Won and D. Keiswetter, "Electromagnetic Induction Spectroscopy," in *Conference on Detection and Remediation Technologies for Mines and Minelike Targets*, Orlando, 1998.
- [29] C. E. Hegel, "Swept range gate radar system for detection of nearby objects". United States of America Patent 5,543,799, 6 August 1996.
- [30] I. Giannakis, S. Xu, P. Aubry, A. Yarovoy and J. Sala, "Signal processing for landmine detection using ground penetrating radar," *IEEE International Geoscience and Remote Sensing Symposium (IGARSS)*, Beijing, pp. 7442-7445, 2016.
- [31] S. Liedtke and S. Tichy, "Method and sensor for detecting foreign bodies in a medium with a radar". United States of America Patent 6366232, 2 April 2002 .
- [32] I. van den Bosch, A. van der Vorst and S. Lambot, "Buried target signature extraction from ground penetrating radar signal based on the equivalence principle," in *Proceedings of the Tenth International Conference on Grounds Penetrating Radar*, Delft, The Netherlands, 2004.
- [33] W. E. Inc, "Induction Balance Metal Detector with Inverse Discrimination". United States of America Patent US4024468, 1977.
- [34] R. Gerd, "Sensor Zum Detektieren Metakischer Objekte". Germany Patent WO2010133501A1.
- [35] H.-B. Lee and D.-H. Kim, "Numerical Analysis of Eddy Current NDT for a Tube with Cracks Using 3D Indirect Biem," *IEEE Transactions On Magnetics*, 1999.
- [36] X.-L. Chen and X.-L. Wang, "The Design of Testing System Based on Eddy Current Technology," *IEEE*, 2011.
- [37] J. LePage, A. Bernalte and D. A. Lindholm, "Analysis of Resistivity Measurements by the Eddy Current Decay," *Journal on Applied Physics*, 1968.
- [38] Z. Zakaria, «Advancements in Transmitters and Sensors for Biological Tissue Imaging in Magnetic Induction Tomography,» *Sensors*, vol. 12, n° 16, pp. 7126-7156, 2012.
- [39] P. Silvester and D. Omeragic, "Sensitivity maps for metal detector design," *IEEE Trans. Geo. Rem. Sens.*, vol. 34, no. 3, pp. 788-792, 1996.

## References

---

- [40] Y. Das, J. E. Mcfee and R. H. Chency, "Time Domain Response of a Sphere in the Field of a Coil: Theory and Experiment," *IEEE Transactions on geoscience and remote sensing*, Vols. GE-22, no. 4, 1984.
- [41] H. Heuer, M. H. Schulze and N. Meyendorf, Non-destructive evaluation (NDE) of composites: eddy current techniques, Woodhead Publishing Limited, 2013.
- [42] D. Roy, B. K. Kaushik and R. Chakraborty, "A novel E-shaped coil for eddy current testing," *Sensor Review*, vol. 33 , no. 4, pp. 363-370, 2013.
- [43] W. Yin and A. J. Peyton, "A planar EMT system for the detection of faults on thin metallic plates," *Institute of Physics Publishing, Meas. Sci. Technol.* , vol. 17, p. 2130–2135, 2006.
- [44] J. Íñiguez, V. Raposo and P. Hernández, "Study of Inhomogeneities in Non-Magnetic Tubes by Means of a Contactless Inductive Technique," *Materials Science Forum*, Vols. 587-588, pp. 258-262 , 2008.
- [45] W. Zhu, W. Yin, C. Davis, P. Hunt, S. Dewey and A. Peyton, "Modelling and experimental study of magnetic induction spectroscopy for rail decarburisation measurement," in *IEEE, Far East Forum on Nondestructive Evaluation/Testing*, Jinan, China, 2014.
- [46] J. Salach, R. Szewczyk and M. Nowicki, "Eddy current tomography for testing of ferromagnetic and non-magnetic materials," *Institute of Physics Publishing, Meas. Sci. Technol.*, vol. 25, no. 2, 2014.
- [47] J. Atzlesberger and B. Zagar, "Detection of inhomogeneities in magneto-conductive objects," in *Eighth International Multi-Conference on Systems, Signals & Devices*, Sousse, 2011.
- [48] C. Bruschini and H. Sahli, "Phase-angle-based EMI object discrimination and analysis of data from a commercial differential two-frequency system," *Det. and Rem. Tech. for Minelike Targets*, vol. 1404, 2000.
- [49] I. Shamatava, K. O'Neill, F. Shubitidze, K. Sun and C. Ao, "Evaluation of approximate analytical solutions for EMI scattering from finite objects of different shapes and properties," *IEEE International Geoscience and Remote Sensing Symposium*, vol. 3, pp. 1550-152a, 2002.
- [50] T. H. Bell, B. J. Barrow and J. T. Miller, "Subsurface discrimination using electromagnetic induction sensors," *IEEE Transactions on Geoscience and Remote Sensing*, vol. 39, no. 6, pp. 1286-1293, 2001.
- [51] S. Tumanski, "Induction coil sensors—a review," *Meas. Sci. Technol.*, vol. 18, p. R31–R46, 2007.
- [52] S. Tumanski, "Magnetic sensors," in *Handbook of Magnetic Measurements*, CRC Press, 2011, pp. 172-186.
- [53] C. P. Bean, R. W. DeBlois and L. B. Nesbitt, "Eddy-Current Method for Measuring the Resistivity of Metals," *Journal on Applied Physics*, 2006.
- [54] J. W. Luquire, W. E. Deeds and C. V. Dodd, "Axially Symmetric Eddy Currents in a Spherical Conductor," *Journal of Applied Physics*, 1970.
- [55] C. V. Dodd and W. E. Deeds, "Analytical Solutions to Eddy Current Probe Coil Problems," *Journal of Applied Physics*, 1968.
- [56] T. Yu and L. Carin, "Analysis of the Electromagnetic Inductive Response of a Void in a Conducting-Soil Background," *IEEE Transactions on Geoscience and Remote Sensing*, 2000.
- [57] Y. Das, J. E. Mcfee, J. Toews and G. Stuart, "Analysis of an Electromagnetic Induction Detector for Real-Time Location of Buried Objects," *IEEE Transactions on Geoscience and Remote Sensing*, 1990.
- [58] Y. Das, J. E. Mcfee and R. H. Chesney, "Determination of Depth of Shallowly Buried Objects by Electromagnetic Induction," *Transactions on Geoscience and Remote Sensing*, 1985.
- [59] R. Gerd, "Metal Detektor". Germany Patent DE102009021804A1, 2010.

## References

---

- [60] K. Pospisil, J. Stryk, M. Korenska and L. Pazdera, "Selected Acoustic Methods for Nondestructive Testing," *NDT in Civil Engineering*, 2003.
- [61] C. Miclea, A. Gheorghiu, V. Tanasoiu, C. F. Miclea and S. Moroianu, "A New and Versatile Sandwich Type Ultrasonic Transducer for NDT Of Different Materials," *NDT in Civil Engineering*, 2003.
- [62] R. Marklein, K. Mayer, P. Ampha and K.-J. Langenberg, "Computer Simulation of Ultrasonic Non-Destructive Testing of Concrete Using the Elastodynamic Finite Integration Technique (EFIT)," *NDT in Civil Engineering*, 2003.
- [63] M. Schickert, "Progress in Ultrasonic Saft-Imaging of Concrete," *NDT in Civil Engineering*, 2003.
- [64] J. Leonhardt, A. Kuster and H. Neff, "Combining Neutron Rackscattering and Active Electro-Magnetic Metal Detection," *IEEE*, 1996.
- [65] C. Andrade, I. Martínez, M. Ramírez and M. García, "Non Destructive Techniques For On Site Measurements Of Reinforcement Corrosion In Concrete Structures," *NDT in Civil Engineering*, 2003.
- [66] C. P. Steinmetz, Lectures on Electrical Engineering, Vol. III, Mineola, Ny, U.S.A: Dover Publications, 2003.
- [67] G. W. Hanson and C. E. Baum, "Asymptotic Analysis of the Natural System Modes of Coupled Bodies in the Large-Separation Low-Frequency Regime," *IEEE Transactions on Antennas and Propagation*, 1999.
- [68] V. A. Sandovskii, V. V. Dyakin and M. S. Dudarev, "Frequency dependence of the magnetic permeability of hollow cylindrical," *Russian Journal of Nondestructive Testing*, 2000.
- [69] D. Swanson and W. Hoefer , Microwave Circuit Modeling Using Electromagnetic Field Simulation, Artech House Microwave Library, 2003.
- [70] Y. K.S, "Numerical Solution of Initial Boundary-Value Problems Involving Maxwell's Equations in Isotropic Media," *IEEE Trans. Ant. Prop.*, Vols. Vol. AP-14, no. 5, pp. 302-307, 1996.
- [71] C. Würsch, "Induktiver Array Sensor zur ortung, klassifizierung, und vermessung von metallischen Objekten in Wänden, Böden, und Decken - Technologie und Realisierung, KTI-Nr. 14469.1 PFIW-IW," Commission for Technology and Innovation, CTI, Bern, Switzerland, 2015.
- [72] ANSYS, "Mechanical APDL Theory Reference," 2015. [Online]. Available: <http://148.204.81.206/Ansys/150/ANSYS%20Mechanical%20APDL%20Theory%20Reference.pdf>.
- [73] W. R. Smythe, Static and Dynamic Electricity, New York, NY: McGraw-Hill Book Co, 1950.
- [74] C. Abu Antoun, C. Würsch, C. Köchli and Y. Perriard, "Smart self-calibrated metal detector, simulated, designed, verified, and used to discriminate single and multiple materials," in *Advances In Magnetism, AIM*, Bormio, Italy, 2016.
- [75] M. L. Burrows, «The theory of eddy-current flaw detection,» The University of Michigan, PhD thesis, Michican, U.S.A., 1964.
- [76] J. R. Wait, Geo-Electromagnetism, New York, U.S.A.: Academic Press, 1982.
- [77] F. S. Grant and G. F. West, Interpretation Theory in Applied Geophysics, Ohio, U.S.A.: McGraw-Hill Companies, 1965.
- [78] F. Shubitidze, K. O'Neill and K. D. Paulsen, "Investigation of broadband electromagnetic induction scattering by highly conductive, permeable, arbitrarily shaped 3-D objects," *IEEE Transactions on Geoscience and Remote Sensing*, vol. 42, no. 3, pp. 540-556, March 2004.
- [79] S. K. Verma, "Quasi-static time-domain electromagnetic response of a homogeneous conducting infinite cylinder," *Geophysics*, vol. 37, no. 1, pp. 92-97, February 1972.

## References

---

- [80] W. Kertz, "Leitungsfähiger Zylinder im transversalen magnetischen Wechselfeld," *Geophysics*, vol. 1, pp. 4-28, 1960.
- [81] J. T. Smith, H. F. Morrison and A. Becker, "Parametric Forms and the Inductive Response of a Permeable Conducting Sphere," Lawrence Berkeley National Laboratory, Berkeley, California 94720.
- [82] C. Abu Antoun, C. Würsch, C. Köchli and Y. Perriard, "Balanced Metal Detector Based on Optimized Frequencies and Spatial Phase Profile Responses to Differentiate Metal Rods," *IEEE Magnetics Letters*, vol. 8, no. 1, pp. 0-5, 2017.
- [83] Y. He, F. Luo, M. Pan, X. Hu, J. Gao and B. Liu, "Defect classification based on rectangular pulsed eddy current sensor in different directions," *Elsevier*, 2009.
- [84] "The British Institute of Non-Destructive Testing," [Online]. Available: [www.bindt.org](http://www.bindt.org).
- [85] J. Van Hese, J. Sercu, D. Pissort and H.-S. Lee, *State of the Art in EM Software for Microwave Engineers*, USA: Keysight Technologies, 2014.

# Curriculum Vitae

Chafic Abu Antoun  
Lagerstr. 2, Buchs SG, Switzerland  
[shafic@shafic.com](mailto:shafic@shafic.com)

Male  
22 June 1979  
Lebanese

## EMPLOYMENT HISTORY

Sep. 2000	<b>Trans Mediterranean Airlines,</b> Beirut, Lebanon	<b>Trainee</b> Maintenance and control on: pneumatic system, hydraulic system, jet engine and landing gear
Sep. 2002	<b>Institut Universitaire de Technologie,</b> Cachan, France	<b>Trainee</b> Design and manufacturing of mechanical parts (CAD-CAM) scholarship granted by the French government
2003	<b>Methode Electronics International,</b> Gau-Algesheim, Germany	<b>Project engineer</b> Design of plastic parts for mechatronic automotive switches
2003-2007	<b>Roland Ruegenberg GmbH</b> Bad Sobernheim, Germany (Also Teetronic GmbH and Vaniatronic GmbH were led by Roland Ruegenberg)	<b>Project engineer</b> Design optimization of floating horn mechanism Production/prototyping of aluminum parts milled by CNC. Implementation of prototype in Mercedes and VW, "Pioniergeist 2005" award Optimization of capacitive based torque sensor by reducing the number of input signals and linearizing the output including electrostatic FEM simulations for validation Design of mechatronic steering wheel switches for Ford Mondeo and Galaxy respecting the electronics, mechanism, mold-ability of the parts and the tolerance stack of the whole assembly. Optimizing the light pipe by light simulation Feasibility study of a position sensor based on permanent magnet and Hall sensors
2006-2007	<b>Hilti AG,</b> Corporate Research & Technology, Schaan, Liechtenstein	<b>Master thesis work</b> Optimization of a gas combustion based fastening tool. Thermodynamics and fluid dynamics using ANSYS, ANSYS CFX, ANSYS ICEMCFD, MATLAB)
2007-pres.	<b>Hilti AG,</b> Corporate Research & Technology, Schaan, Liechtenstein	<b>Research engineer</b> Simulation models of electro-thermal coupling in Lithium Ion batteries Simulation model of transient electromagnetic FEM with eddy currents and EMF. The model is validated with functional demonstrator motors and actuators (ANSYS, MATLAB) Simulation model of transient electromagnetic FEM at medium frequency coupled to heat transfer with a two-way coupling for induction heating, induction hardening manufacturing process Detection by induction sensor 3D simulation CFD motor cooling by conjugate heat transfer High Performance Computing (HPC). Explicit dynamics simulation of impact mechanisms (LSDYNA)

## Curriculum Vitae

---

### EDUCATION

1984-1997	<b>Brummana High School,</b> Brummana, Lebanon	<b>Scientific Bacallaureates</b> Graduation with honors
1997-2000	<b>University of Balamand,</b> EL Koura, Lebanon	<b>B.Sc. in Mechanical Engineering</b>
2000-2002	<b>University of Balamand,</b> EL Koura, Lebanon	<b>M.Sc. in Mechanical Engineering</b> Thesis: 'The Effect of Fiber Waviness on Elastic Behavior of Composite Materials' Student Excellence Award
2005-2007	<b>Stuttgart University,</b> Stuttgart, Germany	<b>M.Sc. in Computational Mechanics of Materials and Structure</b> Thesis: 'Multidisciplinary Optimization of the Thermodynamic Behavior of a Gas Powered Fastening Tool Materials' Thesis funded by Hilti AG Scholarship
2012-2017	<b>École Polytechnique Fédérale de Lausanne,</b> Lausanne, Switzerland	<b>Doctoral assistant (PhD student)</b> Method and Procedure in Metal Detection and Distinctive Discrimination of Size, Shape, and Location of Hidden Single and Multi-Material Targets

### SOFTWARE SKILLS

- CAD                    CATIA V5 R16 (+++), UG NX9 (++) , AutoDesk Inventor 8.0 (++)
- CNC                    Visual Mill 5 (+), Surfcam 2004 (+)
- FEM                    ANSYS 171 (+++), LS-Dyna971 (+), MSC Nastran 4.5 (++)
- CFD                    ANSYS CFX 171 (++)
- Dynamics            MSC Visual Nastran 4D 2003 (+++), Mechanical Dynamics Adams 11 (+)
- Meshing              ANSYS ICEMCFD 171 (++)
- Schematic            Simplorer 17.1 (+) Orcad 10.0 (+), Protel DXP (+)
- Pcb layout            Altium 14 (++)
- Others                Matlab 2013 (++) , MoldFlow Plastic Insight 4.1 (+)

(+++): excellent    (++): good            (+): basic

### PAPERS AND JOURNALS

- Balanced Metal Detector Based on Optimized Frequencies and Spatial Phase Profile Responses to Differentiate Metal Rods, IEEE Magnetic Letters, vol.8, no.1, pp.0-5, Dec. 2017
- Smart self-calibrated metal detector, simulated, designed, verified, and used to discriminate single and multiple materials, Advances in Magnetics, Mar. 2016, Bormio, Italy
- Frequency Analysis of Finite Steel Cylinders and their Comparison to Complex Cylinder-like Targets using an Electromagnetic Induction Sensor, International Conference on Electromagnetics in Advanced Applications (ICEAA), Sep. 2015, Torino, Italy
- Validity Tests of Superposition Principle Based on Forward Model for Electromagnetic Induction Scattering, IEEE Transactions on Magnetics, vol.51, no.3, pp.1-4, March 2015
- Robust and Efficient 3D Model of an Electromagnetic Induction (EMI) Sensor, Journal of International Conference on Electrical Machines and Systems, September 2014, Vol. 3 Number 3
- Validity Tests of Superposition Principle Based on Forward Model for Electromagnetic Induction Scattering, Conference on Electromagnetic Field Computation, (CEFC), May 2014, Annecy, France
- Robust and Efficient 3D Model of an Electromagnetic Induction (EMI) Sensor, International Conference on Electrical Machines and Systems, 2013, Busan, S. Korea
- The Effect of Fiber Waviness on Elastic Behavior of Composite Materials, Proceedings of the American Society for Composites 2002, W. Lafayette, IN, USA
- Micromechanical Formulation of Multilayered Composites in Thermo-elasticity, Proceedings of the American Society for Composites 2001, Blacksburg, VA, USA



## Curriculum Vitae

---

### PATENTS

- Detection Method for a Scanning Detector (EP 17155094.0)
- Scanning Detector and Control Method (EP 16158912.2)
- Machine Tool and Control Method (US 2013/0333904)
- Fastener-Driving Device and Controlling Method (US 2013/0336809)
- Striking Mechanism and Hand-Held Power Tool (US 2010/0206593)
- Linear Motor (US 2009/0127940)

### INTERESTS

Skiing, mountain biking, inline skating, tennis, hiking, psychology, electromagnetics, coupled systems, multi-field simulation

